

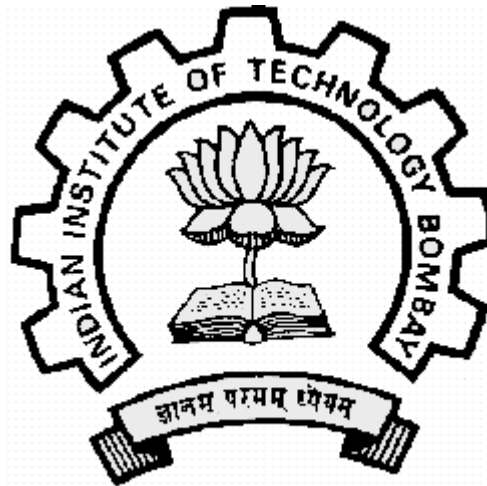
Flow Modeling and Mixing in Packed Bed Reactor

Submitted in partial fulfillment of the requirements
for the degree of

Doctor of Philosophy

by

Gunjal Prashant Ramchandra



Department of Chemical Engineering
Indian Institute of Technology, Bombay
(2005)

Thesis Entitled : Flow Modeling and Mixing in Packed Bed Reactor

by: Gunjal Prashant Ramachandra

is approved for the degree of DOCTOR OF PHILOSOPHY

Examinars _____

Supervisor(s) _____

Chairman _____

Date: _____

Place: _____

INDIAN INSTITUTE OF TECHNOLOGY, BOMBAY, INDIA

CERTIFICATE OF COURSE WORK

This is to certify that Mr. Gunjal Prashant Ramachandra was admitted to the candidacy of the Ph.D. Degree on 1 January 2000 after successfully completing all the courses requirement for the Ph.D. Degree programme. The details of the course work done are given below.

Sr.No.	Course No.	Course Name	Credits
1	CL601	Advanced Transport Phenomena	6
2	CL602	Mathematical and statistical methods in Chem Eng	6
3	CL603	Optimization	6
4	CL605	Advanced Reaction Engineering	6
5	CL608	Fluidization Engineering	6
6	CL682	Computer Aided Design and Engineering	6
7	AE702	Computational Fluid Dynamics	6

I.I.T. Bombay

Dy. Registrar(Academic)

Dated:

*with love,
to my Friends
Parents and
Teachers*

Acknowledgements

This thesis is presentation of the research work carried out in last four years within 'Industrial Flow Modeling Group' of National Chemical Laboratory, Pune, India. This research work comprise of experimental as well as theoretical study of flow inside the packed/trickle bed reactors and its implications on mixing and performance of the reactor. I hope reading this piece of work will provide a good impression about various aspects of the fascinating subject fluid dynamics of gas-liquid flow through porous/packed structures.

This work was carried out under the 'strict guidance (with infinite freedom)' of Dr. V. V. Ranade. I appreciate his enthusiastic nature and long patience. He has been a constant source of inspiration and motivation for me. Long discussions with him were found to be useful for getting clarity of the subject and a seed for new ideas. I would like to thanks to Dr. R. V. Chaudhari for introducing me trickle bed reactor and various aspects of reaction engineering. I would like to thank to Prof. V. G. Rao of IITB for his time-to-time discussions and guidelines during the research work. I would also like to thanks to Research Progress Committee members, Prof. V. A. Juwekar and D. V. Khakhar of IITB for their valuable suggestions and guidelines. I am grateful to Council of Scientific and Industrial Research (CSIR), India and Department of Science and Technology grant (no.

DST/SF/40/99) for financially supporting this research work.

In NCL, before starting research program, I worked with several scientist, Dr. Gupte, Dr. Sabhapati, Dr. Kelkar, Dr. Deshpande, Dr. Zadkar and Dr. Jagganathan. I thank to all of them. I greatly appreciate various kind of support from our group members; Vivek Buwa, Ranjeet Utikar, Avinash Khopkar, Kaustubh Mujumdar, Mohan Rampure, Madhav Kashid, Yogesh Harshe, Ajay Gorasi, Amit Aror, Arawind and Arpita and several other past and present members of Industrial Flow Modelling Group.and division members. I am thankful to our several departmental member; Vinod Nair, Suju Mathew, Yogesh Borole, Sunil Tonde and Avinash Mahajan and many other who made my social life enjoyable. I also appreciate the work support from workshop and other utility departments.

Finally I would like appreciate the great support from my family members during this work.

Gunjal Prashant

Table of Contents

Table of Contents	v
List of Figures	ix
List of Tables	xvi
Nomenclature	xvii
1 Introduction	1
1.1 Motion of Fluids in Packed Bed	2
1.2 Background and Motivation	5
1.3 Objectives	8
1.4 Methodology	9
1.5 Contribution of the Thesis	12
1.6 Outline of Thesis	13
I Microp-scopic Flow Processes	17
2 Single Phase Flow Through Packed Bed	18
2.1 Introduction	19
2.2 Computational Model	23
2.2.1 Governing Equations	26
2.2.2 Boundary Conditions	28
2.3 Result and Discussion	30
2.3.1 Validation of CFD Model	30
2.3.1.1 Comparison with Experimental Data of <i>Suekane et al.(2003)</i>	30
2.3.1.2 Comparison of Results with Analytical Solution	36

2.3.1.3	Comparison of Results with <i>Hill et al.</i> and <i>Dhole et al.</i> . . .	39
2.3.2	Influence of Reynolds number	40
2.3.3	Influence of Packing Arrangement	42
2.3.4	Relative Contributions of Shear Drag and Form Drag	45
2.3.5	Effect of Flow Structure on Heat Transfer	50
2.4	Conclusion	53
3	Liquid Drop Spreading on Solid Surface	55
3.1	Introduction	56
3.2	Previous Work	57
3.3	Present Contribution	61
3.4	Experimental Set-up and Procedure	62
3.5	Computational Model	65
3.5.1	Mathematical Model	67
3.5.2	Solution Domain and Computational Grid	69
3.5.3	Boundary Conditions and Numerical Solution	70
3.5.4	Aspects of VOF Method	72
3.5.5	Geometric interface reconstruction scheme	72
3.5.6	Advection of fluid through the control volume	74
3.5.7	Wall adhesion and the movement of contact line	75
3.6	Results and Discussion	77
3.6.1	Impact of Drop on Solid Surface: Physical Picture/Regimes	77
3.6.2	VOF Simulations of Drop Impact on Solid Surface	78
3.6.3	Influence of System Parameters on Dynamics of Drop	83
3.6.3.1	Influence of Drop Diameter	83
3.6.3.2	Influence of Impact Velocity	86
3.6.3.3	Influence of contact angle and surface tension	93
3.6.3.4	Influence of non-wetting behavior on drop dynamics	94
3.6.3.5	Comments on comparison of experimental and computational results	94
3.6.3.6	Interaction of liquid drop and flat surface	98
3.7	Conclusion	106

II	Reactor Scale Flow Processes	108
4	Experimental Measurements in Trickle Bed Reactors	109
4.1	Introduction	110
4.1.1	Physical picture and flow regimes in trickle bed reactors	110
4.1.2	Previous work	112
4.1.3	Present contribution	114
4.2	Experimental Setup and Operating Procedure	115
4.2.1	Experimental setup	115
4.2.1.1	Operating parameters and procedure	117
4.3	Results and Discussion	118
4.3.1	Dynamics of gas-liquid flows and regime transition	118
4.3.2	Time averaged pressure drop and liquid hold-up	123
4.4	Summary and Conclusions	125
5	Computational Flow Model for Trickle Bed Reactors	130
5.1	Introduction	131
5.1.1	Present Contribution	133
5.2	Computational Model and Boundary Conditions	134
5.2.0.1	Representing non-uniform porosity distribution	135
5.2.1	Model equations	136
5.2.2	Boundary Conditions and Numerical Solution	143
5.3	Results and Discussion	144
5.3.1	Comparison of model predictions with the experimental data	144
5.3.2	Estimation of the fraction of suspended liquid	148
5.3.3	CFD simulations of periodic flow	155
5.4	Summary and Conclusions	163
III	Application of CFD Model	164
6	RTD and Liquid Distribution in TBR	165
6.1	Introduction	166
6.2	Experimental Set-up and Procedure	167
6.2.1	Experimental Set-up	167

6.2.1.1	Operating Parameters and Procedure	168
6.3	Computational Model for RTD Studies	170
6.3.1	Experimental Data of Residence Time Distribution	172
6.3.2	CFD Simulations of Tracer Mixing in Trickle Bed	175
6.3.3	Effect of Bed Heterogeneity on RTD	175
6.3.4	Effect of Capillarity on Tracer Response	176
6.3.5	Flow Mal-distribution in TBR	178
6.4	Conclusion	184
7	CFD Model for Hydrop-processing in TBR	185
7.1	Introduction	186
7.1.1	Previous Work	189
7.2	Applying CFD Model for Hydroprocessing Reactor	191
7.3	Results and Discussion	198
7.3.1	Performance of Laboratory Scale Reactor	199
7.3.2	Comparison of Laboratory and Commercial Scale Reactor	204
7.3.2.1	Hydrodynamic Parameters	204
7.3.2.2	Hydroprocessing Reactor Performance	206
7.4	Conclusion	211
	Bibliography	213
	Summary	224
	Abstract	227
	List of Publications	229
	Index	232

List of Figures

1.1	Different scales involved in Chemical Reactors	4
1.2	Different Scales Involved in the Trickle Bed Reactors	4
1.3	Packed/Trickle Bed Reactor Study Approach	11
2.1	Domain, Computational Grid and Boundary Conditions	25
2.2	Comparison of simulated results of z-velocity with experimental data (Suekane et al. ¹) at different particle Reynolds numbers.	32
2.3	Effect of numerical parameters on z-velocity distribution along x-axis at highest crosssectional area at $y=0$ and $Re_p=204.74$	34
2.4	Comparison of simulated z-velocity distribution with experimental data (Suekane et al., 2003) at various Reynolds numbers (velocity measured at z mid-plane along x-axis at $y=0.0015$)	35
2.5	Comparison of the simulated flow field at three horizontal planes with experimental data (Suekane et al., 2003) at $Re_p=59.78$	37
2.6	Comparison of the simulated flow field with experimental data at three horizontal planes [$Re_p=204.74$ 2000]	38
2.7	Comparison of simulated results with the literature data for low Reynolds number ($Re_p=0.001$)	41
2.8	Comparison of simulated average drag coefficient with the literature data at various Reynolds numbers.	41
2.9	Velocity vectors and z-velocity distribution in rhombohedral cell at various particle Reynolds numbers	44
2.10	Comparison of z-velocity in laminar and turbulent flow conditions along x-axis at highest crosssectional area (at y and $z=0.0015$	46
2.11	Histograms of z-velocity distribution obtained from simulations of liquid flow in 3-D Rhombohedral cell at different Re_p	46

2.12	Histograms of z-velocity distribution obtained from simulations of liquid flow in different unit cells at $Re_p=12.17$ and experimental data of <i>Sederman et al.</i> ² in randomly packed bed $D=4.7\text{cm}, d_p=5\text{mm}$, normalized density distribution	47
2.13	Histograms of x-velocity distribution obtained from simulations of liquid flow in different unit cells at $Re_p=12.17$ and experimental data of <i>Sederman et al.</i> ² in randomly packed bed $D=4.7\text{cm}, d_p=5\text{mm}$, normalized density distribution	47
2.14	Simulated friction factor, shear drag and Ergun equation (Ergun's Constant $E_1 = 180, E_2 = 1.75$, all filled symbols indicate shear drag at the particle surface)	49
2.15	Effect of the flow structure on temperature profile inside SC and FCC cell at various Re_p	51
2.16	Local particle-to-fluid Nusselt number for cubical cell at various Re_p (Symbols simulated values and line are for correlations; Ranz ³ $Nu = 2 + 0.6Pr^{\frac{1}{3}}Re^{\frac{1}{2}}$ Wakao et al. ⁴ $Nu = 2 + 1.1Pr^{\frac{1}{3}}Re^{\frac{2}{3}}$)	51
3.1	Schematic of experimental set-up for studying drop dynamics with high-speed digital camera	64
3.2	Solution domain and boundary conditions b) Typical initial condition at $t=0$	73
3.3	Effect of grid size on oscillation of 4.2mm drop on glass surface	73
3.4	[PLIC for calculating interface approximation and face flux]	76
3.5	[Advection of surface through control volume]	76
3.6	[Moment of a contact line on the wall with no slip boundary condition]	76
3.7	Drop spreading- spreading on glass (a and b) and on Teflon surface (c, d and e)	80
3.8	Drop impact on solid surfaces-oscillations of spreading and recoiling with or without rebound	81
3.9	Comparison of simulation results with experimental data for 4.2mm drop (Case 1) (Average oscillation period=26 ms , Equilibrium drop height =1.55mm)	84
3.10	Comparison of the experimental and simulation results of the drop dynamics for 4.2 mm drop (Case1). (impact velocity =0.22m/s, drop diameter 4.2mm, solid surface: glass)	85
3.11	Drop oscillations with time- Dynamics of drop height and contact angle for non-pretreated glass surface (Case 2)	87

3.12	Drop oscillations with time- Dynamics of drop height and contact angle for pretreated glass surface and simulation comparison (Case 3).(Average oscillation period=11.33, Equilibrium drop height =1.6mm)	87
3.13	Comparison of the experimental data of drop height variation with simulated results (Case 4).(Avg. Oscillation Period: 16.57ms, Final Drop Height: 2.2 mm)	89
3.14	Contours and flow field of spreading and rebounding drop (Case 3)(Avg. Oscillation Period: 16.57ms, Final Drop Height: 2.2mm)	90
3.15	Comparison of the Drop Dynamics with Simulation Results of drop impact on Teflon surface (Case 5)(Impact velocity: 1m/s, drop diameter: 2.5mm, solid surface: Teflon)	92
3.16	Comparison of drop dynamics on glass and Teflon surface (Experimental Conditions: Case 3, Liquid: Water, Solid Surface: Teflon and glass, Impact Velocity:0.3m/s)	95
3.17	Comparison of the experimental data of drop height variation with simulated results (Case 7: Avg. Oscillation Period: 14ms, Final Drop Height: 1.5 mm) . .	96
3.18	Comparison of the experimental and simulation results of the Mercury drop dynamics (Case 8: Avg. Cycle Frequency: 54, Final Drop Diameter: 2mm) . . .	96
3.19	Variation of the Simulated Kinetic, Potential Energy of Drop During Oscillations for Case 3 and 4.	101
3.20	Variation of the Simulated Kinetic, Potential and Surface Energy of Drop During Oscillations for Case 3 and 4.	101
3.21	Variation of viscous dissipation with time for Case 3 and 4	102
3.22	Illustration of gas-liquid and liquid-solid interaction during drop spreading on glass surface at time=7.5ms (Case 3).	104
3.23	Variation of avg. strain rate at gas-liquid interface and drop interfacial area during drop oscillations (Case 3).	105
3.24	Variation of avg. liquid-solid shear stress and drop diameter during drop oscillations (Case 3).	105
4.1	Physical Picture of the Flow in Trickle Bed Reactors	113
4.2	Flow regime map (<i>Sie and Krishna sie</i> ⁵)	113
4.3	Experimental set up	116
4.4	Wall pressure fluctuations in TBR at various liquid flow rates ($V_G = 0.22m/s$)	119
4.5	Power spectral density at various liquid flow rates ($V_G = 0.22m/s$)	121

4.6	Trickle to pulse flow regime transition: Kolmogorov entropy and pressure drop hysteresis ($D = 0.114$ m, $d_p = 3$ mm and $V_G = 0.22$ m/s).	122
4.7	Pressure drop and liquid hold-up hysteresis in TBR at various operating conditions, (Data of $D=7$ cm from <i>Wang et al.</i> ⁶	126
4.8	Pressure drop and liquid hold-up hysteresis in TBR at various operating conditions for $D=11.4$ cm.	126
4.9	Effect of column diameter on pressure drop hysteresis at $V_G = 0.22$ m/s.	127
4.10	Liquid hold up in different trickle bed reactors at $V_G=0.22$ m/s.	127
4.11	Effect of liquid inlet distributor on pressure drop hysteresis ($V_G = 0.22$ m/s, $d_p = 6$ mm, $D = 0.194$)	128
4.12	Liquid hold up for different distributors ($V_G = 0.22$ m/s, $d_p = 6$ mm, $D = 0.194$ m)	128
5.1	Variation of the porosity along radial direction using Mueller (1991) correlation	137
5.2	Bed Model Details and Contours of Simulated Results (C)Liquid Distribution Contours (Bed Diameter 19.4cm, $d_p=0.006$ m, std dev=5%)	137
5.3	Comparison of simulated results of pressure drop for prewetted and non-prewetted beds	148
5.4	Comparison of simulated results of liquid holdup for prewetted and non-prewetted beds	148
5.5	Simulated contours of liquid distribution for prewetted and non-prewetted bed. ($V_L=6$ kg/m ² s, $V_G=0.22$ m/sec, std dev=5%, $D=0.114$ m, $d_p=3$ mm)	149
5.6	Histogram of simulated results of liquid velocity and holdup ($V_L=6$ kg/m ² s, $V_G=0.22$ m/sec, std dev=5%, $D=0.114$ m, $d_p=3$ mm)	149
5.7	Comparison of CFD results with experimental data for $D=0.114$ m	150
5.8	Comparison of CFD results with experimental data with $d_p=3$ mm.	150
5.9	Comparison of CFD results with experimental data ($D=0.114$ m, $V_G=0.22$ m/s)	151
5.10	Comparison of CFD results with experimental data ($D=0.194$ m, $V_G=0.22$ m/s)	151
5.11	Comparison of simulated pressure drop and liquid saturation with literature data	156
5.12	Comparison of simulated pressure drop and liquid saturation with literature data	157
5.13	Comparison of simulated pressure drop and liquid saturation with literature data	160

5.14	Liquid induced periodic boundary condition for simulation ($D = 11.4\text{cm}$, $d_p = 3\text{mm}$)	161
5.15	Simulated Liquid Holdup Variation along Bed Height. ($D=11.4\text{ cm}$, $d_p=3\text{mm}$, std. dev.=5%)	161
5.16	Simulated results of liquid hold-up variation along the height of the bed at different liquid flow rates. ($D=19.4\text{cm}$, $d_p = 3\text{mm}$, $stddev. = 5\%$, $V_G=0.22\text{ m/sec}$)	162
6.1	Experimental set-up of trickle bed reactor for hydrodynamics and RTD study	169
6.2	Solution domain, liquid volume fraction and tracer mass fraction contours for trickle bed reactor	171
6.3	Comparison of pressure drop in TBR with simulation results (Operating conditions: $V_G=0.22\text{m/s}$, Std. Dev.=5%)	173
6.4	Comparison of liquid hold-up in TBR with simulation results (Operating conditions: $V_G=0.22\text{m/s}$, Std. Dev.=5%, $E_1=180$, $E_2=1.75$)	173
6.5	Measured residence time distribution in trickle bed reactor for $d_p=3\text{mm}$ and $V_G=0.22\text{m/s}$	174
6.6	Comparison of experimental RTD response with simulated results (Operating conditions: $V_L=2\text{ kg/m}^2\text{s}$, $V_G=0.22\text{m/s}$, Std. Dev.=5%, $d_p=3\text{mm}$, $E_1=180$, $E_2=1.75$)	177
6.7	Comparison of experimental RTD response with simulated results (Operating conditions: $V_L=1.72\text{ kg/m}^2\text{s}$, $V_G=0.22\text{ m/s}$, Std. Dev.=5%, $d_p=6\text{mm}$, $E_1=500$, $E_2=3.4$)	177
6.8	Liquid volume fraction and tracer mass fraction for bed with center and wall inlets	180
6.9	Liquid volume fraction and tracer mass fraction for bed with center and wall inlets	180
6.10	3-D column grid, tracer injection points and liquid volume fraction contours in uniform and non-uniform inlet conditions (Operating conditions: $V_L = 2\text{kg/m}^2\text{s}$, $V_G = 0.22\text{m/s}$, $d_p = 3\text{mm}$, $Std.Dev. = 5\%$, $E_1 = 180$, $E_2 = 1.75$)	181
6.11	Experimental RTD response in pre-wetted and non pre-wetted bed for non-uniform inlet conditions (Operating conditions: $V_L = 2\text{kg/m}^2\text{s}$, $V_G = 0.22\text{m/s}$, $d_p = 3\text{mm}$, $Std.Dev. = 5\%$, $E_1 = 180$, $E_2 = 1.75$)	182

6.12	Comparison of experimental and simulated RTD with non-uniform inlet (Operating conditions: $V_L = 2\text{kg}/\text{m}^2\text{s}$, $V_G = 0.22\text{m}/\text{s}$, $d_p = 3\text{mm}$, $\text{Std.Dev.} = 5\%$, $E_1 = 180$, $E_2 = 1.75$)	182
7.1	Schematic of Scale up and Scale Down Issues of TBR	187
7.2	Variation of Equilibrium Constants for hydrogenation of mono-, di- and poly aromatics with Temperature.	201
7.3	Comparison of Simulated results of conversion of Aromatic Sulfur Compounds with the Experimental Data at different Temperature. (P=4 MPa, LHSV=2.0 h^{-1} , $Q_G/Q_L=200\text{ m}^3/\text{m}^3$, $y_{H_2S}=1.4\%$)	201
7.4	Comparison of Simulated Results of Effect of Initial Sulfur Compound on Conversion with the Experimental Data. /small(P=4 MPa, LHSV=2.0 h^{-1} , $Q_G/Q_L=200\text{ m}^3/\text{m}^3$, $T_R=320^\circ\text{C}$)	202
7.5	Comparison of Simulated and Experimental conversion of Poly-aromatics and Total-Aromatics at different Temperature. (P=4 MPa, LHSV=2.0 h^{-1} , $Q_G/Q_L=200\text{ m}^3/\text{m}^3$, $y_{H_2S}=1.4\%$)	202
7.6	Comparison of Simulated and Experimental conversion of Mono- and Di-aromatics at different Temperature. (P=4 MPa, LHSV=2.0 h^{-1} , $Q_G/Q_L=200\text{ m}^3/\text{m}^3$, $y_{H_2S}=1.4\%$)	203
7.7	Comparison of Simulated and Experimental results of conversion of all aromatics Compounds at different LHSV. (P=4 MPa, LHSV=2.0 h^{-1} , $Q_G/Q_L=200\text{ m}^3/\text{m}^3$, $y_{H_2S}=1.4\%$)	203
7.8	Variation of Solid Volume Fraction in Radial Direction and Predicted Results of Velocity Distribution along Radial Direction for Laboratory Scale Reaction. ($D_R=0.019\text{m}$, $\epsilon_B=0.5$, LHSV= 2 h^{-1} and $Q_G/Q_L= 200\text{ m}^3/\text{m}^3$)	205
7.9	Variation of Solid Volume Fraction in Radial Direction and Predicted Results of Velocity Distribution along Radial Direction for Commercial Scale Reactor. ($D_R=1.9\text{m}$, $\epsilon_B=0.37$, LHSV= 3 h^{-1} and $Q_G/Q_L= 300\text{ m}^3/\text{m}^3$)	205
7.10	Simulated Pressure drop and Liquid holdup for Laboratory scale TBR. (P=4 MPa, LHSV=2.0 h^{-1} and $Q_G/Q_L=200\text{ m}^3/\text{m}^3$)	207
7.11	Simulated Pressure drop and Liquid holdup for Commercial Scale TBR.(P=4 MPa, LHSV=2.0 h^{-1} and $Q_G/Q_L=200\text{ m}^3/\text{m}^3$)	207

7.12 Comparison between Laboratory and Commercial Reactor: Conversion of Aromatics Sulfur Compound at Different Temperature ($P_{lab\&comm}=4$ & 4.4 MPa, $LHSV_{lab\&comm}=2.0$ 3.0 h^{-1} , $(Q_G/Q_L)_{lab\&comm}=200$ & 300 m^3/m^3 and $y_{H_2S}=1.4\%$)	208
7.13 Comparison between Laboratory and Commercial Reactor: Outlet Sulfur Composition at Different Temperature. ($P_{lab\&comm}=4$ & 4.4 MPa, $LHSV_{lab\&comm}=2.0$ & 3.0 h^{-1} , $(Q_G/Q_L)_{lab\&comm}=200$ & 300 m^3/m^3 and $y_{H_2S}=1.4\%$)	208
7.14 Comparison between Laboratory and Commercial Reactor: Poly and Monoaromatic Conversion at Different Temperature ($P_{lab\&comm}=4$ & 4.4 MPa, $LHSV_{lab\&comm}=2.0$ & 3.0 h^{-1} , $(Q_G/Q_L)_{lab\&comm}=200$ & 300 m^3/m^3 and $y_{H_2S}=1.4\%$)	209
7.15 Comparison between Laboratory and Commercial Reactor: Conversion of Aromatic Sulfur Compound at Different LHSV. ($P_{lab\&comm}=4$ & 4.4 MPa, $T=593$ K, $(Q_G/Q_L)_{lab\&comm}=200$ & 300 m^3/m^3 and $y_{H_2S}=1.4\%$)	209
7.16 Comparison between Laboratory and Commercial Reactor: Conversion of all Aromatic Compounds at Different Pressure($LHSV_{lab\&comm}=2.0$ & 3.0 h^{-1} , $T=593$ K, $(Q_G/Q_L)_{lab\&comm}=200$ & 300 m^3/m^3 and $y_{H_2S}=1.4\%$)	210
7.17 Comparison between Laboratory and Commercial Reactor: Conversion of Aromatics Compound at Different LHSV. ($P_{lab\&comm}=4$ & 4.4 MPa, $T=593$ K, $(Q_G/Q_L)_{lab\&comm}=200$ & 300 m^3/m^3 , $y_{H_2S}=1.4\%$)	210

List of Tables

3.1	Summary of the Previous Work Done on Impact of Drop in Solid Surface	59
3.2	Operating conditions and dimensionless numbers for different cases	79
5.1	Experimental Parameters and Operating Conditions in Present Study	146
5.2	Experimental Parameters and Operating Conditions in Present Study	146
5.3	Frequencies of Different Pulses Obtained From PSD at $V_G=0.22$ m/s	158
7.1	Comparison Between Laboratory Scale and Industrial Scale Reactor Parameters	189
7.2	Comparison Between Laboratory Scale and Industrial Scale Reactor Parameters	193
7.3	Kinetic Parameters for Hydroprocessing Reactions	194
7.4	Comparison Between Laboratory Scale and Industrial Scale Reactor Parameters	198

Nomenclature

Roman Letters

- \hat{n}_w unit normal at wall , see equation (3.11), page 70
- \hat{n} unit normal , page 68
- \hat{t}_w unit tangent at wall , see equation (3.11), page 70
- n surface normal , page 68
- V velocity vector, m/sec
- f_s viscous friction factor
- f_t total frictional factor
- A_{GL} gas-liquid interfacial area, m^2
- a_{GL} specific gas-liquid interfacial area, m^{-1}
- A_{LS} liquid-solid interfacial area, m^2
- $Ar - S$ aromatics sulfur compound
- C concentration, $kmol/m^3$
- C_d drag coefficient
- C_i tracer concentration
- D bed diameter, m
- d_1 and d_2 maximum and minimum diameter of particle with liquid film, m
- d_p particle diameter, m
- $Di - Ar$ di aromatics
- $E(t)$ exit age distribution
- E_1, E_2 Ergun's constant
- f degree of wetting, used in equation , see equation (5.12), page 142

F_D	drag force, N
$F_{K,R}$	interface exchange source for momentum equation, $kg/m^2 sec^2$
F_{SF}	continuum surface force, $kgm/m^2 sec^2$
g	gravitational force, m/sec^2
H_2	Hydorgen
H_i	Henri's Constant, $kmole/m^3/MPa$
J_o	<i>Zeroth</i> order Bessel Function
k_{mono}	backward pseudo-first order rate constant of dearomatization rreaction, $m^3/kg.sec$
k_f	fluid thermal conductivity, W/m-K
K_{ad}	adsorption coefficient, $m^3/Kmol$
k_{ij}^E	dynamic equilibrium constant, dimensionless
k_{mono}	forward pseudo-first order rate constant of dearomatization reaction, $m^3/kg.sec$
k_t	turbulent thermal conductivity, $W/m - K$
L	length, m
L	length, m
<i>mono - Ar</i>	mono aromatics
Pr_t	Prandtl number, $C_p\mu_t/K$
r	radius of column, m in equation , see equation (5.2), page 135
r	reaction rate, $kmol/kg.sec$
r^*	r/D
<i>Tri - Ar</i>	tri aromatics
U_o	superficial velocity, m/sec
A	area, m^2
a,b and c	frequencies, sec^{-1} , page 159
Bo	Bond number, $\rho g d^2/\sigma$
Ca	Capillary number, σ/μ

h	enthalpy
k	kinetic energy, m^2/sec^2
k	thermal conductivity, $W/m - K$
n	direction
nr	number of reactions
Nu	Nusselt number, hd_p/k
Oh	Ohnesorge number, $\mu/(\rho\sigma d)^{0.5}$
P	pressure, Pa
q	heat transfer rate, W
R	radius, m
Re	Reynolds number $Re_p = \frac{\rho U_o d_p}{\mu}$
Re_p	particle Reynolds number $Re_p = \frac{\rho U_o d_p}{\epsilon\mu}$
T	temperature, K
t	time, sec
V	superficial velocity, m/sec
We	Weber number, $\rho d_p V^2/\sigma$
We_α	modified Weber number, $\rho d_p V^2/\sigma(1 + \cos\theta_w)$
u	velocity, m/sec

Greek Letters

α	phase volume fraction
β_G	gas saturation
β_L	liquid saturation
ϵ	dissipation rate, m^2/sec^3
ϵ_B	bed voidage

ϵ_k	volume fraction of k^{th} fluid
κ	curvature , see equation (3.9), page 68
λ_i	solubility
μ	viscosity, Pa.s
ν	kinematic viscosity, m^2/sec
ν_N	molar gas volume, $cm^3/mole$, see equation (7.18), page 197
ϕ	fraction of liquid supported in gas , see equation (5.1), page 133
ρ	Density, kg/m^3
ρ_L	density of liquid, gm/cm^3 at 293 K , see equation (7.18), page 197
σ	surface tension, N/m
σ_{GL}	gas-liquid interfacial tension, N/m
σ_{GS}	gas-solid interfacial tension, N/m
σ_{LS}	liquid-solid interfacial tension, N/m
τ_w	wall shear stress, N/m^2
θ_w	contact angle
ν_t	turbulent kinematic viscosity, m^2/sec
η	wetting efficiency
ω	vorticity
ρ_B	catalyst bulk density

Subscripts

k	k^{th} phase
t	tangential
t	turbulent
b	bulk
F	frictional , page 133

G	gas
i,j,k	directions
L	liquid
obs	observed
p	particle
w	wall

“Fluids wander in the great void, some of these eject and some of these stray in voids, having found no group that they could belong to. A model and image of such wandering fluids is something we have daily before our eyes: Just look when rain fall on sand stones; you will see many tiny streams twisting and turning and moving here and there where the sunlight shows. It’s as if they were in an unending conflict with squadrons coming and going in ceaseless battle, now forming groups, now scattering, and nothing lasting. From this you can imagine the agitation of these fluids in the great emptiness, so far at any rate as so small an example can give any hint of infinite events”

Modified version of De Rerum Natura

‘Nothing in this world is to be feared... only understood’

—Marie Curie

1

Introduction

1.1 Motion of Fluids in Packed Bed

Single or multi-phase flows through packed beds are often encountered in chemical process industries (CPI). Study of motion of fluids through the packing is of interest to several disciplines. These include small systems such as capillary column, flow through porous materials like sand stones/rocks, flows occurring in micro-reactors, and membranes to the medium and large scale systems such as flows in monolith, structured and randomly packed bed reactors. Apart from CPI, packed beds also find application in several other disciplines such as oil recovery, composite material processing, automobiles and environmental/biochemical reactors. Role of packing materials inside the bed is generally to increase the interfacial area and to support the catalyst to enhance rate of desired transformation. Apart from these parameters, fluid dynamics controls the rates of various transport processes, which affect the overall performance of packed bed reactors.

Catalytic packed bed reactors use catalyst particles of different shapes (generally spherical, cylindrical and tri-lobe). These catalyst particles are usually porous. Particles are generally arranged in random or ordered fashion to form a packed bed. Such packed bed reactors are used either for single or multi-phase systems. Packed bed in which gas and liquid phases flow downward, these reactors are generally called as trickle bed reactors (though different flow regimes other than trickle flow regime may occur in such systems). Relatively simple operation and possibility of using high catalyst loadings are typical advantages of these reactors. However, poor heat transfer and possibility of local hotspots, incomplete catalyst wetting and liquid mal-distribution are some of the disadvantages.

Past studies on these reactors were mainly based on development of empirical or phenomenological models for packed bed reactors. For practicing the specific chemistry and catalysis in a best possible way, it is essential to ensure that different phases are well

contacted and well mixed. The only way to ensure this is via thorough understanding of the underlying fluid dynamics. General chemical reactors encompass a broad spectrum of spatio-temporal scales [from micro (nano to micro meters) to macro (tens of meters) (see Figure (see Figure 1.1). Recent advances in understanding of physics of flows, numerical methods and computational resources allow us to investigate fluid dynamics of different scales and synthesize the information to gain an insight into complex fluid dynamics of reactors. In trickle bed reactors, different transport processes occur at different time and length scales (shown schematically in Figure 1.2). On the reactor scale, transport rates are affected by liquid distribution at the inlet, overall variation in porosity and liquid maldistribution along axial and radial direction. Near wall region, porosity of bed varies to a large extent where as in a bulk region, it remains more or less constant. The local variation in porosity influences liquid distribution within the bed. It is therefore essential to understand flow processes on a meso-scale (scale relevant to an assembly of few particles characterized by local value of porosity). Flow processes occurring on scales smaller than such meso-scales, corresponding to scales of characteristic voids in the bed are also important for understanding influence of size and shape of the void on transport rates. Different packing arrangements exist in randomly packed bed reactors and nature of voids formed between particles affects the flow structure inside the void and hence controls mixing, heat and mass transport. In trickle bed reactors, reactions occur at solid surfaces. The effective rate is controlled by heat and mass transport from bed to particle surface and diffusion inside a particle. With this basic introduction to flow processes in trickle bed reactor and the specific background and motivation of the present research is discussed in the following section.

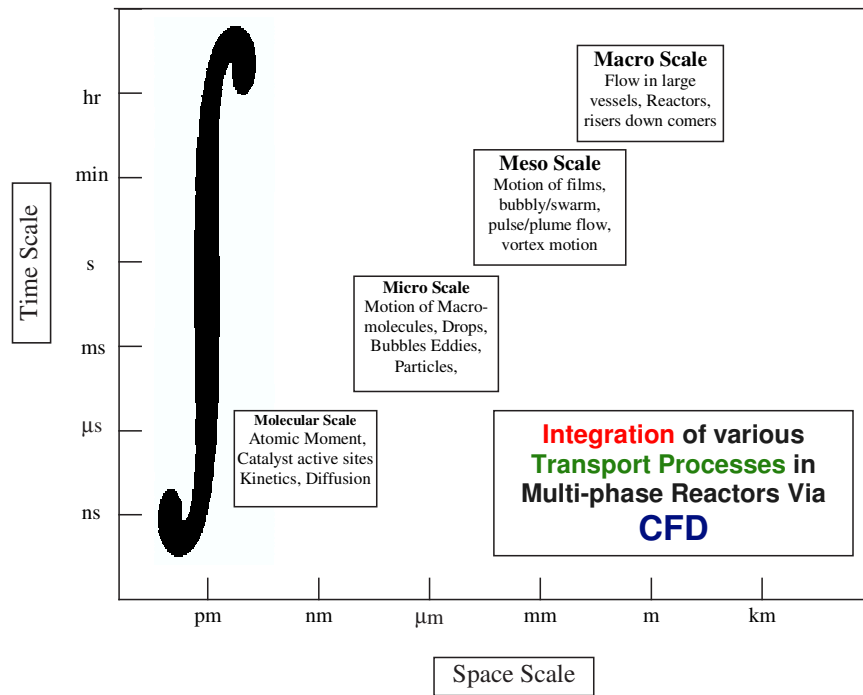


Figure 1.1: Different scales involved in Chemical Reactors

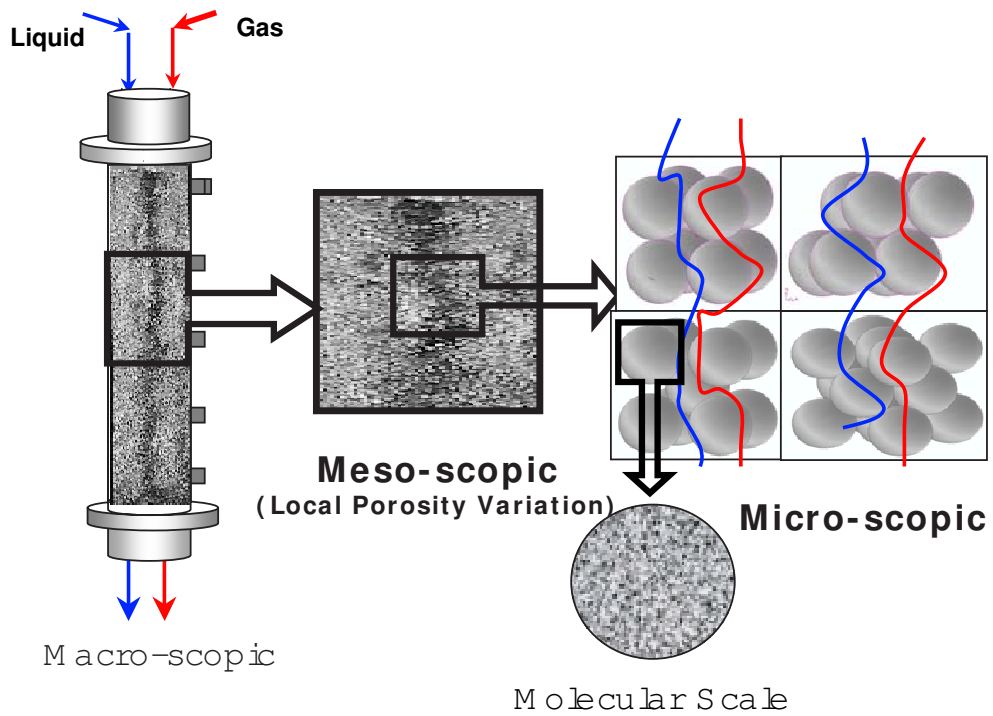


Figure 1.2: Different Scales Involved in the Trickle Bed Reactors

1.2 Background and Motivation

As discussed earlier, in packed bed reactors, various transport processes are associated at different length and time scales. However it is difficult to develop a single generalized model that can capture all the flow processes associated with the packed bed reactors. Packed bed reactors are mainly divided into two categories depending upon particle to bed diameter ratio; low (<13) and high (>13) bed to particle ratio. Systems of low particle to bed diameter ratio (<13) contain relatively few particles. In this case, exact geometry of the packing can be considered while simulating the flow. For single-phase flow, several researcher used such approach as proposed by *Calis et al.*⁷, *Guardo et al.*⁸. The main disadvantage of this approach is when number of particles increases it soon becomes computationally intractable. Alternative approach is to use a unit cell concept. This approach is useful when particles are structured (arranged in a regular fashion). It can be used to understand the influence of particle arrangement on drag, heat and mass transfer characteristics. In this work such an attempt is made.

Trickle bed reactors are generally operated with low liquid velocity; particles in the bed might not be completely wetted by liquid. This might have significant influence on the effective utilization of the bed. Previous researchers have shown that wetting of the bed is path dependent phenomenon (showing hysteresis) controlled by interaction of gas, liquid and solid phases. Since pressure drop and liquid holdup depend on interaction of phases, hence hysteresis was also observed in the pressure drop and liquid holdup. Most of the previous attempts for modeling hysteresis were mainly based on empirical correlations. To develop a physically realistic model, one needs to understand different forces associated with the spreading of a liquid over the solid surface and interaction of gas-liquid and liquid-solid phases with each other. In a trickle bed reactor model, it is almost impossible to consider actual gas-liquid interface and its spatial variation along axial and radial direction.

It is therefore essential to simplify the problem to gain an insight into interaction of a liquid with solid surface. In this work, a case of spreading of a liquid drop on flat and spherical surfaces was studied.

Hydrodynamics of the trickle bed reactors is associated with very complex fluid-fluid and fluid-solid interactions. Different flow regimes exist in trickle bed reactors depending upon the geometry of the reactor and gas-liquid flow rates and their physico-chemical properties. Whilst the fact that there has been enormous data collected on hydrodynamic parameters, the objective of these studies was to correlate the reactor hardware with the hydrodynamic parameters and very little attention was given to investigate details of underlying fluid dynamics. Therefore a systematic experimental study covering different flow regimes in trickle bed reactor is needed. Non-intrusive methods are essential for packed bed reactors because of opaque characteristics. Measurement of wall pressure fluctuations was found to be useful for characterization of the fluid dynamical scales for other multiphase reactors (see *Ranade and Utikar*⁹, *Letzel et al.*¹⁰, *Van Den Bleek*¹¹). This technique was however not applied to understand fluid dynamics of trickle bed reactors. Such an attempt is made here.

Multi-fluid models based on Eulerian-Eulerian technique are being increasingly used to simulate flows in multi-phase reactors (see *Ranade*¹²). Recently *Jiang et al.*¹³ and *Kashiwa*¹⁴ (*Ranade* 12). have developed multi-fluid models for simulating gas-liquid flow in trickle beds. However a detailed validation of these models and the effect of several parameters such as bed porosity, bed scale and capillarity were not studied. Porosity of the bed near wall fluctuates more than at the center of the column. This radial variation of the porosity near the wall is a function of the ratio of particle to bed diameter. Radial variation of porosity is well defined by a correlation given by *Mueller et al.*¹⁵. However, how the porosity varies axially is not well understood. *Jiang et al.*¹³ has used axially averaged Gaussian

distribution. Hence experimental measurements are necessary to characterize axial variation of porosity within the column. However such measurements are not straightforward and require very expensive non-invasive techniques such as magnetic resonance imaging (MRI). Instead, in this work a combination of macroscopic measurements (like residence time distribution) and CFD models were used to shed more light on porosity distribution.

Previous studies on CFD modeling of trickle bed reactors were restricted to global hydrodynamic parameters such as pressure drop and liquid hold. CFD models could be effectively used to understand liquid distribution; wetting of catalyst and capillary effects provided the models are reasonably validated before undertaking such exercise. Most of the previous CFD models were mainly restricted to trickle flow regime. No attempts were made to extend these to simulate periodic operation and spray flow regime. In trickle bed reactor, experimental measurement of fraction of liquid suspended in gas phase is not straightforward. However CFD model can be used to predict the fraction of liquid head on gas phase and solid phase. In this work, we develop and use CFD models for gaining new insights into trickle bed hydrodynamics.

Liquid phase mixing in trickle bed reactors is influenced by bed geometry, capillarity effect, non-uniformities in flow, liquid distribution, channeling and dead zones. In most of the cases, liquid phase mixing is characterized by lumping all these complexities into axial or radial dispersion coefficients. Such lumped dispersion coefficients are usually obtained by carrying out liquid phase tracer studies. In computational flow model, effect of various issues influencing mixing in trickle bed reactors can be studied. It is however, essential to carry out experimental measurements as well to quantify possible uncertainties in predicting flow and mixing in trickle bed reactors.

Previous attempts of modeling of trickle/packed bed reactors were based on average values

bed properties and flow fields. Use of these averaged parameters cause severe difficulties during scale-up and scale-down. Design scale-up and scale-down procedures often require large experimental data at laboratory and pilot scale set-ups. This procedure is always associated with higher cost in terms of money and time. Recent advances in CFD modeling might be fruitfully harnessed to obtain valuable information about flow field inside the reactors. This will greatly facilitate scale-up and scale-down. Such an attempt is made here.

1.3 Objectives

Based on issues discussed in previous section and a critical review of published information, the research for this thesis was planned with following objectives: The detail objectives in this work were;

Particle scale flow processes:

- Understand influence of packing arrangements on flow and heat transfer in packed bed reactors
- Understand interaction of a liquid drop with solid surfaces over a range of surface and liquid phase physical properties

Reactor Scale Flow Processes:

- Generate experimental data to quantify influence of particle diameter, column diameter and flow rates of gas and liquid phases on global hydrodynamics parameters such as pressure drop, liquid hold-up and mixing
- Characterize different flow scales occurring in trickle and pulse flow regime

- Understand influence of wetting on key flow characteristics
- Develop, verify and validate multi-fluid model (Eulerian-Eulerian framework) for simulating gas-liquid flows through packed beds
- Use the developed flow model for gaining insight into key flow characteristics of a trickle bed reactor over a range of design and operating parameters

Application of Flow Models for Performance Evaluation:

- Understand the key issues controlling liquid phase mixing and residence time distribution in the bed using experimental and computational methods.
- Understand causes and influence of liquid phase mal-distribution in trickle bed reactors
- Use computational models to simulate and to understand performance of trickle bed hydrotreating reactor and scaleup and scaledown issues.

Keeping the above objectives in mind, a comprehensive research program was formulated. The applied methodology is briefly discussed in the following.

1.4 Methodology

Overall methodology used to study flow processes occurring in trickle/packed bed reactors is shown in Figure 1.3. Different modeling approaches were used to achieve the objectives listed above.

- Particle scale flow processes were studied using CFD models and experiments. In the first part, single phase flow through few particles was computationally studied to

understand flow characteristics inside the void formed by different packing arrangement of spherical particles. After validation, the computational model was extended to understand influence of packing arrangement on drag and heat transfer characteristics. To understand issues related to capillary pressure, solid surface characteristics and interface interaction, drop spreading on flat and spherical surface was studied experimentally and theoretically. For this purpose, interface-tracking model, Volume of Fluid (VOF), was used. Experiments were carried out over a wide range of operating conditions. From simulated results, gas-liquid and liquid-solid interactions were obtained.

- Hydrodynamic parameters such as pressure drop and liquid holdup were measured in trickle and pulse flow regimes for two column sizes and two particle sizes. With the help of wall pressure fluctuations, a methodology for identification of trickle to pulse flow regime transition was developed. Reactor scale flow model was developed in the Eulerian-Eulerian framework. Effect of various parameters such as column diameter, particle diameter and phase flow rates on reactor hydrodynamic was studied experimentally and theoretically. Developed model was further extended to gain an insight into spray flow regime. The model was also extended to simulate forced periodic flow of trickle bed reactors to mimic some of the features of naturally occurring pulse flow regime.
- The computational model was extended further to predict the liquid phase mixing. Liquid phase maldistribution was studied using RTD technique. The CFD model was evaluated by critically comparing model predictions with the experimental data. CFD model was then applied to predict reactor performance of a hydrotreating reactor. CFD model was also used to understand the Scale-up and scale-down issues of trickle bed reactors.

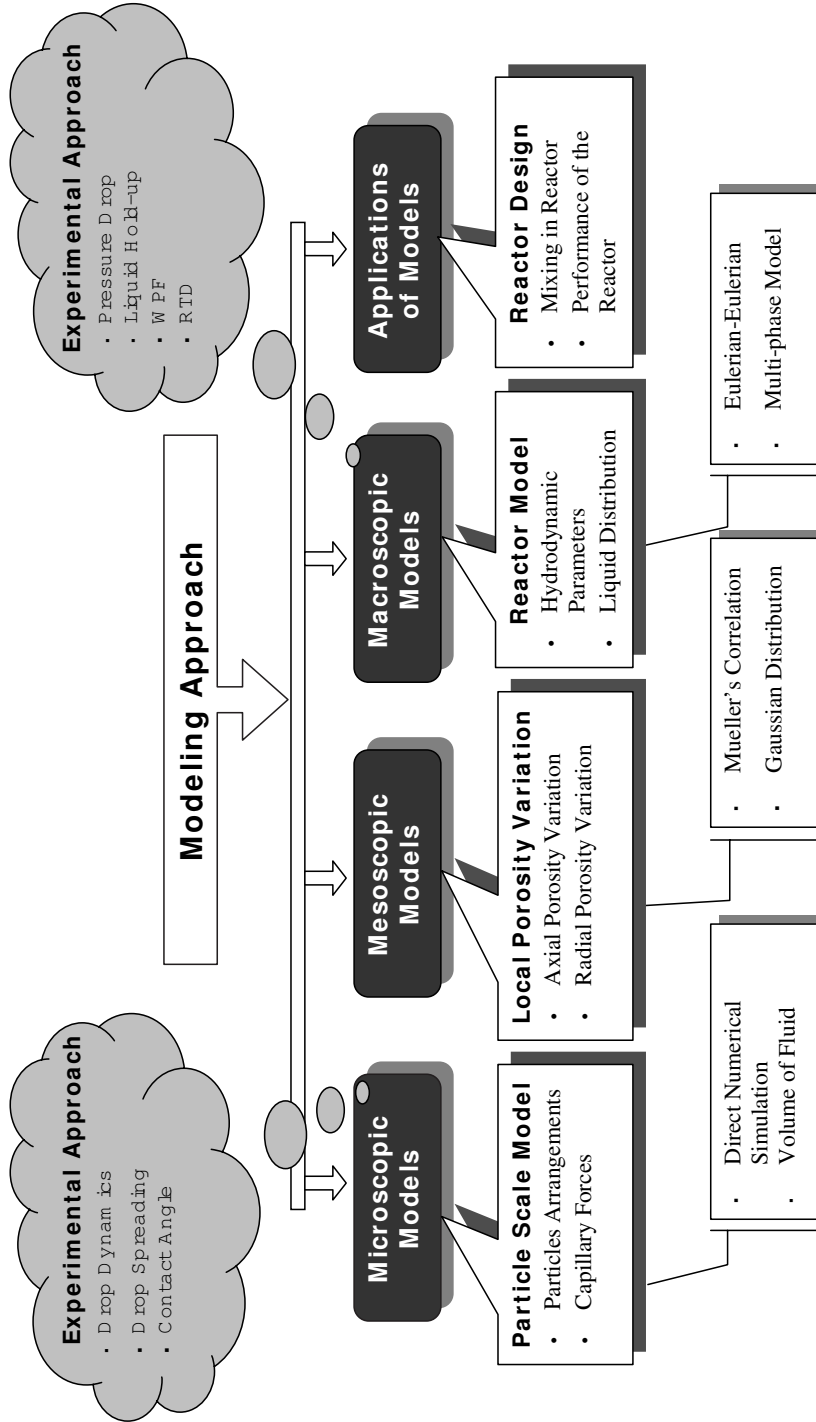


Figure 1.3: Packed/Trickle Bed Reactor Study Approach

1.5 Contribution of the Thesis

This thesis provides a detailed account of multi-scale fluid flow study in a packed bed reactor using experiments as well as CFD modeling techniques. Though there are still some unresolved issues, the overall understanding of flow characteristics inside the packed bed reactors is now better than that was at the start of this work. Some of the important contributions made during this work are summarized in the following:

- Single phase flow through different packing arrangements was simulated over a wide range of Reynolds numbers and its influence on drag and heat transfer was calculated. For same particle drag, mixing and heat transfer characteristics of the bed can be altered using different particle arrangement.
- To understand interaction of liquid with solid surface, spreading of a drop on flat as well as curved surfaces was experimentally studied using high-speed camera. CFD models based on Volume of Fluid approach were developed to gain an insight into interaction of liquid with solid surface. The computational models were validated using experimental data. Simulated results were used to evaluate stresses exerted on interfaces and to examine sensitivity of spreading behavior to the contact angle.
- For understanding the reactor scale flow characteristics, hydrodynamic parameters were measured at different scales of reactor over a wide range of operating conditions. Wall pressure fluctuations were measured to examine various transport scales involved in trickle and pulse flow regimes. A criteria based on Kolmogorov entropy was used to identify the flow regime transition from trickle to pulse flow regime.
- Computational flow model based on Eulerian-Eulerian framework was developed to simulate gas-liquid flows in a trickle bed reactors. Model predictions were found to

agree reasonably well with the experimental results over a wide range of design and operating parameters.

- Validated model was further used for calculating contribution of liquid head in frictional pressure drop. Model was also used to simulate periodic flow operation to understand key features of the pulse flow regime.
- Residence time distribution in trickle bed was measured experimentally for pre-wetted and non-prewetted bed conditions. Mixing in liquid phase was simulated using CFD model and model results were compared with experimental data.
- Developed CFD model was further used to simulate performance of the hydrotreating reactor.

The experimental and computational methods and presented results in this thesis will be helpful for better designing and for enhancing performance of trickle bed reactors.

1.6 Outline of Thesis

This thesis is organized in three Parts. In the first part single phase flow through regular particle arrays was studied. In the second part, gas-liquid flow through packed bed reactor was studied using experimental as well as CFD modeling. In the third part, application of CFD modeling for studying Residence Time Distribution (RTD) and design of trickle bed Hydrotreating reactor is demonstrated. Chapter wise description of this work is given below. In **Chapter 1**, introduction to the thesis is presented. The motivation for undertaking present research was discussed. The specific research objectives and methodology adopted were discussed. The organization of the thesis is briefly discussed.

PART I: Particle Scale Flow Processes in Packed Bed

Chapter 2 describes the study of fluid flow through the array of spheres using the unit cell approach. Different periodically repeating arrangements of particles such as simple cubical, 1d rhombohedral, 3d rhombohedral and face centered cubical geometries were considered. Single-phase flow through these geometries was simulated using computational fluid dynamics (CFD). Model was first validated by comparing predicted results with published experimental and computational results. Validated model was further used to study the effect of particle arrangement/orientation on velocity distribution and heat transfer characteristics. The simulated results were also used to understand and to quantify relative contributions of surface drag and form drag in overall resistance to the flow through packed bed reactors. The model and the results presented here would be useful in elucidating the role of microscopic flow structure in mixing and other transport processes occurring in packed bed reactors.

The process of spreading/recoiling of a liquid drop after collision with a flat solid surface was experimentally and computationally studied to identify the key issues in spreading of a liquid drop on a solid surface. The computational model and key results are discussed in **Chapter 3**. The long-term objective of this study was to gain an insight in the phenomena of wetting of solid particles in the trickle bed reactors. Interaction of a falling liquid drop with a solid surface (impact, spreading, recoiling and bouncing) was studied using a high-speed digital camera. Experimental data on dynamics of a drop impact on flat surfaces (glass and Teflon) is reported over a range of Reynolds number (550-2500) and Weber Number (2-20). Computational fluid dynamics (CFD) model based on the Volume of Fluid (VOF) approach was used to simulate drop dynamics on the flat surfaces. The experimental results were compared with the CFD simulations.

The CFD simulations provide information about finer details of drop interaction with

the solid surface. Information about gas-liquid and liquid-solid drag obtained from VOF simulations would be useful for CFD modeling of trickle bed reactors.

PART II: Reactor Scale Flow Processes in Packed Bed

In **Chapter 4**, we have described key experimental results from our study of gas-liquid flows through packed beds. It was found that bed-wetting condition plays an important role in governing macroscopic flow characteristics such as pressure drop, liquid hold-up and liquid distribution. A new technique based on analysis of wall pressure fluctuations was developed to identify transition from trickle to pulse flow regimes. Effect of several operating parameters on pressure drop and liquid hold-up hysteresis was reported. Effect of bed wetting condition on liquid distribution is studied with mean residence time distribution.

In **Chapter 5**, a comprehensive CFD model was presented to simulate gas-liquid flow through packed beds. Random distribution of bed porosity was represented in the developed computational model. The mathematical model was mapped onto commercial CFD code, FLUENT (of Fluent Inc., USA) using user defined routines. The model predictions were verified by comparing simulated results of overall pressure drop and total liquid saturation with the three independent, previously published experimental data sets. New approach based on CFD model was developed for estimation of the frictional pressure drop and supported liquid hold-up (or saturation) in trickle bed reactors. The CFD model and results provide detailed information about the complex fluid dynamics in trickle bed reactors.

In **Chapter 6**, experimental results showing influence of key design and operating parameters, wetting and non-uniform distribution at the inlet on hydrodynamics and mixing are presented. Application of CFD models for simulating mixing and RTD is also discussed.

The models were further extended to study flow mal-distribution in TBR. Based on these results, current capabilities and limitations of the CFD model are discussed. The model and the results discussed here would be useful to extend application of CFD models for simulating mixing in TBR.

PART III: Applications of CFD model

The extension of computational models to simulate performance of trickle bed hydro-treating reactors is discussed in **Chapter 7**. In this Chapter, developed CFD model was applied to simulate the performance of the laboratory scale reactor. Predicted model results were compared with experimental data of Chowdhury et al.¹⁶. Fluid dynamics of trickle bed reactors is complex and very sensitive to the scale of trickle bed reactors. Therefore, various issues of scaleup and scaledown of trickle bed reactors were studied.

Part I

Microp-scopic Flow Processes

*“Everything should be made as simple as possible,
but not simpler”*

—Albert Einstein

2

Single Phase Flow Through Packed Bed

2.1 Introduction

Single or two-phase flow through packed bed of spheres occurs in many chemical process industries. Flow through complex interstitial geometry formed by bed particles controls mixing and other transport processes occurring in a packed bed. Several experimental and computational studies have therefore been carried out to understand flow through voids of packed beds. Most of the previous studies were restricted to understand the global parameters like pressure drop, drag force exerted on particles and overall voidage of the bed. However, with the new developments in experimental as well as theoretical/ computational techniques, it is now possible to gain detailed insight into the flow through packed bed in order to tailor, monitor and optimize the performance. Recent advances in experimental techniques like magnetic resonance imaging (MRI) provide the detailed information about the flow field (for example, *Sederman et al.*², *Sederman and Gladden*¹⁷, *Suekane et al.*¹). It is, however, difficult to study the influence of all the key parameters extensively via experiments. Instead it will be more effective to use such comprehensive data sets to validate computational models and use the validated models for further investigations. Therefore, several attempts have been made recently to develop computational models for simulating the flow in packed beds (see for example, *Logtenberg et al.*¹⁸, *Calis et al.*⁷, *Dixon and Nijemeisland*¹⁹, *Tobis*²⁰, *Zeiser et al.*²¹ and *Freund et al.*²²).

Computational studies mainly used two approaches. In the first approach, entire packed bed consisting of number of particles (either arrange in a regular fashion or in a random fashion) is considered. *Logtenberg et al.*¹⁸, *Nijemeisland and Dixon*²³, *Calis et al.*⁷ and *Nijemeisland and Dixon*²⁴ among others have used this approach. Computational constraints often limit the size of the bed and number of particles considered in such simulations. For simulating flow in large size packed beds, therefore, often the second approach, called 'unit cell approach' is used. There are two sub-types in the unit cell approach. In the first

type, each particle is assumed to have a hypothetical sphere of influence around it (see *Dhole et al.*²⁵ and references cited therein). Flow equations were solved around a particle placed in a hypothetical sphere of influence (size of which depends on porosity of the bed). This approach, however, ignores differences caused by different particle arrangements and therefore was not used in the present work. In the second type of unit cell approach, a unit 'periodic' cell comprising of a few particles is considered. The packed bed is represented by periodically repeating the unit cell in all the three directions. This approach is being used traditionally to analyze transport processes in packed beds (see for example, *Martin et al.*²⁶, *Sorensen and Stewart*²⁷). Different packing arrangements of particles like simple cubic (SC), rhombohedral and face or body centered cubic (FCC or BCC) can be considered for representing the packed bed. This approach is used in the present work.

Depending upon the flow rates, properties of fluids and loading of solid, different types of flow patterns were observed by several authors (*Seguin et al.*^{28,29} and *Hill et al.*)^{30,31}). At very low flow rates ($Re_p < 1$) where Re_p is particle Reynolds number based on mean velocity in the void space [$Re_p = \frac{\rho U_o d_p}{\epsilon \mu}$], creeping flow exists. Inertial flow regime begins above $Re_p = 10$. This inertial flow regime extends upto $Re_p = 250-350$. With further increase in Reynolds number, transition a flow regime (unsteady flow) occurs until $Re_p = 900$ (*Seguin et al.*²⁹). Transition from laminar to turbulent regime flow in packed beds is difficult to identify and it occurs over a range of Reynolds number. The occurrence of transition to turbulence is a complex function of size and shape of particles and bed packing characteristics. Previous studies [for example, *Seguin et al.*^{28,29} and *Chhabra et al.*³²] indicate that beyond $Re_p = 350$, flow is dominated by eddies and turbulent like structures. *Seguin et al.*²⁹ have experimentally shown that turbulent flow exists beyond $Re_p = 900$. *Jolls and Hanratty*³³, and *Latifi et al.*³⁴ reported that transition occurs over the range of $Re = 300-400$ [$Re = \rho U_o d_p / \mu$]. Based on these studies, it can be assumed that flow becomes turbulent beyond particle Reynolds number of 1000.

*Sangani and Acrivos*³⁵ and *Sorensen and Stewart*²⁷ have analyzed flow through unit cells with particles arranged in SC and FCC patterns several years ago. They have reported drag force exerted on particles at different values of porosity. Their study however was limited to the Stokes flow regime ($Re \rightarrow 0$). The Stokes flow regime exists at very low particle Reynolds number (<0.1) where average drag force on particles is independent of Reynolds number. Considering the usual operating ranges in packed beds, it is however, essential to understand the flow characteristics in the inertial flow regime (particle Reynolds number > 10). Only recently some attempts of analyzing inertial flow in packed beds have been made.

*Durst et al.*³⁶ simulated laminar flow through unit cells and compared simulated pressure drop with experimental data. Details of simulated flow field were neither discussed nor validated. *Maier et al.*³⁷ have carried out lattice Boltzmann simulations of single phase flow through FCC and random packing arrangement of particles. They presented some comparisons of simulated velocity distribution with their experimental results. Their study was restricted to low Reynolds number ($Re=0.5$ to 29). *Tobis*²⁰ has used unit cell approach for simulating turbulent flow in a packed bed. However, detailed flow characteristics and velocity profiles were not discussed. *Hill et al.*³⁰ have carried out the lattice Boltzmann simulations of flow through FCC, SC and random arrangement of particles. Detailed analysis of drag force variation with solid volume fraction and packing arrangement was discussed. *Freund et al.*²² have carried out lattice Boltzmann simulations of flow in a packed bed reactor of a low aspect ratio (5). They studied relative contributions of viscous and form drag in overall pressure drop. Detailed analysis of flow structure in packed bed, velocity distribution and its effect on transport properties is needed. Recently *Magnico*³⁸ has carried out simulations for unit cell and for small tube-to-sphere diameter ratio for the range of Reynolds numbers from 7 to 200. He has demonstrated influence of flow structures on mass transfer with the help of Lagrangian particle tracking. Despite these

modeling efforts, none of the flow simulations (except the attempt by *Freund et al.*²²) were validated by comparison with the experimental data. Most of the studies were restricted to comparison with the overall pressure drop. If the computational models are validated by detailed comparison with the experimental data, such models can be used to understand influence of Reynolds number and particle arrangement on flow structures and therefore on transport processes in packed beds.

Detailed experimental data of flow through packed beds is now available. *Sederman et al.*², *Sederman and Gladden*¹⁷ and *Mantle et al.*³⁹ have experimentally characterized flow in packed beds and have reported measured distributions of axial and transverse velocities in interstitial space. The axial velocity distribution showed a sharp decay and was asymmetrical. The transverse velocity distribution showed exponential decay in both positive and negative directions. Experimental data reported by *Maier et al.*³⁷ also show similar trends of velocity distributions. Recently, *Suekane et al.*¹ have carried out detailed measurements of flow through voids of simple packed bed using magnetic resonance imaging (MRI) and have provided detailed quantitative data. They also reported details of inertial flow structures for different Reynolds number. In this work, we used their experimental data to evaluate the computational model.

The computational model was developed to simulate flow in unit cells of particles with SC, rhombohedral and FCC arrangements. Simulated results were compared with the experimental data for *Suekane et al.*¹ for SC in a laminar flow regime. Effect of grid and grid size distribution and other numerical parameters such as discretization schemes, conversion criteria were discussed. CFD model results were also compared with the analytical solution (given by Sangani and Acrivos 1982) at low Reynolds number ($Re=0.001$) and with the simulated results of *Hill et al.*³⁰ and *Dhole et al.*²⁵ at moderate Reynolds numbers ($Re_p=10-500$). The validated computational model was used to understand influence of

packing arrangement of particles on flow structure using different packing arrangements like FCC and rhombohedral. Detailed comparison of flow fields of cubical, FCC and rhombohedral geometry were presented for wide range of Reynolds numbers (12-2000). Axial and transverse velocity distribution in unit cell was compared with the velocity distribution in a randomly packed bed. The simulated results were also used to quantify relative contributions of shear drag at the wetted area and form drag in overall pressure drop. Effect of flow structure on particle to fluid heat transfer coefficient was studied with the help of this CFD model. The models and results discussed here would be useful for enhancing our understanding of flow through packed beds.

2.2 Computational Model

The approach of unit cells, where packed bed of spheres is represented by geometrically periodic unit cells with different packing arrangements is advantageous to understand flow structures in large packed beds. It is, however, essential to understand possible implications of approximating a packed bed by periodic unit cells. It is well known that symmetry of a flow over a single sphere breaks when particle Reynolds number increases beyond 105 and unsteady flow occurs (*Natarajan and Acrivos*⁴⁰). The unit cell approach is not valid for cases where periodic symmetry of flow is absent despite the symmetric and periodic geometry. Fortunately, when particles are packed closely together in a regular fashion, the onset of symmetry breaking unsteady flow is delayed considerably (*Hill et al.*³⁰). The largest length scale characterizing the interstitial region of the regular arrays is smaller than particle diameter. Therefore, the Reynolds number characterizing the stability of the flow in the interstitial region can be up to approximately 2.5 times larger than critical particle Reynolds number. Secondly, at larger solid volume fractions, the fluid is increasingly confined and hence stabilized by neighboring spheres. For a specific particle Reynolds

number, viscous dissipation will be higher at higher solid volume fraction, and therefore more effective in damping velocity fluctuations. Considering this, in the present work, unit cell approach was used to understand influence of particle Reynolds number and packing arrangement on inertial flow structures in packed beds.

In this work, different packing arrangements of spheres (that is SC, 1D rhombohedral and 3D rhombohedral, FCC) were considered. These are shown in Figure 2.1. In the first part of the present work, a unit cell comprised of four spheres in a simple cubical arrangement ($\epsilon=0.4764$) was selected to facilitate comparison of the simulated results with the experimental data of *Suekane et al.*¹. In order to study influence of particle arrangements, flow simulations of unit cells with 1D rhombohedral arrangement ($\epsilon=0.4525$), 3D rhombohedral ($\epsilon=0.2595$) and face centered cubical (FCC) arrangement ($\epsilon=0.302$) were carried out. Simulations were also carried out for SC and FCC arrangements with different porosity to understand influence of solid fraction on velocity distribution.

The geometry of interstitial space of these unit cells was modeled using GAMBIT 2.0 (of Fluent Inc, USA). Unstructured tetrahedral grids were generated as shown in Figure 2.1. For the SC and FCC unit cells, only one fourth of the domain shown in Figure 2.1 a-c was used for flow simulations because of the inherent symmetry. For the rhombohedral unit cell (3D), however, complete geometry as shown in Figure 2.1b was used for flow simulations. Different computational grids were generated to quantify influence of grid size on the predicted results. These results are discussed in the next section.

Three-dimensional Navier-Stokes equations were used for simulating laminar flow of an incompressible fluid through a packed bed of spheres. The simulated results were compared with the experimental results of *Suekane et al.*¹. The predicted flow results were used to simulate particle to fluid heat transfer by solving enthalpy balance equation. Though

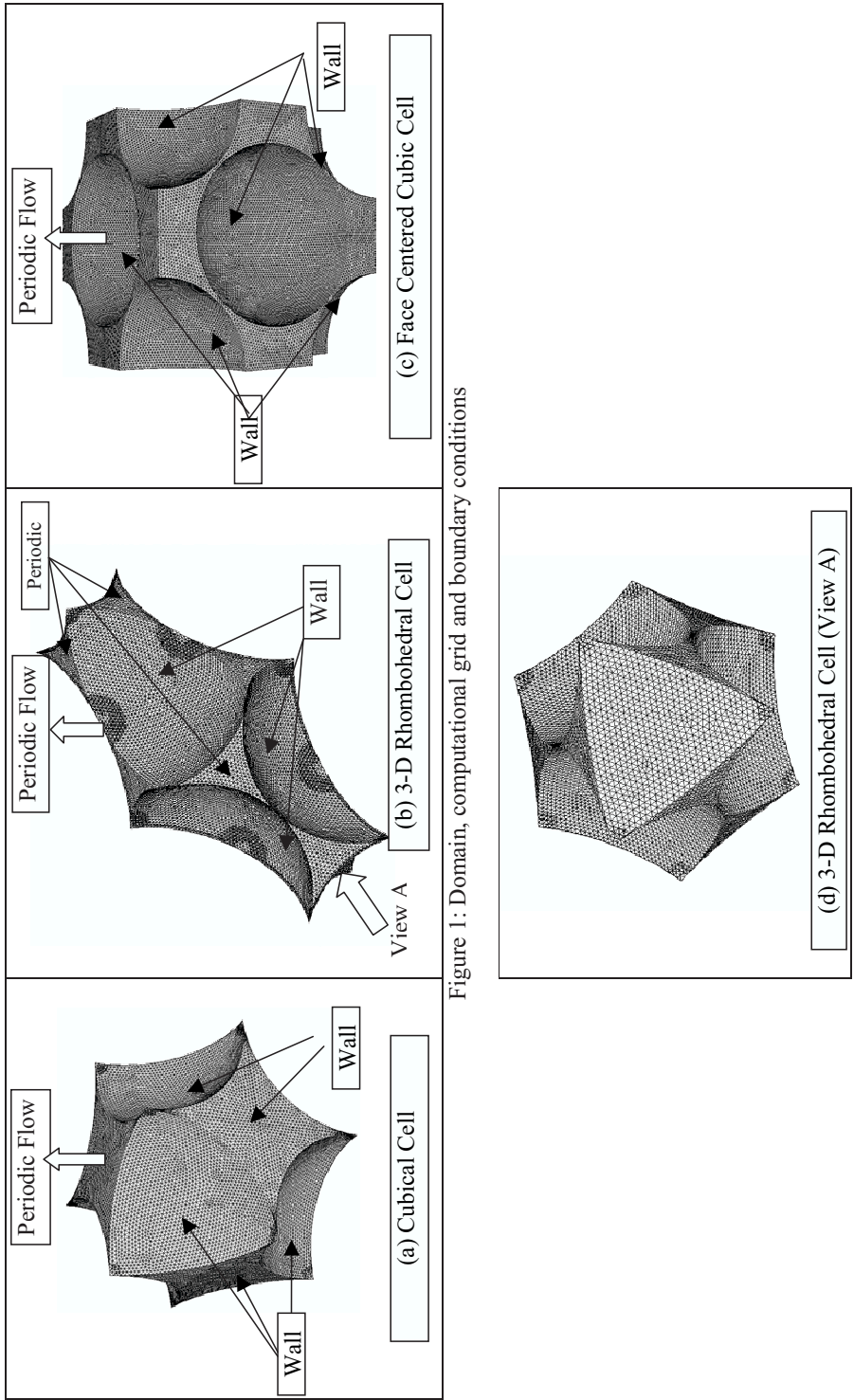


Figure 1: Domain, computational grid and boundary conditions

Figure 2.1: Domain, Computational Grid and Boundary Conditions

the experimental study of *Suekane et al.*¹ was limited to particle Reynolds number up to 204.74, it was thought desirable to use the computational model to understand flow characteristics for particle Reynolds number beyond laminar range. The study of *Seguin et al.*^{28,29} indicated that the flow in packed bed exhibits a transition regime over a large range of particle Reynolds number and the turbulent flow regime may exist beyond $Re_p=900$. Considering the uncertainties in simulating transition flow regime in a complex geometry, some simulations of the flow in packed beds were carried out for turbulent regime (particle Reynolds number of 1000 and 2000). For these cases, Reynolds averaged Navier-Stokes equations (and enthalpy equation) were used along with the standard k- ϵ model of turbulence. In laminar flow regime, turbulent stresses were neglected while in turbulent flow regime turbulent stresses were accounted in the model.

2.2.1 Governing Equations

Reynolds averaged Navier-Stokes Equations for mass and momentum balance for incompressible Newtonian fluid are given by,

$$\frac{\partial u_i}{\partial t} = 0 \quad \dots \dots \dots \quad (2.1)$$

$$\frac{\partial u_i}{\partial t} + \frac{\partial(u_i u_j)}{\partial x_j} = -\frac{1}{\rho} P + \frac{\partial}{\partial x_j} \left[(\nu + \nu_t) \left[\frac{\partial u_i}{\partial x_j} + \frac{\partial u_j}{\partial x_i} \right] \right] \quad \dots \dots \dots \quad (2.2)$$

Where, u_i is the mean velocity in i direction, P is pressure; the turbulent kinematic viscosity ν_t is given as,

$$\nu_t = C_\mu \frac{k^2}{\epsilon} \quad \dots \dots \dots \quad (2.3)$$

In this work, the standard k-ε model of turbulence was used. Transport equations for the turbulent kinetic energy, k, and the dissipation rate, ε may be written as:

$$\frac{Dk}{Dt} = \frac{\partial}{\partial x_j} \left[\left(\nu + \frac{\nu_t}{\sigma_k} \right) \cdot \left[\frac{\partial k}{\partial x_j} + \dots \right] \right] + G + \epsilon \dots \dots \dots (2.4)$$

where,

$$G = \nu_t \frac{\partial u_i}{\partial x_j} \left[\frac{\partial u_i}{\partial x_j} + \frac{\partial u_i}{\partial x_j} \right] \dots \dots \dots (2.5)$$

$$\frac{D\epsilon}{Dt} = \frac{\partial}{\partial x_j} \left[\left(\nu + \frac{\nu_t}{\sigma_\epsilon} \right) \cdot \left[\frac{\partial \epsilon}{\partial x_j} + \dots \right] \right] + \frac{\epsilon}{k} (C_{1\epsilon}G - C_{2\epsilon}\epsilon) \dots \dots \dots (2.6)$$

Standard values of the parameters appearing in Equations 2.3 to 2.6 were used ($C_{1\epsilon} = 1.44$, $C_{2\epsilon} = 1.92$, $C_m = 0.09$, $\sigma_k = 1.0$ and $\sigma_\epsilon = 1.3$, $G = G_{std}/\rho$ and $\epsilon = \epsilon_{std}/\rho$: from *Launder and Spalding*⁴¹). For turbulent flow simulations, various wall functions (standard wall function of *Launder and Spalding*⁴¹; enhanced wall function (*Wolfstein*⁴², *Jongen*⁴³, *Kader*⁴⁴) and non-equilibrium wall function of *Kim and Choudhury*⁴⁵ were used. However, predicted flow field was not significantly influenced by the choice of the wall functions.

The energy conservation equation may be written as:

$$\frac{\partial(\rho h)}{\partial t} + \nabla \cdot (\rho u_i h) = (k + k_t) \nabla^2 T \dots \dots \dots (2.7)$$

where h is enthalpy, k is thermal conductivity and k_t is turbulent thermal conductivity. First term in the right hand side is of the effective conductive heat flux (molecular and

turbulent). The turbulent thermal conductivity is given by,

$$k_t = \frac{C_p \mu_t}{Pr_t} \dots \dots \dots (2.8)$$

2.2.2 Boundary Conditions

In order to model the unit cell as a representative piece of a packed bed, periodic boundary conditions were implemented at all the faces of the unit cell through which flow occurs. Here translational periodic boundary condition is used in which all variables except pressure at periodic planes are same. For a desired particle Reynolds number, superficial velocity and mass flow rates were calculated based on the considered geometry. However, pressure is not periodic; instead the pressure drop is periodic. The local pressure gradient can therefore be decomposed into two parts: the gradient of a periodic component, and the gradient of a linearly-varying component. The linearly-varying component of the pressure results in a force acting on the fluid in the momentum equations. Because the value of pressure gradient is not known a priori, it must be iterated until the specified mass flow rate is achieved in the computational model. This correction of pressure gradient occurs in the pressure correction step of the SIMPLE algorithm where the value of pressure gradient is updated based on the difference between the desired mass flow rate and the actual one. In the present work, we have used under-relaxation parameter of 0.5 and 2 internal iterations to ensure the desired mass flow rate through the periodic cell.

While carrying out experiments on flow through an array of spheres, *Suekane et al.*¹ had closed the side faces of their cubical unit cell. Influence of closing the side faces (by specifying boundary condition as impermeable no-slip walls) as against the open, periodic faces was computationally studied.

For all the vertical faces bounding the solution domain, symmetry boundary conditions were implemented (normal velocity and all other normal gradients were set to zero). No slip boundary condition was implemented on all the impermeable walls (curved solid surfaces in Figure 2.1 a-c). For carrying out heat transfer simulations; constant temperature ($350^{\circ}K$) boundary condition was specified at all the particle surfaces and upstream bulk temperature was specified as $300^{\circ}K$. Heat transfer from particles to the fluid was calculated as;

$$q = hA(T_w - T_b) = -k_f \left[\frac{\partial T}{\partial n} \right]_{wall} \dots \dots \dots (2.9)$$

where n is normal coordinate normal to the wall and k_f is the thermal conductivity of fluid. Temperature gradients obtained from simulations were used to calculate the particle to fluid heat transfer co-efficient.

Simulations of flow (and heat transfer) were carried out using commercial CFD solver, FLUENT (version 6.1.18 of Fluent Inc., USA). The under-relaxation parameters for pressure and velocity were set to 0.05 and 0.1 respectively at the start and were increased up to 0.2 and 0.3 as the solution progressed. For turbulent flow, under-relaxation parameters for turbulent kinetic energy, dissipation rate and turbulent viscosity were used as 0.25, 0.25 and 0.6 respectively. Numerical issues and grid independence of solution are discussed in following sections. Simulations were carried out till the normalized residuals fall below 1×10^{-6} (1×10^{-7} for energy equations) for all the equations. For every simulation, it was ensured that pressure drop per unit length remained constant for several subsequent iterations. Simulations were first carried out with operating parameters used exactly as per those used in the experiments of *Suekane et al.*¹. Validated model was then used to study flow over wide range of the particle Reynolds numbers (12-2000) over different packing arrangements.

2.3 Result and Discussion

In the first section we have compared predictions of the CFD model with the available experimental as well as analytical/ computational results. In the second section, the results on influence of particle Reynolds number and of particle arrangement on flow are discussed. Drag force acting on the particles and contribution of viscous drag in total drag is discussed after it. Finally results pertaining to effect of particle arrangement and flow characteristics on wall to particle heat transfer coefficient are presented.

2.3.1 Validation of CFD Model

The predictions of the CFD model were first compared with the experimental data of *Suekane et al.*¹ measured using MRI technique for different particle Reynolds numbers (12.17 to 204.74). The model predictions were also compared with the analytical solutions presented by *Sangani and Acrivos*³⁵ at the limit of vanishing Reynolds number (<0.01). The simulated results of the present work were also compared with the predicted results of *Hill et al.*³⁰ and *Dhole et al.*²⁵. These results are discussed in the following.

2.3.1.1 Comparison with Experimental Data of *Suekane et al.*(2003)

*Suekane et al.*¹ have carried out detailed measurements of flow through an array of spheres over the range of particle Reynolds number 12 to 205. They reported velocity profiles and details of secondary flow structures for five particle Reynolds numbers (12.17, 28.88, 59.78, 105.5 and 204.74). Since the scatter in the reported experimental data was much lower for the case of Reynolds number of 204.74 (compared to that for the lower values of Reynolds

number), this case was selected for critical evaluation of the computational model. Several numerical experiments were carried out to understand influence of grid size, distribution and discretization schemes. Preliminary simulations were performed with different number of computational cells (33K, 112.5K and 287.5K). Simulated results obtained with different discretization schemes and different computational cells are compared with the experimental data in Figure 2.2. When second order discretization scheme was used, the predicted results with 112.5 K and 287.5 K computational cells were almost the same. All the subsequent simulations were therefore carried out using second order discretization scheme and total number of computational cells more than 150 K.

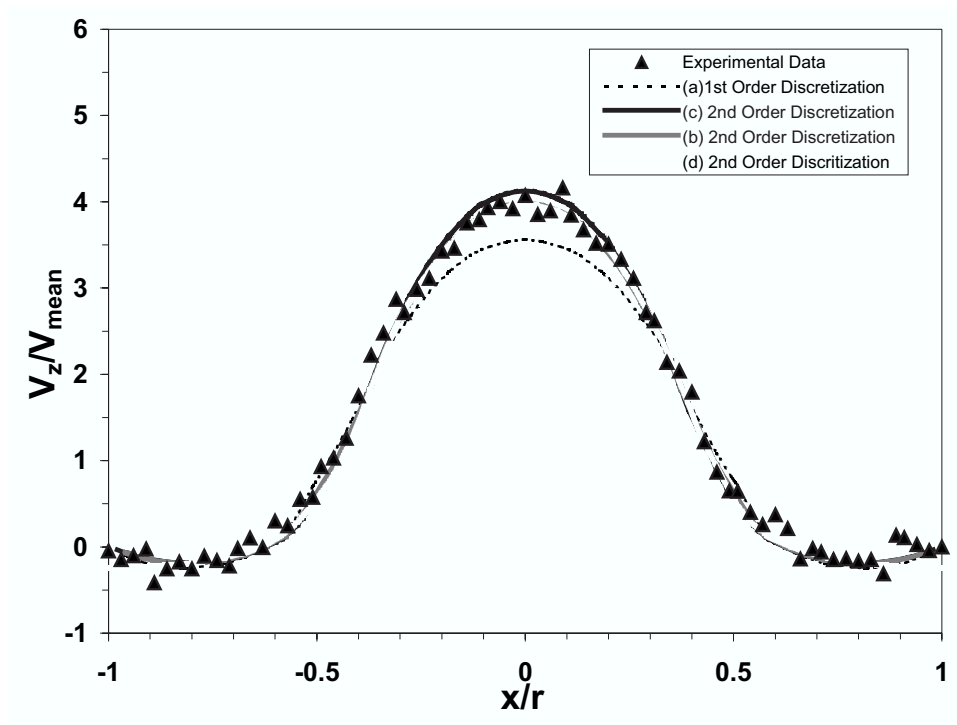


Figure 2.2: Comparison of simulated results of z-velocity with experimental data (Suekane et al.¹) at different particle Reynolds numbers.

After establishing adequacy of computational parameters, simulations were carried out for five values of Reynolds numbers considered by *Suekane et al.*¹. Highest Reynolds number considered in the experiments was 204.74. From previous literature (*Seguin et al.*²⁸, *Chhabra et al.*³²) it was found that flow at this Reynolds number is laminar and hence laminar flow model was used to simulate these cases. Comparison of simulated velocity field (vectors) with the experimental data is shown in Figure 2.3. It can be seen that variation of axial velocity was well captured in the simulated results. At highest Reynolds number ($Re_p=204.74$), where inertial forces are dominant and jet like flow behavior was observed in the experimental flow fields (see Figure 2.3c). Similarly dominant velocity stream through the center of the solution domain was also observed in the simulation. Quantitative comparison of the simulated and the measured z-component of the velocity are shown in Figure 2.4. Simulated results showed good agreement with the experimental data except at the lowest value of Reynolds number (12.17).

Systematic numerical experiments were carried out to understand possible reasons for the observed discrepancies at low Reynolds number. Influence of number of computational cells, distribution of cells within the solution domain and discretization scheme was insignificant as long as total number of computational cells is more than 150 thousand. Other possible source can be round-off errors. At lower values of Reynolds number, the mass flow through the unit cell becomes quite small if viscosity of the considered fluid is water like. To examine this, all the simulations were carried out using double precision solver. Simulations were also carried out by selecting physical properties of fluid in such a way that the mass flow rate at the desired value of particle Reynolds number is not very small to get influenced by round off error. These numerical experiments indicated that the observed discrepancies at $Re_p=12.17$ are not due to numerical errors. It is interesting to note that experimental results also show highest scatter at this particle Reynolds number. Possible difficulties in maintaining a steady flow at a very low flow rate may be one of

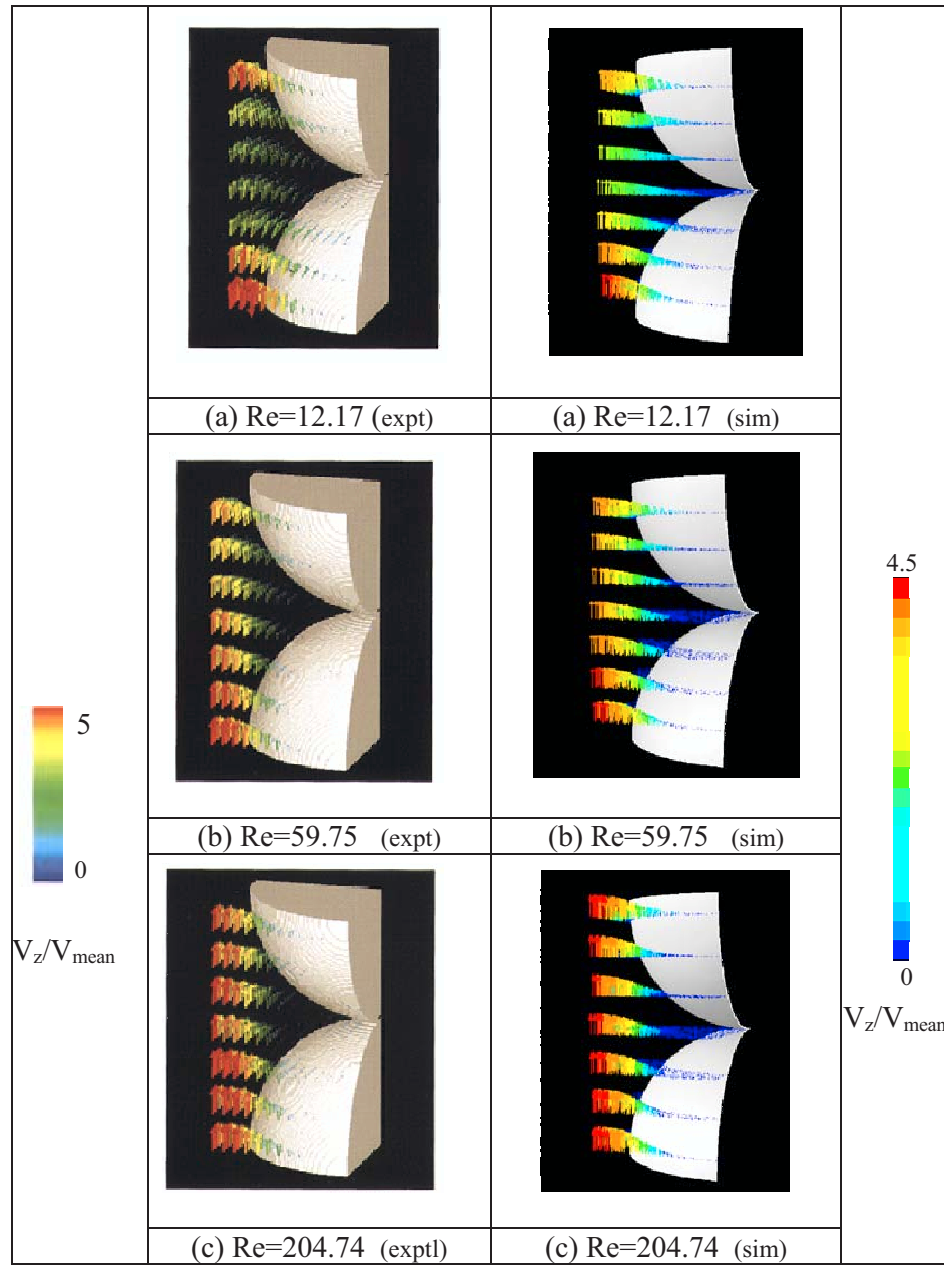


Figure 2.3: Effect of numerical parameters on z-velocity distribution along x-axis at highest cross-sectional area at $y=0$ and $Re_p=204.74$

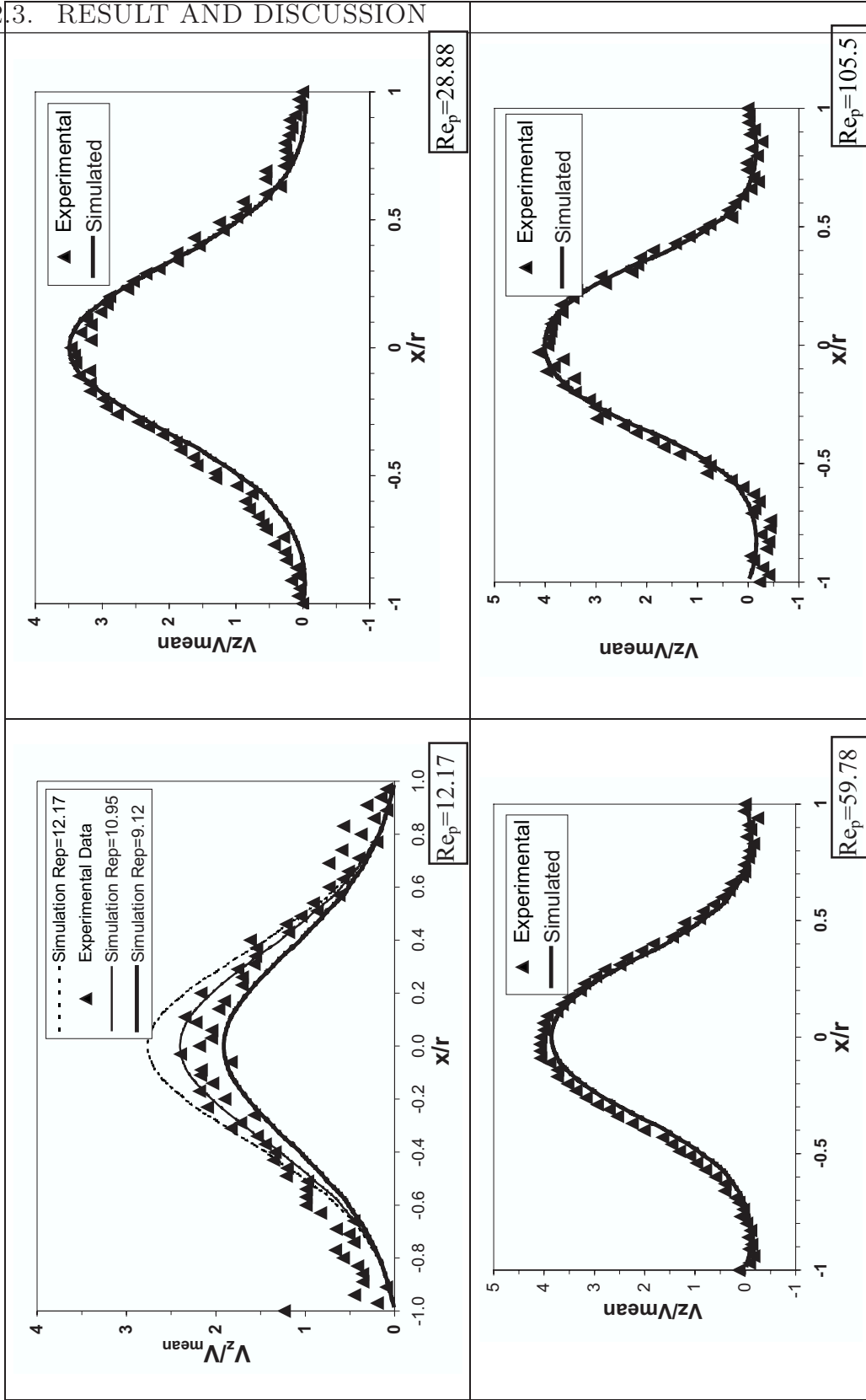


Figure 2.4: Comparison of simulated z-velocity distribution with experimental data (Suekane et al., 2003) at various Reynolds numbers (velocity measured at z mid-plane along x-axis at $y=0.0015$)

the reasons for such scatter. To examine this further; flow simulations were carried out with particle Reynolds number of 10.95 (10% lower flow) and 9.12 (25% lower flow). These results are compared with the experimental data reported at $Re_p=12.17$ in Figure 2.4. It can be seen that the reported experimental data lies in between the predicted results for $Re_p=9.12$ and 10.95.

Simulated results of flow field variation along the flow direction at three horizontal planes were compared with the experimental data in Figure 2.5 (for $Re_p=59.78$) and in Figure 2.6 (for $Re_p=204.74$). At low Reynolds number ($Re_p=59.78$), flow directions normal to the walls of sphere are different for planes A and C. At plane A, fluid moves towards walls of sphere while at plane C, fluid appears to move away from walls of sphere. The computational model captured this experimental observation very well. At higher Reynolds number ($Re_p=204.74$, Figure 2.6), a pair of vortices was observed in experimental measurements carried out at plane A. These vortices were also captured very well in the simulations (see Figure 2.6a). It is noteworthy that at higher Reynolds number (204.74), the observed and simulated flow at plane C are qualitatively different than that observed at lower Reynolds number (59.78). Figures 2.2 to 2.6 indicate very good overall agreement between the simulated and the experimental results. Simulated results not only showed good agreement with the data in the main flow direction but also captured inertial flow structures correctly. The computational model was then used to understand influence of particle Reynolds number and packing arrangement of spheres on key flow characteristics.

2.3.1.2 Comparison of Results with Analytical Solution

*Sangani and Acrivos*³⁵ have presented analytical solutions for flow through regular particle arrangement like SC and FCC at vanishing Reynolds number ($Re_p \rightarrow 0$). At low Reynolds

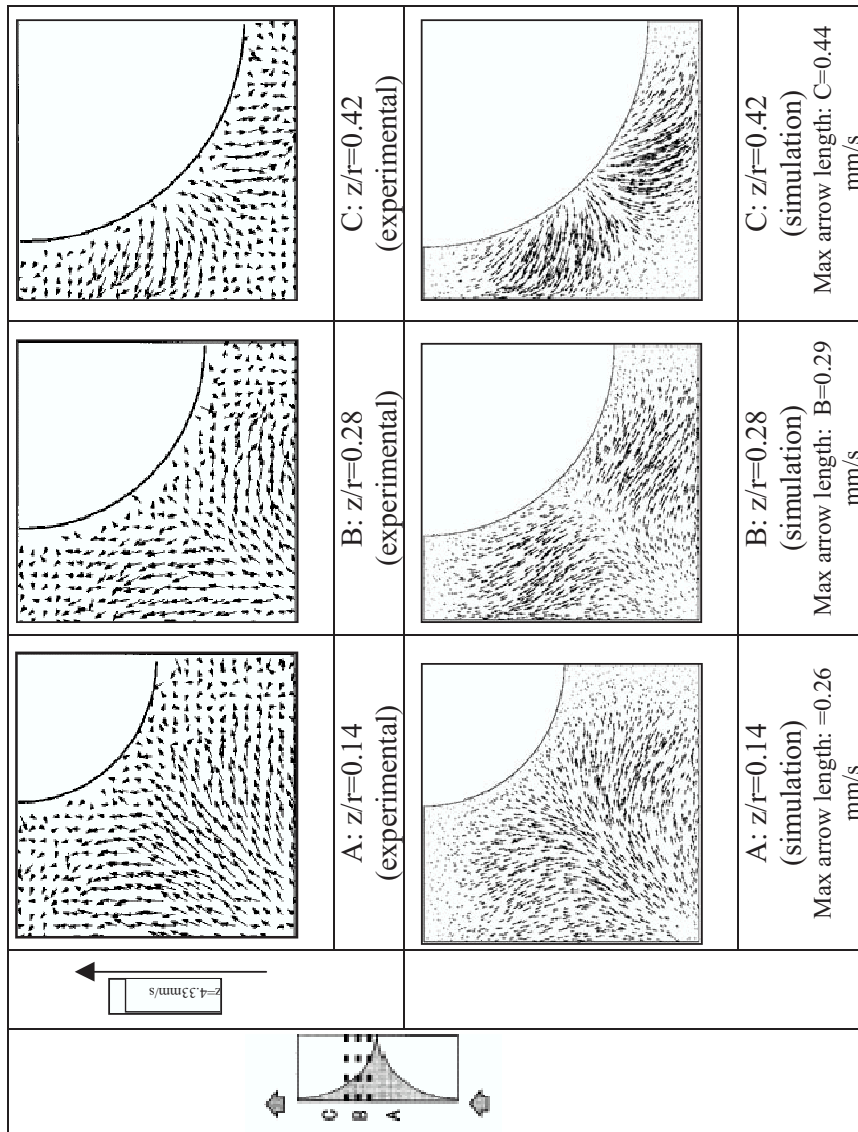


Figure 2.5: Comparison of the simulated flow field at three horizontal planes with experimental data (Suekane et al., 2003) at $Re_p=59.78$

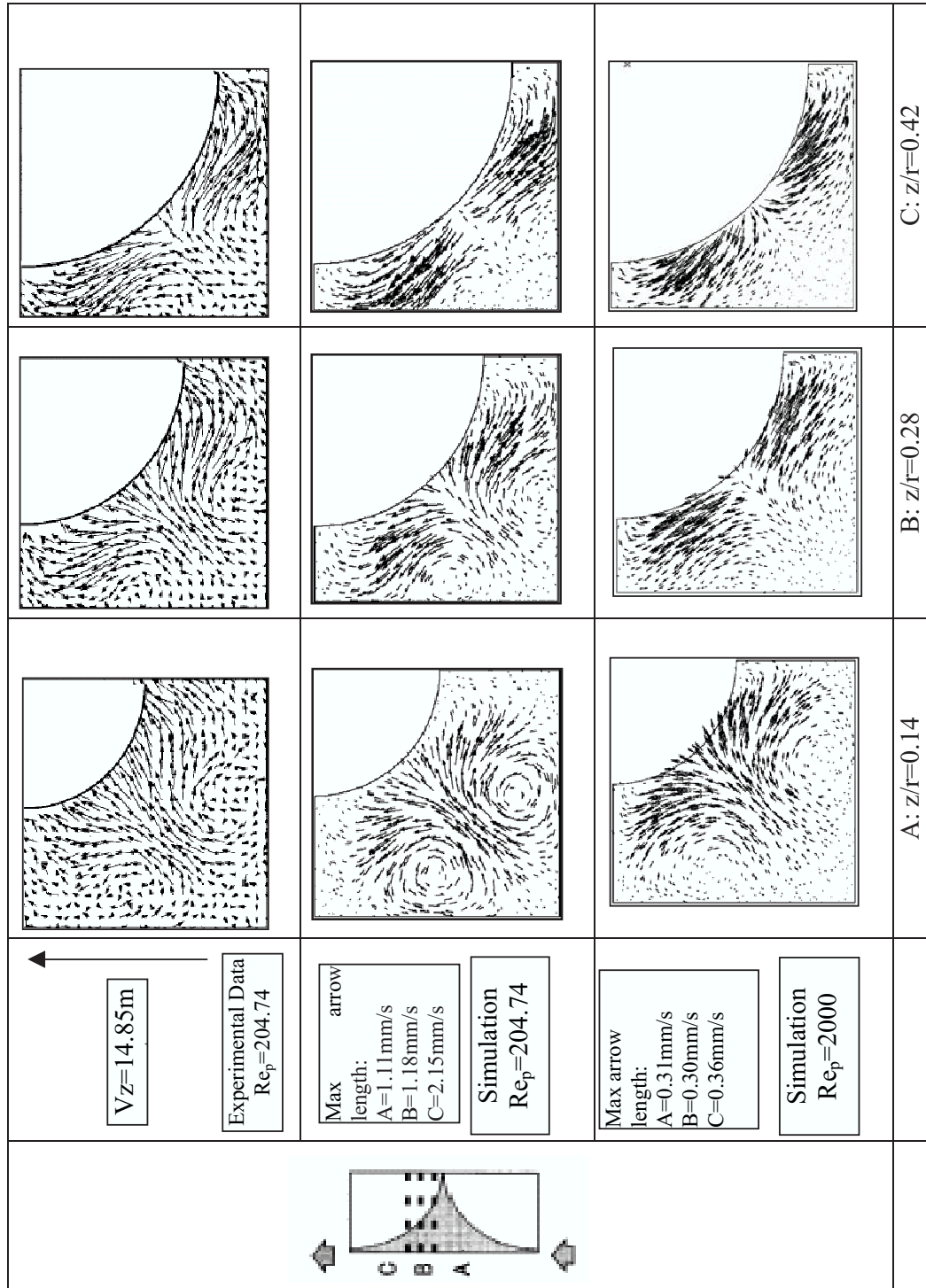


Figure 2.6: Comparison of the simulated flow field with experimental data at three horizontal planes [$Re_p=204.74$ 2000]

numbers, dimensionless drag force on particles $[F/(6\pi\mu RV)]$ is independent of Reynolds number and it is a function of solid fraction (see *Sangani and Acrivos*³⁵, *Hill et al.*³⁰. *Hill et al.*³⁰ have carried out lattice-Boltzmann (LB) simulations and shown that analytical solution given by *Sangani and Acrivos*³⁵ matches well with their LB simulations at low solid volume fractions. In order to compare our computational results with the analytical solution and with the Lattice-Boltzmann simulations of *Hill et al.*³⁰, we have carried out simulations for low Reynolds number ($Re_p=0.001$) with FCC geometry. Predictions of our model are compared with the previous results of *Sangani and Acrivos*³⁵ and *Hill et al.*³⁰ in Figure 2.7a. It can be seen that, our simulated results agree quite well with the results of LB simulations of *Hill et al.*³⁰ and both the results are agreeing well with the analytical solution at low solid volume fraction.

2.3.1.3 Comparison of Results with *Hill et al.* and *Dhole et al.*

In this section, predicted values of average drag force acting on particles are compared with the results of *Hill et al.*³¹ and *Dhole et al.*²⁵ for moderate values of particle Reynolds numbers. *Hill et al.*³¹ has carried out lattice-Boltzmann simulations for FCC geometry for a range of particle Reynolds numbers 40 to 500 where as the approach used by *Dhole et al.*²⁵ is independent of particle arrangement. Results are presented in terms of drag co-efficient defined as:

$$C_d = \frac{2F_D}{\rho V^2 \pi R^2} \dots \dots \dots (2.10)$$

Predicted drag coefficient for FCC and SC geometry with solid volume fraction equal to 0.5 are shown in Figure 2.8b. It can be seen from Figure 2.8b that the results of our model agree reasonably well with the published results. Despite some discrepancies seen in Figure

2.4(for $Re_p=12.17$), the overall results of our computational model can be said to be in good agreement with the experimental as well as previous computational results over a broad range of particle Reynolds numbers. Influence of particle arrangement on velocity distribution, drag force and on heat transfer is discussed in the following after discussing the influence of particle Reynolds number on flow structure.

2.3.2 Influence of Reynolds number

Simulations were carried out for higher Reynolds number i. e. $Re_p=1000$ and 2000 to study the influence of Reynolds number on velocity distribution, drag forces and heat transfer. Only effect of turbulence flow field in SC geometry is discussed here and influence of other parameters such as influence of particle arrangement, drag force and heat transfer is discussed in next respective sections.

Simulated results show that the maximum in profiles of normalized axial velocities increases with increasing Reynolds number for the laminar flow regime ($Re_p=12.17$ to 204.74 Figure 2.4a-d). However, for the turbulent regime ($Re_p=1000$ and 2000), the normalized profiles are almost independent of Reynolds number. The maximum value of normalized velocity is closer to that obtained with the lowest Reynolds number considered in the laminar regime ($Re_p=12.17$). Velocity profiles for the turbulence cases are much flatter than those obtained for the laminar regime. The region of negative velocities near the wall was found to be larger in turbulent flow regime compared to the laminar regime.

Detailed comparison of the predicted results for the turbulent flow regime with experimental data is not possible because of lack of availability of such data. Velocity vectors in transverse planes (planes A, B and C) are shown in Figure 2.6. A pair of symmetric vortices

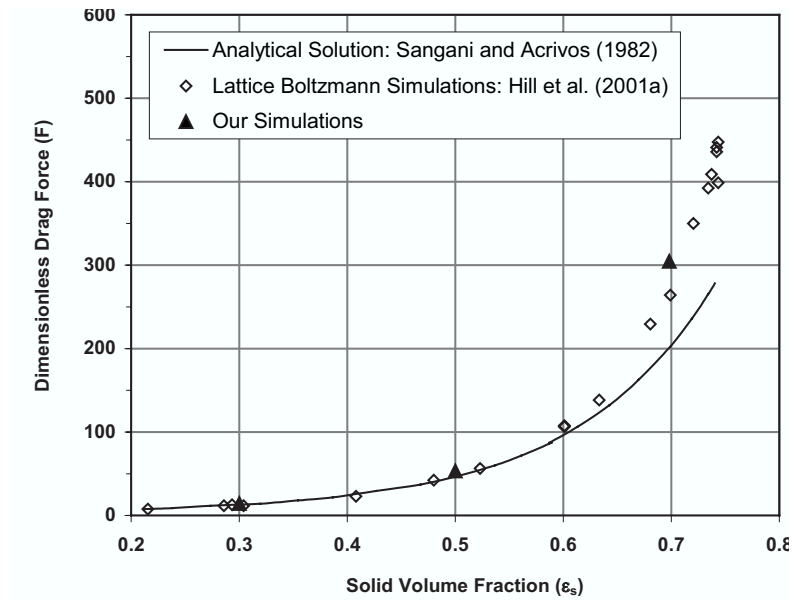


Figure 2.7: Comparison of simulated results with the literature data for low Reynolds number ($Re_p=0.001$)

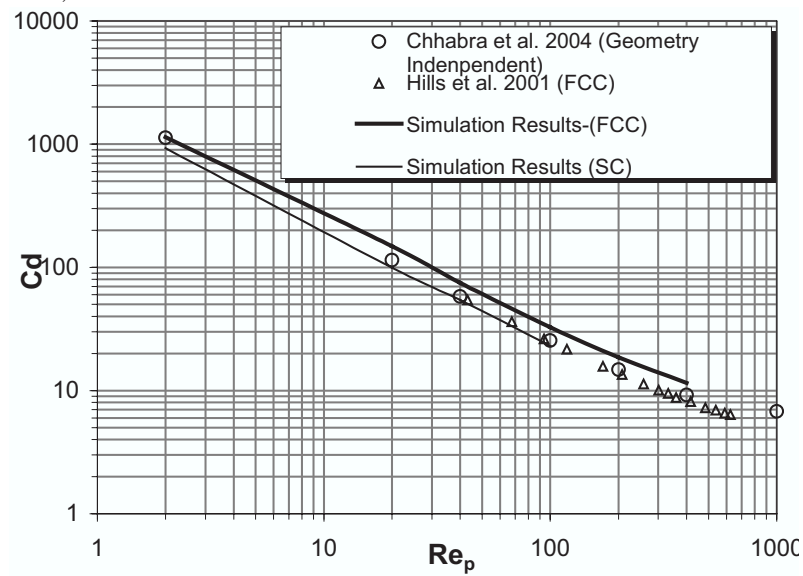


Figure 2.8: Comparison of simulated average drag coefficient with the literature data at various Reynolds numbers.

was observed at plane A for particle Reynolds number of 2000, which was similar to that observed at particle Reynolds number of 204.74. At plane B, flow characteristics obtained for Reynolds number of 2000 were qualitatively similar to those observed at $Re_p=59.78$ and 204.74 (see Figure 2.5C and 2.6ab). At plane C, flow pattern observed for $Re_p=2000$ was found to be similar to that observed for $Re_p=59.78$ (that is fluid appears to move away from the walls of sphere). Knowledge of such detailed flow structure within void spaces will have significant implications for estimation of heat and mass transfer.

2.3.3 Influence of Packing Arrangement

In order to understand influence of packing arrangement of particles in unit cell, simulations were carried out for different particle arrangements: namely 1D rhombohedral ($\epsilon=0.4547$), 3D rhombohedral ($\epsilon=0.2595$) and face centered cubic ($\epsilon=0.302$) arrangements. Simulations were carried out at different particle Reynolds numbers in laminar flow regime ($Re_p=12.17$ -204.74) and in turbulent flow regime ($Re_p=1000, 2000$).

For 1-d rhombohedral arrangement predicted velocity field at different particle Reynolds number is shown in Figure 2.9. It can be seen that flow at lower Reynolds number (12.17 and 59.78) is qualitatively different than that at higher Reynolds numbers (204.74 and 2000). At higher Reynolds number, wake behind the spheres divides the high velocity stream in two parts at periodic planes (see two groups of red vectors in Figure 2.9c and 2.9d). Profiles of predicted normalized z-component of the velocity on periodic plane at $x=0.0015$ are shown in Figure 2.9e. At lower Reynolds number ($Re_p=12.17$), flow profile is bell shape with maximum velocity about twice the mean velocity ($V_{max}=2V_m$). With increase in Reynolds number flow profile is getting flattened and wake behind the solid body starts affecting the flow profiles. At $Re_p=2000$, splitting of high velocity stream into

two parts is obvious from the shown velocity profiles (Figure 2.9e). Comparison of Figure 2.9e and Figure 2.4 clearly demonstrates the influence of packing arrangement on flow in interstitial spaces. It can be seen from Figure 2.4 that for simple cubical (SC) arrangement the ratio of the z-component of velocity and the mean velocity is 2.5 for the lowest Reynolds number and increases up to 4 with increase in Reynolds number. For the rhombohedral arrangement, the value of this ratio is always below 2 (Figure 2.4e). Unlike SC, the flow encounters obstruction and changes direction in rhombohedral arrangement of particles.

Simulations were also carried out for 3D rhombohedral geometry in order to study the influence of geometry orientation on velocity distribution. From Figure 2.8b it is quite clear that geometrical orientation does not make significant variation in overall drag force acting on particle. However results of SC and 1D rhombohedral geometry indicate that there is significant difference in the predicted flow field distribution for these two cases. Figure 2.4 and 2.9 also indicate that particle Reynolds number also plays a significant role in distribution of velocity inside the void. Except the studies of *Maier et al.*³⁷ and *Magnico*³⁸ which report velocity distribution in void at low Reynolds numbers, no information is available in the literature on how particle arrangement and particle Reynolds number influence velocity distribution. The predicted distribution of z-velocity component is shown in Figure 2.10a for 1D rhombohedral geometry at different particle Reynolds numbers. At the lowest Reynolds number ($Re_p=12.17$), z-velocity distribution exhibits a sharp peak and a shoulder. The predicted velocity distributions of rhombohedral arrangement are also similar to the results reported by *Maier et al.*³⁷ and *Magnico*³⁸. As the particle Reynolds number increases, the distribution broadens and distribution becomes bi-modal. However z-velocity distributions for 3D rhombohedral geometry show different trends than the 1D rhombohedral geometry (see Figure 2.11b). For 3D rhombohedral geometry, flatter velocity distribution was observed at low as well as high Reynolds numbers.

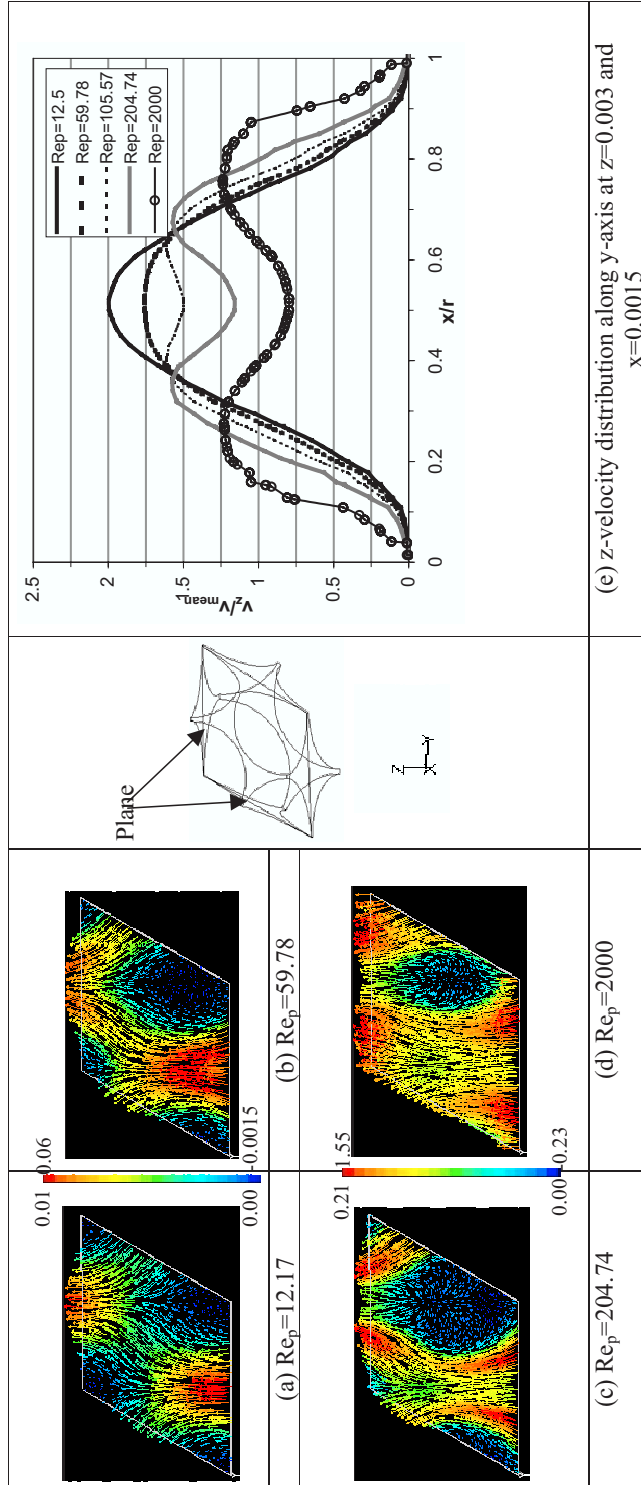


Figure 2.9: Velocity vectors and z-velocity distribution in rhombohedral cell at various particle Reynolds numbers

Distribution of axial component of velocity within the interstitial space for SC, rhombohedral (1D and 3D) and FCC geometry were compared for $Re_p=12.17$ in Figure 2.12a. For SC and 1D rhombohedral geometry, the predicted velocity distribution curves indicate that there are large numbers of cells containing low magnitude axial velocities. However for 3D rhombohedral and FCC geometry flatter velocity distribution was observed. Sederman et al.² have experimentally measured velocity distribution within the packed beds using MRI. Their data for the particle Reynolds number of 16.1 is also shown in Figure 2.12a. The velocity distribution obtained from experimental data of randomly packed bed lies in between the trends observed in different arrangements considered here. Similar trends were observed when distributions of one of the transverse velocity component (x-velocity) in the interstitial space were plotted (see Figure 2.13b).

2.3.4 Relative Contributions of Shear Drag and Form Drag

CFD models provide detailed information about the flow field and pressure distribution within the considered domain. Such information might be used to understand and to quantitatively estimate relative contributions of shear drag and form drag in the overall pressure drop. Overall friction factor for the flow through packed bed may be defined as,

$$\frac{\Delta P}{L} = af_t \frac{1}{2} \rho U_o^2 \quad \dots \dots \dots (2.11)$$

where LHS denotes pressure drop per unit length, f is friction factor, U_0 is superficial velocity and a is ratio of wetted area and volume of cell. From the CFD simulations of flow through unit cells, overall friction factors were calculated using Equation (1) and simulated values of pressure drop per unit length. The predicted values of overall friction factor as a

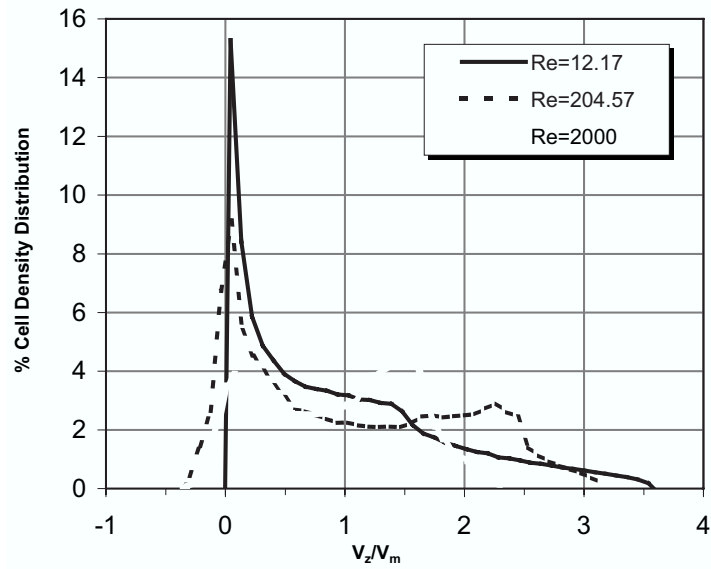


Figure 2.10: Comparison of z-velocity in laminar and turbulent flow conditions along x-axis at highest cross-sectional area (at y and $z=0.0015$)

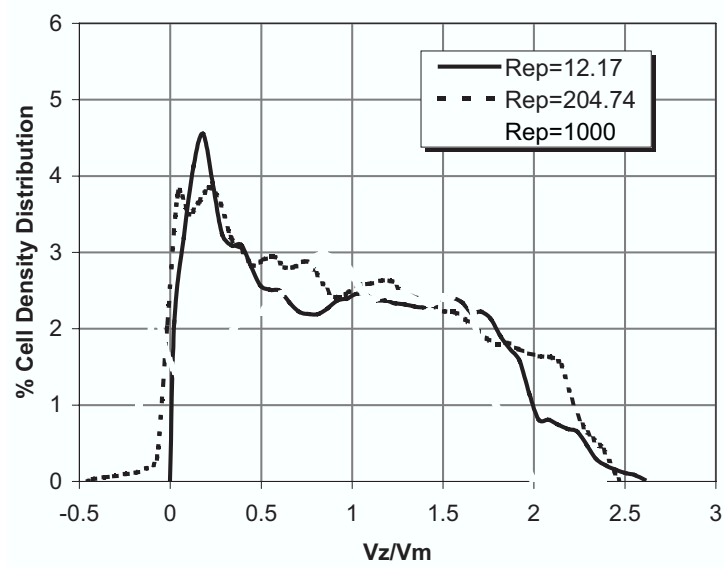


Figure 2.11: Histograms of z-velocity distribution obtained from simulations of liquid flow in 3-D Rhombohedral cell at different Re_p

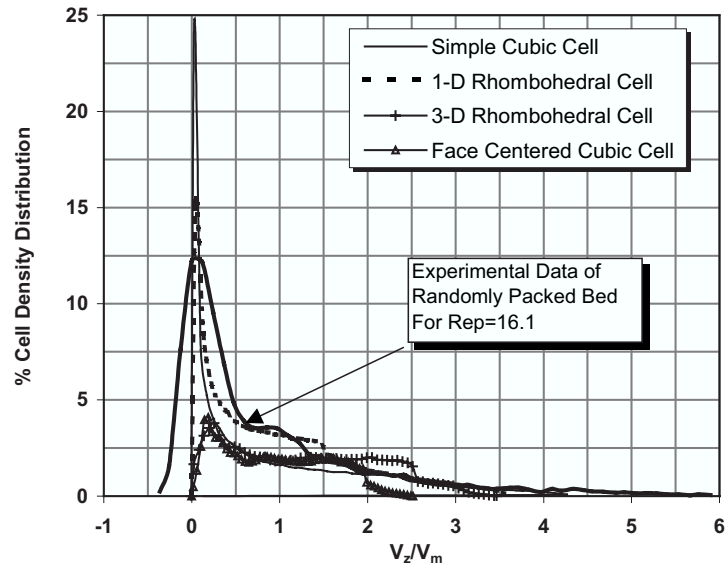


Figure 2.12: Histograms of z -velocity distribution obtained from simulations of liquid flow in different unit cells at $Re_p=12.17$ and experimental data of *Sederman et al.*² in randomly packed bed $D=4.7\text{cm}$, $d_p=5\text{mm}$, normalized density distribution

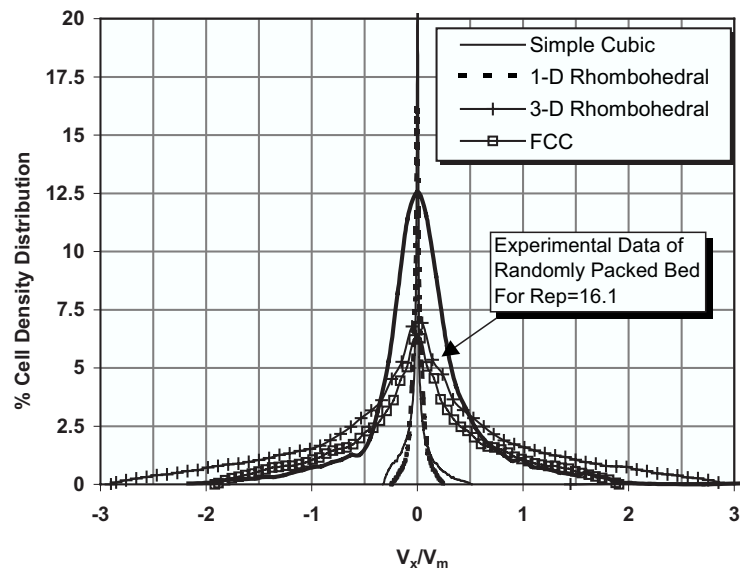


Figure 2.13: Histograms of x -velocity distribution obtained from simulations of liquid flow in different unit cells at $Re_p=12.17$ and experimental data of *Sederman et al.*² in randomly packed bed $D=4.7\text{cm}$, $d_p=5\text{mm}$, normalized density distribution

function of Reynolds number are shown in Figure 2.14. The well-known Ergun's equation can be used to estimate overall friction factor as:

$$f_t = \frac{1}{2} \frac{(1 - \epsilon_B)}{\epsilon_B^3} \left[E_1 + \frac{1 - \epsilon_B}{Re} + E_2 \right] \dots \dots \dots (2.12)$$

where E_1 and E_2 are Ergun's constants and ϵ_B is bed porosity. This equation has been widely used to correlate friction factor for the packed beds and the standard values of E_1 and E_2 are 150 and 1.75 respectively (*Bird et al., 1960*)⁴⁶. *Durst et al. (1987)*³⁶ have critically analyzed the pressure drop in packed beds and have suggested the value of E_1 as 182 instead of 150. The values of friction factor estimated using Equation (2) and values of parameters suggested by Durst et al. (1987) are shown as solid continuous lines in Figure 2.14. It can be seen that the results obtained from the CFD simulations agree with those estimated using Equation (2). It is interesting to note that same values of E_1 and E_2 were able to estimate overall friction factors for all the three packing arrangements considered in this work. Thus the Equation (2) seems to account for the influence of bed porosity on overall friction irrespective of packing arrangement of the bed.

CFD simulations were then used to calculate viscous shear stress at the particle surfaces. The predicted value of viscous shear stress (area averaged) at the particle surfaces was used to obtain viscous friction factor, f_s , as:

$$f_s = \frac{(\tau_w)_{sim}}{1/2 \cdot \rho U_o^2} \dots \dots \dots (2.13)$$

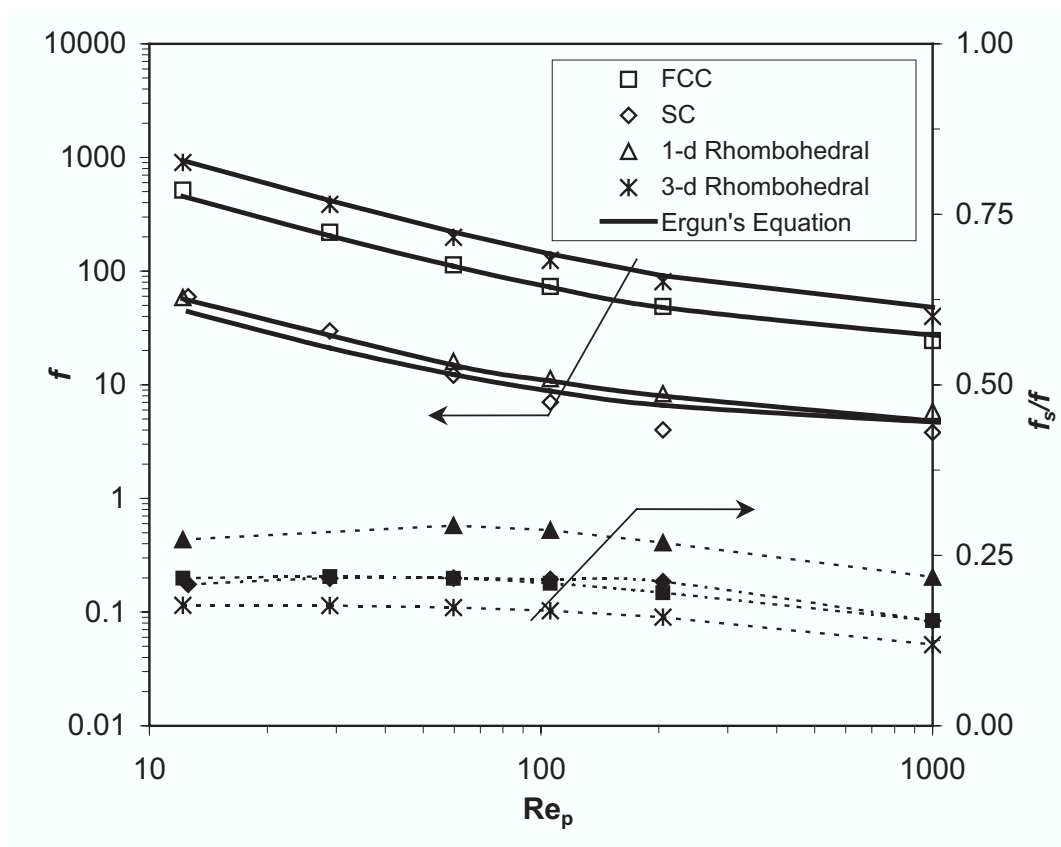


Figure 2.14: Simulated friction factor, shear drag and Ergun equation (Ergun's Constant $E_1 = 180, E_2 = 1.75$, all filled symbols indicate shear drag at the particle surface)

The variation of the ratio of viscous friction factor to the overall friction factor with respect to particle Reynolds number is shown in Figure 2.14 for the three particle arrangements by dotted lines. It can be seen that the relative contribution of surface shear stress (in overall pressure drop) is almost constant for the laminar regime. The value of this ratio is about 0.21 for the SC and FCC arrangement whereas it is about 0.27 for the 1D rhombohedral arrangement. The 3D rhombohedral geometry shows the lowest ratio of viscous to total drag.

2.3.5 Effect of Flow Structure on Heat Transfer

The computational model was used to understand influence of particle Reynolds number and particle arrangement on particle to fluid heat transfer in packed beds. The velocity distribution and re-circulation within the interstitial space is expected to influence particle to fluid heat transfer. Path lines within the interstitial spaces of simple cubic and FCC arrangement are shown in Figure 2.15a. It can be seen that at the lowest higher particle Reynolds number (12.17), the path lines are almost parallel without any circulation. At higher particle Reynolds number (204.74), circulatory flow within the interstitial space was observed for SC arrangement. Comparison of the path lines obtained for the simple cubic and FCC arrangements clearly indicate that unlike for the simple cubic arrangement, flow impinges on particle surface and changes direction several times within interstitial space. For the SC arrangement, bulk of the fluid by-pass the particle surface. Simulated temperature fields for different Reynolds numbers for the SC and FCC arrangement are also shown in Figure 2.15a. The interaction of circulatory flow and predicted temperature field is obvious from these results.

From the simulated values of enthalpy flux at the particle surface, the values of particle

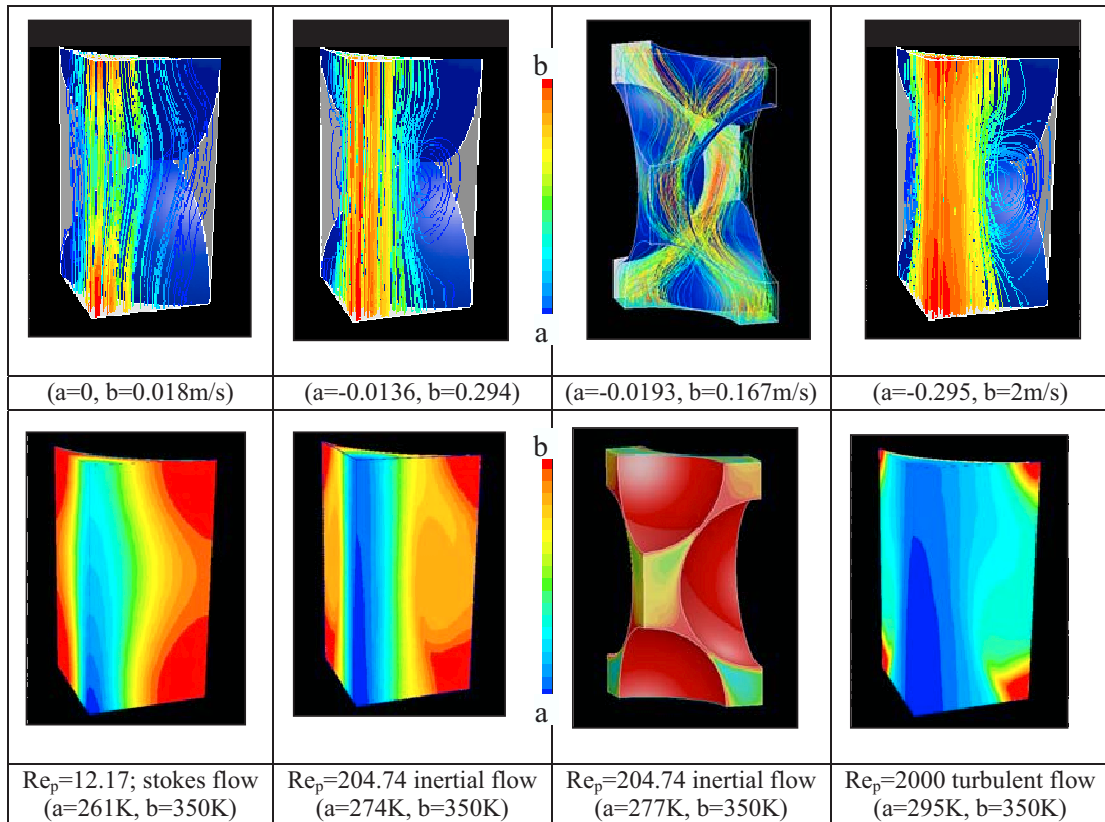


Figure 2.15: Effect of the flow structure on temperature profile inside SC and FCC cell at various Re_p

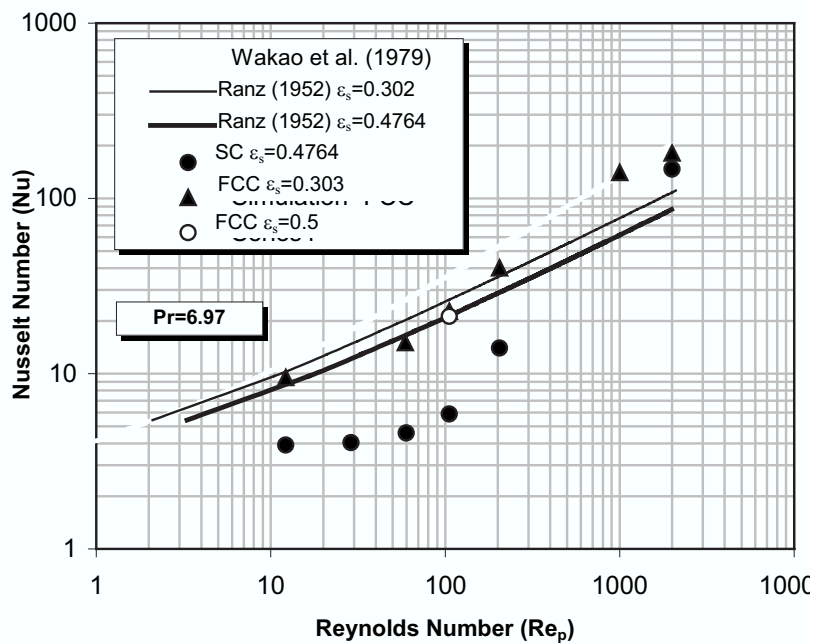


Figure 2.16: Local particle-to-fluid Nusselt number for cubical cell at various Re_p (Symbols simulated values and line are for correlations; Ranz³ $Nu = 2 + 0.6Pr^{\frac{1}{3}}Re^{\frac{1}{2}}$ Wakao et al.⁴ $Nu = 2 + 1.1Pr^{\frac{1}{3}}Re^{\frac{2}{3}}$

to fluid heat transfer coefficients were calculated. The predicted values of Nusselt number for different values of the particle Reynolds numbers are shown in Figure 2.16b for SC and FCC arrangements. Values of Nusselt numbers estimated from the correlations proposed by *Ranz*³ and *Wakao et al.*⁴ are also shown in this figure. It can be seen that the predicted Nusselt number for the FCC arrangement show reasonable agreement with the results of correlation of *Ranz*³. The predicted values of Nusselt number for the SC arrangement were found to be significantly lower than those obtained for the FCC arrangement. It should be noted that simulations for the SC arrangement were carried out with different value of solid volume fraction. In order to separate the influence of solid volume fraction and particle packing arrangement, an additional simulation with a FCC arrangement with solid volume fraction of 0.5 (which is close to that used with the SC arrangement) was carried out. The predicted value of Nusselt number for this case was found to be slightly lower than that obtained for the FCC arrangement with higher volume fraction of solid but much higher than that obtained for the SC arrangement. The predicted overall friction factor was however much closer to that of the SC arrangement since the solid volume fractions are similar. Thus it can be concluded that the observed difference in the predicted Nusselt numbers of the simple cubic and FCC arrangements is mainly because of the differences in flow structures within interstitial space caused by different packing arrangement.

The unit cell approach used in this work for understanding single phase flow through voids of packed bed may be extended for simulating gas-liquid flow through voids of packed bed. Such a study will provide a sound basis for closure terms used in continuum models used to simulated gas-liquid flow through packed beds (see for example, *Gunjal et al.*⁴⁷).

2.4 Conclusion

Computational flow model using a unit cell approach was developed to understand flow and heat transfer in packed beds of spheres. Different packing arrangements namely, simple cubic, rhombohedral (1 and 3D) and face-centered cubic, were considered. The model predictions were verified by comparing the simulation results with the published experimental and computational results. Predicted results showed excellent agreement with the experimental data of *Suekane et al.*¹ for SC geometry. Simulated results showed good agreement with the analytical solution reported by *Sangani and Acrivos*³⁵ at low volume fraction of solids for vanishing particle Reynolds number. The results of the present work also showed good agreement with the results obtained by *Hill et al.*³⁰ with lattice Boltzmann simulation and with the results of *Dhole et al.*²⁵ over a broad range of particle Reynolds number. It was found that the average drag force on particles is not significantly affected by the specific particle arrangement as long as solid volume fraction is the same.

The validated CFD model was used to understand the influence of particle Reynolds number and particle arrangement on velocity distribution within the interstitial space. In laminar flow regime, the predicted magnitude of dimensionless maximum velocity was found to increase with the particle Reynolds number. However, for turbulent flow regime, the magnitude of dimensionless maximum velocity was almost independent of the particle Reynolds number and much lower than that observed with the laminar flow regime. Velocity distribution in 1D rhombohedral geometry was found to be more sensitive to the value of particle Reynolds number compared to the 3D rhombohedral geometry. The predicted velocity distributions for SC and 1D rhombohedral geometries show sharp peaks, which indicate large fraction of void volume with low velocities. However for FCC and 3D rhombohedral geometry, the predicted velocity distribution is significantly flat. Velocity distribution in randomly packed bed (experimental results of *Sederman et al.*² was found

to lie in between these two types (SC and 1D rhombohedral; FCC and 3D rhombohedral).

Total frictional resistance determined from the CFD simulations showed good agreement with the values estimated using the Ergun equation (with $E_1=182$ and $E_1=1.75$) for all the three packing arrangements. Ergun equation was found to over predict the drag coefficient for the turbulent flow regime. The ratio of surface drag to overall drag was almost independent of particle Reynolds number in the laminar flow regime. The values of this ratio obtained for the SC and FCC arrangements were almost the same (0.21). For the rhombohedral arrangement (1D), the relative contribution of form drag was lower than that observed for the SC and FCC arrangements. The 3D rhombohedral arrangement was found to offer maximum form drag.

The predicted values of Nusselt numbers for the FCC arrangement showed reasonable agreement with the correlations of the particle to fluid heat transfer in packed beds. The predicted values of Nusselt number for the SC arrangement were much lower than those obtained for the FCC arrangement. Unlike the FCC, where flow impinges on the obstructing particle and changes directions several times within the 'unit cell', no impingement and direction changes occurs in the SC arrangement. This leads to significantly different heat transfer rates.

Unit cell approach was found to be useful for understanding the flow characteristics in packed bed. The approach and models presented here may provide a basis for extending this study for understanding gas-liquid flow in packed beds.

*“Better to understand a little than to misunderstand
a lot.”*

Anonymous

3

Liquid Drop Spreading on Solid Surface

3.1 Introduction

Interaction of liquid drops with solid surfaces occurs in a variety of processes ranging from spray coating, drying, and cooling to wetting of packings or catalyst pellets. The present study is motivated by the necessity to learn more about fundamental processes in wetting of catalyst pellets in trickle bed reactors. In trickle bed reactors (TBR), gas and liquid phases flow cocurrently downward through the packed bed (of catalyst pellets). Two-phase frictional pressure drop, liquid holdup and degree of wetting are some of the key and essential parameters for designing of these reactors. Wetting of catalyst particles directly affects the utilization of the catalyst bed and performance of the trickle bed reactor. Measurements of degree of wetting in a packed bed reactor are rather difficult and require sophisticated techniques like magnetic resonance imaging, see *Gladden*⁴⁸. These techniques give detailed 3D gas liquid distribution along with flow field information with high spatial resolution. Applicability of such techniques is still in developing stage. Developments in theoretical models and their numerical solution are essential in order to make practical use of these data.

In recent years, computational fluid dynamics based models have been used to understand the complex hydrodynamics of TBR (see for example, *Jiang et al.*¹³, *Gunjal et al.*⁴⁷). Such CFD models may provide better understanding of liquid distribution and wetting phenomenon in trickle bed reactors. However, presently available CFD models (based on Eulerian-Eulerian approach) are unable to capture the observed hysteresis in the operation of trickle beds (see *Gunjal et al.*⁴⁷). The hysteresis observed in trickle beds (of pressure drop, liquid saturation and so on) is directly related to the spreading of liquid on wet or dry solid surfaces. It is therefore important to understand spreading of liquid on solid surfaces (see for example, *Szady and Sundaresan*⁴⁹, *Liu et al.*⁵⁰, *Gunjal et al.*⁴⁷) for making further progress in understanding operation of trickle beds. For understanding wetting, it

is essential to formulate detailed CFD models, which can capture micro-scale processes of interaction of liquid and solid surfaces. Such an attempt is made in this work. The focus was on developing computational models for simulating free surface flows and using these computational models to gain insight and quantitative information about the process of interaction of liquid drop with solid surfaces. It is important to carry out experiments to guide the development and to evaluate the computational models.

In the present work, a case of an interaction of a single liquid drop with flat solid surface was selected as a model problem. In order to understand the effect of various parameters such as liquid velocity, surface tension and wetting and non-wetting conditions, experiments were carried out over a wide range of operating conditions relevant to operation of trickle bed reactor. The process of spreading/recoiling of a liquid drop after collision with a flat solid surface was experimentally and computationally studied to identify key issues in liquid-solid contacting. Before discussing the present work, previous studies are briefly reviewed in the following sub-section.

3.2 Previous Work

Phenomenon of drop impact with solid surface has been extensively studied (see for example, *Stow and Hadfield*⁵¹, *Chandra and Avedisian*⁵², *Scheller and Bousfield*⁵³, *Zhang and Basaran*⁵⁴, *Mao et al.*⁵⁵, *Crookes et al.*⁵⁶, *Bergeron et al.*⁵⁷, *Richard et. al.*⁵⁸, *Rioboo et al.*⁵⁹ and reference cited therein) because of its wide spread applications. *Scheller and Bousfield*⁵³ have studied drop spreading on polystyrene and glass surfaces for a wide range of liquid properties (viscosity 1-300 mPa.s and surface tension 65-72 mN/m). Maximum spread diameter was correlated as a function of the Reynolds and Ohnesorge number (Oh). *Mao et al.*⁵⁵ have experimentally studied drop spreading and rebounding phenomenon at

different values of contact angle (CA) and impact velocity. They have reported experimental data on maximum spread diameter for different impact velocities. *Richard et al.*⁵⁸ have reported the contact time of droplets bouncing on a non-wetted solid surface at various impacting velocities and drop diameter. Previous experimental studies and parameter ranges considered in these studies are summarized in Table 7.1. It may be noted that most of the previous studies were restricted to higher impact velocities (>1 m/s). Very few experimental studies and simulations were carried out with lower (< 1 m/s) impact velocities. Unlike the ranges considered in previous studies, interaction of liquid drops with solid surfaces occurs at much lower velocities in trickle bed reactors (0.05-1.0 m/s). Additional experimental investigations for the ranges relevant to trickle bed reactor are therefore needed.

Interaction of a surfactant containing liquid drop with solid surface might be very different from that of a drop without containing the surfactant. Several studies have been carried out to understand influence of surfactant on dynamics of drop impact with a solid surface (for example, *Pasandideh-Fard et al.*⁶⁰, *Mourougou-Candoni et al.*⁶¹, *Zhang and Basaran*,⁵⁴, *Thoroddsen and Sakakibara*⁶² and *Crooks et al.*⁵⁶. If the characteristic time scale of surfactant diffusion within the drop is larger or comparable with the characteristic time scale of spreading/ recoiling, surfactant concentration within the drop may become spatially non-homogeneous. In such a case, impact dynamics of the drop was found to be very different. Study of *Zhang and Basaran*⁵⁴ suggest that for the relatively low molecular weight surfactants like SDS, surfactant transport rates are fast enough to ensure that surfactant concentration remains uniform within the drop during impact process (even up to impact velocities of 2 m/s). Thus, studies of drop impact process with addition of surfactants like SDS might be useful to isolate and understand influence of surface tension on drop impact process without complications of variation of surfactant concentration within the drop.

Table 3.1.1: Summary of the Previous Work Done on Impact of Drop in Solid Surface

No	Authors	Purpose	Scope	Impact	Contact	Re	We	Method
1	Fukai	Drop	2-D	sd	30-150	1500-4500	37-530	2-D

Most of the previous modeling work was focused on developing either empirical or theoretical models to predict maximum spread or criterion for rebound (*Crooks et al.*⁵⁶, *Mao et al.*⁵⁵). Though such models provide some insight into drop interaction with solids, they are unable to provide detailed information such as: interactions of gas and liquid phases, variation of drop surface area, solid-liquid contact area and velocity field within the drop with time. Such information is needed to provide an insight into wetting and macroscopic closure models used in trickle bed reactor models. Various computational approaches have been used to simulate free surface flows such as drop impact. They are briefly reviewed in the section describing the present computational model. Here, some of the simulation studies are reviewed briefly.

*Fukai et al.*⁶³ have used adaptive finite element method to simulate the impact of a drop on a flat surface. Experiments as well as simulation results were shown at various operating conditions. Consideration of advancing and receding angle was found to be improve results and most of the study was in the range of impact velocity 1-2 m/s. *Pasandideh-Fard et al.*⁶⁰ have carried out simulations of impact of drop using modified SOLA-VOF method. In this study, drop contact angle variation was considered during each time step and simulated results were compared with their experimental data of drop spreading. *Bussmann et al.*⁶⁴ have studied drop splashing with experiments as well as simulations. Average dynamic contact angle measured from experiments was used for simulation and splashing was studied at very high impact velocity (>1.5 m/s). *Davidson*^{65,66} has used boundary integral method to study deformation of a drop on a flat surface. In his study, applicability of the boundary integral method for an in-viscid drop deformation was assessed for different values of Weber number (5-25). Linear viscous term was derived from this study to understand the role of viscosity on drop deformation. Recently *Pasandideh-Fard et al.*⁶⁷ have studied solidification of the molten drop on flat and inclined surfaces with interface tracking algorithm and continuum surface force (CSF) model in a three-dimensional domain.

Most of the previous modeling attempts restricted their simulations to initial period of drop impact; usually just covering a first cycle of spread and recoil (simulations were carried out for time less than about 50 ms). Systematic studies covering several cycles of spread and recoil are needed to evaluate whether CFD models capture the overall dynamics correctly. Such validated models may then be used for gaining better insight into drop flow field under spreading/ recoiling over solid surfaces.

3.3 Present Contribution

The present work was undertaken to develop CFD models to simulate drop impact on a solid surface with lower impact velocities and to provide experimental data to evaluate CFD models. High-speed camera was used to characterize drop impact by measuring drop oscillation periods and spreading and recoiling velocities. Experiments were performed at various impact velocities (0.22 m/s to 4 m/s) for systems covering wide range of contact angles (40 to 180°). Two different surfaces (glass and Teflon) and two liquids: water (with or without surfactant) & mercury, were used to realize different drop interaction regimes. Experiments were carried out for the following three distinct regimes of drop interaction with flat surfaces:

- Oscillations: drop spreads and recoils many times before coming to rest
- Rebounding: drop bounces from the surface
- Splashing: drop breaks into smaller droplets

Static and dynamics contact angles were obtained from experimental images of spreading and recoiling. A VOF based model was used to simulate drop impact phenomenon. Surface

tension and wall adhesion phenomena were accounted. Influence of several parameters such as drop diameter, liquid surface tension and solid surface properties were studied with the help of experiments as well as simulations. Drop oscillation period, rebounding, finger formation and wall adhesion were studied. Drop height variation with time obtained from simulated results were compared with experimental data. From validated simulations, interfacial area and solid-liquid contacting area variation during the oscillatory phase were obtained. Detailed flow field information was found to be useful for calculating gas-liquid and liquid-solid interaction in terms of average shear stress acting at the corresponding interfaces. The reported results and further extensions of the present work would have significant implications for CFD modeling of trickle bed reactors.

3.4 Experimental Set-up and Procedure

The experimental set-up used for studying interaction of a drop with a flat plate is shown in Figure 3.1. The set up consists of a dropper for drop generation, a flat surface on which drop impact was studied, high-speed CCD camera (from Red Lake Imaging, USA) for image capturing, flashlight and image processing software Image Pro (from Media Cybernetics, USA). Drops were generated manually with a dropper. Droppers with 4 mm and 0.5 mm inner diameter and liquids with different surface tension and CA (distilled water with or without sodium dodecyl sulphate [SDS] and mercury) were used to generate drops of diameters ranging from 2.5 mm to 4.2 mm. Surface tension of water was reduced with the help of SDS [0.094 gm SDS was added in 20 ml of water]. This concentration of SDS is well beyond the critical micellar concentration (8.2 mM). Two solid surfaces, namely glass and Teflon, were chosen for the study such that it is possible to cover the relevant range of CA.

It was observed that water drop on glass surface shows varying CA during the process of drop spreading and recoiling. This is due to adsorption of moisture on the surface of glass. In order to minimize the effect of surface moisture on contact angle, the surface was washed with hot water, dried at 80°C for 1 hr and then cooled in a dry environment before performing the experiments. Experiments were carried out on pre-treated (dry) glass surface as well as on non-pretreated surface. The observed dynamics of drop impact with and without such treatment of glass surface showed significant differences which are discussed later in the thesis. Teflon surface was created with the help of Teflon tape wrapping on an acrylic surface. No pre-treatment was needed for this surface.

Liquid drop formed at the tip of the dropper was allowed to fall freely on the solid surface placed below the dropper. The desired drop impact velocity was achieved by varying the dropper height from the plate surface. At high impact velocity (1 m/sec), it was observed that the drop gets deviated from spherical shape. Photographic observations, however, showed that just before the impact, the deviations from spherical shape are not significant [sphericity (d_{min}/d_p ; where d_{min} is minimum diameter of compressed drop) was about 0.98]. Drop diameter just before the impact, drop impact behavior and dynamics were recorded with the help of a high speed CCD camera. Recording was carried out at various frame speeds from 250-500 frames per second. No significant information loss was observed between 125 to 500 frames per second for drop impact velocities up to 1 m/s. Therefore, data for lower values of impact velocity (0.2 m/s) was recorded with 250 fps while for high values of impact velocity (1 m/s), recording speed of 500 fps was used. This high recording speed ensured that minimum eight data points were collected per period of oscillations and there was no loss of critical information between two consecutive frames. The camera was located at 15 cm from the dropper and a zoom lens (18-180/2.5) was used for recording the images. Camera was focused on about 10x10 mm area and images of resolution of 55 pixels/mm were acquired in a movie form. A bright white light was used

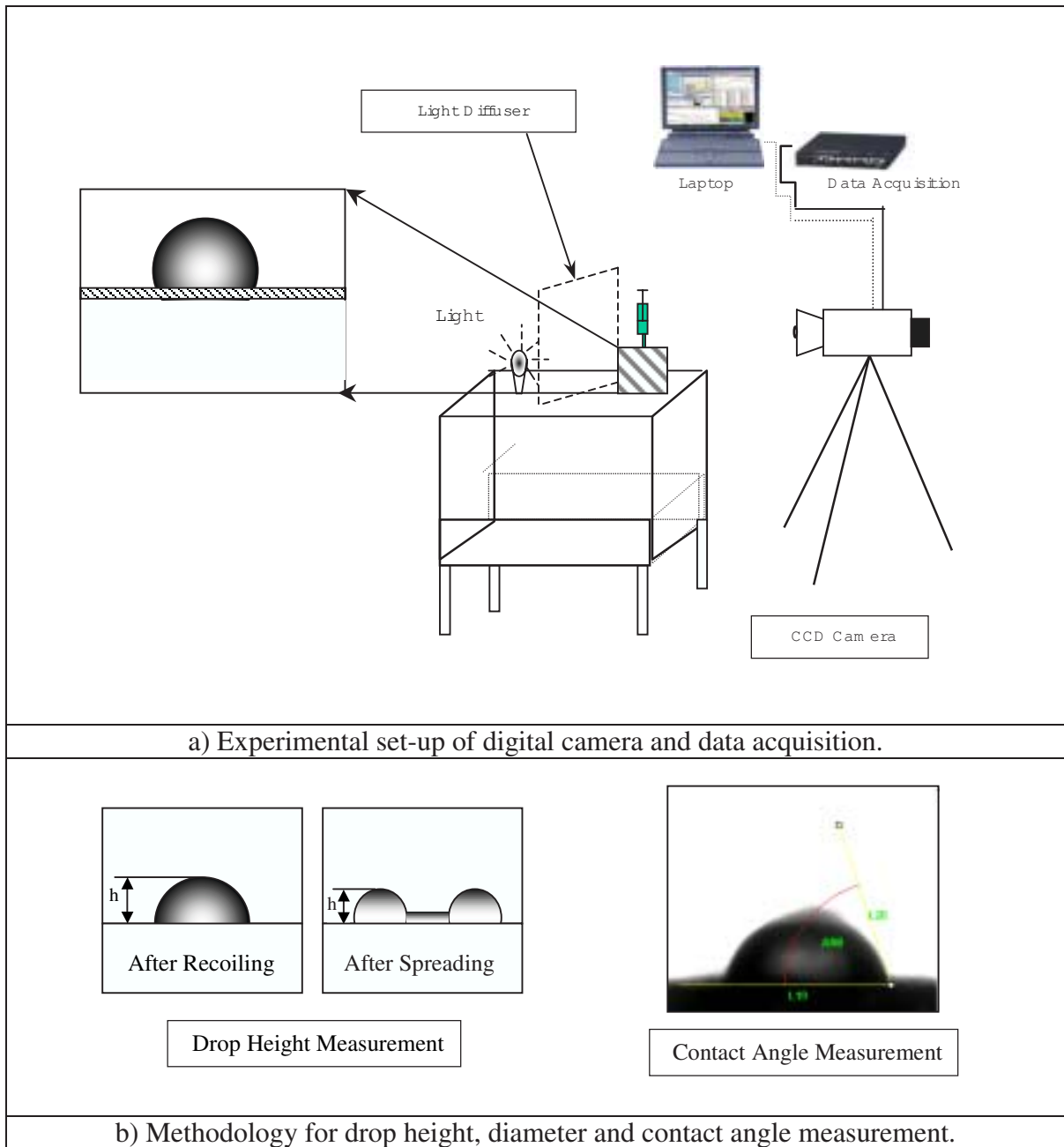


Figure 3.1: Schematic of experimental set-up for studying drop dynamics with high-speed digital camera

in front of the camera and light diffuser was used in between so as to remove harsh shadows from the object.

Recorded images were processed with the help of the image analysis software, Image Pro Plus. For calibration, a test material of known dimension was recorded during each set of experiments. Brightness and contrast of the images were adjusted so that clear three-phase interface position could be measured. Dynamic Contact Angle (DCA), Static Contact Angle (SCA) at interface, drop height and diameter with time were measured (see Figure 3.1b) with Image pro plus. Drop oscillations usually get damped in about 0.5 s. The images of stationary drop were acquired after ensuring that all the oscillations are damped out (3 s). Values of measured SCA of water on glass and Teflon surface were found between $35-75^\circ$ and $110-125^\circ$ respectively. Unlike glass surface, the measured values of SCA for Teflon surface were rather insensitive to the moisture and other surrounding conditions. Contact angle variation with time was also measured and reported. Measured drop height and diameter were made dimensionless by dividing them with the values of drop height and diameter measured when it comes to complete rest. The variations in DCA and dimensionless height or diameter were plotted against time (made dimensionless using measured value of average oscillation time). Drop impact experiments were performed several times to ensure that the measured profiles of drop height/ diameter with respect to time are within 5%.

3.5 Computational Model

Several methods based on are available to simulate free surface flows (see for example, *McHyman*⁶⁸; *Unverdi and Tryggvason*⁶⁹; *Monaghan*⁷⁰; *Fukai et. al*⁶³; *Ranade*⁷¹). Free-surface methodologies can be classified into surface tracking, moving mesh and fixed mesh

(volume tracking) methods. Surface tracking methods define a sharp interface whose motion is followed using either a height function or marker particles. In moving mesh methods, a set of nodal points of the computational mesh is associated with the interface. The computational grid nodes are moved (by interface fitted mesh method or by following the fluid) to retain the sharp interface. Both of these methods retain the sharp interface and therefore simplify analysis near interface. However, mesh or marker particles have to be relocated and re-meshed when interface undergoes large deformations. As the free surface deformation becomes complex, the application of these methods becomes very computation intensive. Another method, which can retain sharp interface, is the boundary integral method (*Davidson*⁶⁶). However, the use of this method is still mainly restricted to two-dimensional simulations.

Volume of the fluid (VOF) method developed by *Hirt and Nichols*⁷² is one of the most widely used methods in modeling of free surfaces. This is a fixed mesh method, in which, the interface between immiscible fluids is modeled as the discontinuity in characteristic function (as volume fraction). Several methods are available for interface reconstruction such as SLIC (simple line interface calculation), PLIC (piece wise linear interface calculations) and Young's PLIC method with varying degree of interface smearing (see, for example, *Rider and Kothe*⁷³; *Rudman*⁷⁴ and *Ranade*⁷¹ for more details). In the present work, VOF method [with PLIC] was used to simulate drop impact on solid surfaces. Gas and liquid phases were modeled as incompressible, Newtonian fluids with constant value of viscosity and surface tension. Flow was assumed to be laminar. It is important to model surface forces and surface adhesion correctly. Continuum Surface Force (CFS) model developed by *Brackbill et al.*⁷⁵ was used in this work. Details of model equations are discussed below.

3.5.1 Mathematical Model

The mass and momentum conservation equations for each phase is given by,

$$\nabla \cdot V = 0 \quad \dots \dots \dots (3.1)$$

$$\frac{\partial(\rho V)}{\partial t} + \nabla \cdot (\rho V \cdot V) = -\nabla P + \mu \nabla^2 V + \rho g + F_{SF} \quad \dots \dots \dots (3.2)$$

Where, V is the velocity and P is the pressure and F_{SF} is the continuum surface force. This single set of flow equations were used throughout the domain and mixture properties as defined below were used. The density of the mixture was calculated as:

$$\rho = \sum_k \alpha_k \rho_k \quad \dots \dots \dots (3.3)$$

where, α_k is the volume fraction of the k_{th} fluid. Any other mixture property, ϕ , was calculated as:

$$\phi = \frac{\sum_k \alpha_k \phi_k \rho_k}{\sum_k \alpha_k \rho_k} \quad \dots \dots \dots (3.4)$$

When in a particular computational cell,

$\alpha_k = 0$: the cell is empty (of the k_{th} fluid).

$\alpha_k = 1$: the cell is full (of the k_{th} fluid)

$0 < \alpha_k < 1$: the cell contains the interface between the k_{th} fluid and one or more other

fluids.

Interface between the two phases was tracked by solution of a continuity equation for volume fraction function as:

$$\frac{\partial \alpha_k}{\partial t} + V_k \cdot \nabla \alpha_k = 0 \quad \dots \dots \dots (3.5)$$

Volume fraction for the primary phase (gas) was not solved and was obtained from the following equation:

$$\sum_k \alpha_k = 1 \quad \dots \dots \dots (3.6)$$

In addition to the mass and momentum balance equations, surface tension and wall adhesion need to be accounted for. Surface tension was modeled as the smoothed variation of capillary pressure across the interface. While representing the surface force in the form of volumetric source terms, tangential stresses at the gas-liquid interface were neglected. Following *Brackbill et al.*⁷⁵, it was represented as a continuum surface force (FSF) and was specified as a source term in the momentum equation as:

$$F_{SF} = \kappa \sigma \left[\frac{\alpha_1 \rho_1 + \alpha_2 \rho_2}{\frac{1}{2}(\rho_1 + \rho_2)} \right] n \quad \dots \dots \dots (3.7)$$

$$n = \nabla \alpha_2 \quad \dots \dots \dots (3.8)$$

$$\kappa = -(\nabla \cdot \hat{n}) = \frac{1}{|n|} \left[\left(\frac{n}{|n|} \cdot \nabla \right) |n| - (\nabla \cdot n) \right] \quad \dots \dots \dots (3.9)$$

where, n is the surface normal, \hat{n} is the unit normal and κ is curvature. Surface normal n was evaluated in the cells containing interface and requires knowledge of amount of volume of fluid present in the cell. Geometric reconstruction scheme (based on piece wise linear interface calculation, PLIC) was used calculate the interface position in the cell. Adhesion to wall influences calculation of surface normal. Formulation and implementation of boundary conditions are discussed after describing the solution domain and computational grids.

3.5.2 Solution Domain and Computational Grid

Experimental images showed that the drop spreading is symmetric at low liquid velocities (<1 m/s). Therefore, for low impact velocities (<1 m/s), axis-symmetric two-dimensional domain was used for carrying out simulations of drop impact. For impact velocities higher than 1 m/s, three-dimensional domain was considered. To minimize demands on computational resources without jeopardizing the ability to capture key features, the solution domain for such 3D simulations was restricted to 90° (instead of full 360°). The axis-symmetric solution domain is shown in Figure 3.2 a and b. The computational grid was generated using GAMBIT 2.0 of Fluent Inc. Since the free surface between gas and liquid changes shape and locations significantly during the course of VOF simulations, uniform grid (with aspect ratio of unity) near the vicinity of the drop (1.5 times d_p) was used and beyond that non-uniform grid was used to reduce computations. Experimental information was used to select appropriate solution domain (such that they were at least 1.5 to 2 times maximum spreading and maximum height achieved during oscillations). During simulations, flow field near the outer surfaces were monitored to ensure that no significant flow occurs there. This indirectly indicates that the size of the domain would not affect the simulation results. Initially simulations were carried out using different grids (see Figure

3.3 c). These results are later discussed in Results and Discussion section.

3.5.3 Boundary Conditions and Numerical Solution

Boundary conditions used in the present work are shown in Figure 3.2 a. Along the symmetry axis, (x-axis in Figure 3.2 a), symmetric boundary condition was imposed in which normal velocity and normal gradients were set to zero, i.e.,

$$u = 0 \quad \text{and} \quad \frac{\partial v}{\partial x} = 0 \quad \quad (3.10)$$

No slip boundary condition was used at the wall where all the components of velocity were set to zero. Treatment of wall adhesion and movement of gas-liquid-solid contact line deserves special attention. When a liquid drop spreads on a solid surface (see Figure 3.2 a), wall adhesion modifies the surface normal as:

$$\hat{n} = \hat{n}_w \cos(\theta_w) + \hat{t}_w \sin(\theta_w) \quad \quad (3.11)$$

where, \hat{n}_w and \hat{t}_w are the unit vector normal and tangential to the wall and θ_w is contact angle at the wall. When contact angle is zero, complete wetting condition occurs and drop spreads on solid surface without oscillations. The surface normal at the wall is not affected by the presence of the wall. For non-zero contact angle, presence of wall will influence the spreading. Although no slip boundary condition (zero velocity on wall) was implemented at the wall boundary, the gas-liquid-solid contact line moves along the wall, presenting a kind of singularity. Details of implementation of wall adhesion boundary condition and

how the singularity was bypassed in the numerical solution are discussed in section 3.5.4 to 3.5.7. Since velocity profiles at the other two planes of the solution domain are not known, constant pressure boundary condition was used at these planes.

The set of model equations were solved with boundary conditions discussed above using the commercial flow solver Fluent 6.0 (of Fluent Inc., USA). Mass and momentum equations were solved using second order implicit method for space and first order implicit method was used for time discretization. Pressure interpolation was performed using body force weighted scheme. This scheme is useful when gravitational force is comparable with pressure force. Pressure implicit with splitting of operator (PISO) was used for pressure velocity coupling in momentum equation. This scheme was used to reduce the internal iteration per time step and (relatively) larger under relaxation parameters can be used.

Initial position of the liquid drop was obtained from recorded experimental data and sphere (assuming the drop was spherical) at the corresponding position was marked in the computational domain. Liquid phase volume fraction was patched as unity ($\alpha_2=1$) in this marked sphere. Drop impact velocity was measured from images acquired by the CCD camera and was assigned to the liquid phase while initiating the simulation. This condition was assumed to be initial condition occurring at time $t=0$ s. Typical developed flow field inside and around the drop after 2-3 time steps are shown in Figure 3.2 b. Time step between one to five microseconds (1-5 msec) was found to capture key features of dynamics of drop impact adequately (simulations using 2×10^{-6} and 4×10^{-6} showed no significant difference in the predicted results). Twenty to thirty internal iterations per time step were performed, which were found to be adequate for bringing down the normalized residuals below 1×10^{-5} . With further increase in time step (5×10^{-6}), required number of internal iterations were found to be increasing. Simulated results were stored for every 1 or 2.5 ms interval (adequate to capture key features of dynamics with time scales of about 16-25

ms). Liquid drop in the simulated results was identified from the computed iso-surface of liquid volume fraction of 1.

3.5.4 Aspects of VOF Method

Numerical aspects of VOF method are discussed in this section. Details of geometric reconstruction scheme used to reconstruct interface position are discussed in Section 3.5.5. Calculation of advected fluxes of volume fraction through the cell faces is discussed in Section 3.5.6. Finally wall adhesion boundary condition and treatment of the gas-liquid-solid contact line on no-slip solid surface is discussed in Section 3.5.7.

3.5.5 Geometric interface reconstruction scheme

Geometric reconstruction scheme was used for representing the interface between immiscible fluids. This scheme is based on the piecewise-linear interface calculation (PLIC). The geometric reconstruction scheme was derived from the work of *Youngs*⁷⁶. *Rider and Kothe*⁷⁷ have generalized this scheme for structured as well as unstructured meshes. In this scheme, a straight-line segment approximates an interface within a computational cell (see Figure 3.4). Note that because of linear approximation, interface is discontinuous from cell to cell. The slope of the line segment, approximating interface within a computational cell, is determined from the interface normal. This interface normal is calculated from the gradients of volume fraction (Equation 3.8).

The algorithm proceeds in following steps: 1) From the known volume fraction field, interface normal is calculated from the gradients of volume fraction (see 3.8). 2) The interface

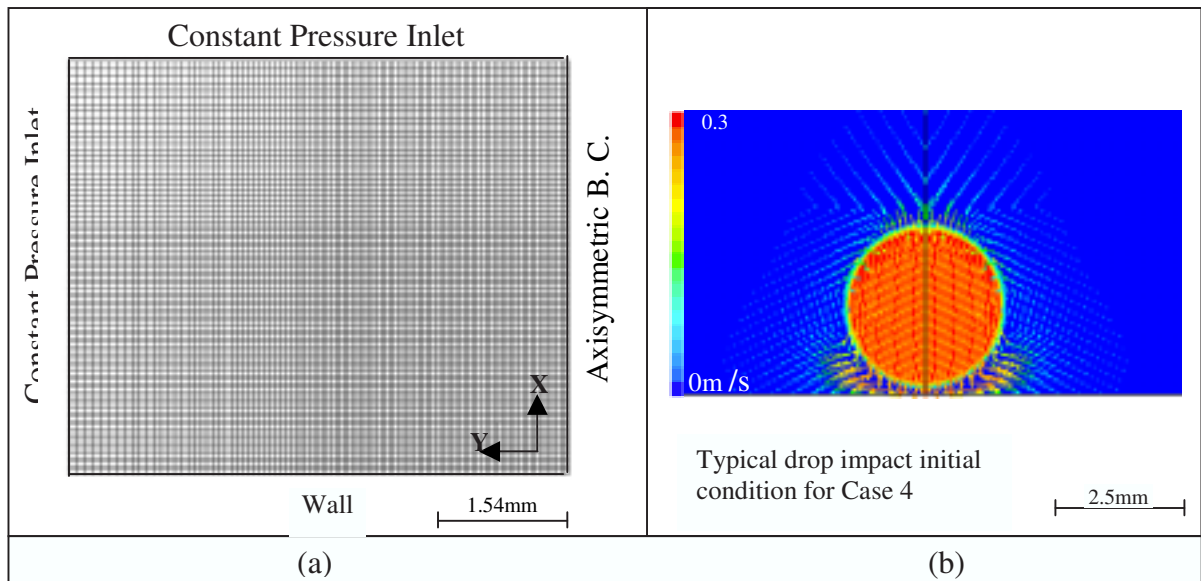


Figure 3.2: Solution domain and boundary conditions b) Typical initial condition at $t=0$

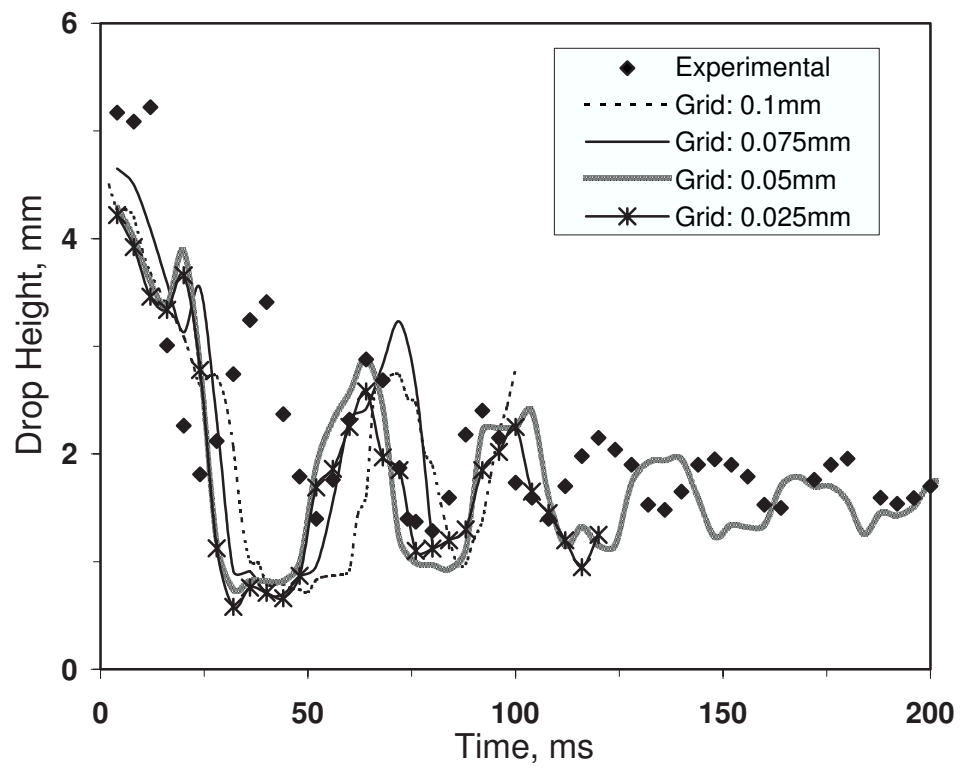


Figure 3.3: Effect of grid size on oscillation of 4.2mm drop on glass surface

position is approximated by drawing a line with following equation:

$$n\hat{x} + c = 0 \dots \dots \dots (3.12)$$

where n is interface normal and c is an adjustable constant. With some initial guess for this constant c , points of intersection of this line and edges of computational cell are obtained. A polygon is constructed from these points of intersection and those vertices of the computational cell, which lie in the fluid 1. If volume of the constructed polygon is same as the volume fraction of fluid 1 in that cell (within stipulated tolerance), the line is assumed to represent the interface in that computational cell. If it is different then line constant c is adjusted using the iterative method (see Rider and Kothe, 1998 for more details).

3.5.6 Advection of fluid through the control volume

Information of the reconstructed interface was used to calculate the amount of fluid advected through the cell faces. Cell face was extruded in the opposite direction to the normal velocity (see vertical shaded portion in Figure 3.5) to the distance normal velocity times the VOF time step (velocity field is know from the solution of momentum equations). The intersection portion (dotted area in Figure 3.5) of extruded volume with sub-section volume (obtained in geometric reconstruction scheme) divided by the extruded volume gives value of face volume fraction. The face volume fraction obtained by this method was then used to calculate the effective advection fluxes of volume fraction at the cell faces. Volume fraction field is then updated by solving usual discretized equations using effective volume fraction fluxes through cell faces.

3.5.7 Wall adhesion and the movement of contact line

For fluids exhibiting non-zero contact angle, presence of wall affects surface normal and wall adhesion needs to be taken into account. Motion of a drop on the solid surface is shown schematically in Figure 3.6. Wall adhesion was modeled in similar manner as that of surface tension in case of gas-liquid interface except that unit normal \hat{n} in this case was evaluated from the contact angle (Equation 3.11). Wall adhesion boundary condition (Equation 3.11) was applicable to those cells, which contain fluid interface and touch the solid surface. The unit tangent \hat{t}_w (in Equation 3.11) is normal to the contact line and tangent to the wall. The tangent \hat{t}_w is directed in to the fluid and computed from Equation 3.8. The unit wall normal \hat{n}_w in Equation 3.11 is directed into the wall. The contact angle was specified from the experimentally measured values.

Movement of the gas-liquid-solid contact line on solid surface may pose unique difficulties since no slip boundary condition is imposed on solid surface. However, in the present numerical implementation of VOF model, the solid wall boundaries coincided with the cell boundaries. No-slip boundary condition was implemented by setting velocity at such cell boundaries (faces) to zero. The velocities at the cell center or cell faces other than those adjacent to the solid surface were not zero. Such non-zero velocities influence volume fraction field and therefore position of the interfaces. Thus, such implementation realizes the movement of the gas-liquid-solid contact line despite specifying no-slip boundary condition at the solid surface.

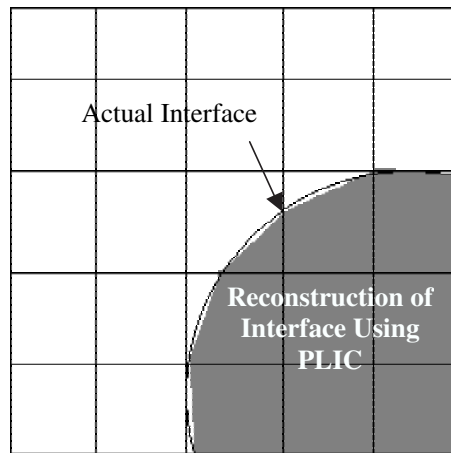


Figure 3.4: [PLIC for calculating interface approximation and face flux]

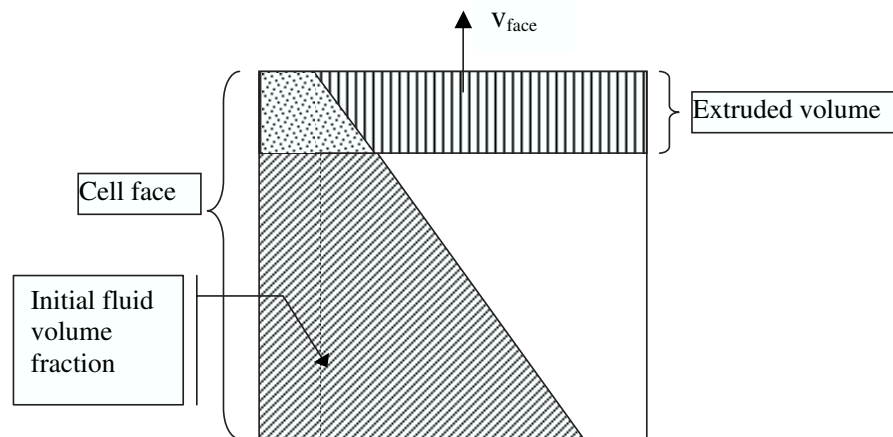


Figure 3.5: [Advection of surface through control volume]

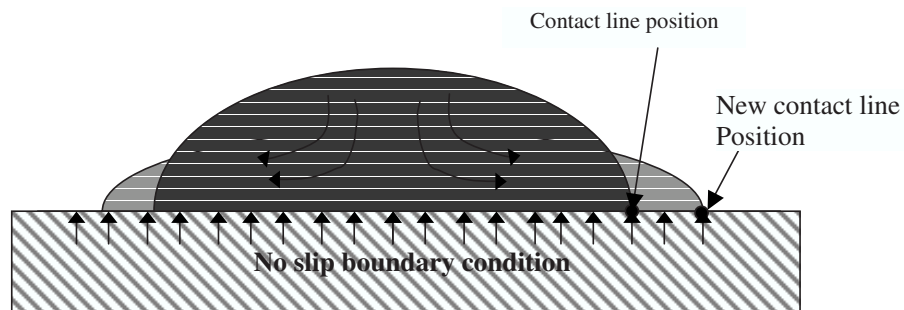


Figure 3.6: [Moment of a contact line on the wall with no slip boundary condition]

3.6 Results and Discussion

3.6.1 Impact of Drop on Solid Surface: Physical Picture/Regimes

Behavior of a liquid drop after impact on a solid surface is determined by interactions of inertial, viscous and surface forces. Drop diameter, impact velocity, liquid properties and nature of solid surface (like CA, roughness and contamination) are some of the key parameters. When a liquid drop impacts on a solid surface, it starts spreading on the surface. The kinetic energy of the drop is dissipated in overcoming viscous forces and in creating new surface area. Surface tension acting at interfaces resists the spread of the drop. Drop reaches its maximum spread and then recoils due to large surface energy of the drop. Such cycles of spreading and recoiling may continue for quite some time. Depending on the surface tension and CA, drop oscillation behavior may exhibit different regimes. The fallen drop may spread on the solid (Figure 3.7 a-b) or may just show a bulging at the center (Figure 3.7 c). If surface is contaminated (here adsorbed moisture) drop spreading is larger (Figure 3.7 b) whereas if surface is pre-treated well (drying) drop height is much larger (Figure 3.7 a). The drops, which spread on solid surface as shown in Figure 3.7 a-c, may recoil and oscillate. If there is sufficient energy while recoiling, drops may rebound (see Figure 3.7 d) from the surface after recoiling (see for example, *Mao et. al.*⁵⁵; *Richard and Quare*⁷⁸). Surface wetting (CA) plays an important role during this process. If the drop experiences less resistance at the surface (high CA) during recoiling, drop may keep on rebounding several times (like a bouncing liquid ball). In some cases, splashing may occur resulting into several smaller droplets on the surface (Figure 3.7 e).

In absence of splashing, liquid drop usually takes between 50-500 ms to come to a rest. The final shape of the drop depends upon the properties of the liquid and the solid surface.

Even after coming to the so-called rest position, drop keeps on spreading due to molecular movement at the surface to form a thin film depending upon the hydrophobic and hydrophilic nature of the surface. This phenomenon was not considered in this work. The scope was restricted to study key dynamic characteristics of the drop impact. In order to study key aspects of different regimes of drop impact, drop diameter, liquid properties (surface tension, viscosity, density) and surfaces were varied to cover the entire range of interest. Details of experiments carried out are listed in Table 7.2 along with the observed flow regimes. Our experimental data and some of the published data are shown in Figure 3.8 in terms of Reynolds number (based on drop impact velocity) and modified Weber number (We_α). Though the data is not sufficient to clearly identify regime boundaries, it may be seen that region in which drop bounces from the surface increases as the value of We_α increases. Regimes observed in the simulated results are also shown in this figure. It can be seen that CFD model was able to capture the regimes correctly. Results of VOF simulations and sensitivity of simulated results to different parameters are discussed in the following section.

3.6.2 VOF Simulations of Drop Impact on Solid Surface

Simulations for 4.2 mm drop diameter with impact velocity 0.22.m/s was carried out in 6x7 mm domain. Simulations were first carried out with an average contact angle of 50° with different grid spacing in domain; 0.1, 0.075, 0.05 and 0.025mm. Drop height variation with time was compared with the experimental data in Figure 3.3 c. It can be seen that simulated results with 0.05 mm and 0.025 mm grids are not significantly different. Therefore all the subsequent simulations were carried out with grid spacing 0.05mm. As mentioned earlier, reduction in time step below 4×10^{-6} s did not affect simulated results and therefore all the subsequent simulations were carried out by setting time step as 4×10^{-6} s.

Table 3.2: Operating conditions and dimensionless numbers for different cases

No	Authors	Purpose	Scope	Impact	Contact	Re	We	Method
1	Fukai	Drop	2-D	sd	30-150	1500-4500	37-530	2-D

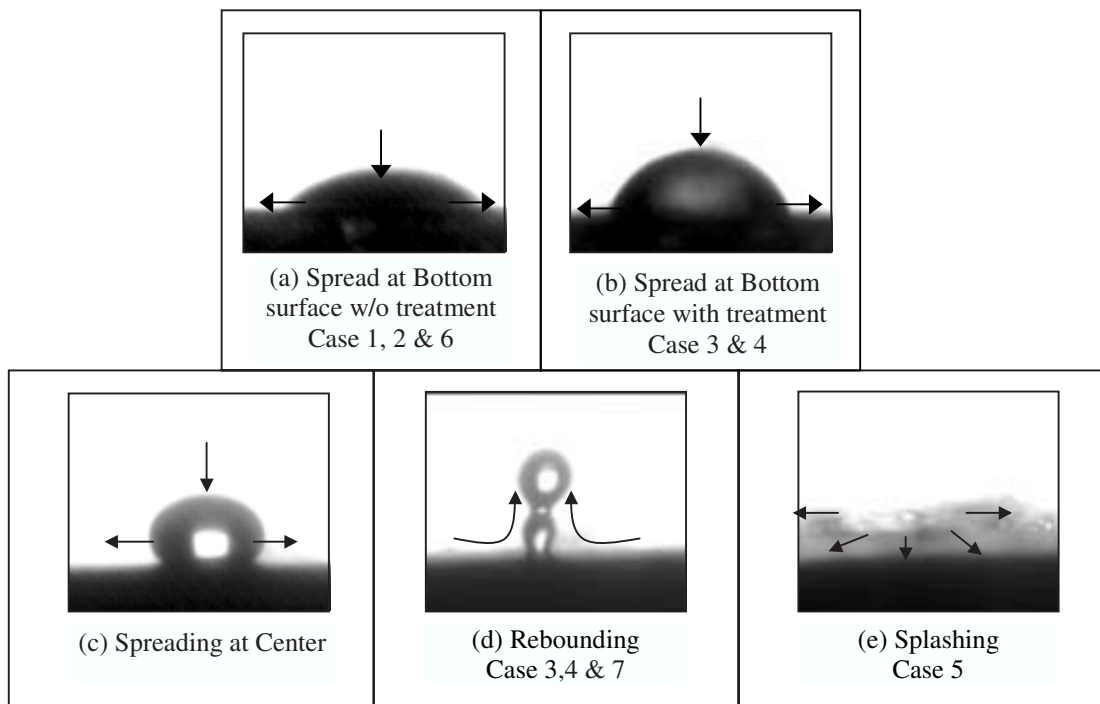


Figure 3.7: Drop spreading- spreading on glass (a and b) and on Teflon surface (c, d and e)

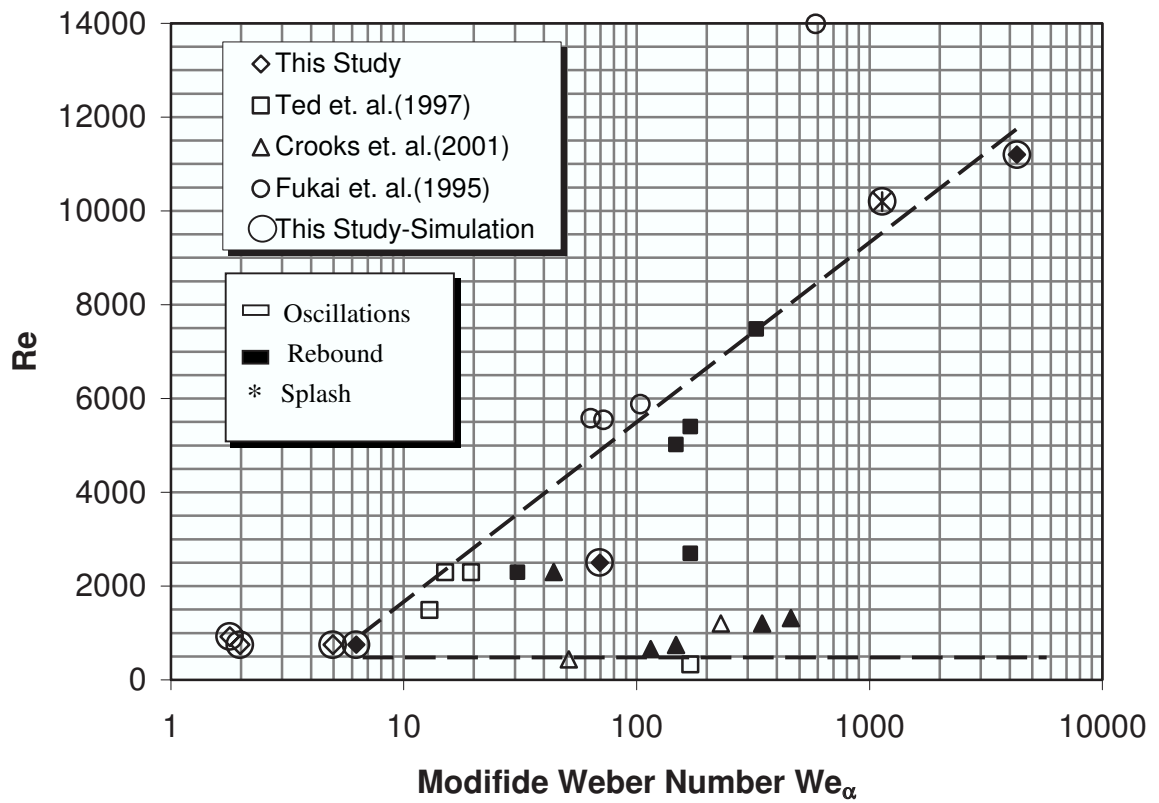


Figure 3.8: Drop impact on solid surfaces-oscillations of spreading and recoiling with or without rebound

In order to study the effect of contact angle on simulated results, simulations were carried out at two values of contact angles (40° and 55°). The simulated variations of drop height are shown in Figure 3.9. It can be seen that simulations with contact angle of 55° are closer to experiments than those obtained with contact angle of 40° . Values of contact angle measured from the experimental images indicate that the value of contact angle is initially higher ($55\text{-}60^\circ$), which subsequently reduces with time to about 40° (see Figure 3.9). It can be seen that measured values of contact angle exhibit maximum or minimum corresponding to spreading or recoiling stage respectively. In other words, advancing contact angle is always higher than the receding contact angle. Values of advancing and receding contact angles were found to decrease with each subsequent oscillation (see Figure 3.9). Considering the significant variation in the measured contact angle, CFD simulations were carried out with time varying values of contact angle. Instead of including all the observed oscillations in the measured contact angle, numerical simulations were carried out with locally averaged values of contact angle (moving average with 20 points). The variation of averaged contact angle was approximated using a step like variation in the numerical model [typically used 15 steps to represent variation during the drop impact process]. Simulated results of drop height variation with time using such varying values of contact angle are also shown in Figure 3.7. It can be seen that agreement is better than that observed in previously two-cases (i.e. using contact angles of 40° and 55°). Hence all further simulations for glass surface were carried out using time variation of locally averaged contact angle.

Simulated results of the drop impact process using dynamic contact angle were compared with the experimental images in Figure 3.10. After the impact on solid surface, the drop starts deforming and spreading (Figure 3.10 b to e). Beyond certain extent of spread, the drop starts recoiling in order to minimize the surface energy (see Figure 3.10 f to h). At this point, drop height starts rising from the center. Inertia developed during the recoiling process lifts the drop height to a considerable extent. Beyond certain increase

of the drop height (Figure 3.10g-h), developed potential energy reverses the flow direction and drop height starts falling (Figure 3.10i). This process continues till drop comes to the equilibrium position. It can be seen that the simulations were able to capture key features of spreading and recoiling. The quantitative agreement between experimental and simulated was improved by implementing time variation of contact angle. The computational model was further evaluated by carrying out simulations for different system parameters. The experimental as well as computational results to understand effects of various parameters on dynamical behavior of drop are discussed in the following sections. Possible reasons for the observed deviation of simulated results from experimental values are discussed after that.

3.6.3 Influence of System Parameters on Dynamics of Drop

3.6.3.1 Influence of Drop Diameter

Influence of drop diameter on dynamics of spreading and recoiling was studied by carrying out experiments with falling drops of diameters 2.5 mm and 4.2 mm (of water) on a flat glass surface. Experimental observations for the case of drop of 4.2 mm diameter are discussed in the previous section. Reynolds numbers (750 and 924) are not much different for the cases of 2.5 mm and 4.2 mm drop. The experiments with 2.5 mm drop showed vary similar oscillations to those observed with the 4.2 mm drop. Bond numbers (Bo), which reflects the relative importance of the gravitation and capillary effects, indicates that the capillary term is quite significant for the case of a 2.5 mm drop (Bo=0.85) compared to that for a case of a 4.2 mm drop (Bo=2.4). Experiments with 2.5 mm drop were carried out with both pre-treated and non-pretreated glass surface. Non pre-treated glass surface contains the moisture on solid surface because of the long exposure to environment (25°C,

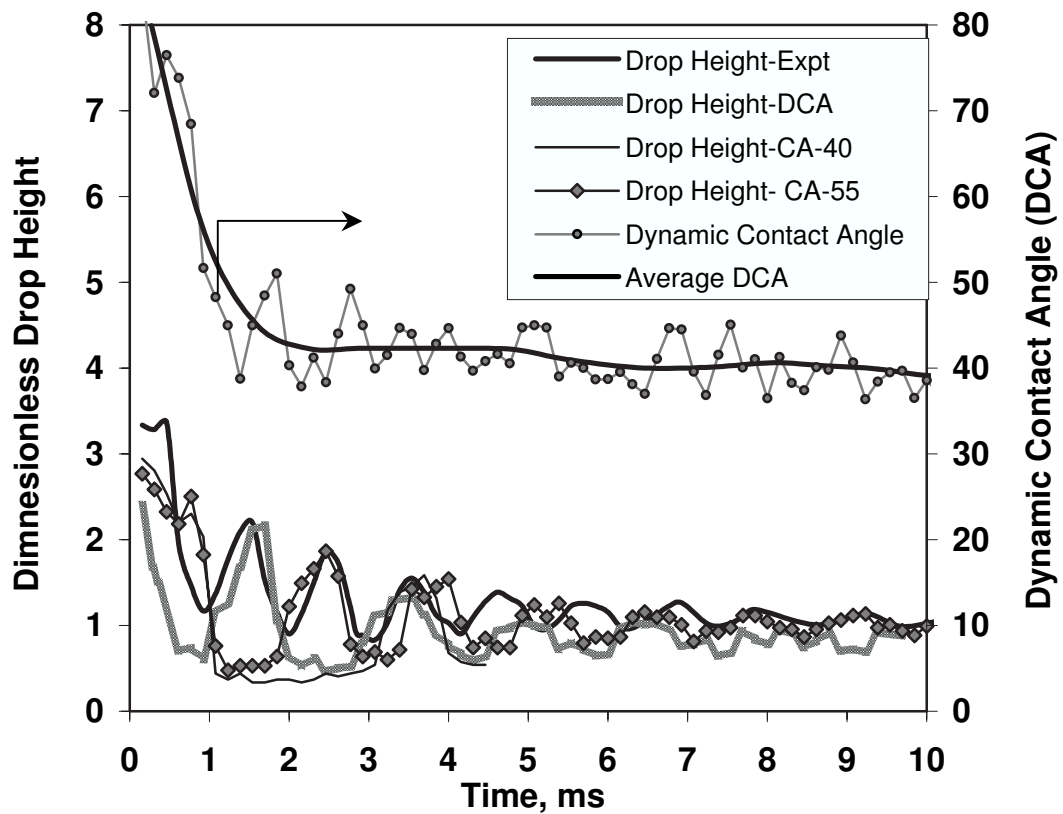


Figure 3.9: Comparison of simulation results with experimental data for 4.2mm drop (Case 1) (Average oscillation period=26 ms , Equilibrium drop height =1.55mm)

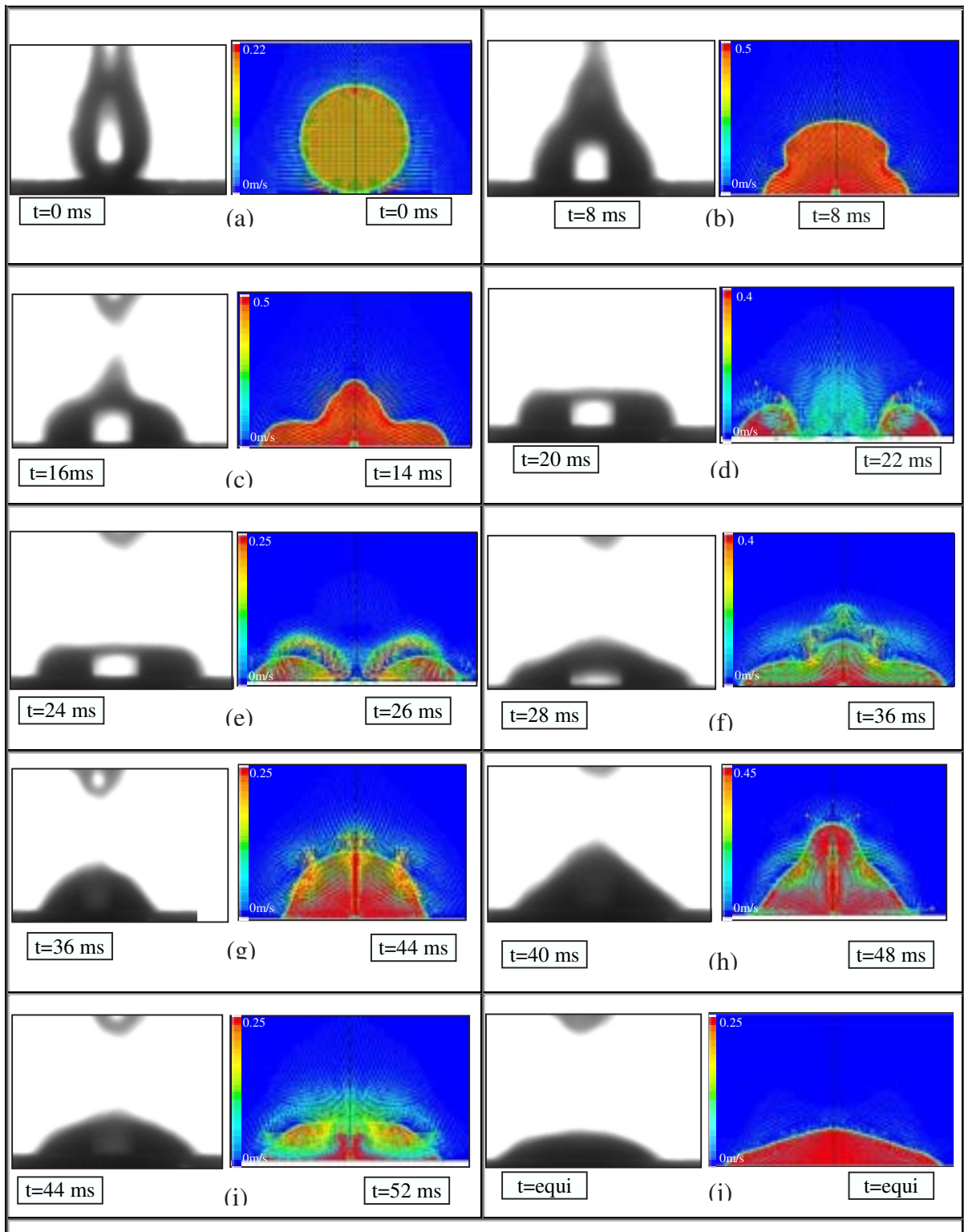


Figure 3.10: Comparison of the experimental and simulation results of the drop dynamics for 4.2 mm drop (Case1). (impact velocity = 0.22m/s, drop diameter 4.2mm, solid surface: glass)

atmospheric pressure and 76% humidity, non-treated surface). The observed variation of contact angle during the process of spreading and recoiling on non pre-treated surface was considerably lower (max=42°, min= 37°, See Figure 3.11 a) than that observed on the pre-treated surface (max=90°, min= 65°, See Figure 3.12 b). It appears that the presence of moisture on the non-treated glass surface affects the drop dynamics considerably. The qualitative behavior of the smaller drop (of 2.5 mm diameter) was similar to that of 4.2 mm drop including ring formation and cycles of spreading and recoiling. It can be seen that values of the time required for the drop to come to rest was reduced from 270 to 158 ms for 2.5 mm drop and of average oscillation period for the 2.5 mm drop was almost 30% of that observed for 4.2 mm drop (18.55 ms and 26 ms). The average amplitude ratio for 2.5 mm drop was also reduced from 1.15 to 1.06. The maximum spread radius and maximum height achieved during the first cycle were found to be 3.4 mm and 1.7 mm respectively. Simulations of impact of 2.5 mm drop on a flat glass surface were carried out at impact velocity 0.3 m/s. Average value of the dynamic contact angle variation with time was used for simulations. Simulated height variation with time was compared with the experimental results in Figure 3.12 b. Maximum height achieved during the first cycle of oscillation was 2.42 mm, which is in reasonable agreement with the value obtained from simulations (2.62 mm).

3.6.3.2 Influence of Impact Velocity

Experiments were carried out to study influence of impact velocity on dynamics of a drop falling on Teflon surface. Teflon surface has less affinity to water molecules as compared with glass surface and hence Teflon surface needed no pre-treatment. Teflon-water SCA was found in the range of 110-120°. Water drop falling on a Teflon surface showed significantly different results than that falling on a glass surface. The drop rebounded from the Teflon

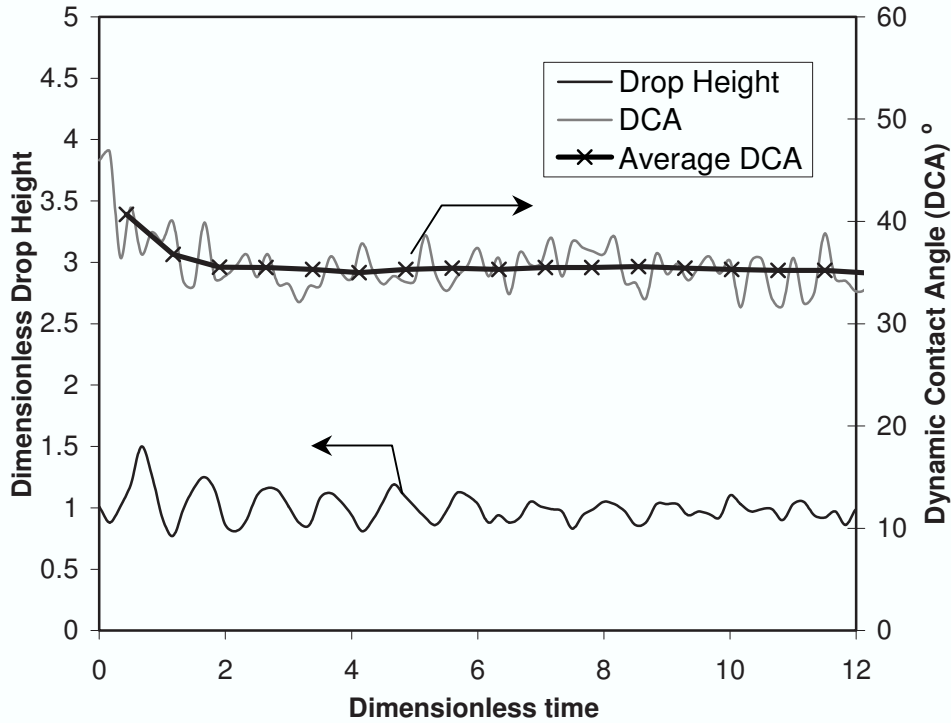


Figure 3.11: Drop oscillations with time- Dynamics of drop height and contact angle for non-pretreated glass surface (Case 2)

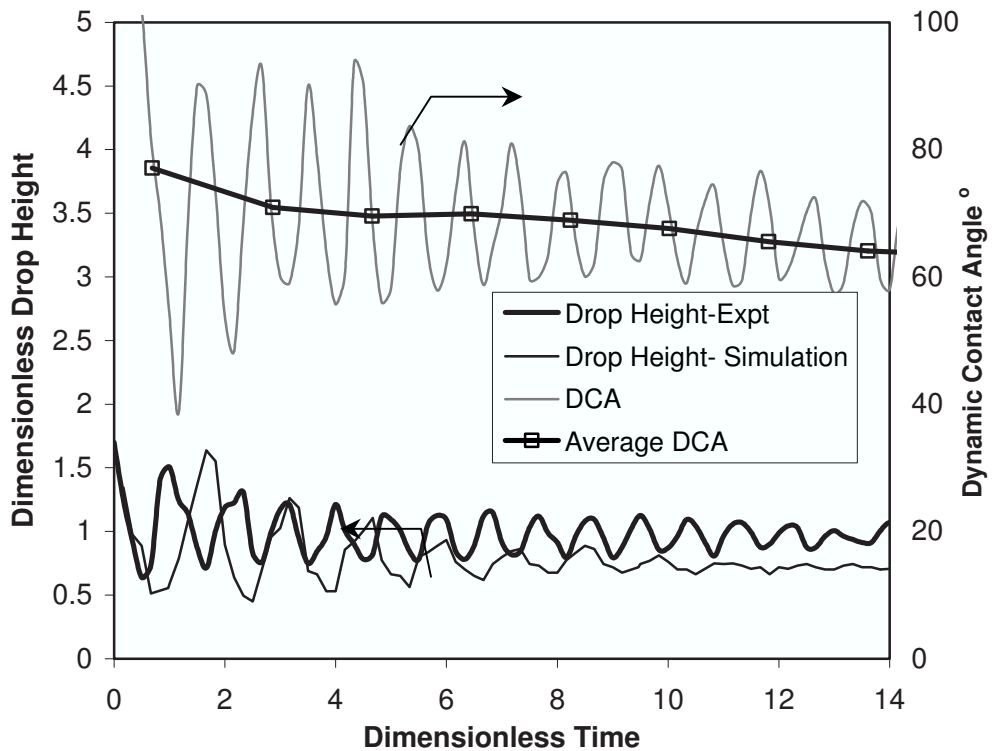


Figure 3.12: Drop oscillations with time- Dynamics of drop height and contact angle for pretreated glass surface and simulation comparison (Case 3). (Average oscillation period=11.33, Equilibrium drop height =1.6mm)

surface even at lower impact velocities (0.3-1 m/s). At high impact velocity (4 m/s), liquid drop was found to disintegrate and caused splashing (see Figure 3.7 e). For this case, inertial forces dominate capillary forces ($Re = 10000$, $Bo = 0.85$). At low liquid velocities, after rebound, the consecutive cycles were showing spreading and recoiling behavior as per Figure 3.7 c (that is, bottom portion of the drop was not found to take part in spreading).

Experimentally measured variation of drop height with time for the drop of 2.5 mm with impact velocity of 0.3 m/s is shown in Figure 3.13. It can be seen that the drop height increases considerably during the first cycle of spreading and recoiling because of rebounding compared to the consecutive cycles. The oscillations due to spreading and recoiling were continued even beyond 465 ms. Overall parameters like average oscillation period and amplitude ratio was found to be 16.57 s and 1.03 respectively. Maximum spread diameter was found to be 3.9 mm and maximum height achieved during the first cycle was 3.25 mm.

Simulations were carried out with two-dimensional solution domains (5 mm x 6 mm) were found to capture the drop rebounding as well as oscillation phenomenon. Comparison with experimental snaps of drop rebound during first cycle is shown in Figure 3.14. After 2 ms simulation, developed flow fields above and below drop is shown in Figure 3.14 a. It can be seen that drop behavior observed in experiments was captured reasonably well in the simulations. Simulations were showing drop spreading, recoiling and rebounding correctly (Figure 3.14 c to g). Recoiling with a bulge at the rim may cause trapping of gas during recoiling process (Figure 3.14 d). *Mehdi-Nejad et al.*⁷⁹ have reported similar bubble entrapment inside an impacting drop. Complete lift of drop (rebound) was observed during recoiling process. The simulated as well as experimental results indicate that the drop shows couple of oscillations while entirely suspended in air. It was observed that the rebounded drop required about 16ms to come back on solid surface. Drop oscillations in air causes local minima in drop height variation curve (first cycle in Figure 3.13). Simulations

showed similar local minima in drop height function. It can be seen that simulations capture the rebound phenomena and subsequent oscillations of spreading-recoiling and can provide complete flow fields of gas and liquid phases. Use of such flow field for better understanding of interphase closures is discussed in the later subsection.

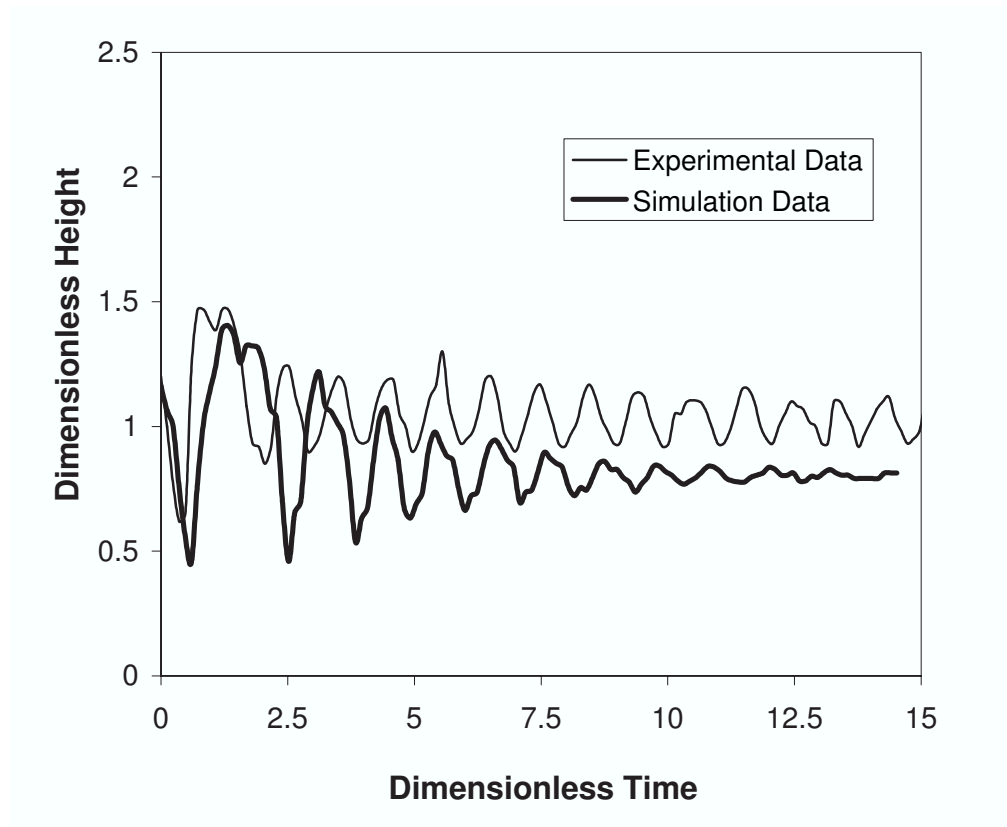
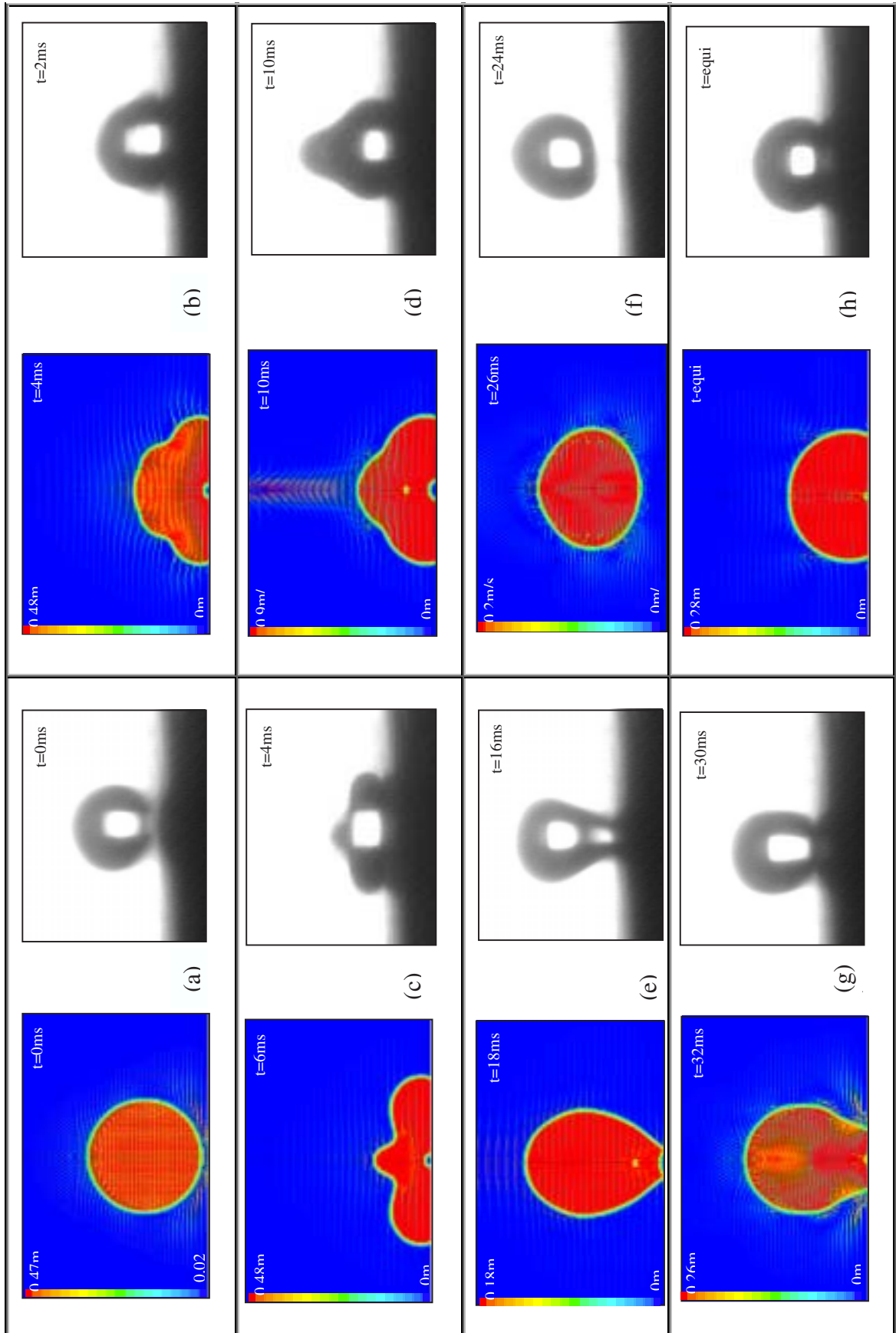


Figure 3.13: Comparison of the experimental data of drop height variation with simulated results (Case 4). (Avg. Oscillation Period: 16.57ms, Final Drop Height: 2.2 mm)

Avg. Oscil-



To quantify these results, simulated drop height variation was compared with the experimental measured data (see Figure 3.13). It can be seen that the predicted oscillation time is larger than the experimentally observed value. Unlike the experimental observations, where the drop spreads from the middle (Figure 3.7 c), simulated results indicate spreading at the bottom. The bottom spreading causes over-prediction of oscillation time due to more resistance offered by the solid surface.

With higher drop impact velocity (Case 4: 1 m/sec), though overall behavior was similar to the case with lower impact velocity (Case 3), the ring formation was found to occur. High-speed images acquired for this case indicated the average oscillation period as 24 ms and average amplitude ratio as 1.05. The maximum spread was found to be 5.88 mm and maximum height achieved during the first cycle was 5.66 mm, which is about 40% more than that observed at impact velocity of 0.3 m/s. From experimental observation, satellite drop formation process just begins at this stage, which is non-symmetric. Two-dimensional axis-symmetric simulations predict the occurrence of drop breakup near the top instead of in the middle. Since smaller fragment was found to break, the predicted height till which it is thrown upwards is higher (11 mm) than that observed in the experiments (5.96 mm). Three-dimensional simulation using 1/4th domain with symmetry was therefore carried out using domain size 5 mm x 5 mm in width and length and 6 mm in height. Simulations were carried out using 0.1 mm grid size for the case with three-dimensional domain. Because of the excessive demands on computational resources, three-dimensional simulations could not be carried out beyond the first cycle of the oscillations (and with finer grids). Despite this, the simulated behavior of the drop was found to be very similar to that observed in the experiments and was able to capture key features reasonably well (Figure 3.15 a-k). The finger formation during recoiling (which was also observed by *Mao et. al*⁵⁵; *Richard and Quare*⁷⁸) was also captured reasonably well in the simulations (Figures 3.15 g-h).

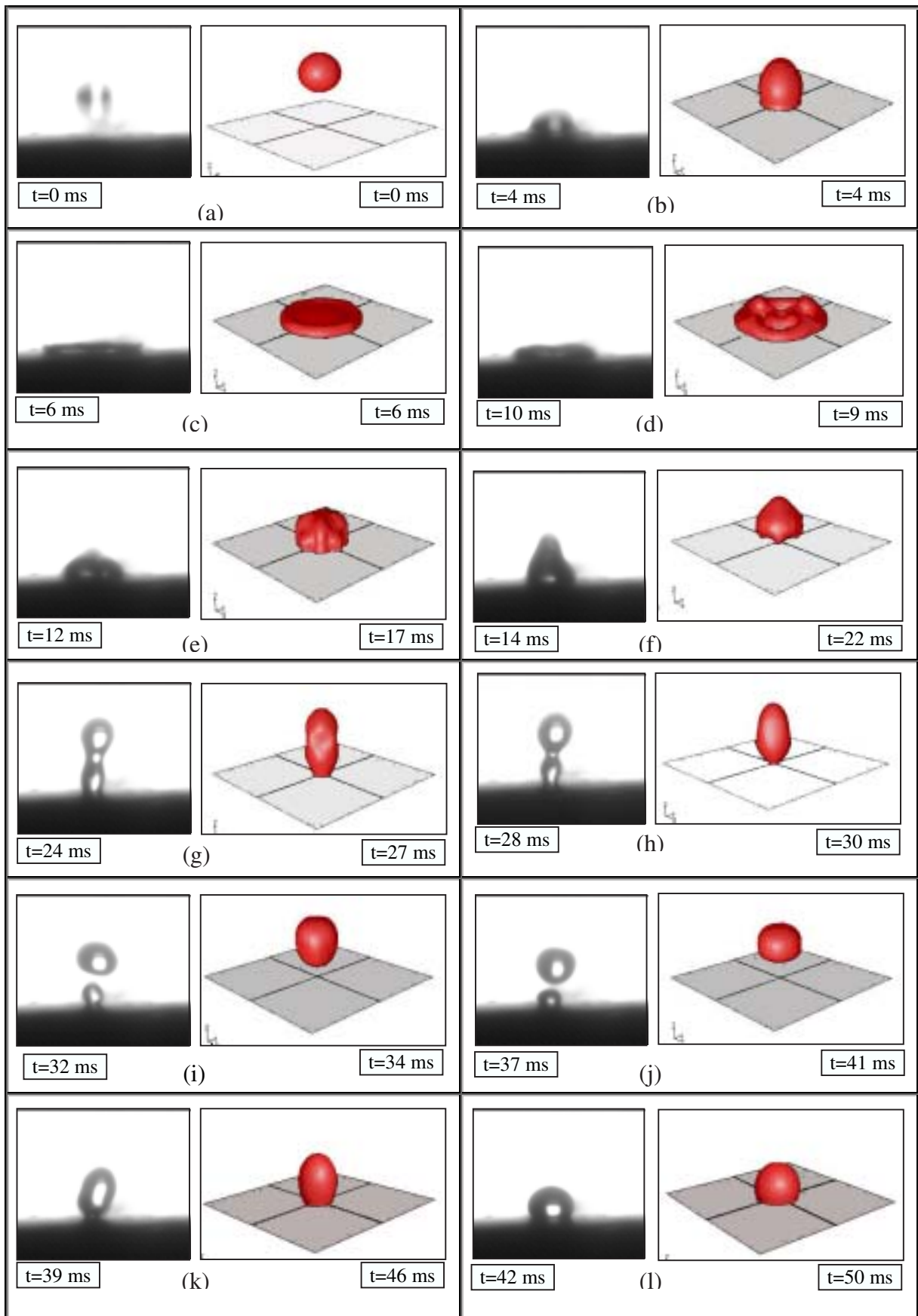


Figure 3.15: Comparison of the Drop Dynamics with Simulation Results of drop impact on Teflon surface (Case 5)(Impact velocity: 1m/s, drop diameter: 2.5mm, solid surface: Teflon)

3.6.3.3 Influence of contact angle and surface tension

Influence of contact angle was studied by comparing drop dynamics of 2.5 mm water drop at impact velocity 0.3 m/sec on a glass and a Teflon surface (Case 2 and 3). We_α increases significantly with increase in contact angle for the same Reynolds and Weber numbers. The experimentally measured variation of drop height with time is shown in Figure 3.16. It can be seen that, the water drop comes to rest much earlier on a glass surface (126 ms) than on a Teflon Surface (>468 ms). Water drop on glass surface (CA-55°) spreads at the bottom (see Figure 3.7 a), where viscous dissipation at the solid-liquid interface damps spreading and recoiling oscillations. Where as, on a Teflon surface (CA-120°), liquid-solid interaction is quite small since drop deformation occurs at the center of the drop (see Figure 3.7 b). This causes oscillations to persist for much longer time than on a glass surface. The values of maximum spread diameter on a glass and a Teflon surface, however, are not very different (glass: 3.6 mm; Teflon: 3.9 mm).

Experiments were carried out with falling drops of SDS solution in water (16 mM solution). The surface tension and SCA on a Teflon surface were found to be 0.038 N/m and 64° respectively (compared to 0.072 N/m and 120° for water). With SDS solution, the time required for the drop to come to rest was much lower than that with water (180 ms compared to >468ms for water). The average oscillation time was reduced to 12.6 ms for SDS solution from 17.6 ms for water. It was observed that with SDS solution (lower surface tension and lower SCA), the drop deformation occurs according to bottom spreading mechanism as shown in Figure 3.7 b instead of 3.7 c. Variation of dynamic contact angle is shown in Figure 3.17. For simulations, average values of the dynamic contact angle were used. Comparison of simulated drop height variation with time with experimental data is shown in Figure 3.17. Simulations show sluggish response compared to the experimental data.

3.6.3.4 Influence of non-wetting behavior on drop dynamics

Experiments were carried out with mercury drops to understand influence non-wetting behavior (static contact angle of nearly 180°). The mercury also has a very high density (13000 kg/m^3) and surface tension (0.4 N/m) compared to water. Experiments were performed with mercury drops falling on a Teflon surface at impact velocity 0.45 m/sec . Mercury drops rebounded several times before exhibiting usual oscillations of spreading and recoiling. Spreading/recoiling behavior was similar to that exhibited by a water drop on a Teflon surface. Experimentally measured variation of drop height with time is shown in Figure 3.18. The bouncing region and oscillation region are indicated with continuous line and dotted line respectively.

Simulations were carried out to simulate impact of mercury drops on a Teflon surface. Comparison of simulated drop height variation with experimental data is shown in Figure 3.18. Both, experimental as well as simulated results show local minima during the first cycle. The average oscillation period was under-predicted in the simulated results (41.3 ms as compared to the experimental value 54 ms). Simulated results were able to capture the multiple bouncing of mercury drop as observed in the experiments.

3.6.3.5 Comments on comparison of experimental and computational results

It was shown that the VOF simulations captured the key characteristics such as drop spreading/ recoiling, bouncing and splashing reasonably well. It should be noted that due to inherent limitations in the VOF formulation, the interface is smeared across the grid size unlike the sharp interface in practice. Despite these limitations, the VOF simulations captured the drop interaction with solid surfaces reasonably well and provided detailed

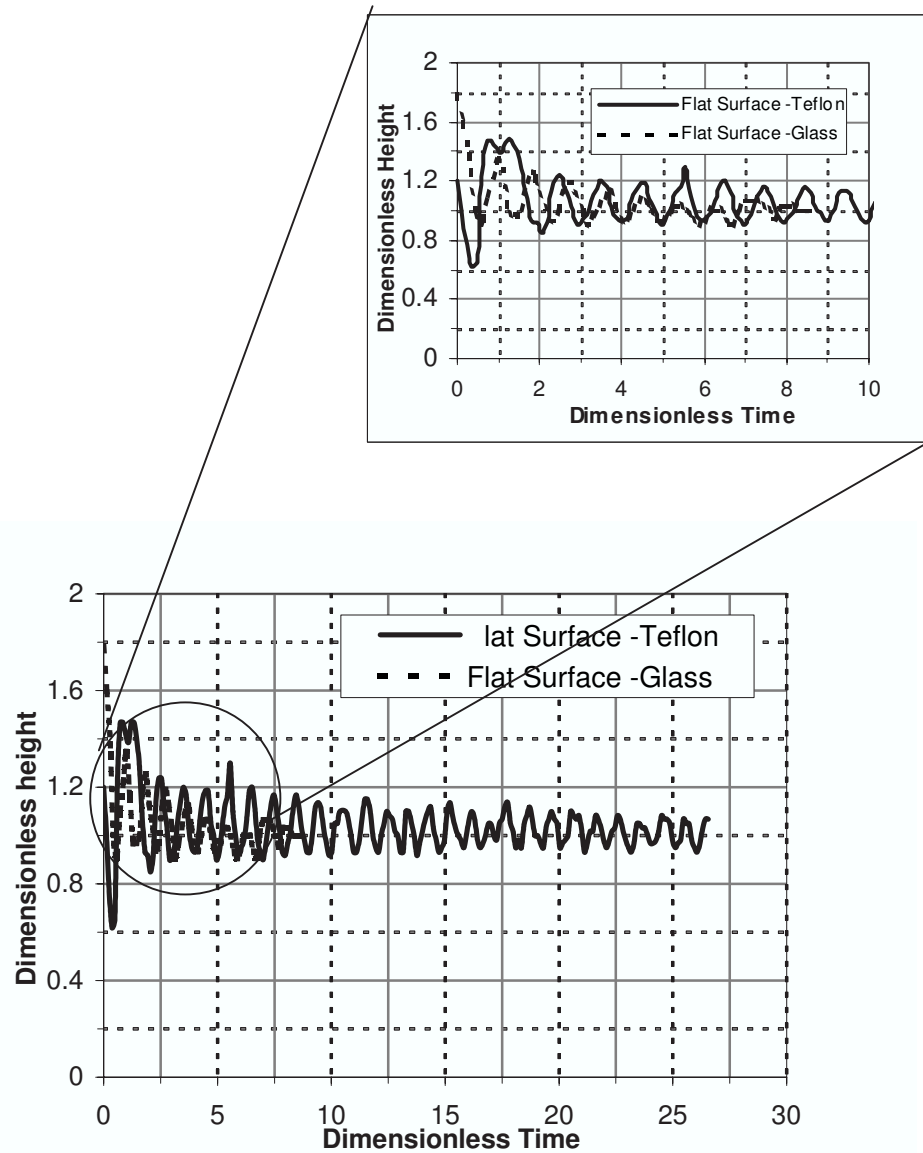


Figure 3.16: Comparison of drop dynamics on glass and Teflon surface (Experimental Conditions: Case 3, Liquid: Water, Solid Surface: Teflon and glass, Impact Velocity:0.3m/s)

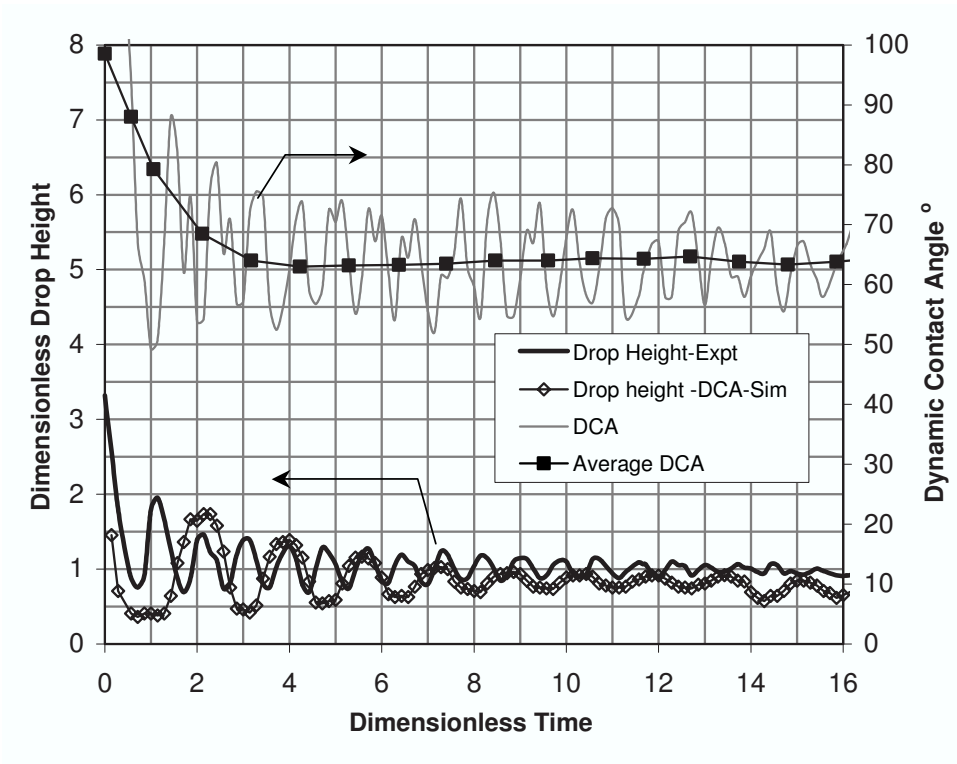


Figure 3.17: Comparison of the experimental data of drop height variation with simulated results (Case 7: Avg. Oscillation Period: 14ms, Final Drop Height: 1.5 mm)

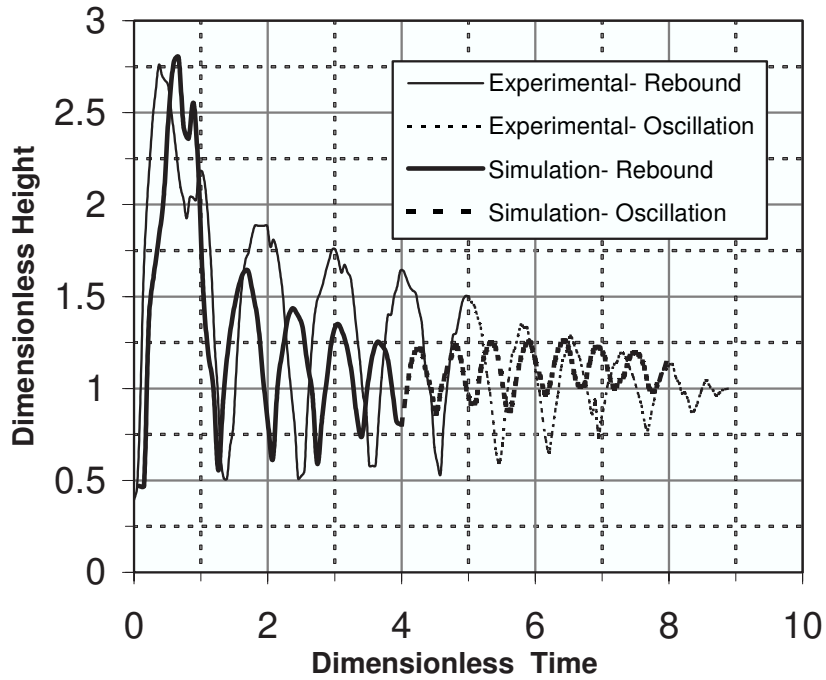


Figure 3.18: Comparison of the experimental and simulation results of the Mercury drop dynamics (Case 8: Avg. Cycle Frequency: 54, Final Drop Diameter: 2mm)

information about the flow field during such interaction process. However, in general simulations over-predicted oscillation time and showed slower oscillations compared to those observed in the experiments.

It may be noted that VOF simulations, at present, are unable to account for microscopic surface characteristics like roughness or contamination. It was observed from the experimental images that contact angle exhibits continuous variation during the spreading and recoiling process. This variation is a strong function of surface characteristics and contamination. Since it was impossible to specify exact initial conditions (drop position and velocities) corresponding to experiments in the VOF simulations, some differences in the experiments and simulations were not unexpected. Possible way to overcome these errors might be to include drop formation process at the dropper while simulating. However, this would significantly increase the demands on computational resources. In the present work, therefore, some differences in the initial conditions between experiments and simulations were accepted under the constraints of available computing resources. The second possible source for the observed disagreement between experimental and simulated results is inadequate representation of varying contact angles in the simulations. As mentioned earlier, we used step-wise approximation of profile of moving average of measured contact angles. If the initial conditions of experiments and simulations were identical, it might have been possible to specify detailed variation of contact angle based on measured values (without moving average and step-wise approximation). This may reduce the quantitative differences in the predictions and experimental data.

While making quantitative comparisons between experimental and simulated results, it should be noted that any differences in initial conditions would amplify the differences between simulated and experimental results as time progresses. Any subsequent errors in specifying time varying contact angle will further enhance the errors. Possible non-

uniformities in surface roughness or adsorbed moisture may also lead to observed differences. Despite these possible sources of errors, it can be stated that VOF simulations presented here were able to capture key processes in drop spreading, recoiling and rebounding for variety of systems. Since the CFD simulations can provide detailed information about flow field, these results can be used to gain better insight into drop interaction with flat plate.

3.6.3.6 Interaction of liquid drop and flat surface

Flow field predicted by VOF models can be used to examine various intricate details of interaction of liquid drop and flat surface. Here we demonstrate this by using the simulated flow field to study energy balance and inter-phase interactions during spreading and recoiling. During drop impact, spreading and oscillation processes, kinetic, potential and surface energies were interchanging among each other and loss of energy occurs through viscous dissipation. Simulated results were used to calculate kinetic energy, potential energy and surface energy variation during the drop impact. Potential and kinetic energy of a drop was calculated by the summing over all the computational cells. Surface energy was calculated using Young-Dupre Equation (*Adamson 1982*⁸⁰):

$$\text{Surface Energy} = A_{GL}\sigma_{GL} + A_{LS}(\sigma_{LS} - \sigma_{GS}) \quad \dots \dots \dots (3.13)$$

where, A_{GL} and A_{LS} are the interfacial area for gas-liquid and liquid-solid phases. σ_{LS} , σ_{GS} and σ_{GL} are the surface tension between liquid-solid interface, gas-solid interface and gas-liquid interface. The unknown term, σ_{GS} , was eliminated by using the following relation:

$$\sigma_{GS} = \sigma_{LS} - \sigma_{GL} \cos(\theta_w) \quad \dots \dots \dots (3.14)$$

where, θ_w is the liquid-solid contact angle. The total energy was calculated by summing the potential energy, kinetic energy and surface energy:

$$PE = \left(\frac{1}{2}\rho V_{cell}^2\right) (vol_{cell}) \dots \dots \dots (3.15)$$

$$KE = h_{cell}\rho g(V_{cell}) \dots \dots \dots (3.16)$$

$$SE = \sigma_{GL} [A_{GL} - (A_{LS} \cos \theta_w)] \dots \dots \dots (3.17)$$

The predicted variation of energies is shown in Figure 3.19 and 3.20 for glass and Teflon surfaces. When a drop spreads to its maximum extent and is about to recoil, its potential energy exhibits minimum. Per cycle of potential energy, there are two cycles of kinetic energy because it passes through maximum during spreading as well as recoiling. It can be seen that amplitude of oscillations is higher for glass surface than that for Teflon surface. Scales of variation of surface energy are higher than the potential and kinetic energy and its variation is very sensitive to the variation in a contact angle. Therefore small errors in the values of contact angle or surface area may corrupt the calculation of total energy. In order to increase the robustness of the calculation of different components of energies, we have analyzed the variation of total viscous dissipation by using the following energy balance at time t:

$$(\sigma_{SL}A_{LS})^o + PE^o + KE^o = \sigma_{GL}A_{GL} + \sigma_{SL}A_{SL} + PE + KE + D \dots \dots \dots (3.18)$$

Where, superscript o denotes quantities evaluated at initial condition (at t=0 sec), D is the total viscous dissipation until time t. The predicted variation of viscous dissipation with

time is shown in Figure 3.21. Despite some fluctuations, the overall variation in dissipation curve shows expected increasing trend.

The detailed flow field predicted by CFD simulations (typical sample of instantaneous flow field predicted by the VOF simulations is shown in Figure 3.22(a) [Case-3, at 7.5 ms after impact, 3D simulations for illustration]) can be used to compute other quantities of interest such as gas-liquid and liquid-solid interaction. Liquid-solid interaction can be determined by calculating the average shear stress exerted by the fluid on the solid surface. Gas-liquid interaction can be studied by calculating the strain rate on gas-liquid interface. Detailed study of gas-liquid interaction (in terms of strain rate), gas recirculation (in terms of vorticity) will be useful for various parametric studies such as inter-phase heat, mass and momentum transfer for multiphase flows. Micro-scopic evaluation of these parameters would eventually be useful for developing better closure terms for complete reactor flow model. Detailed calculations of these parameters for drop impact are discussed below.

The shear stress exerted by spreading liquid on solid surface was calculated as:

$$\tau_w = \mu \frac{\partial v}{\partial x} \quad \dots \dots \dots (3.19)$$

where, v_i is liquid velocity in y direction. Contours of the shear stress exerted on wall are shown in see Figure 3.22b. The maximum shear stress was observed in the region lying between the spreading edge and the central region. Gas recirculatory motion around the drop was quantified by calculating the vorticity as:

$$\omega = \nabla \times V \quad \dots \dots \dots (3.20)$$

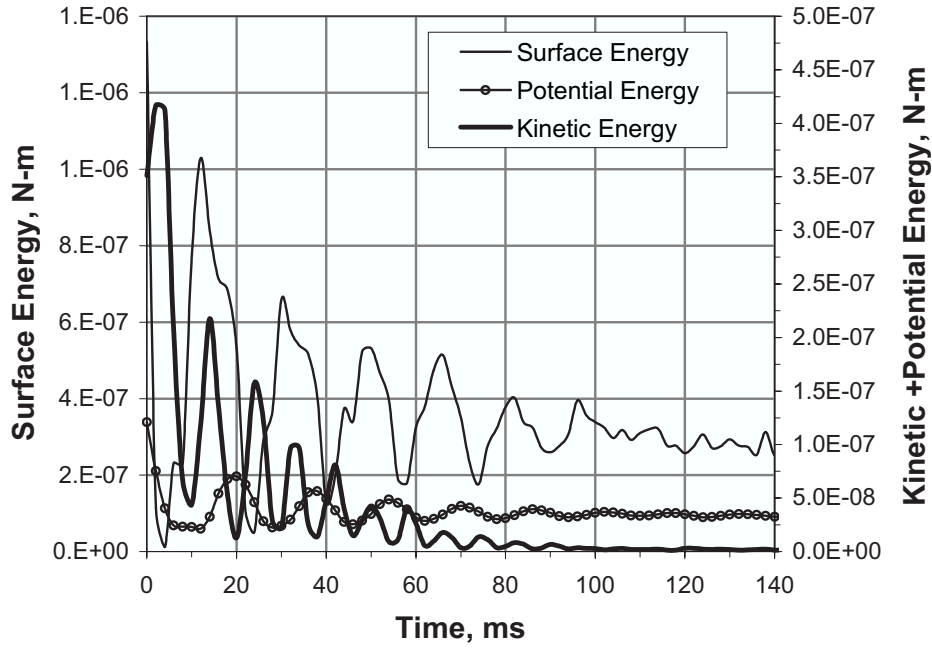


Figure 3.19: Variation of the Simulated Kinetic, Potential Energy of Drop During Oscillations for Case 3 and 4.

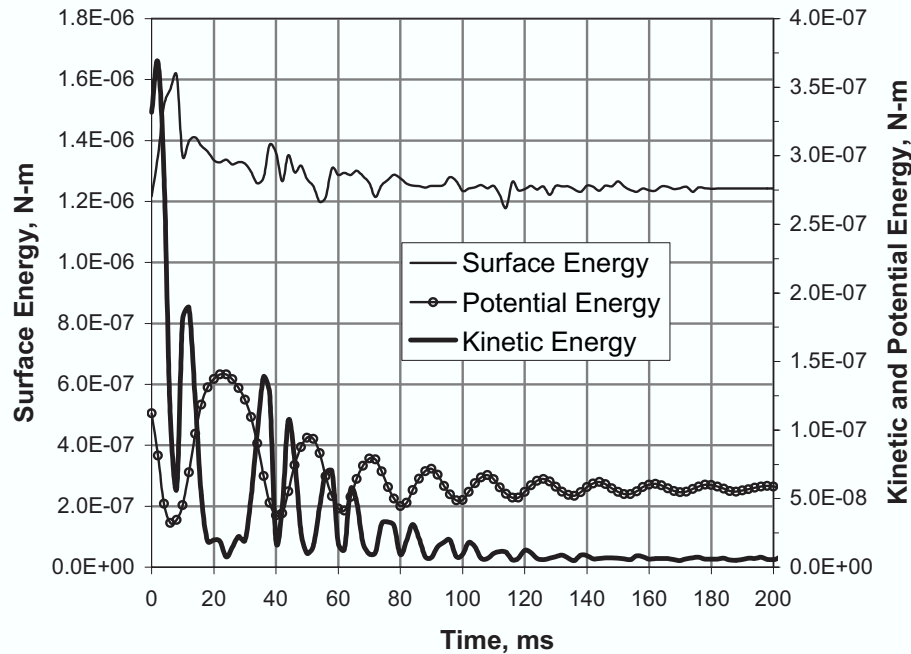


Figure 3.20: Variation of the Simulated Kinetic, Potential and Surface Energy of Drop During Oscillations for Case 3 and 4.

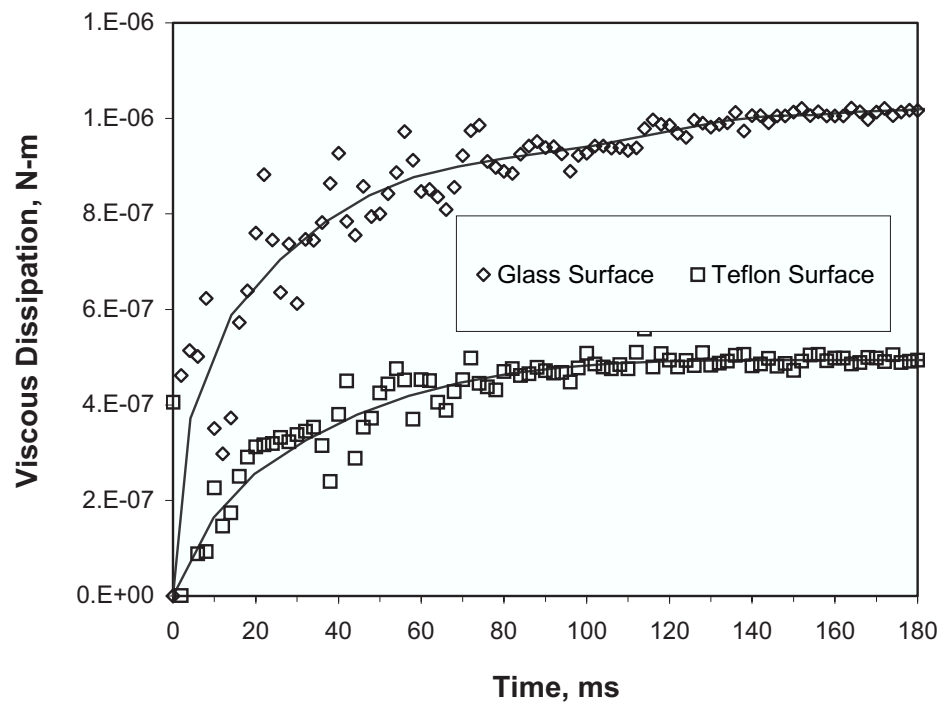


Figure 15: Variation of viscous dissipation with time for Case 3 and 4

Figure 3.21: Variation of viscous dissipation with time for Case 3 and 4

Iso-surface of vorticity (of value 2180 s^{-1}) is shown in Figure 3.22 c. In order to define the shape of the drop, iso-surface of liquid phase volume fraction of 1 is also shown in this figure (in red color). It can be seen that high vorticity occurs at spreading edge, intermediate ridge and at the top surface of the drop. The contours of strain rate on isosurface of liquid phase volume fraction of 1 are shown in Figure 3.22 d. Maximum strain rate was observed in the vicinity of high gas vorticity region.

Strain rate (area weighted averaged) at gas-liquid interface was calculated with time till drop comes to rest. Corresponding variation of drop surface area (calculated from surface integral over the iso-surface of liquid) along with strain rate are plotted in Figure 3.23 a. During each cycle of oscillation, drop comes to rest during end of the (a) spreading process and (b) recoiling process. In the time duration between these rest positions, drop accelerates and decelerates where interaction among the phases increases. It can be seen from Figure 3.23 a that strain rate is higher during spreading process than recoiling process. Maximum drop interfacial area was observed when drop spreads completely and strain rate is minimum at this point. Shear stress (area weighted average) exerted by flowing liquid over solid was calculated during the whole process of drop oscillation. Shear stress and corresponding variation in drop diameter is shown in Figure 3.24 b. It can be seen that shear stress on solid surface increases during acceleration and deceleration processes. Shear stress during spreading stage is always higher than that while recoiling.

Thus, VOF simulations of the type discussed in this work provide useful information about the interaction between gas and liquid as well as liquid and solid phases during the spreading and recoiling stages. These models have potential to account for solid surface curvatures (see for example, *Gunjal et al.*⁴⁷). Currently efforts are under way to extend these models to simulate spreading of liquid on curved surfaces of void space in a typical packed bed. Such efforts may eventually provide useful information about inter-phase interactions of

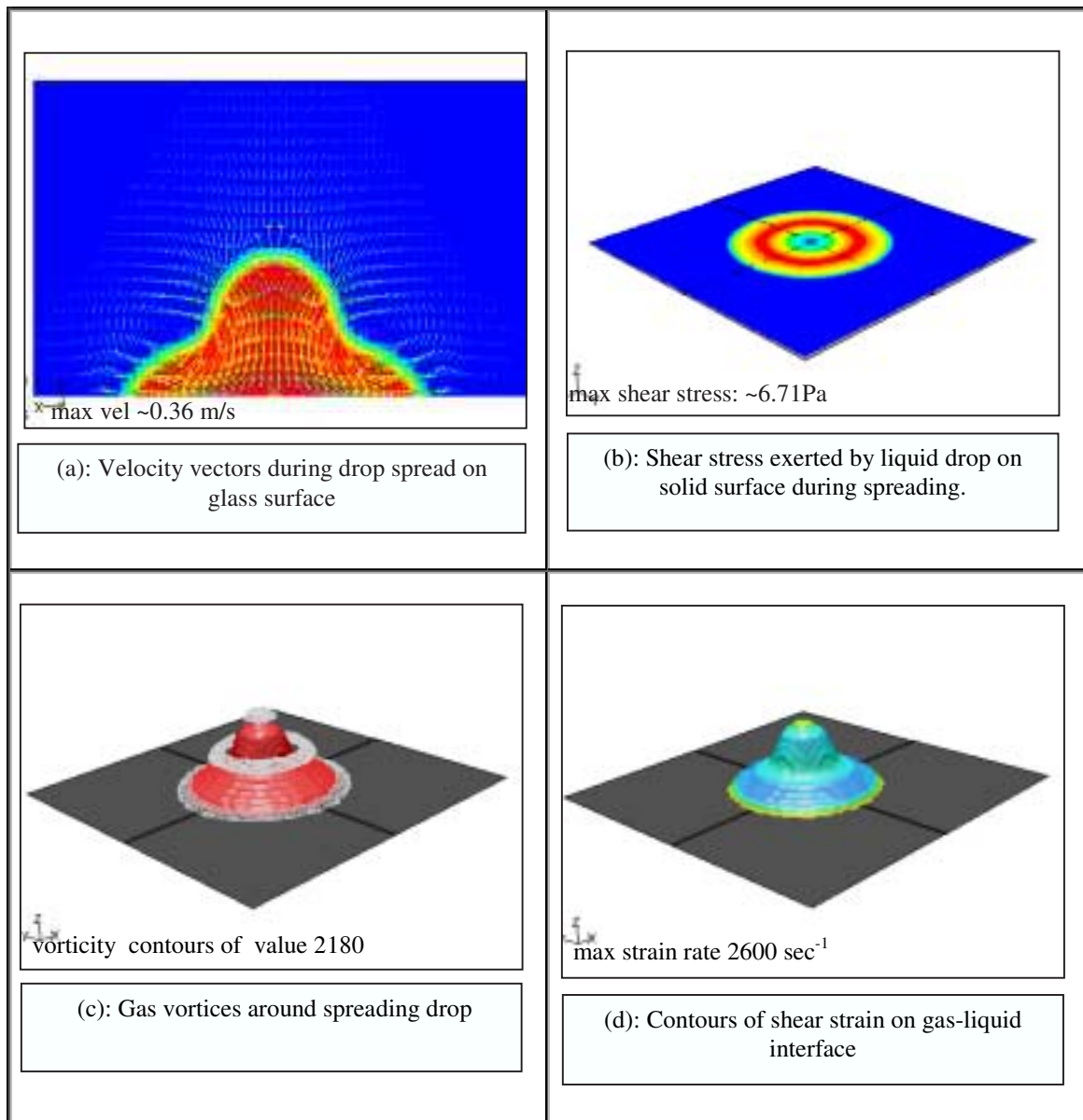


Figure 3.22: Illustration of gas-liquid and liquid-solid interaction during drop spreading on glass surface at time=7.5ms (Case 3).

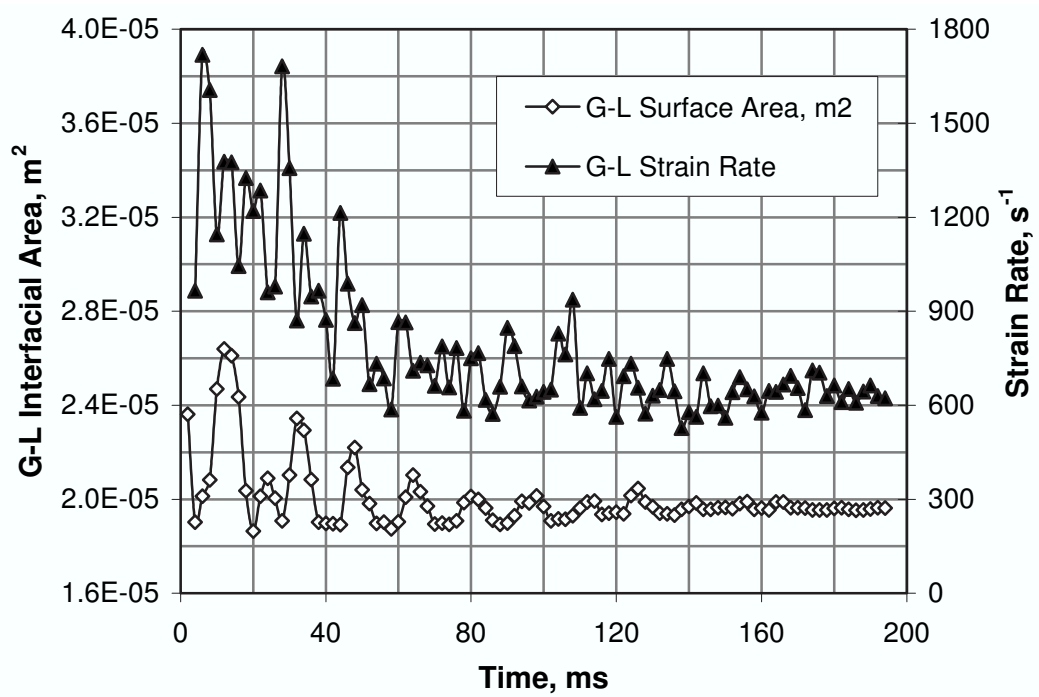


Figure 3.23: Variation of avg. strain rate at gas-liquid interface and drop interfacial area during drop oscillations (Case 3).

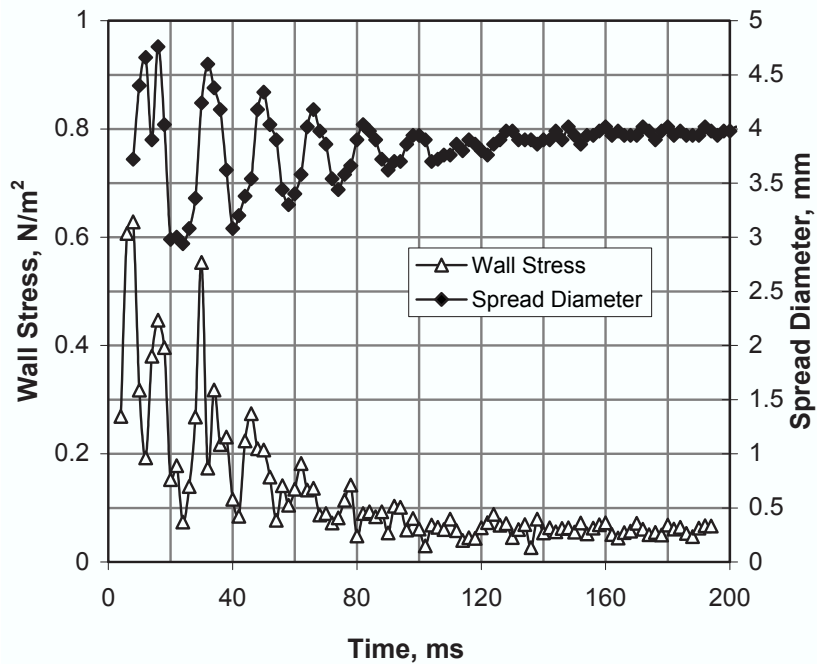


Figure 3.24: Variation of avg. liquid-solid shear stress and drop diameter during drop oscillations (Case 3).

gas-liquid flows in packed beds.

3.7 Conclusion

We have studied the dynamics of a drop impact process on flat surface experimentally as well as computationally. Experiments were carried out over a wide range of operating conditions ($Re = 550 - 10300$; $We_a = 1.5 - 10000$). Unlike most of the previous studies, the emphasis was on studying drop interaction with low impact velocities (< 1 m/s). Experimental data of drop deformation (shape/ height/ diameter) during spreading and recoiling (rebounding) processes was obtained till drop attains equilibrium position on the flat surface. The detailed VOF simulations were carried out and the predicted results were compared with the experimental data. The CFD simulations were also used to gain an insight into drop interaction with flat surfaces. The key findings of the study are discussed below:

Dynamic variation of contact angle was found to be significant for liquid-solid systems whenever contact angles were low ($\theta_w < 90$). Overall reduction of contact angle with time for water-glass or water-SDS-Teflon systems were much larger than that observed with water-Teflon or mercury-Teflon systems.

Adsorbed surface moisture (for glass surface) alters the dynamics of the drop considerably and dynamic variation of the contact angle was significantly larger for pre-treated glass surface than non pre-treated surface.

Average contact angle decreases during oscillations of drop. Agreement between simulated and experimental results was improved when average contact angle variation with time

was used instead of using equilibrium value.

Spreading mechanism affects the dynamics of drop and depends upon the surface and liquid properties. For example, 2.5 mm water drop on Teflon surface was found to rebound (Case 4). When surfactant (SDS) was present, rebounding of water drops did not occur. VOF simulations also showed similar behavior.

Microscopic factors such as molecular movement of liquid contact line, surface roughness and surface tension variation in drop might affect the drop dynamics considerable. It is difficult to consider these processes in model because of different spatial and temporal scale. Despite neglecting these processes, VOF simulations were found to capture key features of drop interaction (spreading/ recoiling, rebounding and break-up) with solid surface reasonably well.

In cases where drop rebounded from solid surface, nose of drop (upper most point of drop) was found to exhibit local minimum while suspended in air. VOF simulations also showed similar behavior.

VOF simulations provide detailed information about the interaction between gas and liquid as well as liquid and solid phases. The models and approach presented here may be extended to understand spreading of liquid on curved surfaces of void space in a typical packed bed, which may eventually provide useful information about modeling of gas-liquid flows in packed beds.

Part II

Reactor Scale Flow Processes

“Experiments serves not only to confirm theory, but differs from it without disturbing it, it leads to new truths which theory only has not been able to reach”

—Dalembert

4

Experimental Measurements in Trickle Bed Reactors

4.1 Introduction

Trickle-bed reactors (TBR) are widely used in chemical process industries because of their flexibility and simplicity in operation for low as well as high throughputs. In trickle-bed reactors gas and liquid phases flow co-currently downward through a fixed bed of catalyst particles. Under commonly used operating conditions, gas flows as a continuous media while liquid trickles over solid particles. A trickle-bed reactor behaves close to plug flow for gas as well as for liquid phases and has smaller liquid holdup (higher solid holdup) compared to the slurry and ebullating bed reactors. The typical applications of trickle-bed reactors include hydrocracking, hydro-desulfurization, and hydro-denitrogenation of gas oil, catalytic dewaxing of gas oil and lube oils, oxidation and hydrogenation of organic compounds, and wastewater treatment. Accurate understanding of hydrodynamics of trickle-bed reactors and knowledge of how it changes with key design (particle and reactor diameter, distributor, and so on) and operating parameters (gas and liquid flow rates, periodic operation, and so on) are therefore essential. Several studies have been carried out to understand and to quantify hydrodynamics of trickle-bed reactors. In this work, we report results of detailed investigation of hydrodynamics of tricklebed reactors using experimental as well as computational tools. Experimental part of this study is reported in this chapter and computational part is presented in next chapter. The physical picture of gas-liquid flow through a trickle bed and review of previous studies are briefly discussed in the following sections.

4.1.1 Physical picture and flow regimes in trickle bed reactors

When gas and liquid flow co-currently downward through a packed bed of solid particles, several flow regimes were found to occur depending upon operating and design parameters.

When gas and liquid flow rates are small, liquid flows down in the form of a film over a solid surface. This regime is called a film flow (see Figure 4.1a) in which both phases are continuous (or semicontinuous). In this regime, depending on the liquid flow rate, the solid surface may be completely or partially wetted. At low liquid flow rates, if the gas flow increases, interaction of the gas phase with liquid film flowing over a solid surface increases. Eventually, at certain gas velocity, gas starts entraining part of the liquid. Thus, under such a condition, part of the liquid flows down in the form of suspended droplets in the gas phase and part of the liquid flows down in the form of film over a solid surface (like in Figure 4.1b). This regime is called trickle flow regime. More often than not, the film flow regime is also clubbed with the trickle flow regime. If the gas flow rate increases further, a stage may come when all the liquid flows down in the form of suspended droplets. This regime is called a spray flow regime (see Figure 4.1c). When the liquid flow rate is increased at high gas velocity, two distinct gas and liquid rich bands (pulses) flow downward through the packed bed. This regime is called a pulse flow regime. If the liquid flow rate is increased further, a stage comes when gas becomes a dispersed phase (see Figure 4.1d) and flows down in the form of bubbles. This regime is called a bubbly flow regime.

A typical flow regime map for a trickle-bed reactor is shown in Figure 4.2 (taken from *Sie and Krishna*⁵). Out of these flow regimes, most of the trickle-bed reactors are operated in trickle and pulse flow regimes. Flow characteristics in these regimes are extremely complex and associated with the interaction of the fluids in the bed. For example, in a trickle flow regime, spreading of liquid over the catalyst surface is controlled by the nature of the solid surface and its dry or wetted condition. In a pulse flow regime, pulse formation, pulse frequency, and holdup affect the hydrodynamic characteristics. Identification of different flow regimes and knowledge of their flow characteristics are essential because other transport processes such as heat and mass-transfer rates are dependent on flow regimes and extent of interaction among gas, liquid, and solid phases. Knowledge of how flow regimes

and key hydrodynamic parameters are influenced by design and operating parameters is also essential for scale-down (designing laboratory experimental setup and experiments) and for scale-up (using laboratory experimental data for designing industrial reactors). Previous studies on these aspects are briefly reviewed in the following.

4.1.2 Previous work

Most of the experimental studies on trickle-bed hydrodynamics were restricted to trickle and pulse flow regimes. Several ways have been used to identify flow regime transition from trickle to pulse. *Latifi et al.*^{81, 82} have used a microelectrode technique to determine the flow regime transition in trickle-bed reactors. However, detailed information on frequency distribution in a pulse flow regime has not been reported. In recent years, nonlinear time series analysis has been extensively used to characterize flow regime transitions in bubble columns and fluidized-bed reactors (see for example, *Drahos et al.*⁸³, *Letzel et al.*¹⁰, *Lin et al.*⁸⁴). Relatively few attempts have been made to use these techniques for identifying flow regime transitions in trickle-bed reactors. *Krieg et al.*⁸⁵ studied flow regimes in trickle beds with wall pressure fluctuations and power spectral density (PSD). Their study indicated that visual techniques are not able to capture regime transitions accurately. They used variation in pressure fluctuations and conductance values to identify regime transition. *Horowitz et al.*⁸⁶ have used nonlinear timeseries analysis tools such as rescaled range analysis and correlation dimension to find the flow regime transition. Recently, *Urseanu et al.*⁸⁷ have identified flow regime transition based on standard deviation in pressure drop. However, this technique could not give sharp boundary at which transition occurs. It is essential to develop easy to use techniques to identify flow regime transitions in trickle-bed reactors.

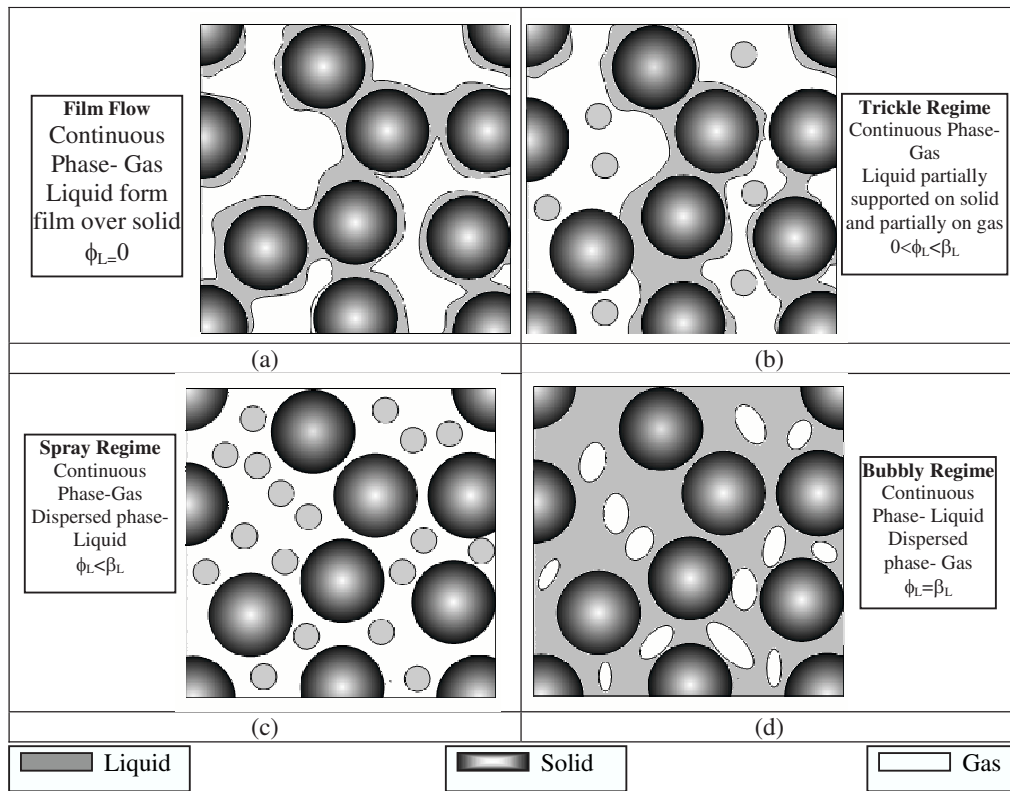


Figure 4.1: Physical Picture of the Flow in Trickle Bed Reactors

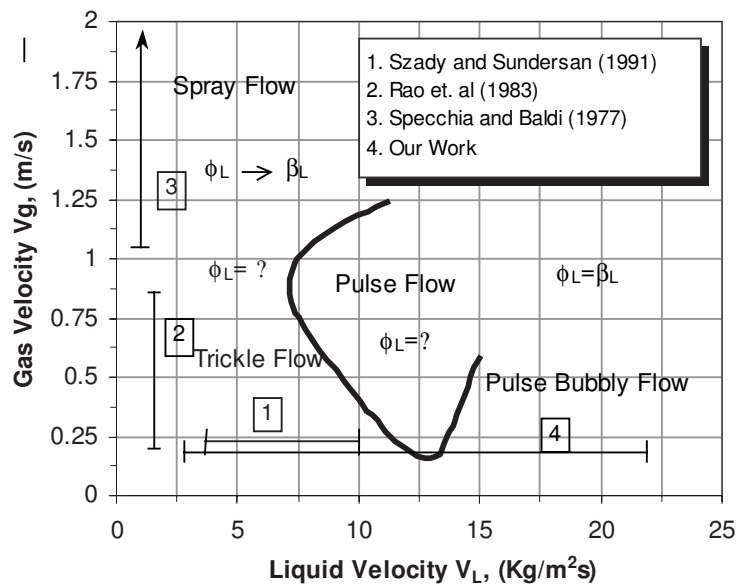


Figure 4.2: Flow regime map (*Sie and Krishna sie*⁵)

A large number of studies were carried out for measurement of pressure drop and liquid holdup in trickle beds (see for example, *Al-Dahhan et al.*⁸⁸, *Saez and Carbonell*⁸⁹, *Herskowitz and Smith*⁹⁰ and references therein). However, studies which addressed effect of prewetted and nonprewetted bed conditions on pressure drop/liquid holdup (and their hysteresis) are rather few. The hysteresis of pressure drop and liquid holdup in trickle beds was first observed by *Kan and Greenfield*^{91,92}. They explained the phenomenon based on the formation of liquid bridges and surface tension. *Christensen et al.*⁹³ and *Levec et al.*^{94,95}, observed that the radial distribution of the liquid in the bed changes depending on whether the liquid flow rate increases or decreases and stated it as a cause for hysteresis. *Rode et al.*⁹⁶ have also reported multiple hydrodynamics states in various flow regimes of trickle-bed reactors. *Chu and Ng*⁹⁷ modeled the packed bed by arranging the packing in a cubical structure and considered the lower branch of hysteresis as filament flow with the upper branch as film flow. *Ravindra et al.*⁹⁸ reported experimental data on hysteresis by reconciling the previous results. *Melli and Scriven*⁹⁹ studied hysteresis theoretically in a two-dimensional bed. It is however necessary to obtain systematic experimental data to understand and to quantify hysteresis in trickle beds. Such a systematic data set is also needed for evaluating computational models of gas-liquid flow through trickle beds.

4.1.3 Present contribution

In this study, we have measured hydrodynamics parameters such as pressure drop and liquid holdup of trickle bed reactors. wall pressure fluctuations were measuremented to identify prevailing flow regime in trickle beds. A criterion based on Kolmogorov entropy calculated from the measured pressure fluctuation time series is proposed to identify flow regime transition. Influence of particle and column diameter was studied by carrying out experiments on two columns (of diameter 0.114 m and 0.194 m) with two sets of particles

(3 mm and 6 mm diameter spherical particles). Effect of pre-wetted and un-wetted bed conditions on pressure drop and liquid hold-up was reported for a range of operating conditions ($V_G=0.22-0.44 \text{ kg/m}^2\text{sec}$, $V_L=2-24 \text{ kg/m}^2\text{sec}$). Influence of liquid distribution on hysteresis was studied by using spary and perforated liquid distributor.

4.2 Experimental Setup and Operating Procedure

4.2.1 Experimental setup

Trickle bed reactors (made up of perspex) of 0.114 and 0.194 m diameter and 1 m height were set-up for experimental study. The schematic of experimental set-up is shown in Figure 4.3. Gas and liquid were introduced in the column at the top. Gas and liquid flow rates were measured with the calibrated rotameters. The distributor plate was made up of stainless steel with uniform 3 mm holes, which were arranged in triangular pitch of 3 mm. Glass beads of 3 or 6 mm diameters were filled in the column such that beads are placed compactly in the column. Voidage of the column was measured using liquid drainage method. The measured voidage of the columns were found to be 0.37 for 3 mm particle and 0.356 for 6 mm particles. Two pressure sensors were used to measure the pressure drop. Top pressure sensor was located at distance of 32 cm from the top. The distance between the two pressure sensors was 0.5 m. Glass beads were supported at the bottom by a stainless steel plate having 3 mm holes with 3 mm triangular pitch.

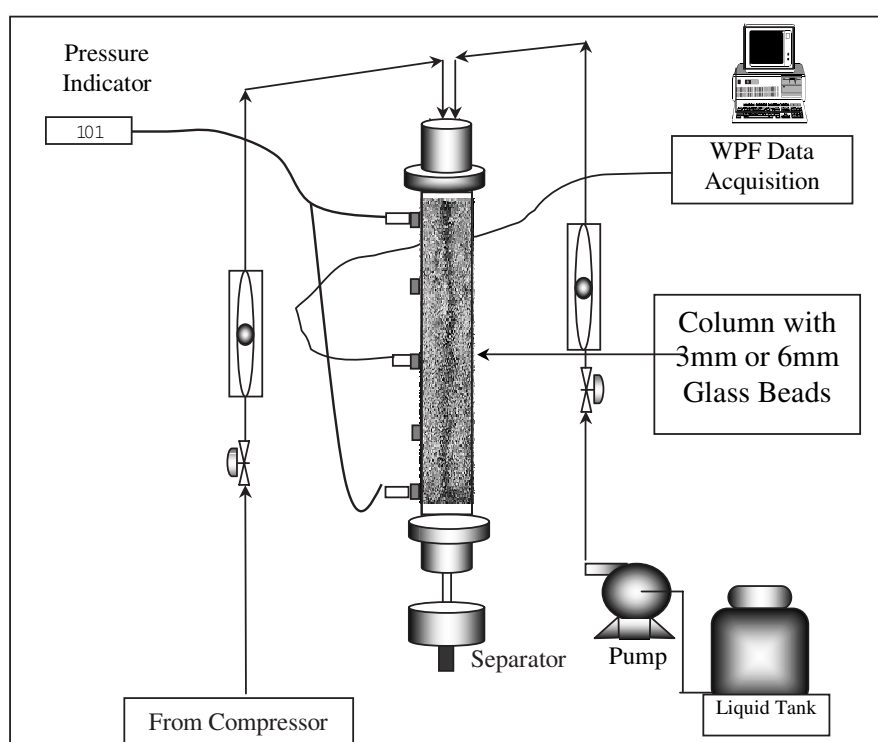


Figure 4.3: Experimental set up

Wall pressure fluctuations were measured using a voltage output pressure transducer (having working capacity 5psi PCB Piezotronics Inc., USA, Model 106B50). These transducers were powered by ICP Battery power units (PCB Piezotronics Inc., USA, Model 480E06), which also act as amplifiers. The amplified signal was transferred to a microcomputer via a junction box. The analogue output of the ICP battery was first converted to a digital format using a 16-bit A/D PCMCIA converter card (nCode Inc. UK) and then stored into the microcomputer using dAtagate software (nCode Inc., UK). Wall pressure fluctuations were measured with the help of pressure transducer flush mounted at the middle (0.5 m) of the column (to minimize the end effect). Pressure fluctuations were recorded at the 200 and 400Hz.

4.2.1.1 Operating parameters and procedure

Experiments were performed for two particle sizes (spherical particles of 3 mm and 6 mm diameter). Pressure drop, dynamic liquid hold-up and tracer concentration at the outlet were measured for the range of gas (0-0.44 m/s) and liquid (3-10 mm/sec) superficial velocities. Before the start of each experiment, air was passed through the column at least for 5-6 hrs to ensure that complete dry bed conditions are achieved. For a nonwetted bed, the liquid flow rate was gradually increased and pressure drop and dynamic liquid holdup were measured. Dynamic liquid holdup was measured by switching off the inlet air and liquid flows and by collecting the drained liquid.

Experiments were performed for the constant gas flow rate (0.22 and 0.44 m/s) and for the range of the liquid superficial velocity (0.002-0.024 m/s). Liquid flow rate was gradually increased for a particular flow rate of gas and pressure fluctuation data was collected. Acquired data was analyzed to examine the influence of sampling frequency, number of

data points and low pass filter frequency on the processed results. This analysis showed that the sampling frequency of 200 Hz and 2^{15} data points are adequate. Based on the preliminary analysis as well as results of *Krieg et al.*⁸⁵, the low pass filter of 20 Hz was used for all the subsequent data processing.

4.3 Results and Discussion

4.3.1 Dynamics of gas-liquid flows and regime transition

Wall pressure fluctuations were measured for various liquid flow rates at constant gas velocity (0.22 m/s). Typical wall pressure fluctuations data at various liquid flow rates is shown (after low pass filtering) in Figure 4.4. In a trickle flow regime, weak fluctuations in the pressure signal were observed (Figure 4.4). Amplitude of pressure fluctuations increases as one moves from trickle to pulse flow regime (Figure 4.4). The pulsing was observed at a liquid flow rate above $11 \text{ kg/m}^2\text{s}$ (Figure 4.4). The pulsing observed at this liquid flow rate was uniform in nature. The nature of pulsing remained relatively uniform up to the liquid velocity of $15 \text{ kg/m}^2\text{s}$ (Figure 4.4). Nonuniformity of pulsing started with a further increase in liquid flow rate ($17.4 \text{ kg/m}^2\text{s}$). Beyond this point, further increase in liquid flow rate ($20 \text{ kg/m}^2\text{s}$), gas-liquid dispersed flow was observed. In this operating regime, pressure signals were highly nonuniform (Figure 4.4).

Power spectra of acquired wall pressure fluctuations data at different liquid flow rates are shown in Figure 4.5. For single-phase flow, the figure shows a dominant peak at low frequency (<0.5), which is inherent in the system.

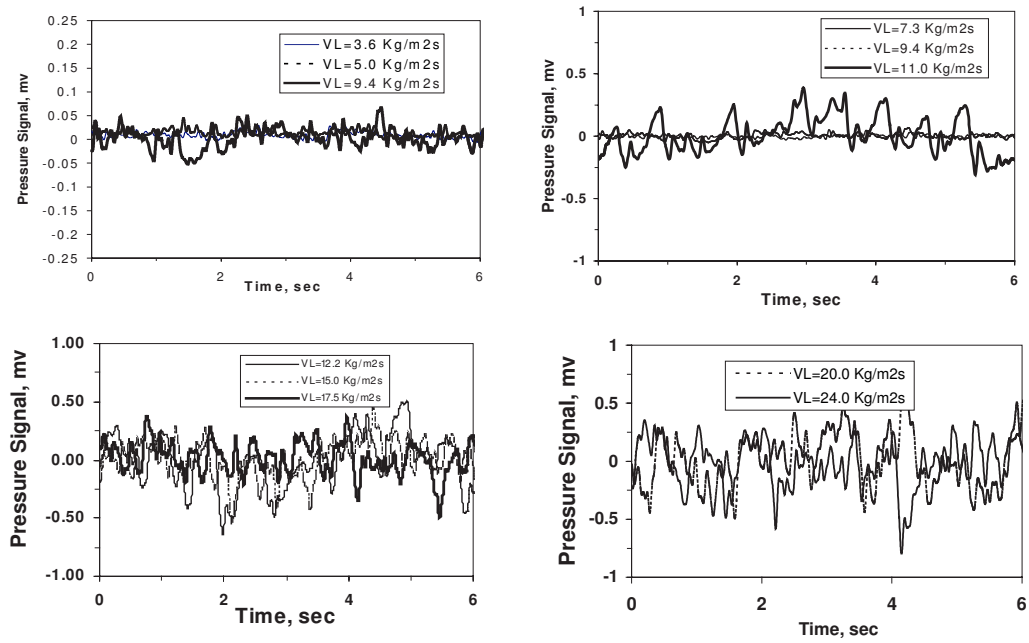


Figure 4.4: Wall pressure fluctuations in TBR at various liquid flow rates ($V_G = 0.22 \text{ m/s}$)

This frequency remained dominant at all liquid flow rates. In the trickle flow regime (up to $7 \text{ kg/m}^2\text{s}$) other frequencies were absent. For liquid flow rates higher than $7 \text{ kg/m}^2\text{s}$, peaks at frequencies higher than 1 Hz appear in the power spectrum. Between liquid flow rates of 9.4 and $11 \text{ kg/m}^2\text{s}$, transition from trickle to pulse flow regime was observed and a distinct peak of frequency 1.85 Hz was observed at liquid flow rate $11 \text{ kg/m}^2\text{s}$ (Figure 4.5b). At higher liquid flow rate (above $15 \text{ kg/m}^2\text{s}$), more peaks appear in the power spectrum (Figure 4.5c). Generally, the key characteristic frequency was within the range of 1-2 Hz with some smaller peaks around 3-4.0 Hz (Figure 4.5b). At higher liquid flow rates (dispersed bubble pulse flow regime, Figure 4.5d), the spectrum becomes wider, indicating a large number of temporal scales interacting with each other.

There are a number of ways one can use to obtain information about key dynamic characteristics from the acquired time series. Here we have characterized the dynamics of trickle beds using the Kolmogorov entropy. The wall pressure fluctuations data were processed using **AnTS** (**A**alysis of **n**on-linear**T**ime **S**eries, see *Ranade and Utikar*⁹ for more details) with a low pass frequency of 20 Hz. The Kolmogorov entropy represents the rate of information loss of the system. Following Schouten et al.¹⁰⁰, the maximum likelihood estimate of Kolmogorov entropy was obtained using 2^{15} data points (32768 data points sampled with a frequency of 200 Hz). The cutoff length was set equal to the average absolute deviation of the entire time series and the delay time was chosen equal to the sample interval time. The entropy values were calculated with embedding dimension set to the average number of points per cycle (see *Ranade and Utikar*⁹ for a detailed discussion).

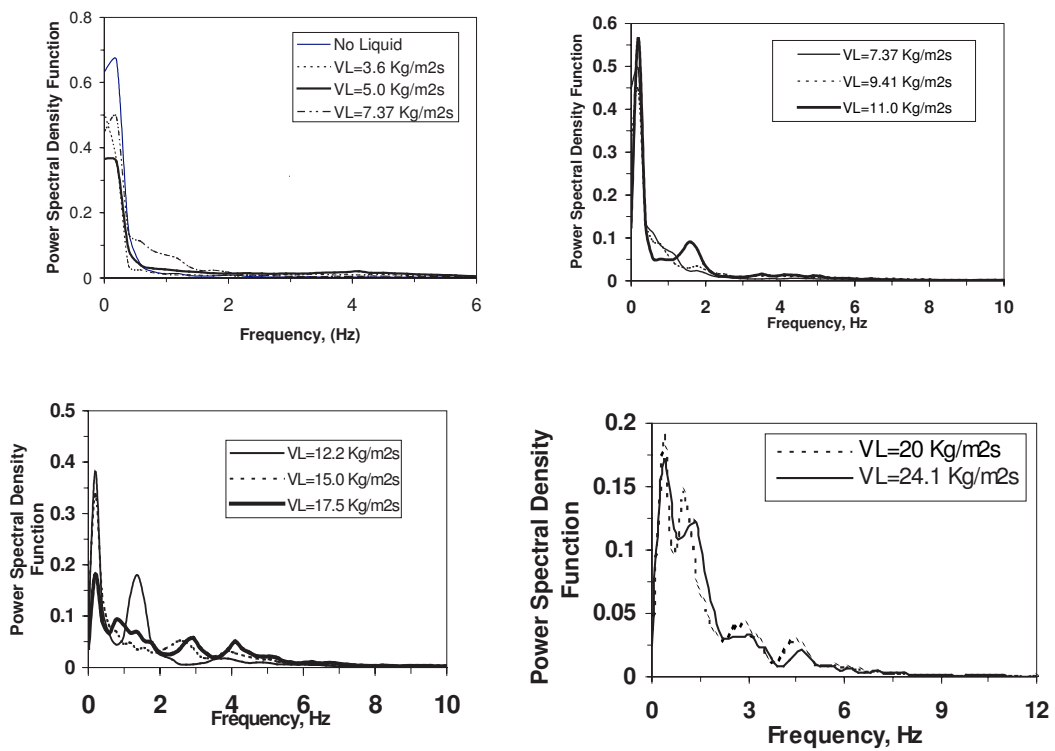


Figure 4.5: Power spectral density at various liquid flow rates ($V_G = 0.22 \text{ m/s}$)

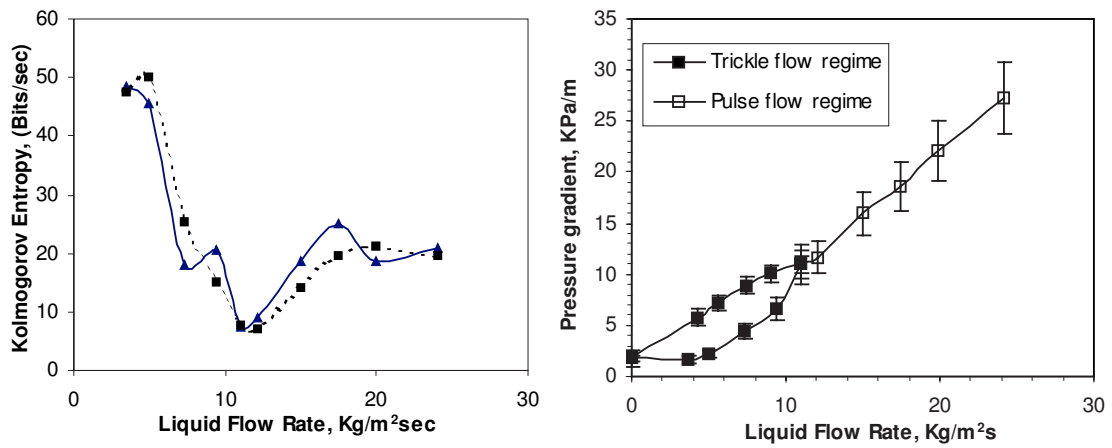


Figure 4.6: Trickle to pulse flow regime transition: Kolmogorov entropy and pressure drop hysteresis ($D = 0.114$ m, $d_p = 3$ mm and $V_G = 0.22$ m/s).

The variation of the Kolmogorov entropy with liquid flow rate is shown in Figure 4.6a. The value of Kolmogorov entropy decreases continuously with liquid flow rate until it reaches a value of $11 \text{ kg/m}^2\text{s}$ (from 50 to 7 bits/ s). The lowest value of the Kolmogorov entropy was found to coincide with the transition from trickle to pulse flow regime. It can be seen from Figure 4.6a that variation of Kolmogorov entropy indicates a sharp transition from trickle to pulse flow regime. It should be noted that the transition from trickle to pulse flow regime may not always be that sharp. At higher liquid velocity (above $11 \text{ kg/m}^2\text{s}$), in the pulse flow regime, the Kolmogorov entropy increases with an increase in liquid flow. In a dispersed bubble pulse flow regime (above $20 \text{ kg/m}^2\text{s}$), the Kolmogorov entropy remained more or less constant. It can be seen that variation of Kolmogorov entropy can be conveniently used to accurately identify regime transition from trickle to pulse flow regimes.

4.3.2 Time averaged pressure drop and liquid hold-up

Two-phase pressure drop per unit length and dynamic liquid holdup at different liquid flow rates for prewetted and non-prewetted bed conditions were measured. To estimate the total liquid holdup in the bed, the static liquid holdup was calculated from the correlation of *Saez and Carbonell*⁸⁹ and was added to the measured dynamic liquid holdup. Static holdup is a function of Eotvos number (\ddot{E}), contact angle at the gasliquid contact line, and geometry of packing and was calculated as follows,

$$\epsilon_{SL} = \frac{1}{20 + 0.9\ddot{E}} \dots \dots \dots (4.1)$$

Where,

$$\ddot{E} = \frac{\rho_L g d_P^2 \epsilon^2}{\sigma_L (1 - \epsilon^2)^2} \dots \dots \dots (4.2)$$

Where, ρ_L and σ_L is the density and surface tension of liquid phase. At all gas velocities static hold up for 3 mm and 6 mm particles was 0.049 and 0.048 respectively.

Typical time-averaged pressure drop data at various liquid velocities is shown in Figure 4.6b. It can be seen that the pressure drop variation with liquid flow rate shows two branches: the lower bench is for the nonprewettted bed (increasing liquid flow rate mode) while the upper bench shows data for the pre-wettted bed (decreasing liquid flow rate mode). When the liquid flow rate was slowly increased from zero in a dry bed, the lower branch was obtained. The bed becomes completely wet just before transition to a pulse flow regime occurs. When the liquid flow rate was decreased slowly back to zero from the higher liquid velocity, pressure drop variation showed hysteresis and followed an upper branch. For a dry bed, the capillary pressure acting on the solid-liquid contact line is dominant, which restricts the spreading within the bed. Thus the liquid flows through the confined region of the bed. This pattern gets disrupted at the flow transition point. When the liquid flow rate was decreased, due to radial spreading and vigorous mixing earlier, there is a larger amount of gasliquid interfacial interaction, which results in higher pressure drop along the upper branch. The pressure difference between the upper and lower branch may vary considerably depending on the extent of prewetting and intermediate values can be obtained through various inner loops. Similar trends of hysteresis were observed for liquid holdup in the bed as well.

Influence of particle size on pressure drop hysteresis is shown in Figure 4.7. It can be seen that the magnitude of hysteresis decreases with an increase in particle diameter. Sim-

ilar results were reported by *Wang et al.*⁶ whose data is also shown in Figure 4.7. As the particle diameter increases, characteristic dimension of interstitial space also increases. Therefore, capillary pressure becomes less dominant. Overall pressure drop also decreases with increase in particle diameter. Therefore, magnitude of pressure drop hysteresis decreases with increase in particle size. The effect of gas velocity on hysteresis loop is shown in Figure 4.8. It can be seen that the magnitude of hysteresis in pressure drop is not very sensitive to the gas velocity. At higher gas velocity, transition of the pulse flow regime occurs at lower liquid velocity.

With increase in column diameter, the observed pressure drop was found to increase slightly (see Figure 4.9). The variation of total liquid holdup as a function of liquid velocity for two column diameters is shown in Figure 4.10. It can be seen that there is no significant change in the observed liquid holdup with bed diameter. Since hysteresis behavior depends on initial flow distribution in the bed, experiments were carried out with two types of liquid distributors (spray and a perforated plate). The magnitude of pressure drop hysteresis observed with the spray distributor was smaller than that for the perforated plate distributor (Figure 4.11). Visual inspection also confirmed that the spray distributor was able to realize better liquid distribution within the bed. Similar results were also observed for the hysteresis in liquid holdup (Figure 4.12). The data collected in this work will be useful for evaluating computational models.

4.4 Summary and Conclusions

In this study, we have experimentally investigated hydrodynamics of trickle beds. Experiments were carried out on two columns (of diameter 0.114 m and 0.194 m) with two sets of particles (3 mm and 6 mm diameter spherical particles). Effect of prewetted and

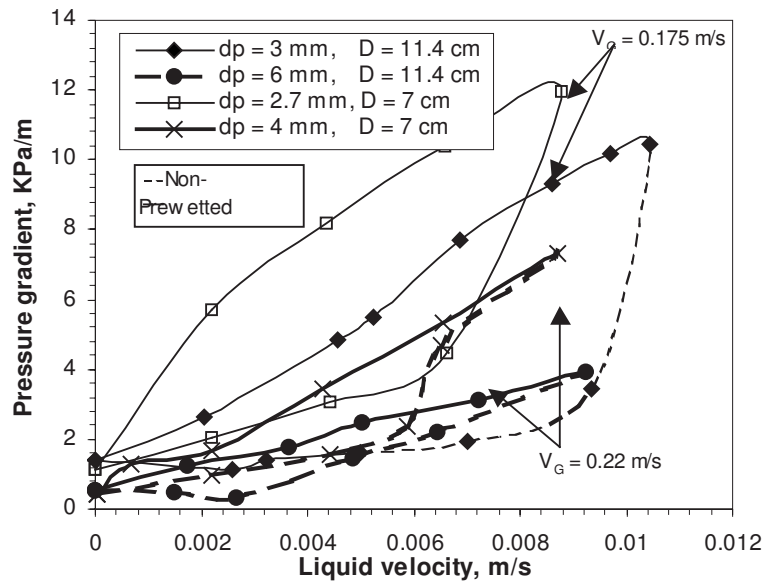


Figure 4.7: Pressure drop and liquid hold-up hysteresis in TBR at various operating conditions, (Data of $D=7$ cm from Wang *et al.*⁶)

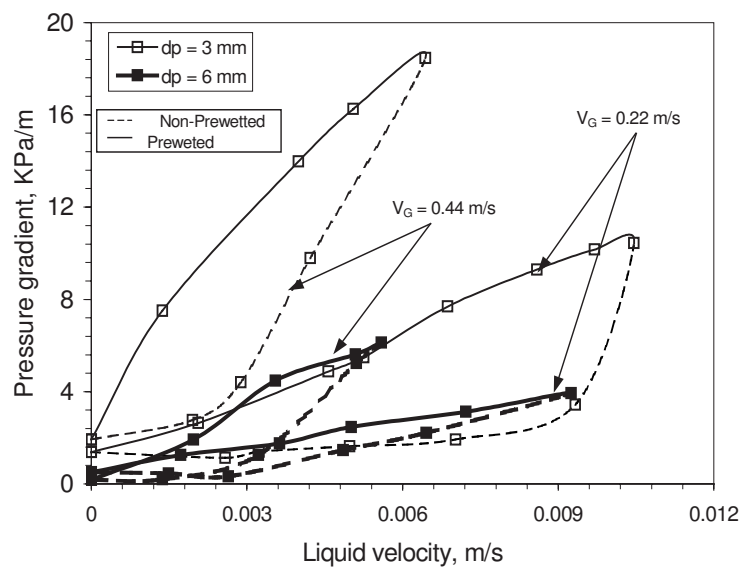


Figure 4.8: Pressure drop and liquid hold-up hysteresis in TBR at various operating conditions for $D=11.4$ cm.

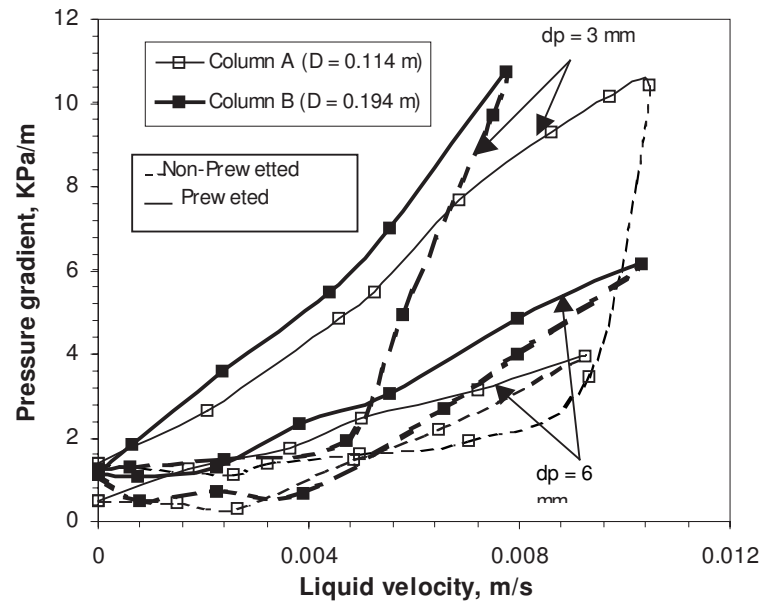


Figure 4.9: Effect of column diameter on pressure drop hysteresis at $V_G = 0.22$ m/s.

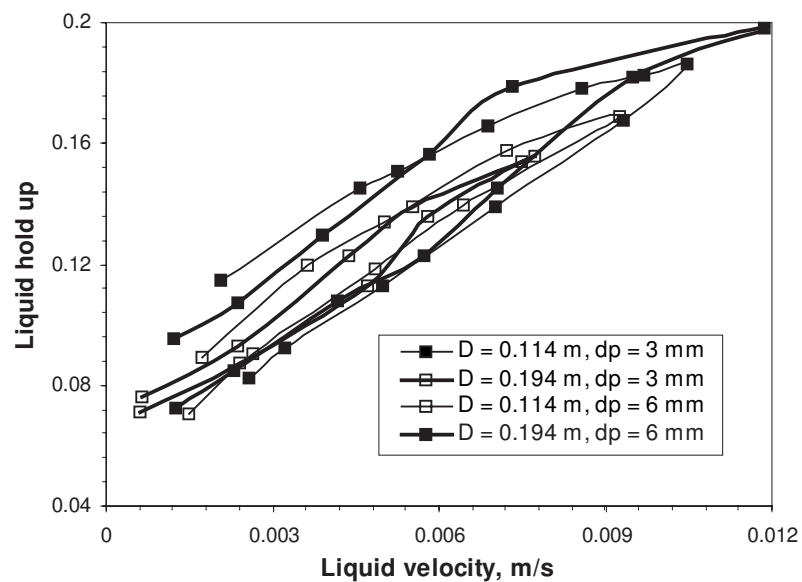


Figure 4.10: Liquid hold up in different trickle bed reactors at $V_G = 0.22$ m/s.

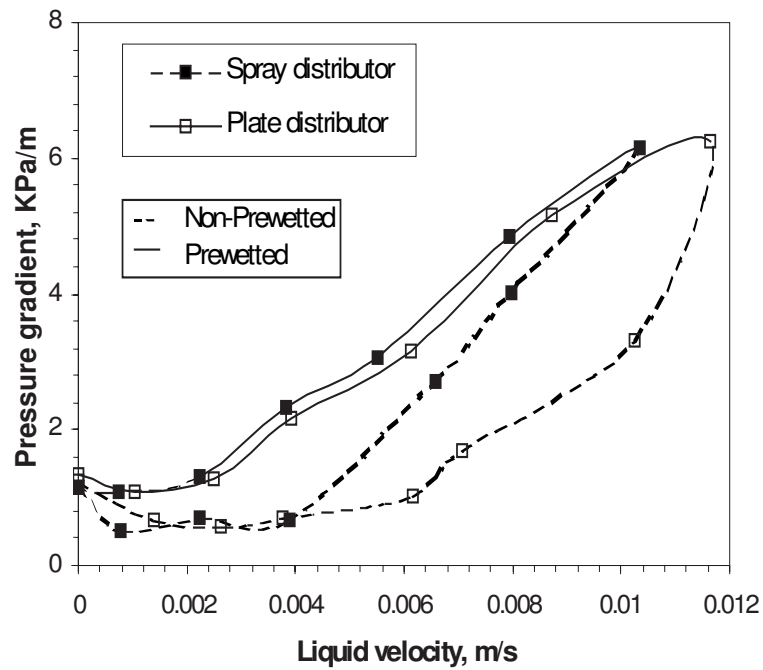


Figure 4.11: Effect of liquid inlet distributor on pressure drop hysteresis ($V_G = 0.22$ m/s, $d_p = 6$ mm, $D = 0.194$)

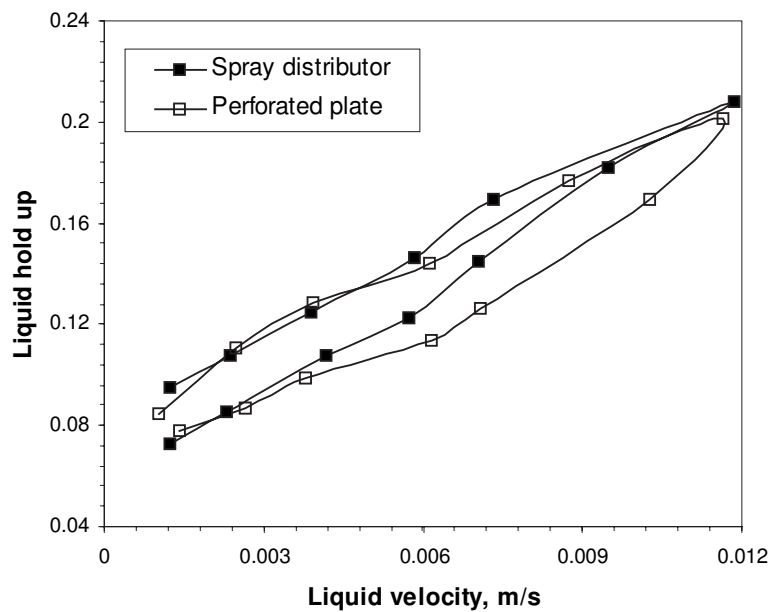


Figure 4.12: Liquid hold up for different distributors ($V_G = 0.22$ m/s, $d_p = 6$ mm, $D = 0.194$ m)

non-pretreated bed conditions on pressure drop and liquid hold-up was studied for a range of operating conditions ($V_G = 0.22-0.44 \text{ kg/m}^2\text{s}$, $V_L = 2-24 \text{ kg/m}^2\text{s}$). Wall pressure fluctuations were measured and analyzed using chaos theory. This analysis provides an accurate identification of transition from trickle to pulse flow regime and also provides valuable information on pulse frequency distribution. Key findings of this study are as follows:

- a. Kolmogorov entropy calculated based on wall pressure fluctuations can provide a useful technique for identifying transition from trickle to pulse flow regime. The technique is non-intrusive and is applicable over a wide range of operating conditions.
- b. Analysis of time series data provides valuable information about characteristic pulse frequencies. At low liquid flow rates ($V_L = 11-12.2 \text{ kg/m}^2\text{s}$), a single dominant frequency indicating a uniform pulse rate was observed. At higher liquid flow rates ($V_L > 12.2 \text{ kg/m}^2\text{s}$), two or three different frequencies of pulses were observed.
- c. Time averaged pressure drop and liquid hold up showed hysteresis with respect to liquid velocity. The observed trends in such hysteresis as well as values of time averaged pressure drop and liquid hold-up were almost independent of column diameters studied in this work (0.114 m and 0.194 m diameter).
- d. The spray distributor was found to perform better than the plate distributor and showed lower hysteresis.

*“Therefore O students study mathematics and do not
build without foundations”*

— Leonardo Da Vinci

5

Computational Flow Model for Trickle Bed Reactors

5.1 Introduction

In recent years, computational fluid dynamics (CFD) based models are showing promising results for a variety of complex reactors. Several efforts are also being made to develop computational flow models for trickle bed reactors. *Attou et al.*¹⁰¹ have developed a one-dimensional flow model for prediction of global hydrodynamic parameters. Because it is one dimensional, their model can not take account of radial variation in bed porosity. Jiang et al.¹³ have developed a two-dimensional CFD model including variation of bed porosity. This model was able to capture some of the key features of hydrodynamics of trickle beds. Iliuta et al.²⁴ and Souadnia and Latafi²⁵ have used the CFD model for predicting hydrodynamics characteristics over a wide range of operating parameters. *Gunjal et al.*⁴⁷ have used similar CFD model for studying liquid phase mixing and liquid distribution. However, both of these studies were restricted to trickle flow regime. None of the CFD models published so far were used to simulate spray or pulse regimes.

Trickle bed reactors, in which gas and liquid phases flow co-currently downward through the packed bed (of catalyst pellets), are used in several chemical industries. Accurate knowledge of prevailing flow regime, global parameters like two-phase frictional pressure drop and volume fraction of liquid and the knowledge of gas-liquid flow field within the bed is essential for design of trickle bed reactors. Most of the relevant design variables like gas-liquid, liquid-solid mass transfer and heat transfer are often estimated using the knowledge of two phase frictional pressure drop and volume fraction of liquid. Frictional pressure drop for single-phase flow through packed bed reactor can easily be obtained from the observed pressure drop and fluid hold-up/ saturation. For gas-liquid flow in a packed bed, relationship between net pressure drop and frictional pressure drop is not straightforward because of the possibility of part of the liquid hold-up being supported by the bed in some of the prevailing flow regimes (see *Boyer et al.*¹⁰²)

Numerous authors have studied and reported experimental data on pressure drop and liquid saturation in trickle bed reactors (see for example, *Al-Dahhan et al.*¹⁰³, *Saez and Carbonell*⁸⁹, *Herskowitz and Smith*⁹⁰). Different authors have estimated static head contribution in the overall pressure drop differently. It is useful to consider possible flow regimes while discussing the relationship between frictional pressure drop and overall observed pressure drop. When gas and liquid flow through a packed bed, four different flow regimes may exist. A typical flow regime map reported by *Sie and Krishna*⁵ and schematics of flow regimes are shown in Figure 4.1. At low liquid velocity and high gas velocity, spray regime may prevail in the column in which most of the liquid flows in the form of droplets through a continuous gas phase. Low gas velocity and high liquid velocity forms the other extreme, in which liquid phase becomes a continuous one through which gas flows in the form of bubbles. In this paper, we use frictional pressure drop based on gas phase, which is assumed to be a continuous phase. Liquid phase is assumed to be either a semi-continuous or dispersed phase (the case in which liquid phase is continuous as in packed bubble column is not considered here). With low superficial velocity of gas and liquid, a trickle flow regime may prevail. In this regime, part of the liquid may flow in the form of film over solid surface and part of the liquid may flow in the form of dispersed droplets. Knowledge of what fraction of liquid flows in the form of a film and what fraction flows in the form of droplets is essential for accurate estimation of the mass transfer.

Simulation of pulse flow regime requires a detailed understanding of complex interactions of liquid spreading on a solid surface, capillary forces and gas flow. Though underlying physics of such complex flows is not completely understood, computational models may shed some light on such complex flows. Recently Professor Dudukovic and his group initiated CFD modeling of periodic operation of trickle beds (private communications, 2004). This approach may be extended to understand differences and similarities between periodic operation (liquid rich- gas rich feed) and pulse flow regime. For simulating spray

flow regime, it is necessary to develop ways of estimating the fraction of liquid suspended in the gas phase. The observed pressure drop in trickle beds can be related to flow frictional pressure drop as:

$$\left(\frac{dP}{L}\right)_F = \left(\frac{dP}{L}\right)_{obs} + \rho_G g \beta_G + \rho_L g \beta_L \phi_L \dots \dots \dots (5.1)$$

where, β_G and β_L are the gas and liquid saturation respectively. ϕ_L is the fraction of liquid suspended in gas phase in the form of droplets. Considering the small magnitude of gas density, the second term of the right hand side is usually neglected. In trickle beds, depending upon operating regime, the fraction of liquid suspended in gas phase varies from 0 to 1. In the film flow regime, all the liquid flows in the form of film and the fraction of liquid suspended in the gas phase is zero. In such a case, frictional pressure drop is same as that of the observed pressure drop. However, for trickle and spray flow regime, estimation of the fraction of liquid suspended in gas phase (ϕ_L) is not straight forward. CFD based models may be used to gain some insight into this.

5.1.1 Present Contribution

In this study, we have used wall pressure fluctuation measurements to identify prevailing flow regime in trickle beds. A criterion based on Kolmogorov entropy calculated from the measured pressure fluctuation time series is proposed to identify flow regime transition. Influence of particle and column diameter was studied by carrying out experiments on two columns (of diameter 0.114 m and 0.194 m) with two sets of particles (3 mm and 6 mm diameter spherical particles). Effect of pre-wetted and un-wetted bed conditions on pressure drop and liquid hold-up was reported for a range of operating conditions

($V_G=0.22-0.44 \text{ kg/m}^2\text{s}$, $V_L=2-24 \text{ kg/m}^2\text{s}$). A comprehensive CFD model was developed to predict measured hydrodynamic parameters. The model was evaluated by comparing with the experimental data. A new method is proposed to predict frictional pressure drop and fraction of liquid hold-up suspended in the form of drops using the developed CFD model. Predictions of CFD model were compared with the present and some of the published experimental data. CFD model was also used to understand hydrodynamics of trickle beds with periodic operation. The experimental data as well as computational models discussed here will have significant implications for understanding and designing of trickle bed reactors.

5.2 Computational Model and Boundary Conditions

In trickle bed reactors, catalyst pellets are usually packed randomly. The random packing of pellets of specific shape almost always leads to non-uniform porosity distribution within the bed. *Jiang et al.*¹⁰⁴ showed that appropriate representation of such a non-uniform porosity distribution in a CFD model is essential for qualitatively and quantitatively correct flow simulations. In this work, we have used approach of *Jiang et al.*¹⁰⁴ to incorporate non-uniform porosity distribution in a CFD model. Eulerian-Eulerian approach is used here to simulate flow in trickle bed reactors. An important aspect in development of a realistic CFD model of gas-liquid flow in trickle bed reactor is the formulation of appropriate closures for inter-phase momentum exchange terms. The details of implementation of non-uniform porosity and model equations are discussed below.

5.2.0.1 Representing non-uniform porosity distribution

Numerous studies on porosity distribution in randomly packed beds are available (see for example, *Mantle et al.*³⁹ and *Stephenson and Stewart*¹⁰⁵ for experimental study and *Spedding and Spencer*¹⁰⁶ for computational study). These experimental and computational studies have shown that the porosity is higher near the vicinity of the wall and it fluctuates significantly in the near wall region (of width of about 4 to 5 particle diameters). The magnitude of fluctuations is a strong function of a ratio of column diameter to particle diameter (for $D/d_p > 15$, fluctuations are within 1% whereas for lower values of D/d_p , fluctuations may rise up to 30%). *Mueller*¹⁵ has proposed a correlation for radial variation of axially averaged porosity as a function of column diameter, particle diameter and average porosity. This correlation is fairly general and represents the available experimental data with reasonable accuracy. In the present work, we have used this correlation (reproduced below as Equation 5.2) to represent radial variation of axially averaged bed porosity.

$$\epsilon(r) = \epsilon_B + (1 - \epsilon_B)J_o(ar^* e^{br}) \dots \dots \dots (5.2)$$

where,

$$a = 8.243 - \frac{12.98}{(D/d_p - 3.156)} \quad \text{for } 2.61 \leq D/d_p \leq 13.0$$

$$a = 7.383 - \frac{2.932}{(D/d_p - 9.864)} \quad \text{for } 13.0 \leq D/d_p$$

$$b = 0.304 - \frac{0.724}{(D/d_p - 3.156)}$$

$r^* = r/D$ and J_o is the zeroth order Bessel Function

The predicted radial variation of bed porosity for 11.4 cm and 19.4 cm column diameter is shown in Figure 5.1.

*Jiang et al.*¹⁰⁴ has shown that porosity variation in the axial direction (at any radial location) is close to Gaussian distribution. The value of standard deviation of such distribution decreases with an increase in the ratio of column diameter to particle diameter and eventually approaches zero for very small (compared to column diameter) particles. The porosity distribution within the randomly packed bed may thus be represented by imposing random fluctuations (following the Gaussian distribution) over the axially averaged porosity estimated by Mueller's correlation. For generating such a distribution, the column was divided into 25000 cells (50 in radial direction and 500 in axial direction). For each radial position, radial porosity value for each subsection was obtained from Mueller's correlation and assigned for that particular cell. For cells located at same radial location along the axial direction, porosity values were assigned by drawing random number from the Gaussian distribution of specified standard deviation around the value obtained from the Mueller's correlation. Simulated porosity distribution for two-dimensional bed with a typical experimental configuration used for trickle bed studies (column diameter: 0.194 m, column height: 1 m, particle diameter: 0.006 m, average porosity: 0.37) for 5% standard deviation are shown in Figure 5.2[B]. Examination of these porosity distributions indicate that the fluid dynamics of trickle beds with random porosity distribution is likely to be different from those with uniform bed porosity.

5.2.1 Model equations

Several different approaches such as percolation theory approach (*Crine et al.*¹⁰⁷), network model (*Thompson and Fogler*¹⁰⁸), Eulerian-Eulerian approach with the multi-fluid models (*Jiang et al.*¹³, *Yin et al.*¹⁰⁹, *Attou and Ferschneider*¹¹⁰ and *Grosser et al.*¹¹¹) and lattice Boltzmann type models (*Mantle et al.*³⁹) have been applied to simulate gas-liquid flow in a packed beds. *Grosser et al.*¹¹¹ and *Attou and Ferschneider*¹¹⁰ have used a one-dimensional

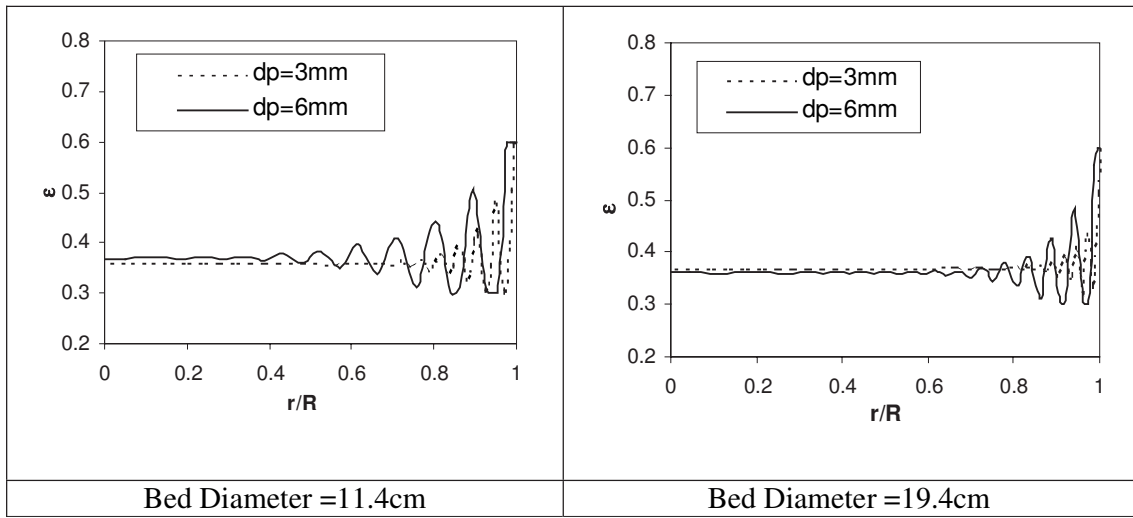


Figure 5.1: Variation of the porosity along radial direction using Mueller (1991) correlation

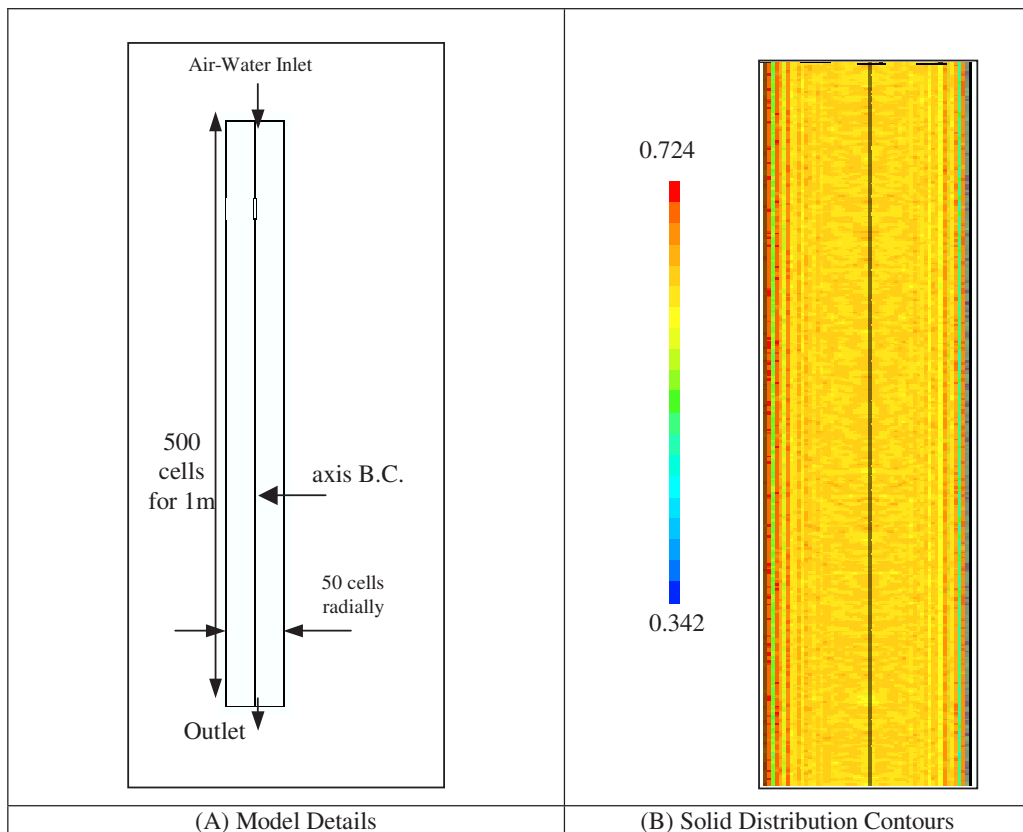


Figure 5.2: Bed Model Details and Contours of Simulated Results (C)Liquid Distribution Contours (Bed Diameter 19.4cm, $d_p=0.006m$, std dev=5%)

flow model with uniform porosity distribution in the bed. The Eulerian-Eulerian approach with the two-dimensional multi-fluid models with spatial variation of porosity appears to be most suitable for reactor engineering applications (*Kashiwa et al.*¹⁴, *Jiang et al.*¹³ and *Ranade*¹²) and was selected for the present work. In this approach, continuum approximation is applied for all the phases. Volume averaged mass and momentum balance equations for the k_{th} fluid can be written as:

Mass balance equation:

$$\frac{\partial(\epsilon_k \rho_k)}{\partial t} + \nabla \cdot (\epsilon_k \rho_k U_k) = 0 \quad \dots \dots \dots \quad (5.3)$$

Momentum balance equation:

$$\frac{\partial(\epsilon_k \rho_k U_k)}{\partial t} + \nabla \cdot (\epsilon_k \rho_k U_k U_k) = -\epsilon_k \nabla P + \nabla \cdot (\epsilon_k \mu \nabla U) + \epsilon_k \rho_k g + F_{K,R}(U_k - U_R) \quad \dots \quad (5.4)$$

Where, ϵ_k represents the volume fraction of each phase, ρ_k is the density of the k_{th} phase. U_k is the cell velocity of the k_{th} phase. P is a mean pressure shared by all the phases present in the system. $F_{K,R}$ is the inter-phase momentum exchange terms. It is assumed that there is no inter-phase mass transfer. The mass balance Equation 5.3 therefore, does not have any source term on the right hand side. The left hand side of Equation 5.4 represents the rate of change of momentum for k_{th} phase. The right hand side represents, pressure forces, gravitational acceleration, average shear stresses and inter-phase momentum exchange. If the flow is turbulent, additional terms comprising turbulent stresses will appear in right hand side. However, for macroscopic flow modeling in packed beds the contribution of the turbulent stress terms to overall momentum balance equation is not significant (*Jiang et al.*¹³). Turbulent stresses were therefore not considered in the present work.

Considering that the solid bed is supported at the end and is stationary, the velocity field of the solid phase was set to zero and volume fraction of the solid phase was fixed at the initially specified value (based on the generated random porosity distribution discussed in the previous section). The mass and momentum balance equations for the solids phase were therefore not solved. In order to close the set of equations, it is necessary to formulate appropriate models for inter-phase coupling terms, $F_{K,R}$.

In the present work, the gas phase was treated as a primary phase. The frictional pressure drop referred in the present work is based on the gas phase. When gas flows through the packed bed in absence of any liquid flow, the presence of solids in the bed exerts drag on flowing gas phase and leads to much higher pressure drop than that may occur in absence of the packed bed. The pressure drop in the packed bed is usually correlated using the Ergun equation or its variants (*Al-Dahhan et al.*⁸⁸, *Holub et al.*¹¹², *Saez and Carbonell*⁸⁹). Inter-phase coupling terms may therefore be formulated based on similar equations. The presence of liquid flow, however, leads to additional inter-phase exchanges, which need to be formulated correctly. Different approaches viz, relative permeability model (*Saez and Carbonell*⁸⁹, *Grosser et al.*¹¹¹), slit model (*Holub et al.*¹¹³) and two-fluid interaction model (*Attou and Ferschneider*¹⁰¹ and *Attou et al.*¹¹⁰) have been proposed to formulate inter-phase momentum exchange terms. Available information is not really sufficient to conclude the best model and most of these models fit the experimental data to about the same degree of accuracy. The model of *Attou et al.*¹¹⁰, which includes gas-liquid interaction force, has a more theoretically sound basis. These authors (*Attou and Ferschneider*¹⁰¹, *Attou et al.*¹¹⁰) have also shown a good agreement between model predictions and experimental data. The model of *Attou et al.*¹¹⁰ was developed for the regime in which liquid flows in the form of film. In this work, we have explored the possibility of using this model for simulating flow regimes in which part of the liquid may flow in the form of droplets. Considering the results presented by *Attou et al.*¹¹⁰ which showed good agreement over the range of

conditions in which there is a significant possibility of existence of part of the liquid in the form of drops, we expect that the model will perform reasonably well over the trickle and spray flow regimes. The inter-phase coupling terms $F_{K,R}$ (given here by Equations 5.5 to 5.7) proposed by *Attau and Ferschneider*¹⁰¹ are rewritten in terms of interstitial velocities and phase volume fractions as (instead of superficial velocities and saturation):

Gas-Liquid momentum exchange term:

$$F_{GL} = \epsilon_G \left(\frac{E_1 \mu_G (1 - \epsilon_G)^2}{\epsilon_G^2 d_P^2} \left[\frac{\epsilon_S^2}{(1 - \epsilon_G)} \right]^{0.667} + \frac{E_2 \rho_G (U_G - U_L) (1 - \epsilon_G)}{\epsilon_G d_P} \left[\frac{\epsilon_S^2}{(1 - \epsilon_G)} \right]^{0.333} \right) \quad (5.5)$$

Gas-Solid momentum exchange term:

$$F_{GS} = \epsilon_G \left(\frac{E_1 \mu_G (1 - \epsilon_G)^2}{\epsilon_G^2 d_P^2} \left[\frac{\epsilon_S^2}{(1 - \epsilon_G)} \right]^{0.667} + \frac{E_2 \rho_G U_G (1 - \epsilon_G)}{\epsilon_G d_P} \left[\frac{\epsilon_S^2}{(1 - \epsilon_G)} \right]^{0.333} \right) \quad (5.6)$$

Liquid-Solid momentum exchange term:

$$F_{LS} = \epsilon_L \left(\frac{E_1 \mu_L (1 - \epsilon_G)^2}{\epsilon_L^2 d_P^2} + \frac{E_2 \rho_L U_G (1 - \epsilon_S)}{\epsilon_L d_P} \right) \quad (5.7)$$

It must be noted that a pressure shared by all the phases is used in the momentum balance equation (Equation 5.4). However, when two immiscible phases are in contact with each other, interfacial tension causes the fluids to have different pressures. Such a pressure difference (capillary pressure) for the gas and liquid phase may be written as:

$$P_G - P_L = 2\sigma \left(\frac{1}{d_1} - \frac{1}{d_2} \right) \quad (5.8)$$

where, d_1 and d_2 are the maximum and minimum diameter of the sphere with liquid film formed by the flowing liquid. More details of relating d_1 and d_2 to particle diameter, porosity and the minimum equivalent diameter of the area between three particles in contact are given in *Attou and Ferschneider*¹⁰¹. Capillary pressure affects the liquid distribution and may set-up gradients of liquid hold-up within the packed bed.

Several investigators have analyzed capillary forces (for example, *Grosser et al.*¹¹¹; *Attou and Ferschneider*¹⁰¹; *Jiang et al.*¹³ and references cited therein). *Grosser et al.*¹¹¹ have studied onset of pulsing in trickle beds using linear stability analysis. Their analysis suggests that the competition between the inertial and capillary forces leads to a situation in which steady state flow is not possible, implying the pulsing in trickle beds. In the present work, the pulsing regime was not considered and the scope was restricted to trickle and spray flow regimes. *Grosser et al.*¹¹¹ have proposed the capillary pressure as an empirical function of the liquid saturation:

$$P_G = P_L - \sigma \frac{\epsilon_s E_1^{0.5}}{(1 - \epsilon_S) d_P} \left[0.48 + 0.036 \ln \frac{1 - \beta_L}{\beta_L} \right] \dots \dots \dots (5.9)$$

The order of magnitude analysis indicates that the magnitude of the capillary forces is rather small compared to the magnitudes of inter-phase drag forces. *Attou and Ferschneider*¹⁰¹ have obtained the following expression for the capillary pressure term based on geometric estimates of d_1 and d_2 and with empirical factor F to account for high-pressure operations as:

$$P_G - P_L = 2\sigma \left(\frac{1 - \epsilon}{1 - \epsilon_G} \right)^{0.3333} \left(\frac{5.416}{d_p} \right) F \left(\frac{\rho_G}{\rho_L} \right) \dots \dots \dots (5.10)$$

where,

$$F\left(\frac{\rho_G}{\rho_L}\right) = 1 + 88.1\frac{\rho_G}{\rho_L} \quad \text{for} \quad \frac{\rho_G}{\rho_L} < 0.025 \quad \dots \dots \dots (5.11)$$

Under typical operating conditions of trickle beds, quantitative comparison of the capillary pressures estimated from Equation 5.9 and Equation 5.10 are not very different (within 10%). Considering the geometric basis used by *Attou and Ferschneider*¹⁰¹, Equation 5.10 was incorporated in the present CFD model.

It must be noted here that in trickle beds, the pressure drop required to maintain specified gas and liquid throughputs is history dependent. Pressure drop at any specific liquid velocity measured with increasing liquid velocity is more than that measured with decreasing liquid velocity (see for example, *Szady and Sundaresan et al.*⁴⁹. Capillary phenomenon is one of the contributing factors of this observation. *Jiang et al.*¹³) have attempted to simulate this phenomenon by introducing an empirical factor, f , related to the degree of wetting in their capillary pressure formulation as:

$$P_G - P_L = (1 - f)P_c \quad \dots \dots \dots (5.12)$$

For a prewetted or a fully wetted bed, f was set to one, implying zero capillary pressure. For a non-wetted bed, f is set to zero (*Jiang et al.*¹³). As will be seen later in this work, the difference in the predicted pressure drop with and without considering capillary terms is not as high as the observed magnitude of the hysteresis of the pressure drop. In the present work, therefore, all the simulations were carried out with setting f equal to unity (fully wetted bed) unless mentioned otherwise.

For incorporating the capillary pressure in the CFD model, gradients of capillary pressure must be formulated as:

$$\frac{\partial P_G}{\partial z} - \frac{\partial P_L}{\partial z} = \frac{2}{3} \sigma \frac{5.416}{d_P} \left(\frac{\epsilon_s}{1 - \epsilon_G} \right)^{-2/3} \left(\left(\frac{1}{1 - \epsilon_G} \right) \frac{\partial P_{\epsilon_S}}{\partial z} + \left(\frac{\epsilon_s}{(1 - \epsilon_G)^2} \right) \frac{\partial \epsilon_G}{\partial z} \right) F \frac{\rho_G}{\rho_L} \quad (5.13)$$

The Equation 5.13 was used to express the gradients of liquid pressure (PL) in the liquid phase momentum equations in terms of gradients of gas pressure (PG) to incorporate the capillary pressure terms.

5.2.2 Boundary Conditions and Numerical Solution

Above set of model equations was implemented in commercial software FLUENT 6 (of Fluent. Inc., USA) using user defined routines. Porosity for each cell was assigned with the help of user defined subroutine and the velocity of the solid phase was set to zero. Flat velocity profile was implemented for gas and liquid phases as an inlet boundary condition. It is necessary to formulate appropriate combination of interstitial velocity and volume fraction for specifying the inlet boundary conditions. To minimize the discontinuity at the inlet, we estimated the overall liquid volume fraction, $\langle \epsilon_L \rangle$, using the available correlations and used it to specify inlet boundary conditions as:

$$U_{L_{in}} = \frac{(V_L/\rho_L)}{\langle \epsilon_L \rangle} \quad U_{G_{in}} = \frac{(V_G)}{\langle 1 - \rho_L \rangle} \dots \dots \dots (5.14)$$

where V_L and V_G are the mass fluxes of liquid and gas respectively (kg/m^2s) and ρ_L and ρ_G are the densities of liquid and gas respectively. No slip boundary condition was used for

all the impermeable walls. Momentum exchange between the phases was set in the model using user-defined subroutines in Fluent 6. No slip boundary condition was used for all the impermeable walls. Momentum exchange between the phases was set in the model using user-defined subroutines. Unsteady simulation was carried out with a time step of 0.005 sec. Preliminary numerical experiments were carried out to obtain grid independent results. These numerical experiments indicated that the predicted values of overall pressure drop and liquid saturation become insensitive to further grid refinement (four times increase in the number of grid cells and use of higher order discretization scheme caused less than 5% change in pressure drop and less than 0.75% change in liquid volume fraction).

5.3 Results and Discussion

5.3.1 Comparison of model predictions with the experimental data

Predictions of the CFD model discussed in the previous section were first compared with our experimental data in a trickle flow regime for 0.114 m and 0.194 m column diameter (see details in Table 5.1). Effect of pre-wetted and non-prewetted bed conditions were considered in the model using capillary pressure acting at the interface. Validated model was then used to simulate some of the published experimental data covering a wide range of operating conditions (see Table 5.2). For this purpose three different data sets (from *Szady and Sundaresan*⁴⁹; *Rao et al.*¹¹⁴ and *Specchia and Baldi*¹¹⁵) were selected. The CFD model was then used to estimate the extent of suspended liquid in a trickle flow regime and to simulate periodic operation of trickle beds to obtain insight into a pulse flow regime. As discussed earlier, measurements of pressure drop and liquid hold-up for trickle bed reactor showed hysteresis with liquid velocity. Observed hysteresis is associated

with the capillary pressure acting on three phase contact line. Accurate representation of capillary term in the CFD model is difficult. In this work, we have used the capillary pressure model developed by *Attou et al.*¹⁰¹. The simulations were carried out by setting the value of ' f ' to one for pre-wetted beds and to zero for a dry bed. The simulated results are compared with the experimental data in Figures 5.3 and 5.4. As observed in the experiments, simulated results showed lower pressure drop for the dry bed compared to the pre-wetted bed. The predicted magnitude of the hysteresis is however lower than that observed in the experiments. For the dry bed (lower branch as well as the initial part of the upper branch), experimental data showed non-linear variation of pressure drop with liquid velocity. However, simulated results showed almost a linear variation. The inadequate representation of capillary forces is the most likely cause of this discrepancy. Non-linearity appears even in the upper branch mainly because, when liquid velocity is reduced, partial dry-out may occur in the bed making it similar to the non-prewetted bed. Simulated contours of liquid hold-up for pre-wetted bed and non-prewetted bed are shown in Figure 5.5. Liquid distribution in prewetted bed is relatively uniform as compared to the non-prewetted bed conditions (Figure 5.5(A)). . It can be seen from Figure 5.6 that velocity and hold-up distributions within the bed for liquid phase for a pre- and non-prewetted beds are substantially different. Distributions for the prewetted bed are wider than non-prewetted bed.

Table 5.1: Experimental Parameters and Operating Conditions in Present Study

Specifications	Column A	Column B
Dimeter, m	11.4×10^{-2}	19.4×10^{-2}
Packing Height, m	1	1
System	Air-Water	Air-Water
Gas Velocity, m/sec	0.22-0.44	0.11-0.22
Liquid Mass Flow Rate, kg/m^2sec	0.20	0-10
Packings	Spherical Glass Beads	Spherical Glass Beads
Partical Diameter, mm	3 and 6	3 and 6
Porosity of Bed	0.36	0.37

Table 5.2: Experimental Parameters and Operating Conditions in Present Study

Case	Data Source	D/d_p	Bed Characteristics	V_G m/sec	$V_L \times 10^3$ m/sec	Ergun's Constant E_1 and E_2
1	<i>Szady and Sundaresan</i> ⁴⁹	55	3mm spherical $\epsilon_b = 0.37$	0.22	0.2-0.8	215 and 1.75
2	<i>Specchia and Baldi</i> ¹¹⁵	29.6	2.7 mm sperical $\epsilon_B = 0.38$	0.2-0.8	2.8	500 and 3
3	<i>Rao et al.</i> ¹¹⁴	15.4	3mm spherical $\epsilon_B = 0.37$	1.5-5.5	1	215 and 3.4

For a pre-wetted bed, simulated results of pressure drop for the 0.114 m diameter of a column are compared with the experimental data (Figure 5.7) for gas velocities 0.22 m/s and 0.44 m/s. Simulated results over predict pressure drop for 3 mm particle at low gas velocity (0.22 m/s) and under-predict for high gas velocity ($V_G=0.44$ m/s). However for 6 mm particles, simulated results show reasonable agreement with the experimental data. The disagreement at low liquid velocity for $V_G=0.44$ m/s may be due to dry-out phenomenon at high gas flow rate. Influence of column diameter on agreement between simulated and experimental data is shown in Figure 5.8. It can be seen that agreement is better for 6 mm particles than for 3 mm particles. Another Possible inadequacies in representation of appropriate porosity distribution for 3 mm particle may be one of the reasons for such disagreement. Simulated values of the total liquid hold-up in column of 0.114 m diameter are compared with the experimental data in Figure 5.9. Simulated results show good qualitative as well as quantitative agreement with the experimental data. Similar agreement was also found for liquid hold-up in 0.194 m diameter column (see Figure 5.10). The simulated results can also be used to gain an insight in to hydrodynamics of gas-liquid flow through trickle beds.

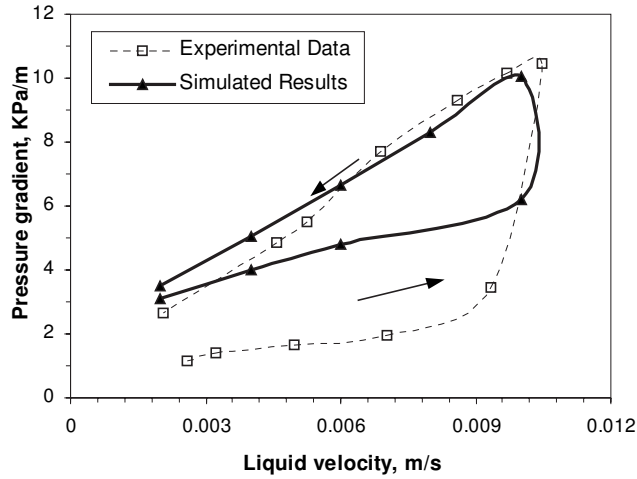


Figure 5.3: Comparison of simulated results of pressure drop for prewetted and non-prewetted beds

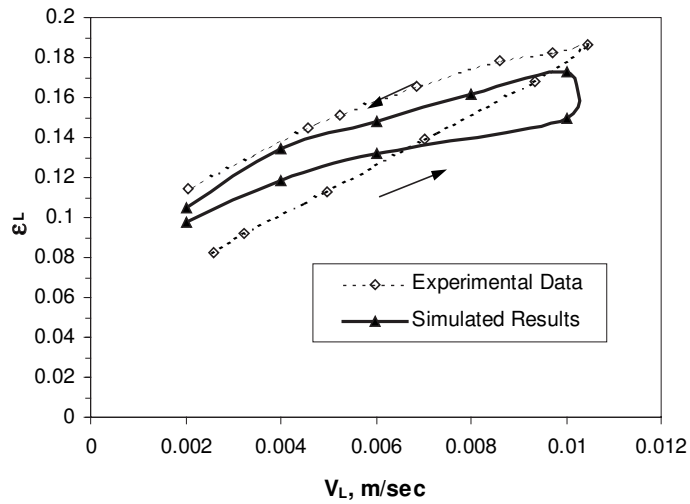


Figure 5.4: Comparison of simulated results of liquid holdup for prewetted and non-prewetted beds

5.3.2 Estimation of the fraction of suspended liquid

In order to cover the wider range of operating conditions, three independent experimental data sets were selected for evaluating the computational model. Details of bed character-

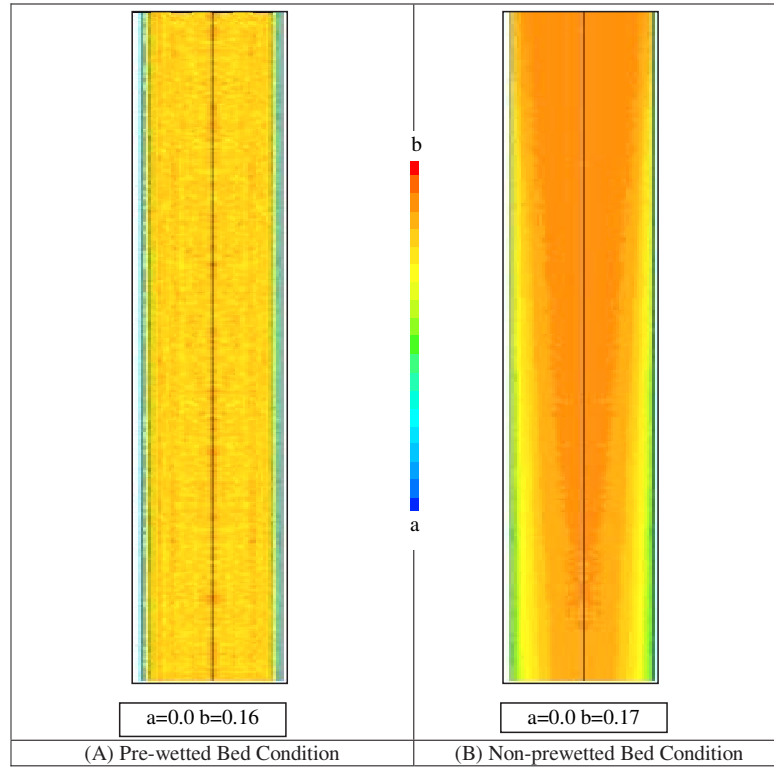


Figure 5.5: Simulated contours of liquid distribution for prewetted and non-prewetted bed. ($V_L=6 \text{ kg/m}^2\text{s}$, $V_G=0.22\text{m/sec}$, std dev=5%, $D=0.114\text{m}$, $d_p=3\text{mm}$)

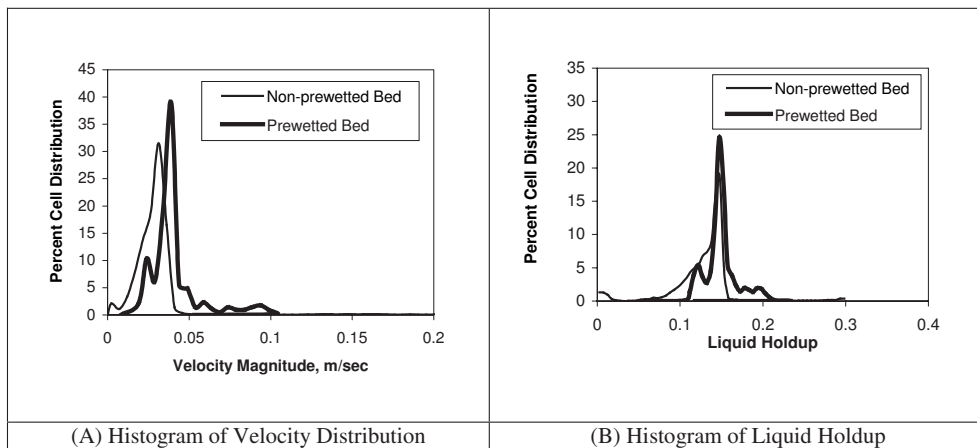


Figure 5.6: Histogram of simulated results of liquid velocity and holdup ($V_L=6 \text{ kg/m}^2\text{s}$, $V_G=0.22\text{m/sec}$, std dev=5%, $D=0.114\text{m}$, $d_p=3\text{mm}$)

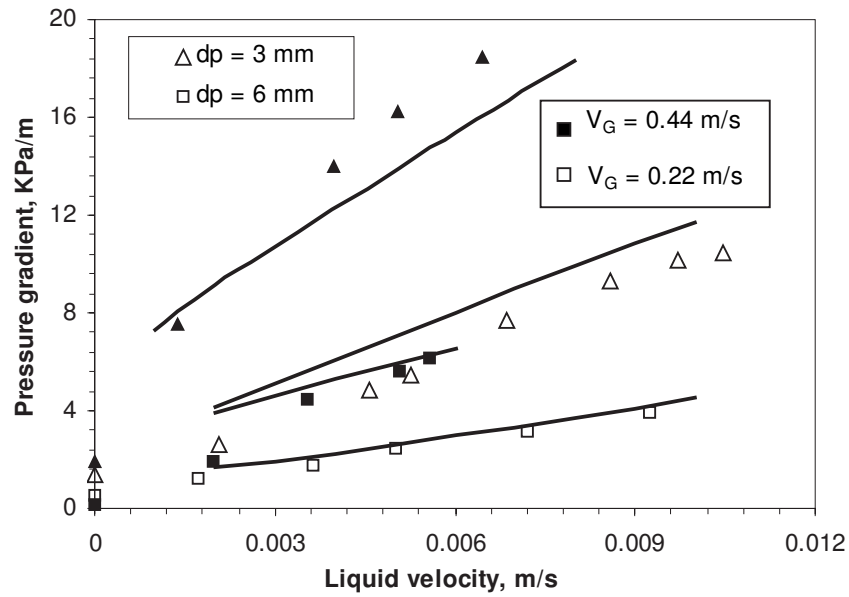


Figure 5.7: Comparison of CFD results with experimental data for $D=0.114$ m

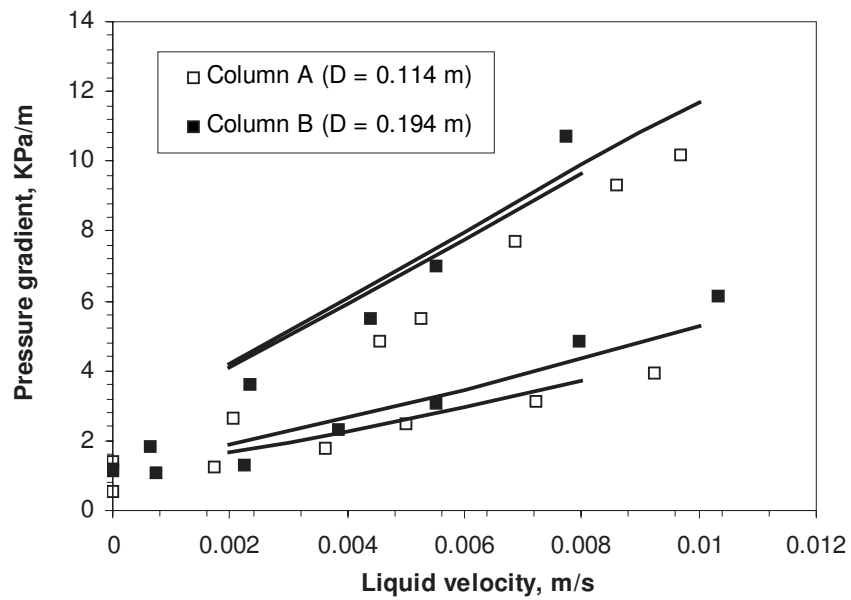


Figure 5.8: Comparison of CFD results with experimental data with $d_p=3$ mm.

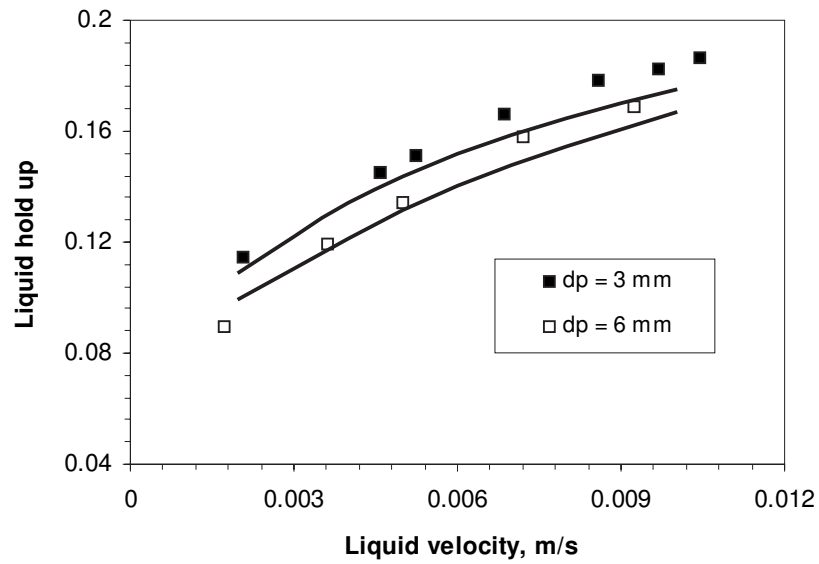


Figure 5.9: Comparison of CFD results with experimental data ($D=0.114$ m, $V_G=0.22$ m/s)

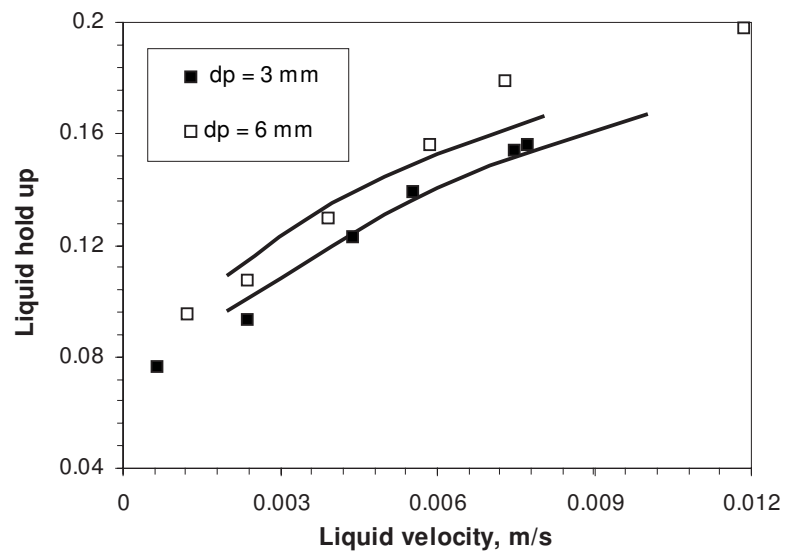


Figure 5.10: Comparison of CFD results with experimental data ($D=0.194$ m, $V_G=0.22$ m/s)

istics and operation conditions used in these three cases are summarized in Table 5.2. In Case 1, the column to particle diameter (D/d_p) ratio was much higher compared to the other two cases. In Case 1 variation of pressure drop and liquid saturation was studied with change in liquid mass flow rate, while effect of change in gas mass flow rate on hydrodynamic parameters was studied in the other two cases. the gas mass flow rate in Case 3 was much higher than the other two cases. Comparison of the experimental data with the simulated results is discussed in the following section.

Simulated results were compared with the experimental data of *Szady and Sundaresan*⁴⁹ for pressure drop and total liquid saturation is shown in Figures 5.11 (only upper branch of pressure drop curve is shown here). The predicted results showed the correct trends of variation of the pressure drop and liquid saturation with liquid mass flow rate. The values of Ergun's (E_1 and E_2) constants used in the closure models represent the bed packing characteristics. In this case, $E_1 = 215$ and $E_2 = 1.75$ were used for carrying out the simulations. At low liquid velocities, model showed good agreement with the experimental data. At higher liquid velocities ($8 \text{ kg/m}^2\text{s}$), the model underpredicted the pressure drop values. This may be because of the possible transition from trickle flow to pulse flow regime. Model predictions for pressure drop and liquid saturation for experimental data of *Specchia and Baldi*¹¹⁵ is shown in Figure 5.12. In this case, higher values of Ergun's constants ($E_1 = 500$ and $E_2 = 3$) were used in the model. These values are close to the values suggested by *Holub et al.*¹¹³. In this case, model predictions are showing good agreement with the experimental data of pressure drop and liquid saturation. A third set of data from *Rao et al.*¹¹⁴, which was obtained for very high gas velocities compared to earlier data sets (1 to $8 \text{ kg/m}^2\text{s}$) was also used for evaluating the model predictions. As the velocity of the gas phase increases ($>1.5 \text{ kg/m}^2\text{s}$), the trickle flow regime may change to a spray flow regime. It can be seen from Figure 5.12 that the model predictions showed good agreement with the experimental data for the high gas velocity cases as well (with

$E_1=215$ and $E_2=3.4$). Though, the value of E_2 looks rather high, it is well within the range of values used by previous investigators (see a review given by *Holub et al.*¹¹²).

The overall predictions of simulated results are showing reasonable agreement with the experimental data of various studies. The basic CFD model developed in this work uses two parameters (E_1 and E_2) to match the predicted observed pressure drop with the reported experimental data. Reported results indicate that with appropriate values of these parameters, CFD model is able to predict the overall liquid saturation correctly for the range of gas and liquid velocities. Encouraged by such agreement, the CFD model developed here was used to estimate frictional pressure drop and supported liquid saturation. For gas-liquid co-current down flow in trickle bed reactors, we propose to use the following equation to relate the observed pressure drop and frictional pressure drop for the gas phase:

$$\left(\frac{dP}{L}\right)_{GL} = \left(\frac{dP_f}{L}\right)_{GL} - \rho_L g \phi_L \dots \dots \dots \text{where...}, \phi_L \beta_L \dots \dots \dots (5.15)$$

Where β_L is the total liquid saturation and ϕ_L is the liquid saturation supported by the gas phase. Contribution of the gas phase density in the static head component is neglected in Equation 5.15. If none of the liquid is supported by the gas phase, the value of ϕ_L becomes zero. Most of the authors have used such a formulation and have equated observed pressure drop with frictional pressure drop for the gas phase. In the other extreme, some authors have assumed that all of the liquid is supported by the gas phase and equated the value of ϕ_L to β_L (for example, *Turpin and Huntington*¹¹⁶). Both of these models allow calculation of frictional pressure drop from the experimentally measured values of overall pressure drop and total liquid saturation. The behavior of trickle bed reactors is more likely to be between these two representations. That means the packed bed would support part of the liquid and part of the liquid may contribute to the static head. However, this intermediate behavior leads to two unknowns (frictional pressure drop and ϕ_L) in Equation 5.15.

To estimate these two unknown variables of interest, measurement of net pressure drop across the bed is not sufficient and it is necessary to devise alternative ways. The most obvious way to obtain these two unknowns is to carry out experimental measurements at two values of gravitational acceleration (say, g_1 and g_2). If these two values of gravitational acceleration are not very different, the overall pressure drop, frictional pressure drop and liquid saturation may be assumed to be the same for these two sets of experiments. In such a case, the desired two unknown variables may be obtained as:

$$\left(\frac{dP_L}{L}\right) = \frac{g_1 \left(\frac{dP_f}{L}\right)_2 - g_2 \left(\frac{dP_f}{L}\right)_1}{g_1 - g_2} \dots \dots \dots (5.16)$$

$$\phi_L = \frac{\left(\frac{dP_f}{L}\right)_2 - \left(\frac{dP_f}{L}\right)_1}{\rho_L(g_1 - g_2)} \dots \dots \dots (5.17)$$

It is, however, rather difficult to carry out pressure drop measurements in trickle bed reactor under different values of gravitational acceleration. If an appropriate computational model is available to simulate gas-liquid flow through a packed bed, it is easier to carry out numerical experiments for two different values of gravitational acceleration. In this work, we have developed a comprehensive CFD model and have simulated gas-liquid flows in trickle bed reactors at two values of gravitational acceleration (9.7 and 9.9 m/s^2) under different operating conditions. Since the difference in these two values of gravitational acceleration is small, the overall pressure drop, frictional pressure drop and liquid saturation are not expected to vary significantly. Simulations were carried out for two values of gravitational acceleration. Following Equations 5.16 and 5.17, frictional pressure drop and liquid saturation supported by gas phase were calculated. The predicted values of supported liquid saturation are shown by a dotted line in Figure 5.11a to 5.12c. It can be seen from Figure 5.11a that fraction of liquid supported by gas phase increases with liquid

velocity. The results shown in Figures 5.11b and 5.12 indicate that fraction of supported liquid saturation increases with gas velocity though increase in gas velocity decreases total liquid hold-up or saturation. At very high gas velocity (see Figure 5.12) almost all the liquid hold-up is supported by gas phase, indicating the spray flow regime.

5.3.3 CFD simulations of periodic flow

In many industrial practices, liquid induced periodic operations are preferable because reactor operation with natural pulsing is difficult for large reactors. It is worthwhile to apply present CFD model to simulate periodic operation of a trickle bed. This will also help to gain an insight into features of pulse flow regime. In natural pulse flow regime, liquid enriched pulses form after some distance from the inlet and they accelerate while moving downward. Formation of pulses is associated with complex interactions among capillary forces, wall adhesion and the convective forces. If the model equations adequately represent this underlying physics and numerical solution does not add any artificial diffusivity, the simulated results should be able to capture the transition from trickle to pulse flow regime. However, the current understanding of physics of pulse formation and its implementation in the CFD model is not adequate for this purpose. An alternative way to gain some insight into pulse like flow in trickle beds is to simulate periodic operation of trickle beds with induced pulses by manipulating inlet liquid velocity. *Boelhouwer et al.*¹¹⁷ have compared the key features of natural pulsing and induced pulsing trickle beds. Their results showed that the variation between natural pulsing and induced pulsing is within 25%. Following this, we have simulated flow in trickle beds operated with liquid induced pulsing maintaining the same average flow rates. The frequency of liquid induced pulsing was set from the experimental measurements of natural pulsing.

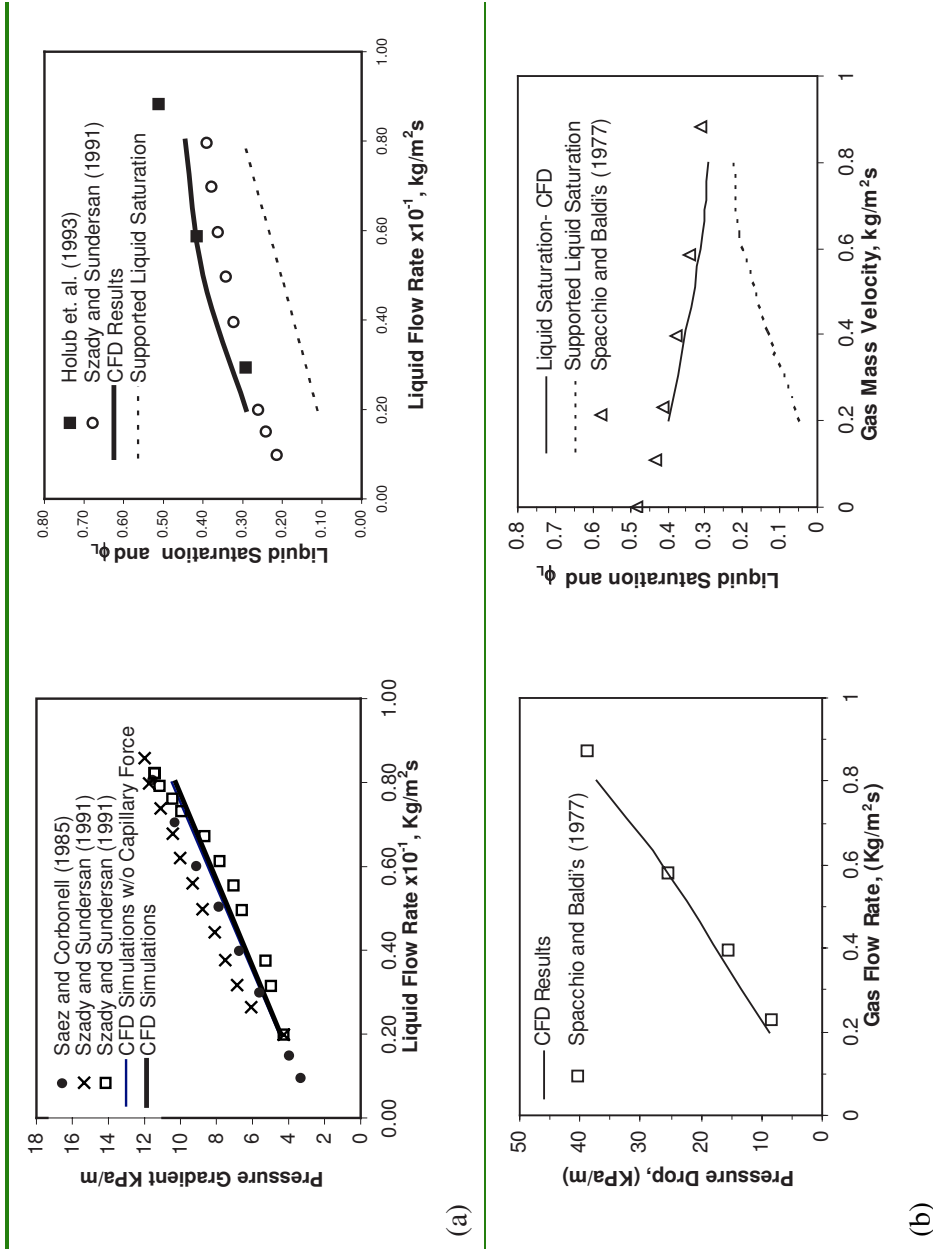


Figure 5.11: Comparison of simulated pressure drop and liquid saturation with literature data

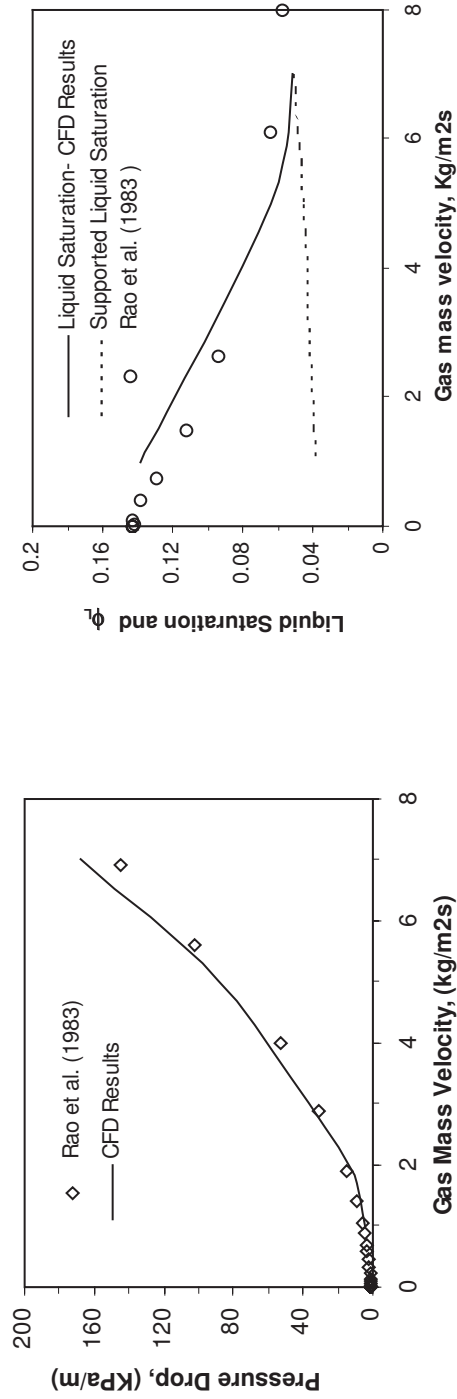


Figure 5.12: Comparison of simulated pressure drop and liquid saturation with literature data

As discussed earlier, at low liquid flow rates (11-12 kg/m^2sec), pulse frequencies are quite uniform (see pressure signal in Figure 5.13A and a single peak in PSD at 1.56 Hz shown in Figure 5.13 D). At higher liquid flow rates ($V_L > 12.2 kg/m^2s$), non-uniform pulsing was observed (see Figure 5.13B). Pressure signals indicate that at high liquid flow rates, one big pulse (Figure 5.13 C(a)) is associated with secondary small pulses (Figure 5.13 C (b and c)). Up to $V_L = 15 kg/m^2s$, one primary and one secondary dominant frequency was observed. Above $V_L = 15 kg/m^2s$, one primary and two secondary frequencies were observed. Characteristic frequencies of such pulses at different liquid flow rates are reported in Table 5.3. This information of natural pulse flow was used to specify appropriate inlet boundary conditions for the CFD model. The simulations of liquid induced periodic operation were carried out for different liquid flow rate ($V_L = 11-24 kg/m^2s$) at a gas flow rate of $V_G = 0.22$ m/s.

Table 5.3: Frequencies of Different Pulses Obtained From PSD at $V_G = 0.22$ m/s

Liquid Flow Rate <i>kg/m²sec</i>	<i>a, sec⁻¹</i>	<i>b, sec⁻¹</i>	<i>c, sec⁻¹</i>
11.0	1.562	-	-
12.2	1.367	3.7	-
15	2.73	3.9	-
17.5	0.78	2.92	4.1
20	0.97	2.92	4.49
24	1.36	3.125	4.68

At lower liquid flow rate of $V_L=11 \text{ kg/m}^2\text{s}$, observed natural pulse frequency of 1.56 Hz was specified as an input parameter for a liquid induced periodic flow model (as shown in Figure 5.14). The simulations for periodic operation were carried out using inter-phase drag coupling terms similar to those used for a trickle flow regime. For this case, the predicted pressure drop was within 20% of the observed pressure drop. Predicted liquid holdup variation with time along the length of the column is shown in Figure 5.15. At higher liquid flow rates (with non-uniform pulsing) the predicted pressure drop was lower than the observed pressure drop. The predicted liquid hold-up contours for uniform and non-uniform periodic flows are shown in Figure 5.16. To examine possible influence of induced pulsing frequency, simulations were carried out at two different frequencies i.e. 0.97 Hz and 2.92 Hz at $V_L = 20 \text{ kg/m}^2\text{s}$. Contours of simulated liquid hold-up at these two pulsing frequencies are shown in Figures 5.16C and D respectively. Interestingly the predicted pressure drop for these two frequencies was within 1%. Thus, hydrodynamics of periodic operation of trickle beds was not found to be sensitive to the exact value of induced pulsing frequency.

The approach, models and results discussed here can provide useful basis for further work on extending CFD models for simulating trickle bed reactors.

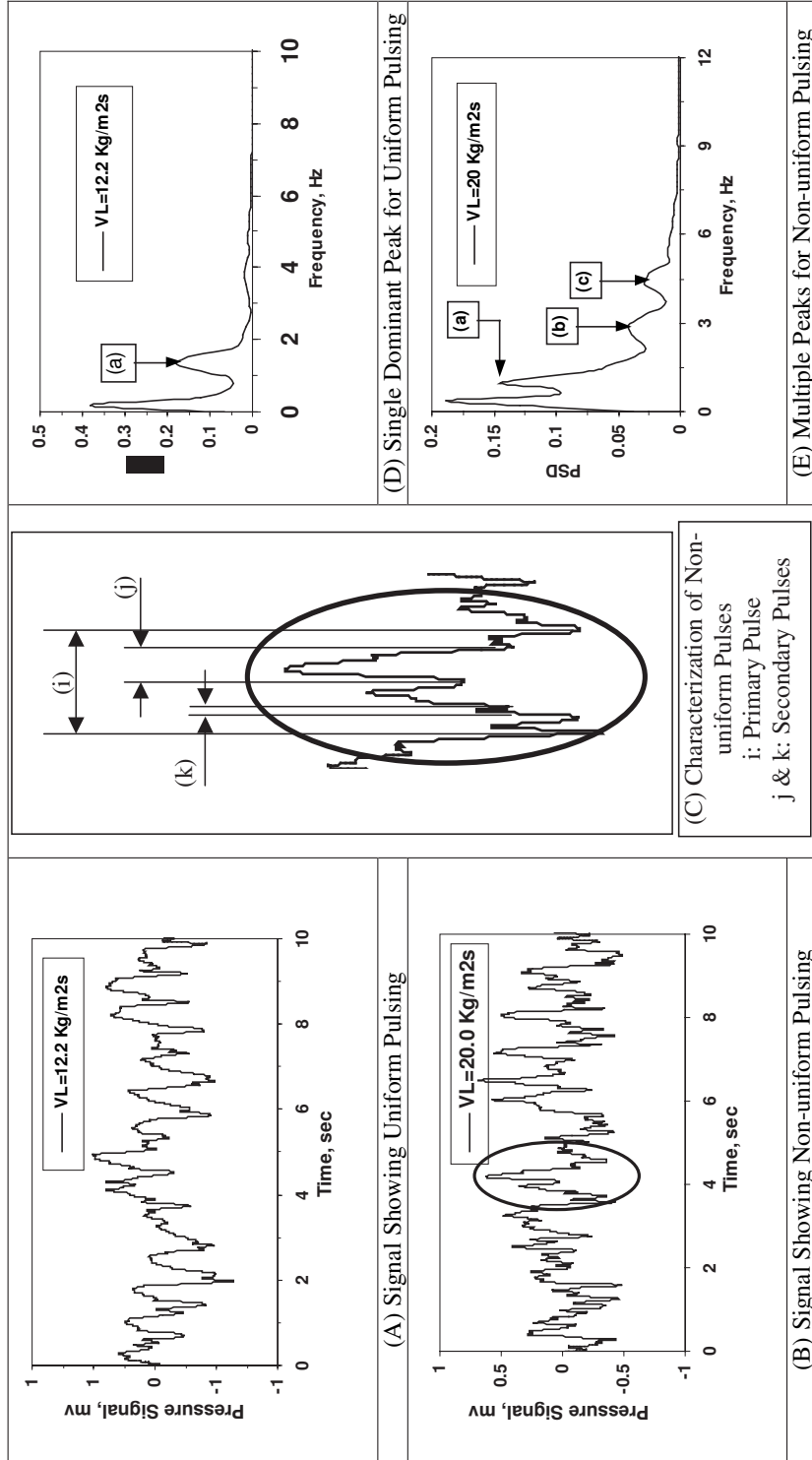


Figure 5.13: Comparison of simulated pressure drop and liquid saturation with literature data

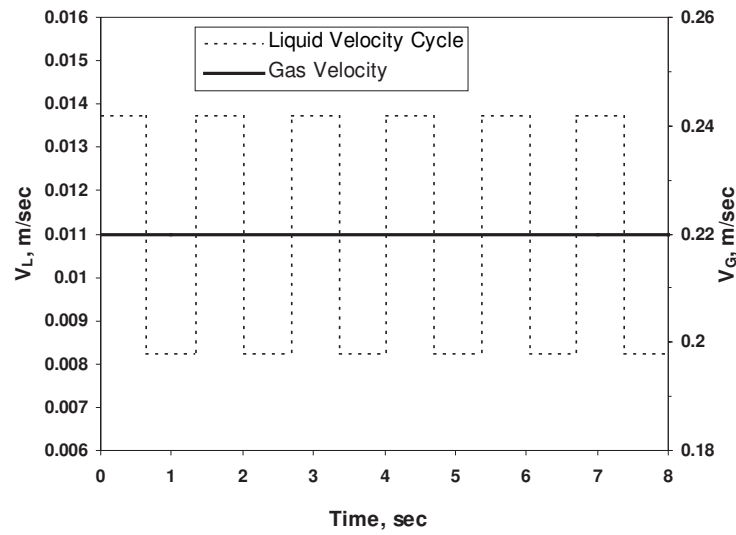


Figure 5.14: Liquid induced periodic boundary condition for simulation ($D = 11.4\text{cm}$, $d_p = 3\text{mm}$)

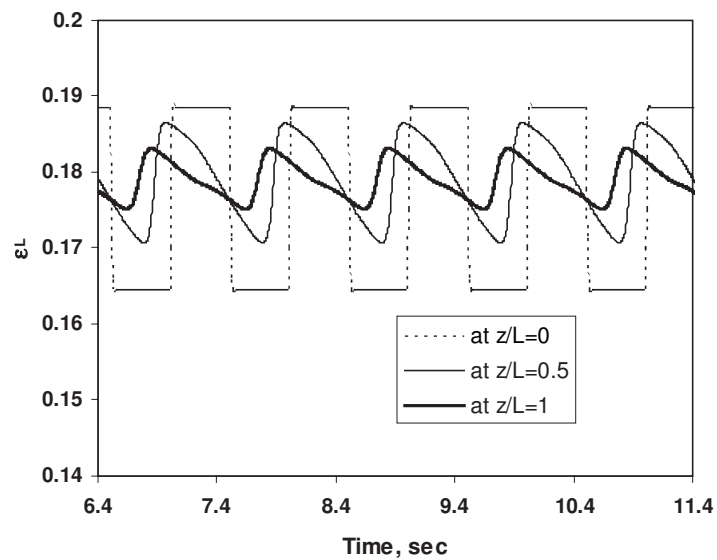


Figure 5.15: Simulated Liquid Holdup Variation along Bed Height. ($D=11.4\text{ cm}$, $d_p=3\text{mm}$, std. dev.=5%)

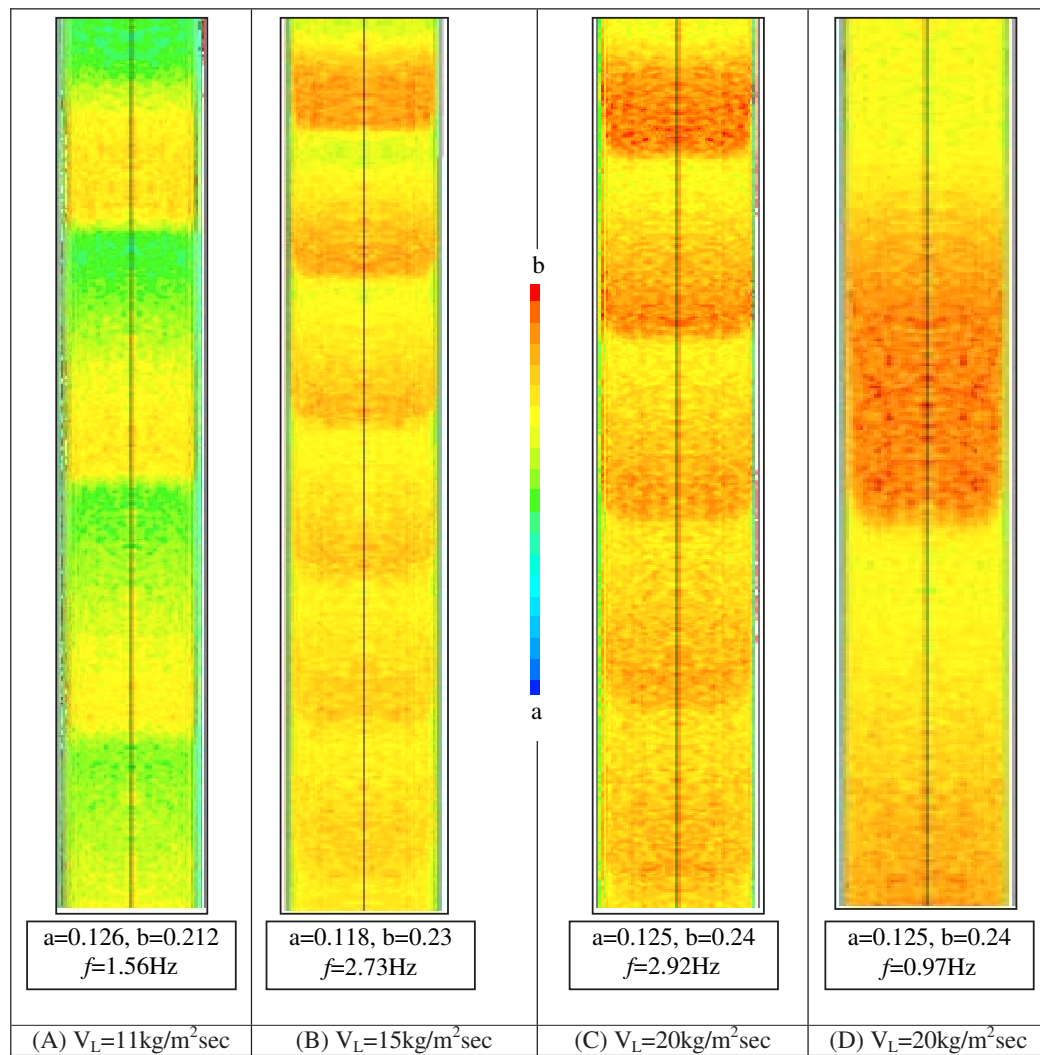


Figure 5.16: Simulated results of liquid hold-up variation along the height of the bed at different liquid flow rates. ($D=19.4\text{cm}$, $d_p = 3\text{mm}$, $stddev. = 5\%$, $V_G=0.22\text{ m/sec}$)

5.4 Summary and Conclusions

In this study, A comprehensive CFD model was developed to predict measured hydrodynamic parameters. The model was evaluated by comparing with the experimental data. A new method is proposed to predict frictional pressure drop and fraction of liquid hold-up suspended in the form of drops using the developed CFD model. The CFD model was then extended to understand hydrodynamics predictions of trickle beds with periodic operation. The key findings of this study are as follows;

- a. The computational model developed in this work showed reasonable agreement with the experimental data for the pre-wetted beds. The model was also able to capture the trends observed in hysteresis correctly. However, quantitative predictions of hysteresis were lower than experimentally observed values. This highlights the need for further research on development of better capillary models.
- b. The proposed method of simulating trickle bed performance at two values of gravitational acceleration was able to estimate liquid hold-up supported by gas. The approach can be used to identify existence and to quantify extent of spray regime in trickle beds.
- c. Simulations with induced periodic flow indicated that predicted pressure drop is insensitive to the exact value of induced pulsing (within the range investigated in this work). Simulations of periodic flow through trickle beds can be used to understand some of the key features of natural pulse flow regime. The approach will also be useful to evaluate capillary models.

The experimental data as well as computational models discussed here will have significant implications for understanding and designing of trickle bed reactors.

Part III

Application of CFD Model

“A scientist can discover a new star, but he cannot make one. He would have to ask an engineer to do that.”

- Gordon L. Glegg, American Engineer, 1969.

6

RTD and Liquid Distribution in TBR

6.1 Introduction

Liquid flow distribution and mixing are key parameters for designing of trickle bed reactors. Residence time distribution (RTD) was used for many years to analyze and characterize the flow non-idealities and mixing because of the un-availability of detailed flow information inside the reactor. RTD is a useful tool to understand many aspects of the trickle bed reactor such as kinetic processes (*Ramachandran and Smith*¹¹⁸), wetting characteristics (*Schwartz et al.*¹¹⁹), channeling (*Oliveros et al.*¹²⁰), flow maldistribution (*Hanratty and Dudukovic*¹²¹) and liquid mixing (*Higler et al.*¹²², *Gulijk Coen*¹²³). Hydrodynamics and mixing in trickle bed reactors are governed by several factors including non-uniform porosity distribution of the bed, capillary forces, wetting and non-uniform distribution of flow at the inlet. Large variation in hydrodynamic parameters such as pressure drop, liquid holdup and liquid distribution has been observed for prewetted bed and non-prewetted bed (see for example, *Szady and Sundaresan*⁴⁹). Conventional modeling approach uses uniform porosity and velocity through the bed and lump all the non-idealities in flow and mixing in dispersion coefficient. Tracer experiments are carried out in TBR and the dispersion coefficient is fitted based on outlet tracer response, which is expected to represent complex flow, mixing, wetting, channeling, stagnancy and dead zones in TBR. Extrapolation based on such lumped models is uncertain and often inadequate for design purposes.

Computational fluid dynamics (CFD) based models are recently being applied to simulate flow in TBR (see for example, *Jiang et al.*¹³, *Gunjal et al.*¹²⁴). In this work, we extended CFD model to simulate and to understand hydrodynamics and RTD in trickle bed reactors. The objective of the work was to understand the flow non-idealities and contribution of various parameters such as bed heterogeneity, capillarity, flow distribution on it using computational fluid dynamics and residence time distribution in trickle bed reactor. In this work, experiments were carried out to study the hydrodynamic parameters such as pressure

drop and liquid hold-up for complete wetting and non-wetting conditions at different operating conditions. A comprehensive two-dimensional and three-dimensional CFD models were developed, in which bed heterogeneity and capillary models were incorporated. Mixing and RTD were simulated using the CFD model. Simulated results were compared with experimental data. Experiments as well as model predictions showed interesting results for non-wetted and prewetted bed conditions. The current capabilities and limitations of the CFD model are discussed. The model and the results discussed here would be useful to extend application of CFD models for simulating mixing in TBR.

6.2 Experimental Set-up and Procedure

6.2.1 Experimental Set-up

The schematic of experimental set-up is shown in Figure 6.1. Gas and liquid were introduced in the column at the top. Gas and liquid flow rates were measured with the calibrated rotameters. The distributor plate was made up of stainless steel with uniform 3mm holes arranged in triangular pitch of 3 mm. Glass beads either of 3 mm or 6 mm diameter were filled in the column such that beads are placed compactly in the column. Voidage of the column was measured using liquid drainage method. The measured voidage of the columns were found to be 0.37 for 3 mm particle and 0.356 for 6 mm particles. Two pressure sensors were used to measure the pressure drop. Top pressure sensor was located at distance of 32 cm from the top. The distance between the two pressure sensors was 0.5 m. Glass beads were supported at the bottom by a stainless steel plate having 3 mm holes with 3 mm triangular pitch. Liquid was collected in a cup at the bottom of the column after gas was separated from the side outlet. Cup was made-up of aluminum material

with 5 cm inner diameter. Conductivity probe was hold inside the cup to measure the tracer concentration. Salt solution (concentration 50 gm/l) was used as a tracer. Tracer was injected with the help of a syringe placed at a distance of 16.6 cm from the top of the packed bed. The needle of the syringe was extended up to the bed center. For each experiment, 20 ml of tracer was injected. Output signals of conductivity probe as well as pressure probes were acquired with 16 bit PCMCIA card, a laptop computer and dAtagate software (of nCode Inc., UK).

6.2.1.1 Operating Parameters and Procedure

Experiments were performed for two particle sizes (spherical particles of 3 mm and 6 mm diameter). Pressure drop, dynamic liquid holdup and tracer concentration at the outlet were measured for the range of gas (0-0.44 m/s) and liquid (3-10 mm/s) superficial velocities. Before starting of each experiment, air passed through column for 5-6 hr so that complete dry bed conditions are achieved. For non-wetted bed, liquid flow rate was gradually increased and pressure drop and dynamic liquid hold-up were measured. Dynamic liquid hold-up was measured by switching off inlet air and liquid flows and by collecting the drained liquid. At steady state, 20 ml of tracer was injected through the syringe. The injection time was approximately about 3-4 s. The conductivity probe signal was collected online with data acquisition frequency of 100 Hz. Data was acquired for 200 s.

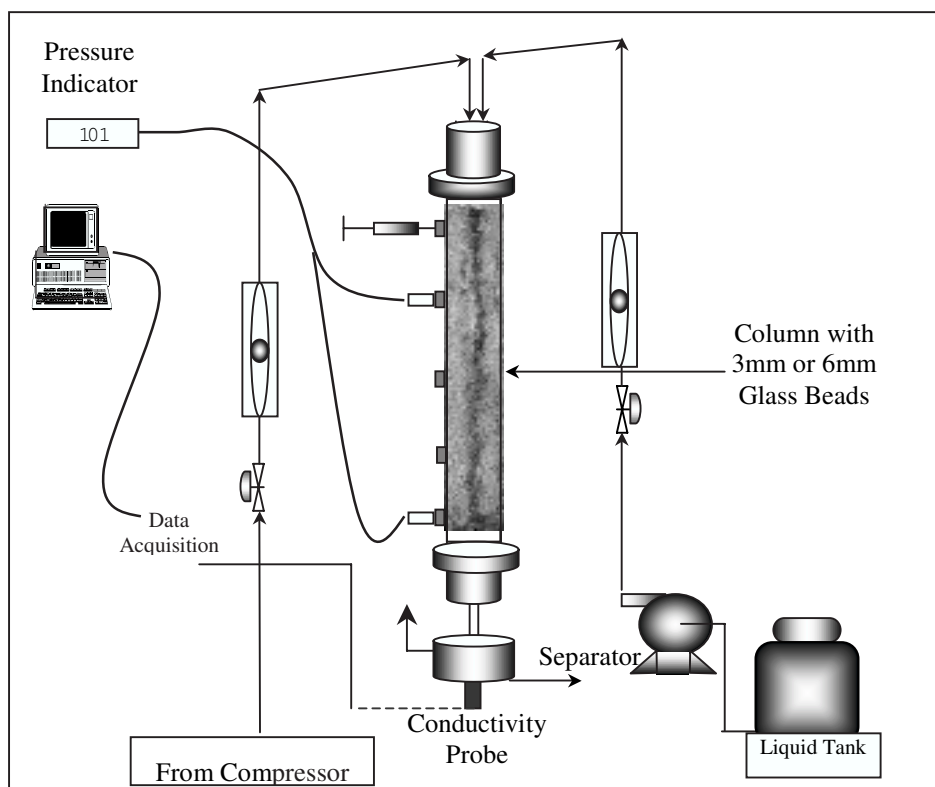


Figure 6.1: Experimental set-up of trickle bed reactor for hydrodynamics and RTD study

6.3 Computational Model for RTD Studies

Simulations were carried out for 3 mm and 6 mm particle diameter. The predicted values of pressure drop and liquid hold-up were compared with experimental data. The values of Ergun's constants E_1 and E_2 were set to 180 and 1.75 for 3 mm diameter particle bed and 500 and 2.4 for 6 mm diameter particle bed respectively. Similar values were used to the particles of 3 mm and 6 mm in the previous studies (see a review of *Holub et. al.*¹¹²). Simulations were carried out with and with out considering the capillary pressure terms. Figure 6.2b shows the contours of the liquid distribution in bed simulated for pre-wetted bed and non pre-wetted bed. Comparison of simulated results and experimental data is shown in Figure 6.3 and 6.4). Unlike experimental data, the simulated results showed much less difference in the pressure drop values obtained for pre-wetted bed and non pre-wetted bed (200 Pa/m). The reasons for this discrepancy are not obvious and need further studies on capillary, wetting and inter-phase closure models. Simulated results of pre-wetted bed were found to be in good agreement with experimental data of pressure drop and total liquid hold-up. The CFD model was therefore extended to simulate mixing and residence time distribution in TBR.

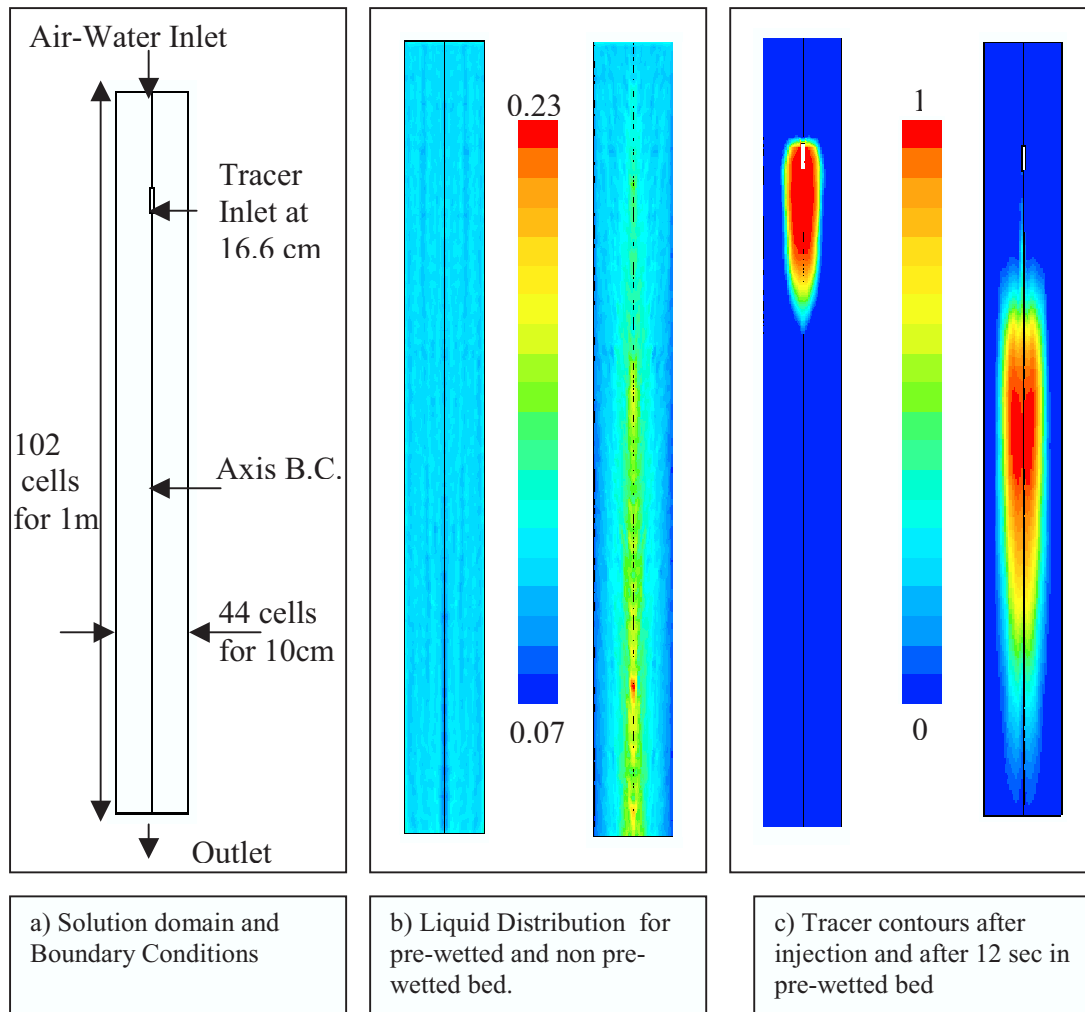


Figure 6.2: Solution domain, liquid volume fraction and tracer mass fraction contours for trickle bed reactor

6.3.1 Experimental Data of Residence Time Distribution

Exit age distribution shows the time history of the tracer flow path through packed bed. Liquid flow in packed bed was affected by severe parameters like liquid distributor, bed interstitial geometry, properties of liquid and capillarity. From the outlet tracer concentration, exit age distribution was calculated as:

$$E(t) = \frac{C_i}{\int_0^{\infty} C_i dt} \dots \dots \dots (6.1)$$

Exit age distribution $E(t)$ of tracer in trickle bed reactor was measured at different operating conditions and plotted as a function of time. Measured values of $E(t)$ for 3 mm particle are shown in Figure 6.5. At low liquid flow rates ($2-3 \text{ kg/m}^2\text{s}$), large variation in $E(t)$ response curve was observed for pre-wetted and non pre-wetted bed. Liquid is more dispersed for pre-wetted bed than non pre-wetted bed (see Figure 6.5). At low liquid flow rate, in non pre-wetted bed, liquid flow was restricted to confined region within the bed and hence exit age distribution shows dominant plug flow characteristics. As liquid flow rate increases, the observed difference in the exit age distributions for pre wetted and non pre-wetted conditions reduces. At high liquid flow rates ($10\text{kg/m}^2\text{s}$), where capillary pressure effect is negligible, $E(t)$ variation is almost path independent. For 6 mm chaparticle bed, at low liquid flow rates liquid dispersion was less compared to 3 mm particle bed. Similar to the pressure drop hysteresis, the difference in the exit age distributions for prewetted and non pre-wetted was less for 6 mm particle bed. Effect of capillary pressure is in 3 mm particle bed is stronger than 6 mm particle bed.

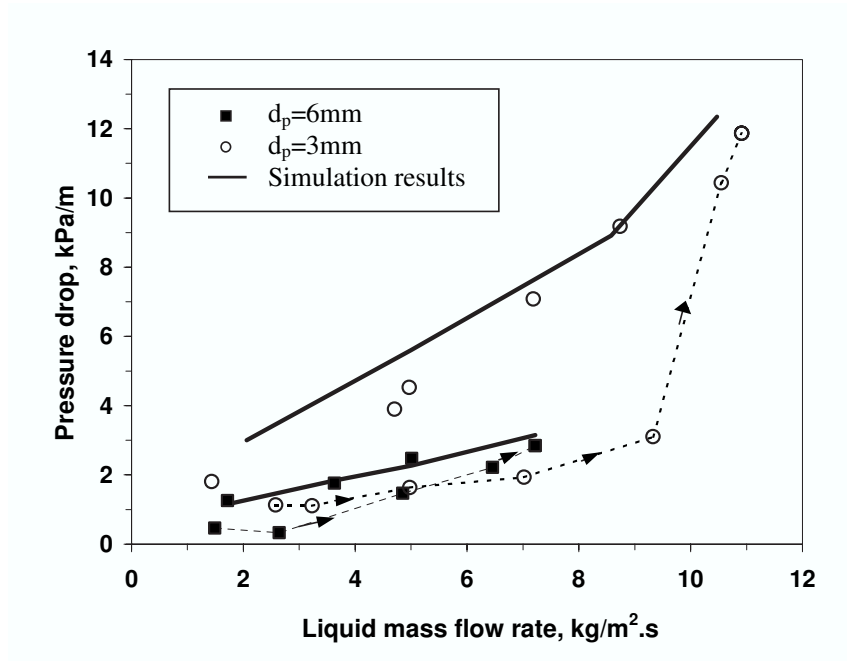


Figure 6.3: Comparison of pressure drop in TBR with simulation results (Operating conditions: $V_G=0.22\text{m/s}$, Std. Dev.=5%)

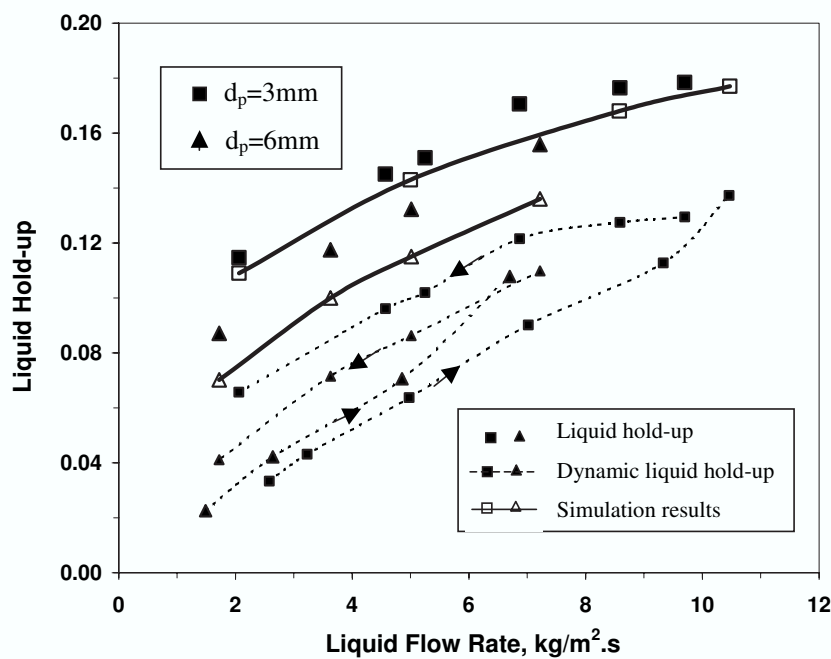


Figure 6.4: Comparison of liquid hold-up in TBR with simulation results (Operating conditions: $V_G=0.22\text{m/s}$, Std. Dev.=5%, $E_1=180$, $E_2=1.75$)

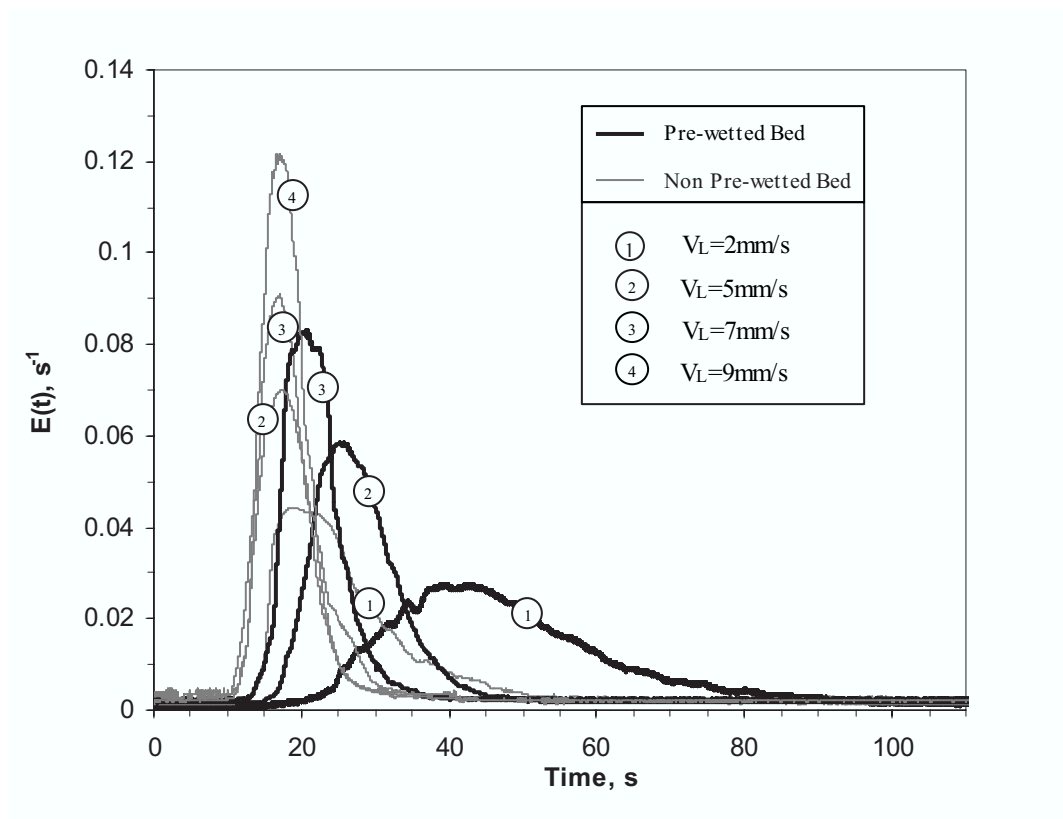


Figure 6.5: Measured residence time distribution in trickle bed reactor for $d_p=3\text{mm}$ and $V_G=0.22\text{m/s}$

6.3.2 CFD Simulations of Tracer Mixing in Trickle Bed

Preliminary simulations were carried out to examine influence of liquid velocity, bed heterogeneity and capillary pressure on liquid dispersion and RTD. Results of these numerical experiments are discussed in the following before the simulated RTD results are compared with the experimental data.

6.3.3 Effect of Bed Heterogeneity on RTD

To understand influence of bed heterogeneity on liquid tracer response in trickle beds, simulations were carried out for beds with different porosity: (a) uniform porosity (b) radially varying porosity according to Equation 5.2 (c) randomized bed porosity with 5% standard deviation super imposed on Equation 5.2 (d) randomized bed porosity with 10% standard deviation super imposed on Equation 1. For case b, transverse velocity component is almost absent and liquid flows vertically downwards. As randomness in porosity increases (std. dev. 5 and 10%), magnitude of liquid phase velocity in transverse direction increases. Tracer simulations of these cases were carried out and simulated RTD response at different bed heterogeneity with the experimental data was compared. It was observed that without inclusion of random porosity in the computational model, simulated RTD shows qualitatively different behavior than that observed in experiments. It is, however, difficult to experimentally measure the extent of bed heterogeneity. The experimentally measured tracer RTD curve falls in between simulated curves obtained with 5% and 10% standard deviation. In absence of quantitative measurement of bed heterogeneity of the trickle bed used in the experiments, all the subsequent simulations were carried out by considering 5% standard deviation.

6.3.4 Effect of Capillarity on Tracer Response

Experimental data of pressure drop and tracer response show that capillary pressure plays a major role in liquid distribution and hydrodynamics of the trickle bed. Most of the industrial trickle bed reactors are operated at low liquid flow rate where non-wetting conditions are most likely to occur. To understand influence of pre-wetting on RTD, simulations of tracer mixing were carried out at pre-wetted conditions (without considering the capillary pressure in the model) and at non pre-wetted bed conditions (with considering the capillary pressure). The simulated results are shown in Figure 6.2b for 3 mm particle size. It can be seen that liquid flow is confined to the central region for the case of non pre-wetted bed unlike the pre-wetted bed, where it is uniformly distributed. Exit age distributions for 3 mm and 6 mm particle beds under pre-wetted and non-prewetted conditions were compared with the experimental data in Figures 6.6 and 6.7 respectively. It can be seen that agreement between simulated results and experimental data is much better for the bed with 6 mm particle than that with 3 mm particle. Capillarity effect is dominant for bed with 3 mm particles. The current models used for capillary effect appear to be unable to capture the microscopic details of wetting and its effect on pressure drop and mixing. Other possible reason for the observed discrepancy may be inadequate accuracy of representing local variation of bed porosity. It should be noted that while assigning the variation of bed porosity, simulations 5% standard deviation was assumed for both, 3 mm and 6 mm particle beds. Particle diameter is likely to affect the degree of heterogeneity of the bed. Unfortunately, quantitative information about such influence is not available at present. Despite some of these issues, it may be said that the agreement between simulated and experimental results is encouraging. The model was therefore extended to examine the possibility of simulating flow and mixing in TBR with non-uniform inlet.

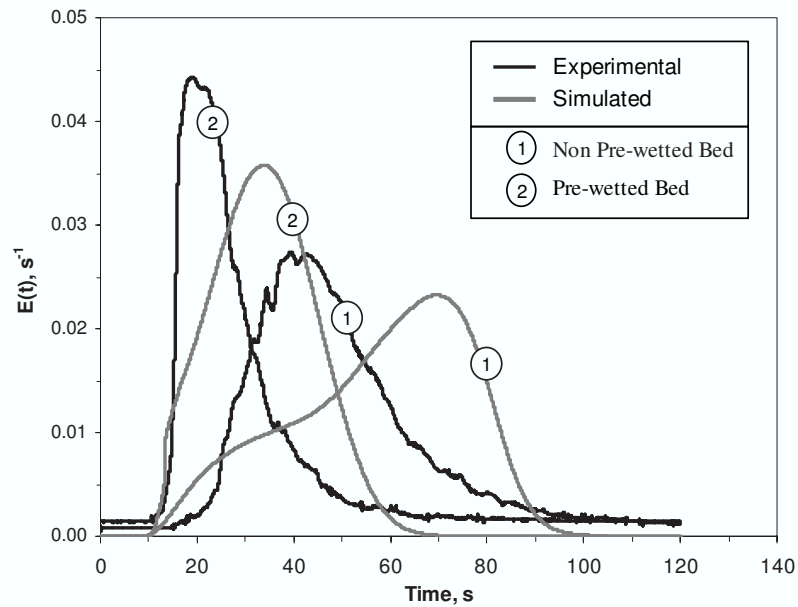


Figure 6.6: Comparison of experimental RTD response with simulated results (Operating conditions: $V_L=2 \text{ kg/m}^2\text{s}$, $V_G=0.22\text{m/s}$, Std. Dev.=5%, $d_p=3\text{mm}$, $E_1=180$, $E_2=1.75$)

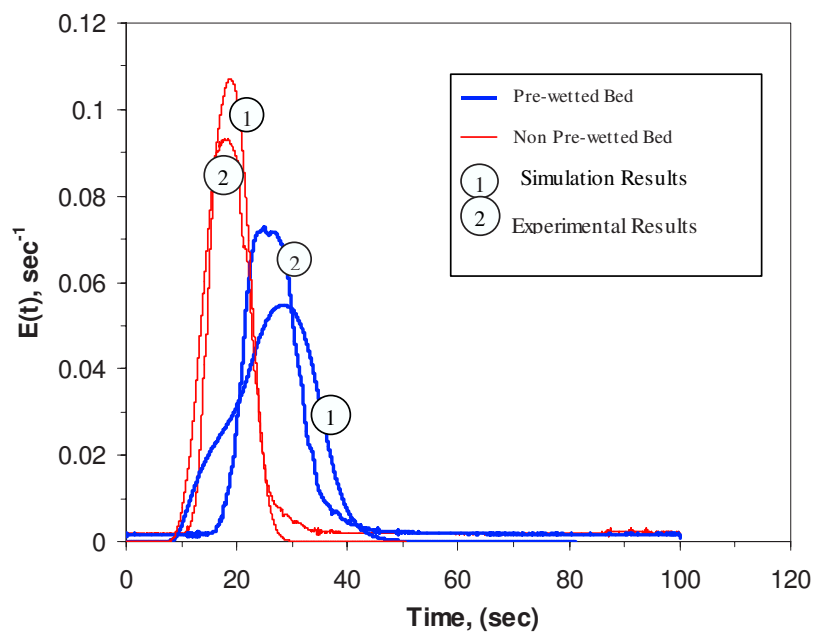


Figure 6.7: Comparison of experimental RTD response with simulated results (Operating conditions: $V_L=1.72 \text{ kg/m}^2\text{s}$, $V_G=0.22 \text{ m/s}$, Std. Dev.=5%, $d_p=6\text{mm}$, $E_1=500$, $E_2=3.4$)

6.3.5 Flow Mal-distribution in TBR

Liquid flow mal-distribution may occur in trickle bed reactors due to several possible reasons like non-uniform liquid distribution at the inlet, local porosity distribution and capillarity action. Previous attempts to study liquid mal-distribution were mainly experimental (for example, *Sapre et al.*¹²⁵). Recently, *Song et al.*¹²⁶ used CFD model to examine mixing in packed beds (with Pall rings). In this work, with the help of CFD model, now it is possible to simulate the tracer path in non-uniform liquid inlet operating condition. As discussed before, the present model incorporates random porosity distribution and capillary terms. For non-uniform liquid inlet, it may be necessary to consider full three-dimensional solution domain. However, before we discuss results obtained with such 3D cases, results of some numerical experiments carried out with two-dimensional domain are discussed to bring out key features of mal-distribution.

Two cases were considered: Case a- liquid enters through an annular region ($r/R > 0.75$) near the wall of the column and Case b- liquid enters through the central region ($r/R < 0.5$) of the column. Simulations were carried out for non pre-wetted bed at liquid flow rate of $2 \text{ kg/m}^2\text{s}$. Simulated results for the 3 mm particle diameter are shown in Figure 7. It can be seen that liquid distribution becomes more uniform when liquid is introduced through the central region (Figure 6.8a (L)) compared to the case with wall inlet (Figure 6.8b(L)). The extent of non-uniformity was found to be larger in the case of 6 mm particle compared to that of 3 mm particle. Contours of the tracer mass fraction at 10 sec after injection are also shown in Figure 6.8 (T). For center inlet flow condition, tracer flows faster through the bed showing plug flow like behavior for both the cases i.e. 3 mm and 6 mm particle sizes. For liquid inlet near wall, tracer contours show prolonged tail since the tracer injection location was in stagnant zone of the bed. Figure 6.9 shows corresponding exit age distribution curves. It can be seen that mean residence time of tracer for the case

of liquid entering through the center is much less than that for the case with the wall inlet. Liquid holdup may vary in this two cases considerably due to wall effect which causes difference in mean residence time. In actual practice, non-symmetric liquid distribution often occurs and hence, it was decided to carry out specific experiments to understand influence of non-uniform liquid inlet.

Rather than selecting symmetric central or annular region, experiments were deliberately carried out with asymmetric liquid inlet. Experiments were carried out by allowing liquid to pass through 25% area of the total inlet (see Figure 6.10a). Experiments were carried out for two tracer injection locations located at 16.6 cm from the top: one at the middle of the inlet region and the second at the column center (as shown in Figure 6.10a). Experimental RTD was measured for both the locations with pre-wetted as well as non pre-wetted bed conditions. Experimental RTD responses at different injection locations are shown in Figure 6.11. It can be seen that, for non pre-wetted bed, mean residence time obtained with in-stream injection (location A) is close to plug flow behavior. This indicates poor liquid dispersion in radial direction due to non pre-wetted condition. Such poor dispersion in radial direction causes a prolonged tail in RTD for the case with off-stream (location B) tracer injection (see Figure 6.11). Contrary to this, for the pre-wetted bed, the injected tracer quickly spreads in radial direction and therefore there is not a significant difference in the tracer response for the pre-wetted and non pre-wetted bed.

It is essential to consider full 3D solution domain to simulate tracer mixing with asymmetric liquid inlet. For the 3D solution domain, random porosity variations along axial and tangential direction were imposed on axially averaged porosity given by Equation 5.2. Figure 6.10a shows the body fitted grid used for the column. Few highly skewed cells were omitted from the domain to avoid the numerical instability. Simulations were carried out for two cases, uniform inlet and non-uniform inlet (liquid entering through 25% of the

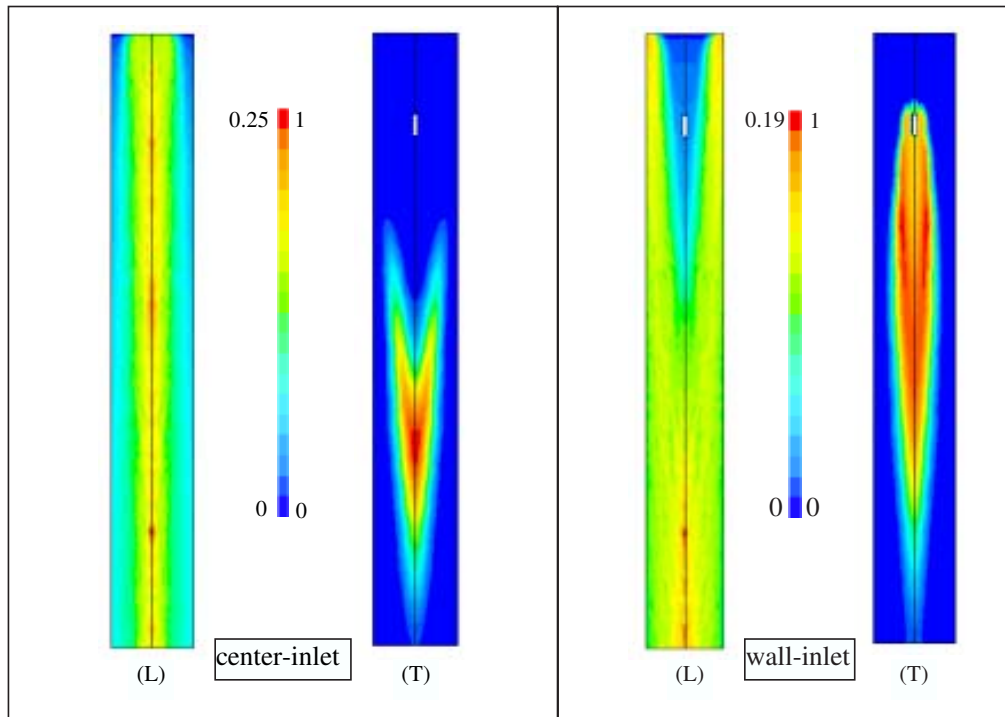


Figure 6.8: Liquid volume fraction and tracer mass fraction for bed with center and wall inlets

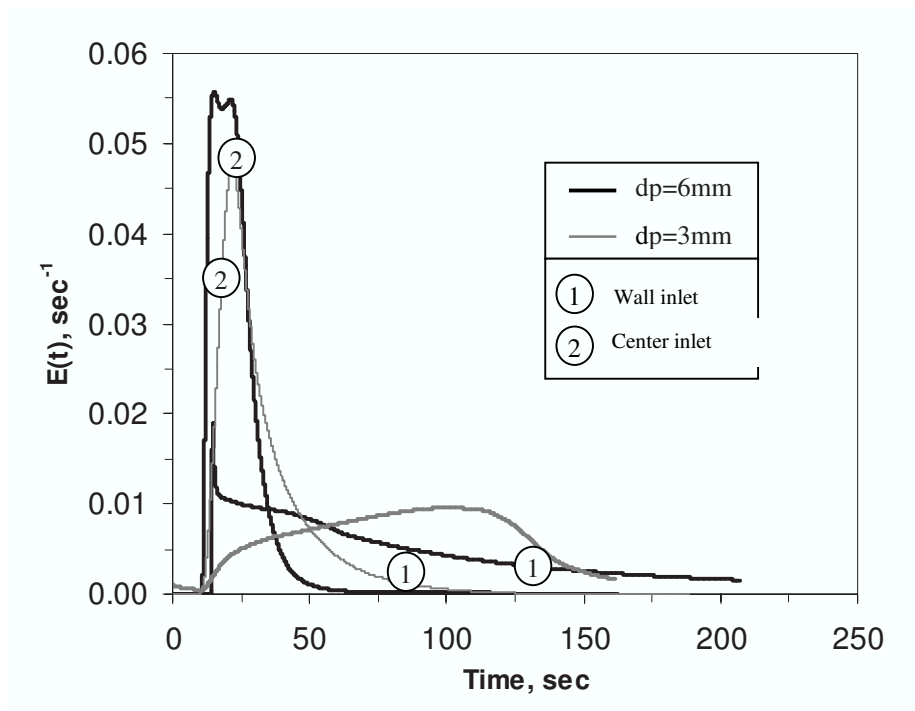


Figure 6.9: Liquid volume fraction and tracer mass fraction for bed with center and wall inlets

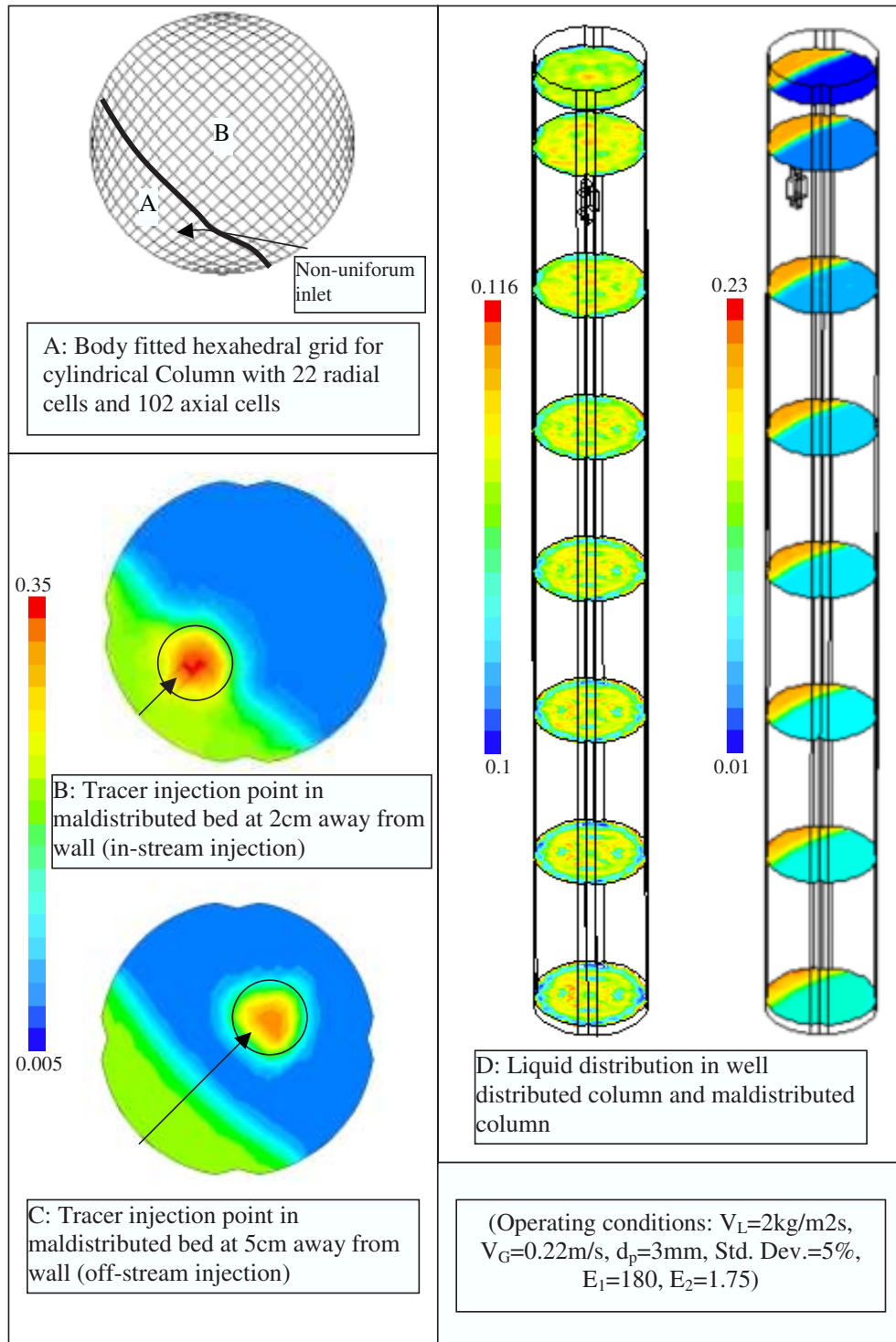


Figure 6.10: 3-D column grid, tracer injection points and liquid volume fraction contours in uniform and non-uniform inlet conditions (Operating conditions: $V_L = 2\text{kg/m}^2\text{s}$, $V_G = 0.22\text{m/s}$, $d_p = 3\text{mm}$, $\text{Std.Dev.} = 5\%$, $E_1 = 180$, $E_2 = 1.75$)

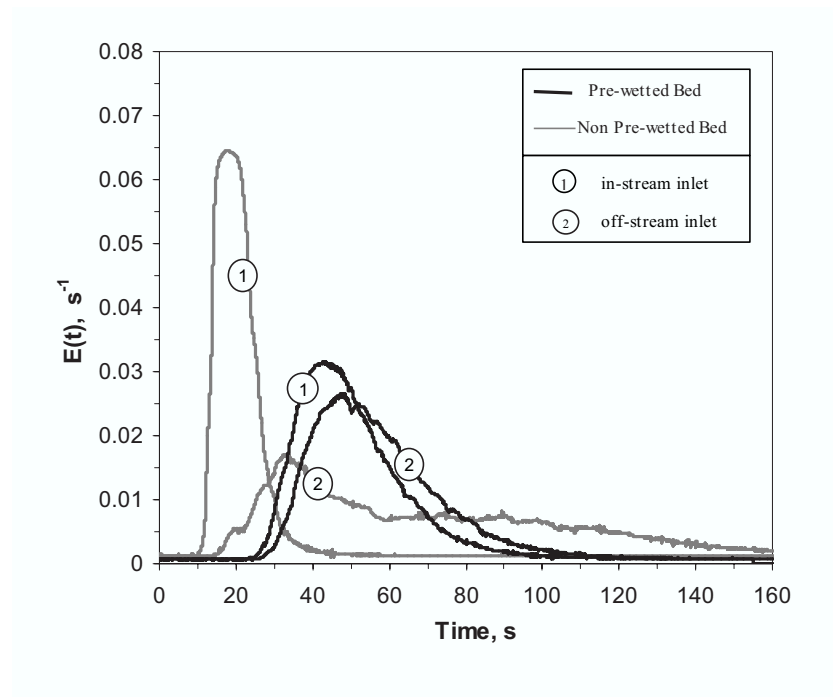


Figure 6.11: Experimental RTD response in pre-wetted and non pre-wetted bed for non-uniform inlet conditions (Operating conditions: $V_L = 2kg/m^2s$, $V_G = 0.22m/s$, $d_p = 3mm$, $Std.Dev. = 5\%$, $E_1 = 180$, $E_2 = 1.75$)

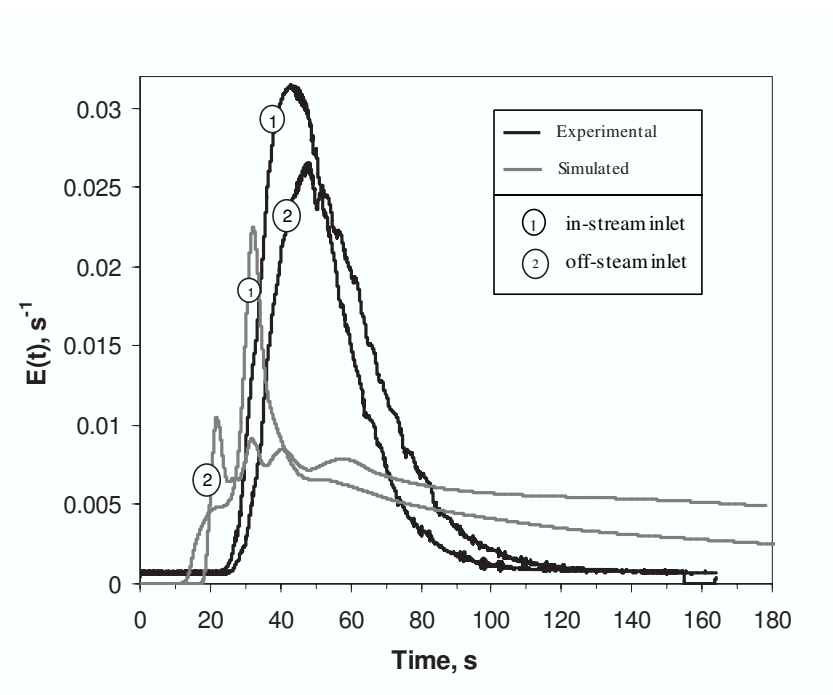


Figure 6.12: Comparison of experimental and simulated RTD with non-uniform inlet (Operating conditions: $V_L = 2kg/m^2s$, $V_G = 0.22m/s$, $d_p = 3mm$, $Std.Dev. = 5\%$, $E_1 = 180$, $E_2 = 1.75$)

column area) for the liquid phase. Uniform air inlet was specified for both of these cases. Tracer mixing simulations were carried out for two-tracer location used in the experiments (locations A and B shown in Figure 6.10a). Contours of predicted tracer mass fraction for the two cases are shown in Figure 6.10b and 6.10c. Corresponding predicted distributions of liquid hold-up are shown in Figure 6.10d. Since the simulations were carried out for pre-wetted bed, non-uniformities in liquid distribution reduce along the length of the column. However, significant non-uniformities were still found to be present even at the column outlet.

The simulated RTD curves for the two tracer injection locations for pre-wetted bed case are shown in Figure 6.12. Experimental data of non-uniform liquid inlet (see Figure 6.11) shows that pre-wetted bed condition improves the liquid distribution considerably. Unlike the experimental results, the simulated results show long tails in the predicted tracer response. These results indicate that the model is predicting very poor radial dispersion than the actual dispersion occurring in the TBR. Poorer radial mixing is very severe for the case of off-stream injection leading to extremely long tail. For this case, the simulations were stopped before the entire tracer came out of the TBR. Inadequate accounting of the variation of bed porosity and the wetting and capillary processes are the most likely reasons for the observed under-prediction of radial dispersion. Further studies on these aspects, especially the role of gradients of liquid volume fraction and radial dispersion of tracer in liquid phase, need to be carried out. The models and results presented here would be useful for such further studies on radial mixing of tracer in trickle beds.

6.4 Conclusion

Liquid distribution and mixing (residence time distribution) in trickle bed reactors was studied using experiments and computational flow model. Different modeling issues such as porosity distribution within the bed, capillary pressure model and grid size were discussed. Present study suggests that capillary pressure (or wetting) has dominant effect on liquid distribution than the porosity distribution. Though current capillary pressure models are unable to quantitatively predict hysteresis in pressure drop, CFD model gives encouraging trends for tracer residence time distribution and liquid mixing in pre-wetted and non pre-wetted beds. CFD model was also able to capture the influence of non-uniform and asymmetric liquid inlet. For asymmetric liquid inlet, simulation results show under prediction of dispersion. Inadequate accounting of the variation of bed porosity and the wetting and capillary processes are the most likely reasons for the observed under-prediction of radial dispersion. The models and results presented here would be useful for further studies on radial mixing of tracer in trickle beds.

“Engineering refers to the practice of organizing the design, construction and operation of any artifice which transforms the physical world around us to meet some recognized need. ”

— GFC Rogers

7

CFD Model for Hydrop-processing in TBR

7.1 Introduction

CFD models and results presented in previous chapters were mainly focused on predictions of hydrodynamic parameters and liquid phase mixing. It is essential to extend the CFD models to include chemical reactions for predicting performance of trickle bed reactors. Though these reactors are simple in operation, hydrodynamics is often a complex function of operating parameters, fluid properties and scale of reactor. The extended CFD models therefore appear to be a promising tool for understanding key issues in scale up and/ or scale down of trickle bed reactors. The models can also be used to improve the performance of the existing reactors. General procedure for scale up of trickle bed reactor is shown schematically in Figure 1. It involves collection of reliable kinetic data for a given catalyst and operating conditions (STEP I shown in Figure 1). For this STEP to be successful, one should ensure that the observed reaction rates in the laboratory reactor are not transport limited. CFD models can prove to be useful to ensure this. More importantly, when this data to be used for scaling up, CFD models can contribute significantly by providing ability to predict interaction of fluid dynamics and chemical reactions. CFD models can account for influence of reactor hardware (particle size, porosity, porosity distribution, wetting characteristics and so on) on fluid dynamics and therefore on overall performance (conversion, selectivity and so on). Because of complex interaction with fluid dynamics and other transport processes, which are scale sensitive, the reaction rate data collected at laboratory scale reactor cannot be directly used to scale-up and to design industrial scale reactors. Often some scale-down experiments need to be designed specifically to understand some of the key issues in large-scale operations. Scaling down is equally complex, if not more. Recent advances in computational fluid dynamics (CFD) show promising results in understanding fluid dynamics and its interactions with chemical reactions, which can bridge the gap between performances observed on laboratory scale reactor and on commercial scale reactor (STEP-II). Previous studies suggest that reactor/particle diam-

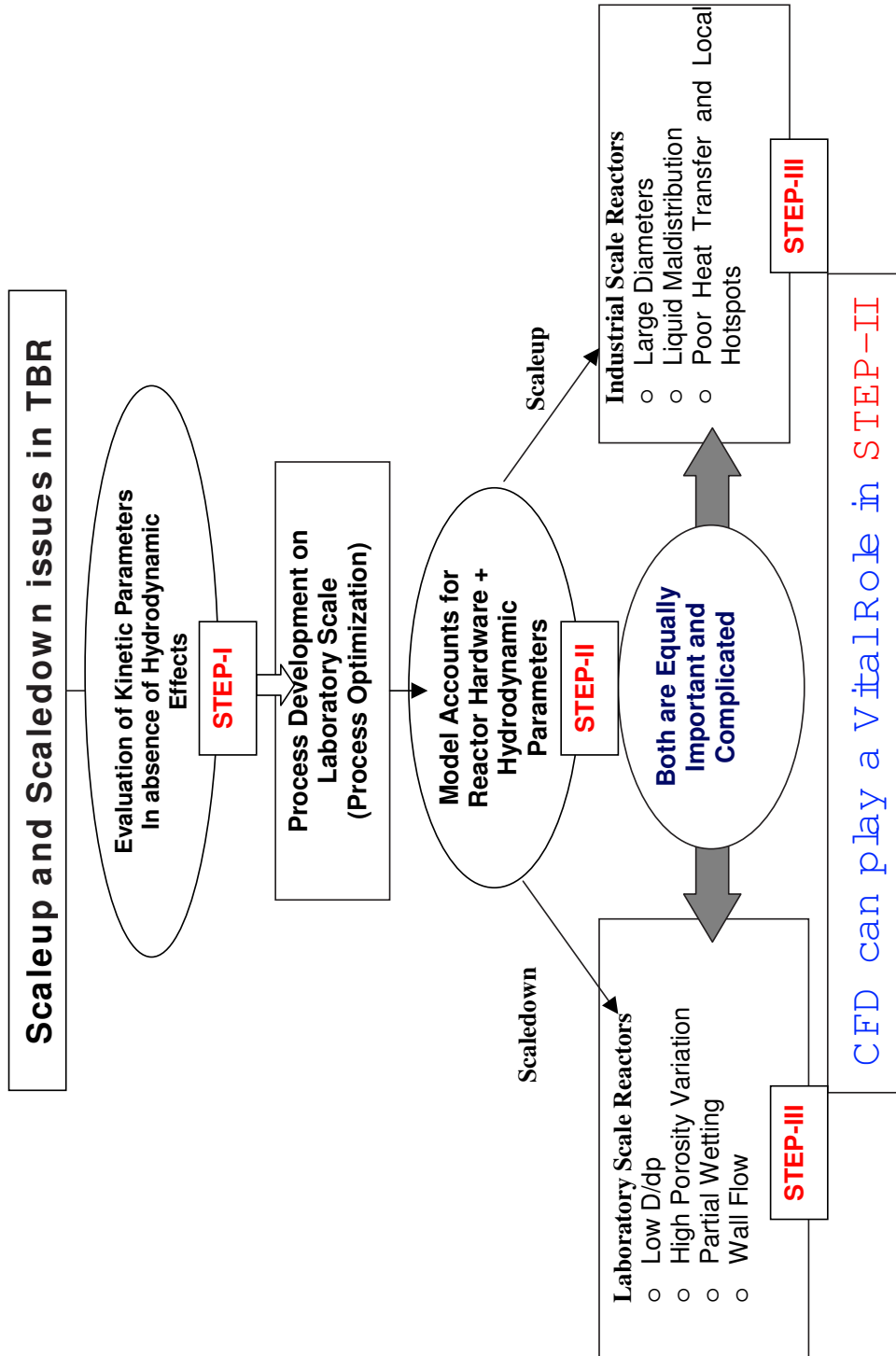


Figure 7.1: Schematic of Scale up and Scale Down Issues of TBR

eter ratio, reactor volume, bed porosity, wetting, channeling and liquid maldistribution, dispersion and isothermal/adiabatic operation are the critical issues which get affected significantly due to the reactor scale (as shown in STEP-III, Figure 1). Typical range of the laboratory and commercial scale reactor parameters is shown Table 7.1. Usually aspect ratio (D/L) of commercial reactor is quite different from that of laboratory scale reactors. Hence superficial gas-liquid velocities in laboratory reactors are much lower than those in commercial reactors. Such lower superficial liquid velocity significantly affects the overall performance and heat and mass rates by erducing wetting efficiencies and increasing dispersion. On the other hand in commercial scale reactors, because of large bed diameters, liquid maldistribution and poor heat transfer rate are the major problems. Column to particle diameter ratio in laboratory reactors are quite low (<50). Hence porosity variation near wall is larger which causes liquid bypassing and different hydrodynamic characteristics. Various issues of scale up or scale down of trickle bed reactors (STEP-III) and the present capabilities of CFD model suggest that CFD models can play a vital role in understanding the scale up and scale down issues of the TBR. Though there are some unresolved issues in applications of CFD models to trickle bed reactors (discussed in previous chapters), it is worthwhile to study how CFD model can help in scale up and scale down of trickle bed reactors. Such an attempt is made here.

Table 7.1: Comparison Between Laboratory Scale and Industrial Scale Reactor Parameters

Reactor Variables	Pilot Reactor	Industrial Reactor
Length, m	0.5-2.0	10-25
Diameter, m	0.5-4	1-4
WHSV, $kg/m^3/h$	2350	2300
G/O Ratio	100-500	100-500
Liquid Superficial Velocity, m/sec	0.0008-0.0025	0.008-0.025
Gas Superficial Velocity, m/sec	0.0148	0.148-22
Dispersion	Significant	Poor
Wetting	0.1-0.6	0.6-1
Mal-distribution	Significant	Significant
Wall effect	Considerable	Negligible

7.1.1 Previous Work

Most of the previous work on scale up was limited to the study of trickle bed reactors kinetics and issues related with it. The scale up procedure in most of these studies involves assumption of plug flow (see for example, *Henry and Gilbert*¹²⁷, *Iannibello et al.*¹²⁸, *Skala et al.*^{{? Skala1991, Froment et al.}¹²⁹ and *Tsamatsoulis et al.*^{Tsamatsoulis1995}) and pseudohomogeneous first order kinetics. Effects of hydrodynamics on rate parameters are often neglected. *Korsten and Hoffman*¹³⁰ have developed a detailed three-phase model for trickle bed reactor for hydrodesulfurization of vacuum gas oil. This model accounts for gas-liquid and liquid-solid mass transfer and Langmuir-Hinshelwood type kinetics. The model was used to predict the performance of the pilot scale experimental results. However, this model was not tested for scale up studies.

Recently several attempts were made to develop plug flow model for trickle bed reactors. Different issues of trickle bed reactor modeling were raised in such studies. *Chen et al.*¹³¹ have simulated hydro-processing reactor using a 2d model, which accounts for spatial variation of temperature. However effects of porosity distribution and local velocity variation

were neglected in this model. *Chowdhury et al.*¹⁶ studied modeling of hydrodesulfurization and hydrogenation of aromatic compounds of diesel. Detailed kinetic parameters were evaluated using laboratory scale reactors. Isothermal plug flow model was developed to simulate the performance of the reactor. However, applicability of this model to commercial reactor was not studied. *Pedernera et al.*¹³² have studied performance of laboratory scale reactor using kinetic model developed by *Chowdhury et al.*¹⁶. Wetting efficiency and liquid holdup data were measured using MRI, which could be useful for improving model predictions. *Avraam et al.*¹³³ have developed axial dispersed plug flow model for hydroprocessing of light oil feed stock. Even though model has considered detailed kinetic parameters and appropriate energy and mass balance over reactor, model has to rely on empirical correlations for holdups, pressure drop and wetting efficiency.

Although previous studies were focused on development of models for hydroprocessing units, very few attempts were made to extend these models to simulate performance of commercial reactor or to understand issues related to scale up and scale down. Recently *Rodriguez and Ancheyta*¹³⁴ have studied performance of laboratory and commercial scale reactor using plug flow model for the case of hydroprocessing of vacuum gas oil. In this study, they found that performance of commercial scale reactor is better than that of laboratory scale reactor. Incomplete wetting and isothermal operation may lead to lower performance than commercial reactor. *Bhaskar et al.*¹³⁵ has studied performance of hydroprocessing reactors using experiments as well as modeling. Their study also indicates that simulated performance of industrial scale reactor is better than that of experimental data obtained with laboratory scale. However detailed analysis of issues related to scale-up and scale-down was not attempted. Recently CFD based models showed promising results in predicting hydrodynamic parameters of trickle bed reactors (*Jiang et al.*¹³, *Gunjal et al.*^{47, 124}). However, applicability of these models for simulating performance of hydroprocessing reactors was not studied/demonstrated. *Jiang et al.*¹³⁶ have studied scale down

issues of trickle bed reactors using CFD model. However, this study has not been applied to any actual reactor.

In light of this brief review of previous work, we have attempted to extend and to use CFD model for prediction of performance of hydroprocessing reactors with emphasis on understanding issues related to scale up and scale down trickle bed reactors. For this purpose, computational flow models were developed for laboratory scale and commercial scale reactors. Detailed variation of porosity and inter-phase interaction of flowing fluids were accounted in the model. Operating conditions and details of reactor specifications were considered from the published experimental data of *Chowdhury et al.*¹⁶ and *Bhaskar et al.*¹³⁵. In the hydroprocessing system, reactions involving hydrogenation of aromatic and sulfur compound were considered and their kinetics parameters were taken from the studies of *Chowdhury et al.*¹⁶. For the laboratory scale reactor, numerical experiments were carried out to investigate the sensitivity of the model parameters such as porosity distribution and effect of grid size. Simulations were then carried out to study the effect of operating temperature (593-653 K), pressure (20-80 MPa), LHSV (1-5 h^{-1}) and initial H_2S (1.0-2.5 %) concentration. Predicted results were compared with the experimental data. Model was then used to simulate performance of the commercial hydro-processing unit. Study carried out here will be useful for exploring the advantages of CFD model for understanding scale up and scale down issues of the trickle bed reactors.

7.2 Applying CFD Model for Hydroprocessing Reactor

In hydroprocessing reactor, various reactions occur: some are desired reactions and some are not. Hydrodesulfurization, hydroaromatization and hydrogenation of olefins are the desired reactions, whereas hydrocracking and coking are undesired reactions. Here in this case

study, we have considered major reactions such as hydrodesulfurization and hydrodearomatization reactions in the model and other minor reactions were neglected (see *Chowdhury et al.*¹⁶ and *Bhaskar et al.*¹³⁵). Reactor configuration and operating conditions were similar to that of (see *Chowdhury et al.*¹⁶) Model equations were written based on the following assumptions. Assumptions:

1. Pressure remains constant (pressure drop is insignificant compared to the operating pressure).
2. Trickle bed reactor is operated isothermally (efficient heat transfer)
3. Ideal gas law is applicable.
4. Liquid phase reactants are non-volatile (negligible vapor pressure).
5. Gas-liquid mass transfer is the limiting resistance.
6. The catalyst particles are completely wetted.

The following reactions were considered in this work:



Rate expression for these reactions is given by

$$k_{ij}^E = k_{ij,0} e^{-(E_{ij}/T)(1/T-1/T_0)} \dots \dots \dots (7.5)$$

$$r_{Poly} = -k_{Poly}C_{Poly} + k_{-Poly}C_{Di} \dots \dots \dots (7.6)$$

$$r_{HDS} = \frac{kC_{L,H_2}^{0.56} C_{L,S}^{1.6}}{1 + K_{ad}C_{L,H_2S}} \dots \dots \dots (7.7)$$

$$r_{Mono} = -k_{mono}C_{mono} + k_{-Mono}C_{Naph} \dots \dots \dots (7.8)$$

$$r_{Di} = -k_{Di}C_{Di} + k_{-Di}C_{Mono} \dots \dots \dots (7.9)$$

where, r is the rate of reaction in *kmol/kg.sec*, C is concentration of reactant in *kmol/m³* and k is the rate constant. Kinetic parameters for above reactions are listed in Table 7.3.

Table 7.2: Comparison Between Laboratory Scale and Industrial Scale Reactor Parameters

Oil Properties	Details
Oil Density, <i>kg/m³</i>	865
Ar-S %	1.67
Poly-Ar %	2.59
Di-Ar %	8.77
Mono-Ar %	17.96
Naphthenes	19.25

Table 7.3: Kinetic Parameters for Hydroprocessing Reactions

Kinetic Parameters	Values
$K_{AD}, m^3/kmol$	50000
$K, Dimensionless$	$2.5 \times 10^{12} e^{(-19384/T)}$
$k_{mono}^*, m^3/kg.s$	$6.04 \times 10^2 e^{(-12414/T)}$
$k_{Di}^*, m^3/kg.s$	$8.5 \times 10^2 e^{(-12140/T)}$
$k_{Poly}^*, m^3/kg.s$	$2.66 \times 10^5 e^{(-15170/T)}$

A 2d CFD model was first developed for the laboratory as well as commercial scale reactor. In this model axial and radial porosity distribution was accounted within the bed (details of porosity implementation in CFD model is given in Chapter 5). Mass and momentum balance equations for each phase and its solution procedure are described in Section 5.2 of Chapter 5. Using the CFD model, gas-liquid flow inside the TBR was simulated. The predicted flow field (velocities and volume fractions of different phases) was further used for solving species transport equations for simulating hydroprocessing reactor. These equations are discussed in the following. Mass balance equations for each i^{th} species was written as:

$$\frac{\partial \epsilon_k \rho_k C_{k,i}}{\partial t} + \epsilon_k \rho_k U_k C_{k,i} = - \epsilon_k \rho_k D_{i,m} \dot{C}_{k,i} + \epsilon_k \rho_k S_{i,k} \dots \dots \dots (7.10)$$

where, C_i , k is the concentration of species in k_{th} fluid, r_k and ϵ_k is the density and volume fraction of the k_{th} fluid respectively. S_i is the source for addition or consumption of i^{th} species from k_{th} fluid.

Volume averaged properties of fluid were used for calculating fluxes across the control cell. Two-film theory was used for accounting mass transfer. The resistance in gas-liquid film was considered as the rate limiting resistance.

The source term for species i in gas phase can be written as:

$$S_{i,G} = -K_{GLi}a_{GL} \left[\frac{C_{Gi}}{H_i} - C_{Li} \right] \dots \dots \dots (7.11)$$

The corresponding source term for specis i in liquid phase may be written as,

$$S_{i,L} = K_{GLi}a_{GL} \left[\frac{C_{Gi}}{H_i} - C_{Li} \right] + \rho_B \eta \sum_{j=1}^{j=nr} r_{ij} \dots \dots \dots (7.12)$$

where, r is the rate of reaction in kmol/kg.sec, nr is the number of reactions and ρ_B is catalyst bulk density, kg/m^3 , η is wetting efficiency.

For non-volatile species in liquid phase, because of negligible liquid solid mass transfer resistance and fast diffusion, source term becomes,

$$S_{i,L} = \rho_B \eta \sum_{j=1}^{j=nr} r_{ij} \dots \dots \dots (7.13)$$

Variation of Oil Density with temperature and pressure was calculated using the Standing-Katz correlation as presented in *Ahmed*¹³⁷.

$$\rho_{L(P,T)} = \rho_{o,L} + \Delta\rho_{p,L} - \Delta\rho_{T,L} \dots \dots \dots (7.14)$$

$$\Delta\rho_{(P,L)} = [0.167 + 16.181 \times 10^{0.425\rho_{o,L}}] \times \left[\frac{P}{1000} \right] - 0.01 \times [0.299 + 263 \times 10^{-0.0603 \times \rho_{o,L}}] \times \left[\frac{P}{1000} \right]^2$$

$$\Delta\rho_{T,L} = [0.0133 + 152.4 \times (\rho_{o,L} + \Delta\rho_{P,L})^{-2.45}] \times [T - 520] - [8.1 \times 10^{-6} - 0.0622 \times 10^{-0.764 \times (\rho_{o,L} + \Delta\rho_{P,L})}] \times [T - 520]^2$$

ρ_o is the density at standard conditions (15.6; 101.3 kPa) in lb/ft^3

P is pressure in psia. T is the temperature in $^{\circ}R$ Oil Viscosity can be calculated from the following equation due to Glasso, as published in *Ahmed*¹³⁷ In terms of API gravity this equation gives viscosity in mPa s, with temperatureis given in $^{\circ}R$,

$$\mu = 3.141 \times 10^{10} \times (T - 460)^{-3.444} \times [Log_{10}(API)]^a \dots \dots \dots (7.15)$$

where,

$$a = 10.313 \times [log_{10}(T - 460)] - 36.447 \dots \dots \dots (7.16)$$

Viscosity of Hydrogen was taken from the literature. Density of Hydrogen under process conditions was calculated from Ideal Gas Law. Mass Transfer Coefficients was calculated using the following correlation by *Goto and Smith*¹³⁸.

$$\frac{k_i^L a_L}{D_i L} = \alpha_i \frac{G_L}{\mu_L}^{\alpha_2} \dots \dots \dots (7.17)$$

Henry’s constant can be calculated from the following equation as published in *Korsten and Hoffman*¹³⁰

$$H_i = \frac{\nu_N}{\lambda_i \rho_L} \dots \dots \dots (7.18)$$

where ν_N is the molar gas volume in cc per mole. λ_i is the solubility and ρ_L is the density of oil in grams per cubic cm under process conditions and ρ_{20} is the density at 293 K. The solubility of hydrogen is given as (*Korsten and Hoffman*¹³⁰)

$$\lambda_{H_2} = a_0 + a_1T + a_2\frac{T}{\rho_{20}} + a_3T^2 + a_4\frac{1}{\rho_{20}^2} \dots \dots \dots (7.19)$$

where,

$$a_0 = -0.559729, a_1 = -0.42947 \times 10^{-3}, a_2 = -3.07539 \times 10^{-3}, a_3 = 1.94593 \times 10^{-6}, a_4 = -0.835783$$

The solubility of hydrogen sulfide is given by the following equation. T is in °C.

$$\lambda_{H_2S} = e^{(3.3670 - 0.008470 \times T)} \dots \dots \dots (7.20)$$

Throughputs and operating conditions for laboratory and commercial scale reactor are given in Table 7.4. Details of boundary conditions for CFD model are discussed in Section 5.3 of Chapter 5. For species transport equation, it was assumed that gas and liquid enter at reactor operating temperature and pressure. Gas and liquid inlet concentrations are listed in Table 7.2. For a given LHSV and flow rate ratio (Q_G/Q_L), superficial velocity for gas and liquid was calculated and assigned as normal velocity boundary condition in the CFD model. The model equations were solved using FLUENT without considering any reactions (following procedure similar to that discussed in Chapter 5). The converged steady state solution (flow field and volume fractions of all the phases) was used as a starting point for solution of species balance equations. The flow field was assumed to be insignificantly affected by chemical reactions. Therefore, momentum equations were not solved while solving species balance equations. It was ensured that obtained simulated results were

Table 7.4: Comparison Between Laboratory Scale and Industrial Scale Reactor Parameters

Parameters	Laboratory Scale Reactor	Commercial Scale Reactor
Reactor Diameter, m	0.019	1.9
Bed Length, m	0.5	8
Particle Diameter, m	0.0024	0.0015
Bed Porosity	0.50	0.36
LHSV, h^{-1}	1-5	1-5
Operating Pressure, MPa	20-80	22-88
Operating Temperature, K	573-653	573-673
Initial H_2S Conc., v/v %	0.5-8	0.5-8

numerical error free by providing enough number of grid points and use of higher order discretization schemes (QUICK). Simulated results of CFD model and hydroprocessing reactor performance at laboratory scale and commercial scale reactors are discussed in the following.

7.3 Results and Discussion

For studying performance of laboratory and commercial scale reactor performance, we have considered two different cases. In laboratory scale reactor study, system similar to

*Chowdhury et al.*¹⁶ has considered. Experimental setup and operating parameters details are given in Figure 7.2 and Table 1 (for more details refer *Chowdhury et al.*¹⁶). For industrial scale reactor, reactor geometry and operating parameters were considered from the industrial operating cases given by *Bhaskar et al.*¹³⁵. Details of reactor configuration and operating parameters for commercial scale reactor are given in Table 2. First we have developed 2d CFD model for laboratory scale reactor in which details axial and radial porosity distribution is considered (for more details about CFD model, refer *Gunjal et al.*¹²⁴). Knowledge of velocity and phase distribution inside the reactor was used as base model for reaction engineering model. Three phase heterogeneous model for hydroprocessing reaction (as reported earlier) was used to predict the performance of the laboratory as well as commercial scale reactor performance. Effect of reactor scale on hydrodynamic parameters and its implications on performance of reactor is discussed in following sections.

7.3.1 Performance of Laboratory Scale Reactor

In laboratory scale reactor, hydrodesulfurization and hydrogenation of aromatic compounds were considered. Variation of equilibrium constants for aromatic compounds was plotted in Figure 7.3. Equilibrium constant for polyaromatic compound variation is flat as compared with mono and di-aromatic compound. For lower temperature (<613 K) $K_{poly} > K_{di} < K_{mono}$ and at high temperature (>613 K) order is reverse. Conversion of aromatics sulfur compound at different reactor operating temperature is plotted in Figure 7.4. In order to study the sensitivity of the porosity assigned in computational model, simulations were carried out using uniform porosity and in another case axial and radial variation of porosity with 5% std. dev. about mean porosity. Results indicate that conversion of aromatic sulfur compound is higher in uniform porosity case (about 15%). These results indicate that appropriate porosity distribution is needed to account for laboratory

scale reaction, as variation of porosity near wall is large. Effect of porosity distribution on velocity is discussed in next section.

Effect of initial concentration of H_2S on conversion of aromatic sulfur compound is plotted in Figure 7.5. It can be seen from the graph, model results over predict results for lower values of initial H_2S concentration and under predicts for higher values of initial concentration of H_2S . Observed discrepancy in results may be due to at lower initial H_2S concentration, rate inhibition due to H_2S absorption may not be dominant but however at higher initial concentration of H_2S due rate inhibition (Langmuir type kinetic expression) causes lower conversion. Obvious question is why this not observed in plug flow model results of *Chowdhury et al.*¹⁶. One thing noted in this case is, in CFD model detailed variation of porosity, hence liquid bypass as wall effects were well considered in CFD compared with conversional modeling approach. However wetting efficiency in laboratory scale reactor is quite low which has not been considered in model yet. Hence higher rate of inhibition at high initial concentration H_2S may be expected from CFD model predictions.

Simulated results of conversion of aromatic hydrocarbons are plotted in Figure 7.6 (poly- and total-aromatics) and in Figure 5b (mono- and di-aromatics). It can be seen from the plotted results that model over predicts when compared with the experimental data. Variation of predicted conversion of all aromatic compounds with LHSV is shown in Figure 7.7. In this results, model over predict the conversion of aromatic compound. This indicates that when one account effect of porosity distribution, model predictions are higher than that of conversional 1d model. As discussed earlier, one need to account for wetting efficiency, which is quite low in laboratory reactors. In the study of *Pedernera et al.*¹³², using MRI experiments, it has been shown that wetting efficiency varies from 0.14 to 0.4 for laboratory scale reactors. Operating parameters and reaction conditions are of *Chowdhury et al.*¹⁶ and *Pedernera et al.*¹³² are relatively similar. Hence it is important to

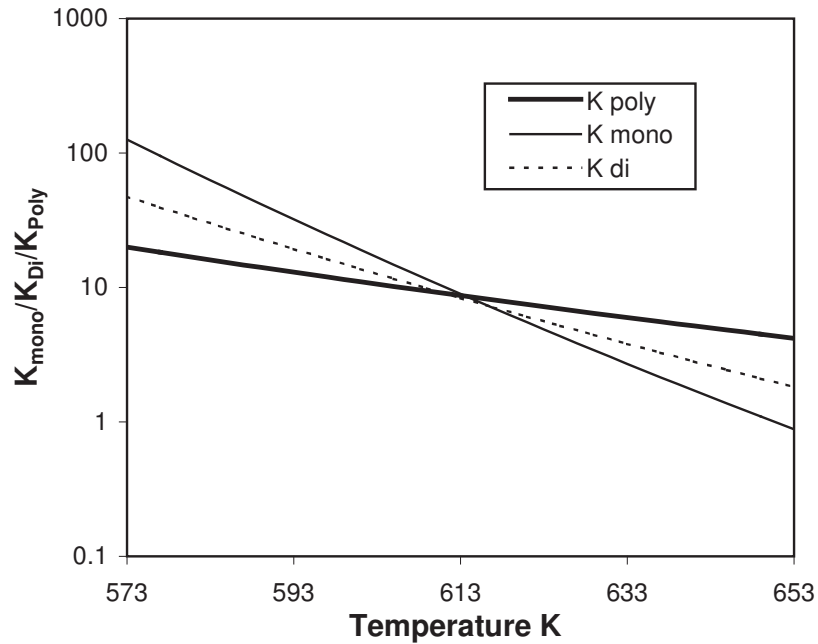


Figure 7.2: Variation of Equilibrium Constants for hydrogenation of mono-, di- and poly aromatics with Temperature.

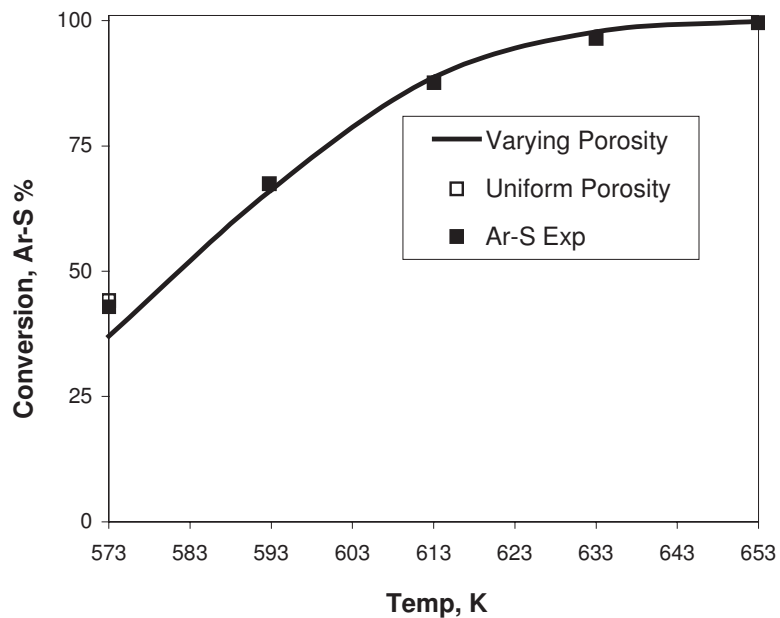


Figure 7.3: Comparison of Simulated results of conversion of Aromatic Sulfur Compounds with the Experimental Data at different Temperature. ($P=4$ MPa, $LHSV=2.0$ h^{-1} , $Q_G/Q_L=200$ m^3/m^3 , $y_{H_2S}=1.4\%$)

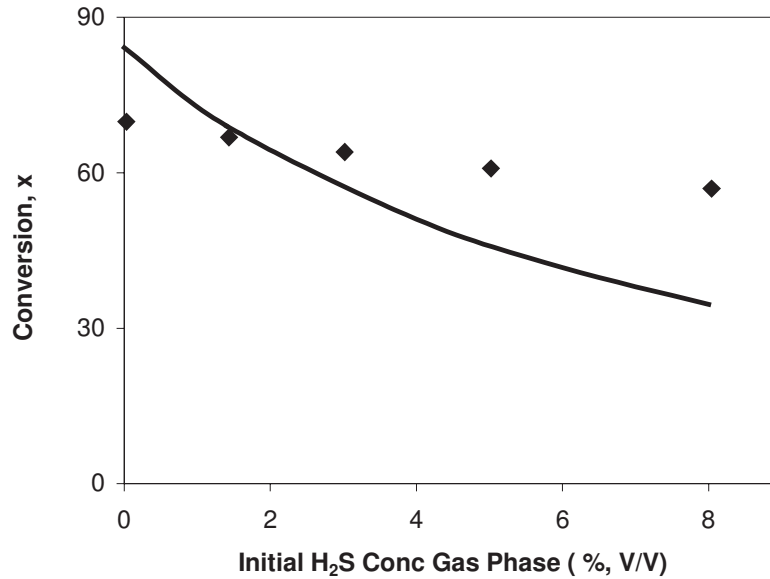


Figure 7.4: Comparison of Simulated Results of Effect of Initial Sulfur Compound on Conversion with the Experimental Data. (P=4 MPa, LHSV=2.0 h^{-1} , $Q_G/Q_L=200 m^3/m^3$, $T_R=320^\circ C$)

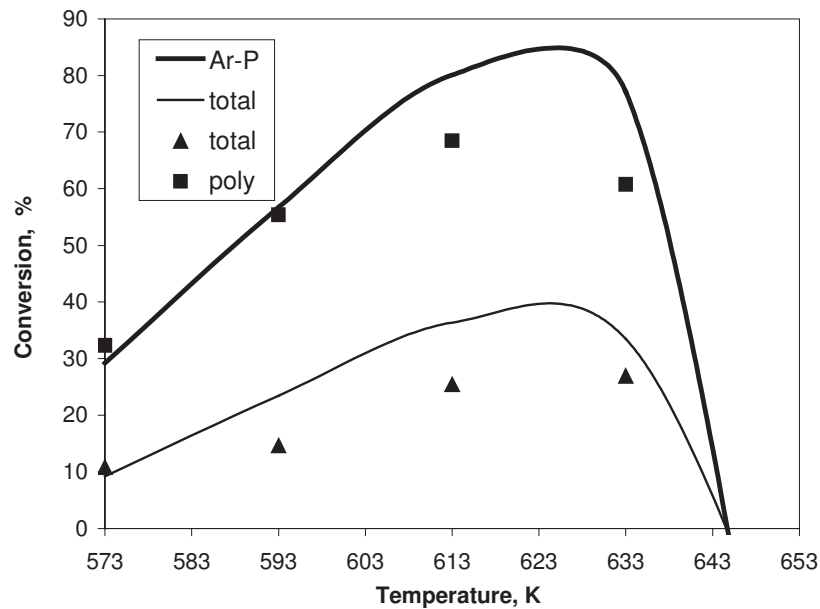


Figure 7.5: Comparison of Simulated and Experimental conversion of Poly-aromatics and Total-Aromatics at different Temperature. (P=4 MPa, LHSV=2.0 h^{-1} , $Q_G/Q_L=200 m^3/m^3$, $y_{H_2S}=1.4\%$)

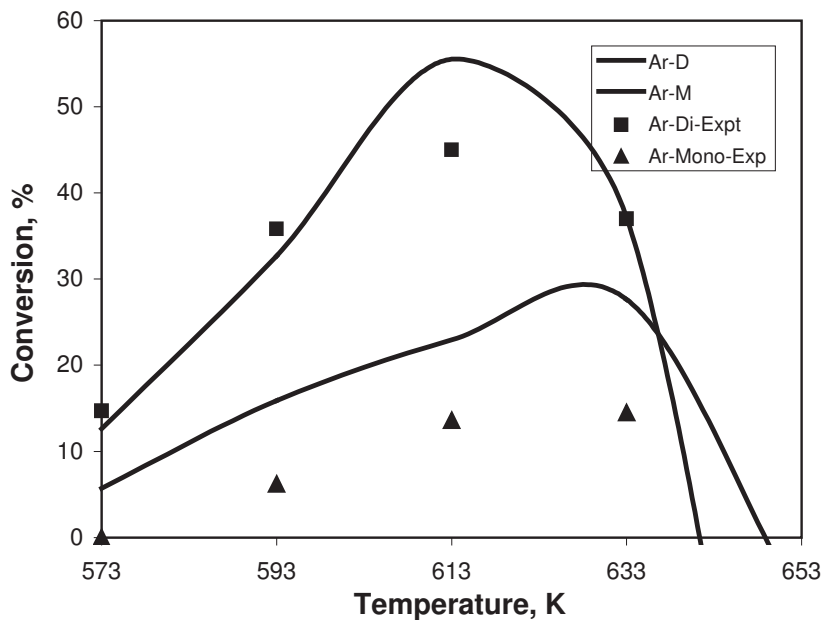


Figure 7.6: Comparison of Simulated and Experimental conversion of Mono- and Diaromatics at different Temperature. ($P=4$ MPa, $LHSV=2.0$ h^{-1} , $Q_G/Q_L=200$ m^3/m^3 , $y_{H_2S}=1.4\%$)

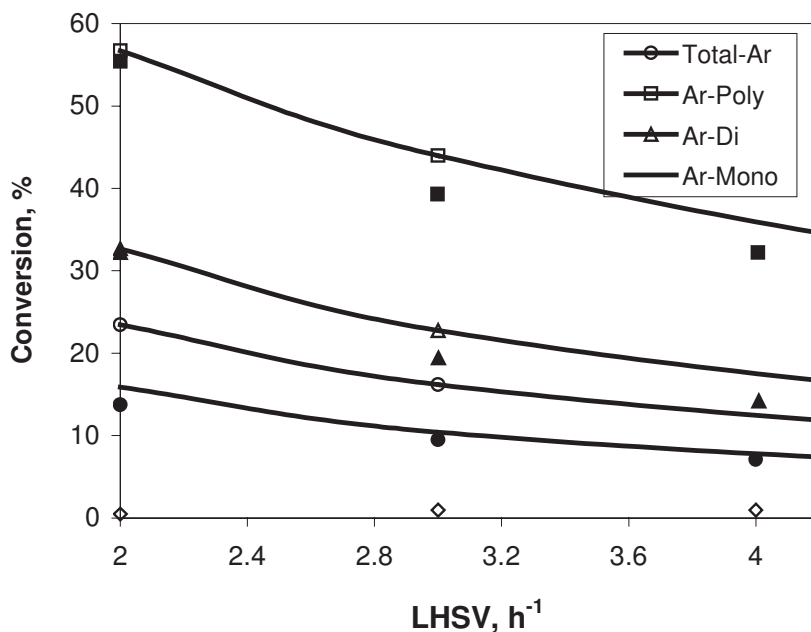


Figure 7.7: Comparison of Simulated and Experimental results of conversion of all aromatics Compounds at different LHSV. ($P=4$ MPa, $LHSV=2.0$ h^{-1} , $Q_G/Q_L=200$ m^3/m^3 , $y_{H_2S}=1.4\%$)

consider the effect of wetting in model. Present CFD model is further extended to predict the performance of the commercial reactor. Before evaluating performance of commercial reactor, predicted variation of the hydrodynamic quantities in commercial and laboratory reactors are discussed in following section.

7.3.2 Comparison of Laboratory and Commercial Scale Reactor

7.3.2.1 Hydrodynamic Parameters

Hydrodynamics parameters of trickle bed reactors were obtained from CFD simulations of laboratory scale reactors and commercial scale reactor. Porosity distribution in laboratory scale reactor is quite different from commercial scale reactor. In Figure 7.8, solid phase distribution is plotted along radial direction from the axis of column. Due to low D/d_p ratio (7), variation of porosity near wall is quite higher, which oscillates even at the center of the column. Predicted liquid phase velocity profiles in radial direction are shown in Figure 7.8. It can be seen from figure velocity profile also shows oscillatory behavior due to porosity variation. In commercial reactor, however, fluctuations in solid holdup are quite low (see Figure 7.9) as compared with laboratory scale reactors. Ratio of local solid fraction to average solid fraction in laboratory reactors varies from 0.8 to 1.4, however for commercial reactor this variation is negligible. Ratio of interstitial velocities to superficial velocity for laboratory.

Predicted average pressure drop per unit length and liquid holdup for laboratory reactor is plotted in Figure 7.10. Predicted pressure drop per unit length is in the order of few Pascal and liquid holdup varies from 0.02 to 0.07 for 1-8 h^{-1} variation in LHSV. For similar experimental setup, *Pedernera et al.*¹³² has found that liquid holdup varies from 0.04 to

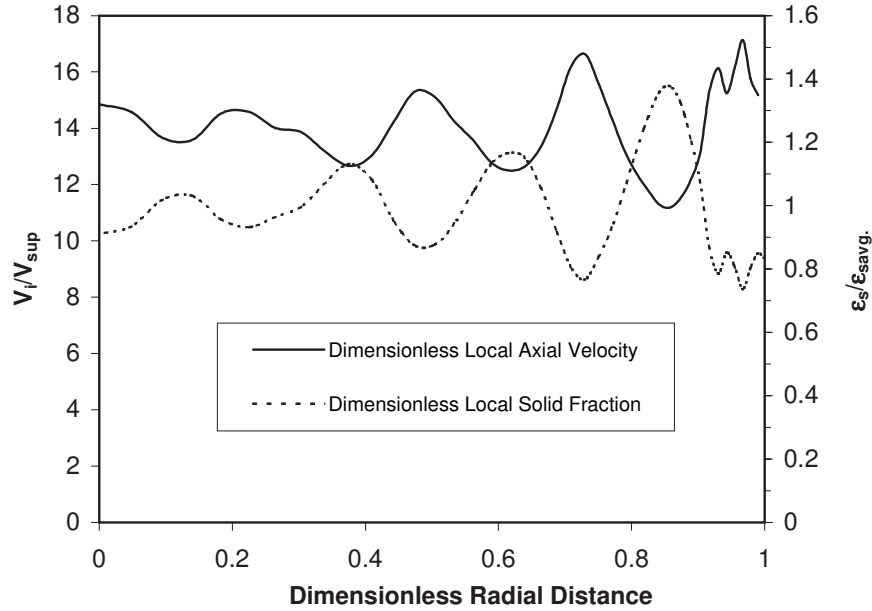


Figure 7.8: Variation of Solid Volume Fraction in Radial Direction and Predicted Results of Velocity Distribution along Radial Direction for Laboratory Scale Reaction. ($D_R=0.019\text{m}$, $\epsilon_B=0.5$, $\text{LHSV}=2\text{ h}^{-1}$ and $Q_G/Q_L=200\text{ m}^3/\text{m}^3$)

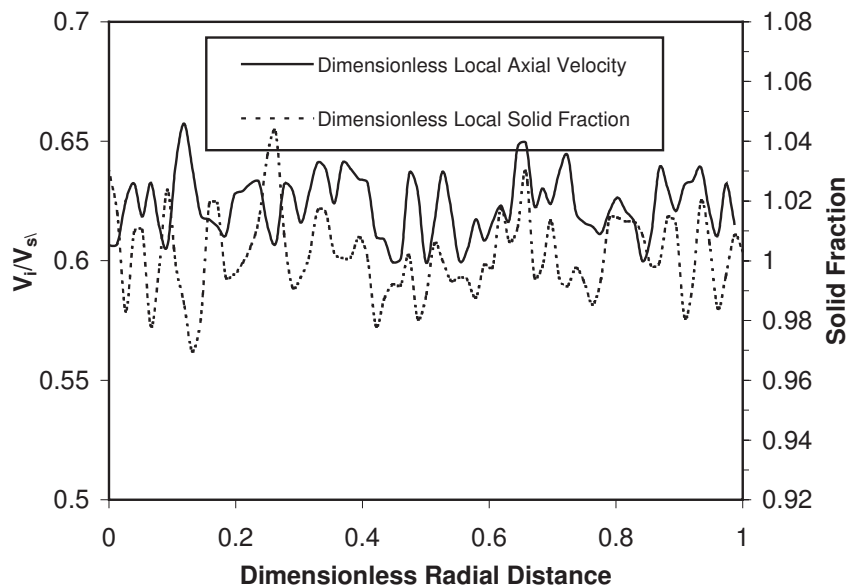


Figure 7.9: Variation of Solid Volume Fraction in Radial Direction and Predicted Results of Velocity Distribution along Radial Direction for Commercial Scale Reactor. ($D_R=1.9\text{m}$, $\epsilon_B=0.37$, $\text{LHSV}=3\text{ h}^{-1}$ and $Q_G/Q_L=300\text{ m}^3/\text{m}^3$)

0.15 when liquid velocity increased from 0.21 to 2.3 mm/sec at $V_G=11$ mm/sec for air water system. In this case with actual reaction condition, predicted liquid holdup varies from 0.01 to 0.07 when liquid velocity varied from 0.06 to 0.5 mm/sec for a particular Q_G/Q_L ratio of 200. Predicted pressure drop per unit length and liquid holdup profiles for commercial reactors are shown in Figure 7.11. Pressure drop per unit length for commercial reactors are in the $O10^4 - 10^5$ and liquid holdup varies from 0.14 to 0.18 for 1-4 h^{-1} variation in LHSV at $Q_G/Q_L=300$. Unfortunately experimental data for hydrodynamic parameters for laboratory scale as well as commercial scale reactor at operating condition is not available for comparison. Developed CFD model was further used to predict the performance of the commercial reactor and compared with that of laboratory scale reactor and these results are discussed in next section.

7.3.2.2 Hydroprocessing Reactor Performance

Velocity profiles and phase distribution inside the laboratory and commercial scale reactors were obtained using CFD model. Hydroprocessing reactor performance was simulated using developed CFD model. From Figure 7.12, it can be seen that conversion at the outlet of laboratory scale reactor is lower than that of commercial reactor. Outlet sulfur concentration for commercial reactor much lower and high temperature reactor performance does not get much affected (see Figure 7.13). Similar trends were observed when conversion of poly- and total-aromatic compounds was compared with laboratory scale reactor at different temperatures (See Figure 7.14).

However, at low temperature (593 K), difference in performance of the laboratory and commercial reactor is quite higher at different LHSV as shown in Figure 7.15. Performance of the commercial scale reactor is always observed better for example, when conversion of

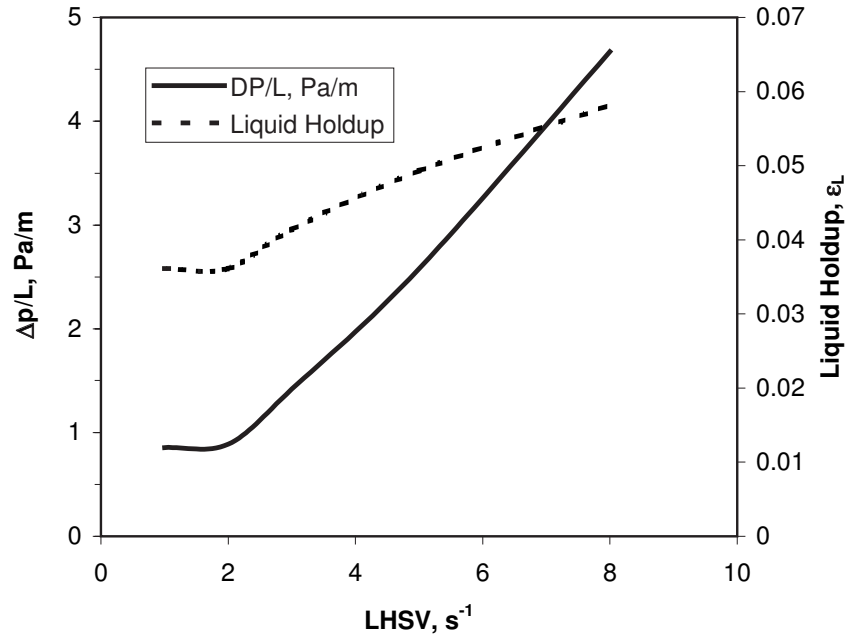


Figure 7.10: Simulated Pressure drop and Liquid holdup for Laboratory scale TBR. (P=4 MPa, LHSV=2.0 h⁻¹ and $Q_G/Q_L=200 \text{ m}^3/\text{m}^3$)

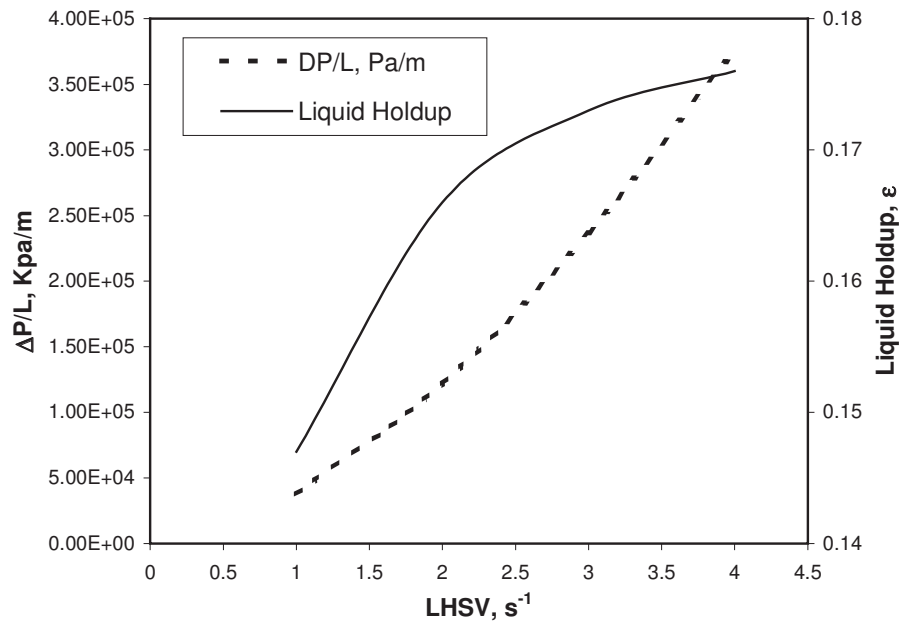


Figure 7.11: Simulated Pressure drop and Liquid holdup for Commercial Scale TBR. (P=4 MPa, LHSV=2.0 h⁻¹ and $Q_G/Q_L=200 \text{ m}^3/\text{m}^3$)

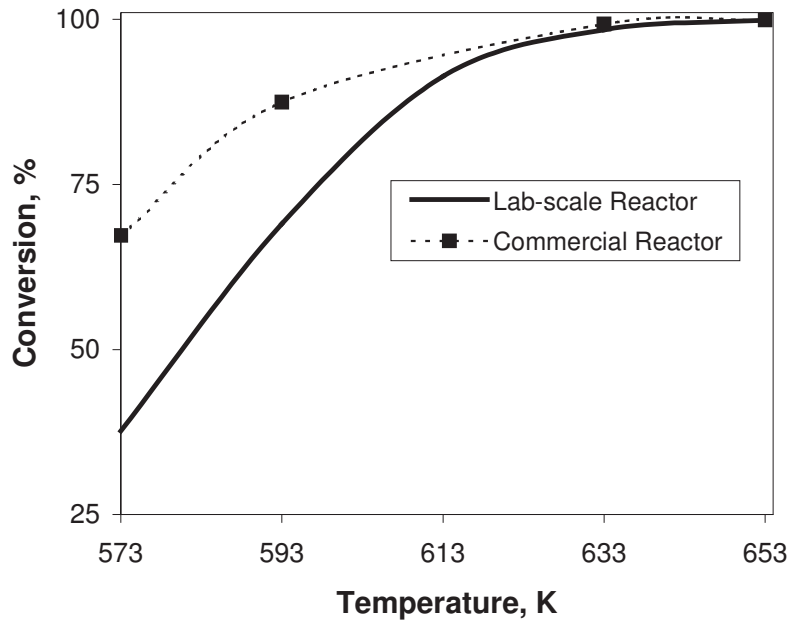


Figure 7.12: Comparison between Laboratory and Commercial Reactor: Conversion of Aromatics Sulfur Compound at Different Temperature ($P_{lab\&comm}=4$ & 4.4 MPa, $LHSV_{lab\&comm}=2.0$ 3.0 h^{-1} , $(Q_G/Q_L)_{lab\&comm}=200$ & 300 m^3/m^3 and $y_{H_2S}=1.4\%$)

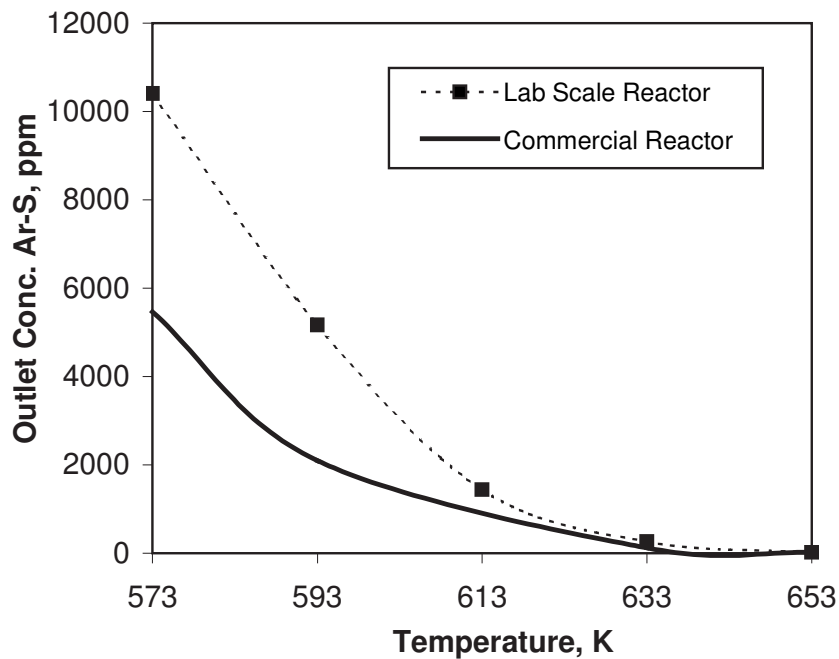


Figure 7.13: Comparison between Laboratory and Commercial Reactor: Outlet Sulfur Composition at Different Temperature. ($P_{lab\&comm}=4$ & 4.4 MPa, $LHSV_{lab\&comm}=2.0$ & 3.0 h^{-1} , $(Q_G/Q_L)_{lab\&comm}=200$ & 300 m^3/m^3 and $y_{H_2S}=1.4\%$)

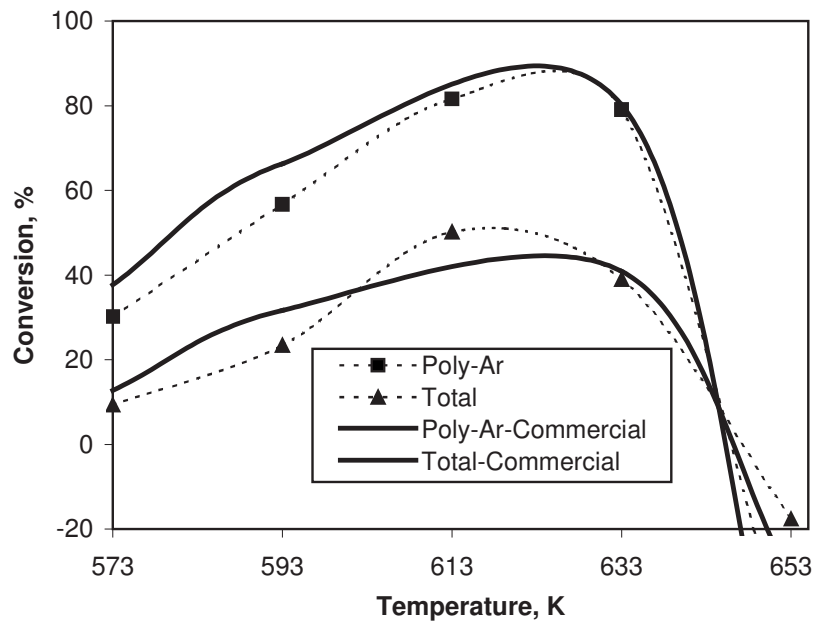


Figure 7.14: Comparison between Laboratory and Commercial Reactor: Poly and Mono-aromatic Conversion at Different Temperature ($P_{lab\&comm}=4$ & 4.4 MPa, $LHSV_{lab\&comm}=2.0$ & $3.0\ h^{-1}$, $(Q_G/Q_L)_{lab\&comm}=200$ & $300\ m^3/m^3$ and $y_{H_2S}=1.4\%$)

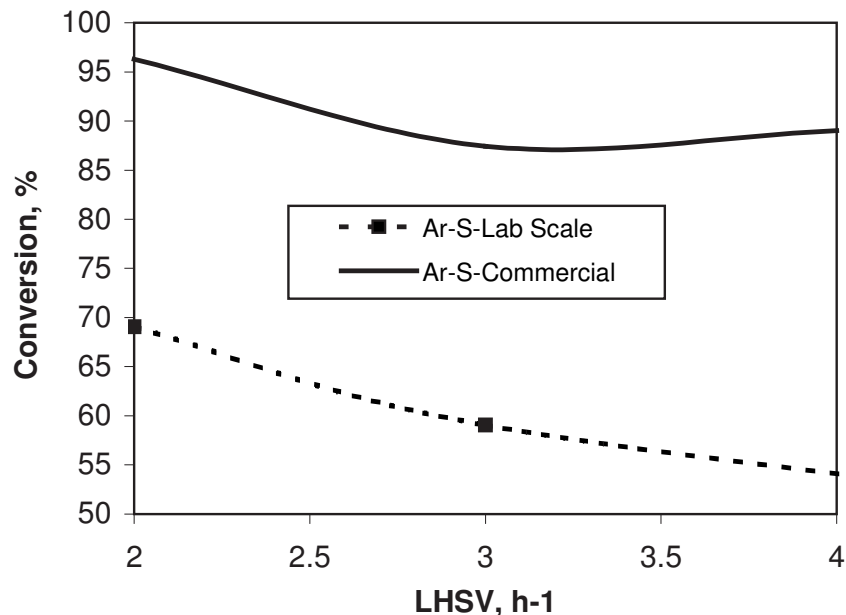


Figure 7.15: Comparison between Laboratory and Commercial Reactor: Conversion of Aromatic Sulfur Compound at Different LHSV. ($P_{lab\&comm}=4$ & 4.4 MPa, $T=593\ K$, $(Q_G/Q_L)_{lab\&comm}=200$ & $300\ m^3/m^3$ and $y_{H_2S}=1.4\%$)

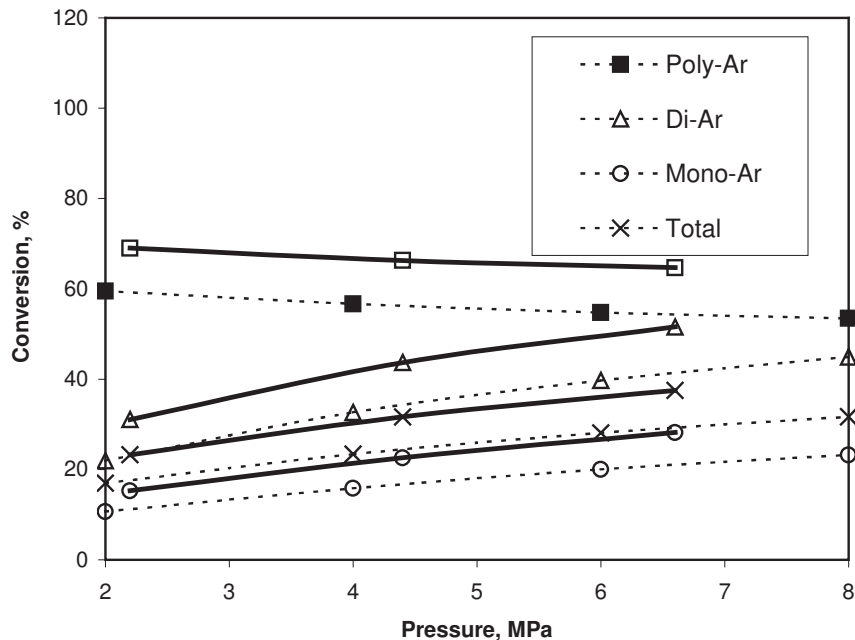


Figure 7.16: Comparison between Laboratory and Commercial Reactor: Conversion of all Aromatic Compounds at Different Pressure ($LHSV_{lab\&comm}=2.0$ & $3.0\ h^{-1}$, $T=593\ K$, $(Q_G/Q_L)_{lab\&comm}=200$ & $300\ m^3/m^3$ and $y_{H_2S}=1.4\%$)

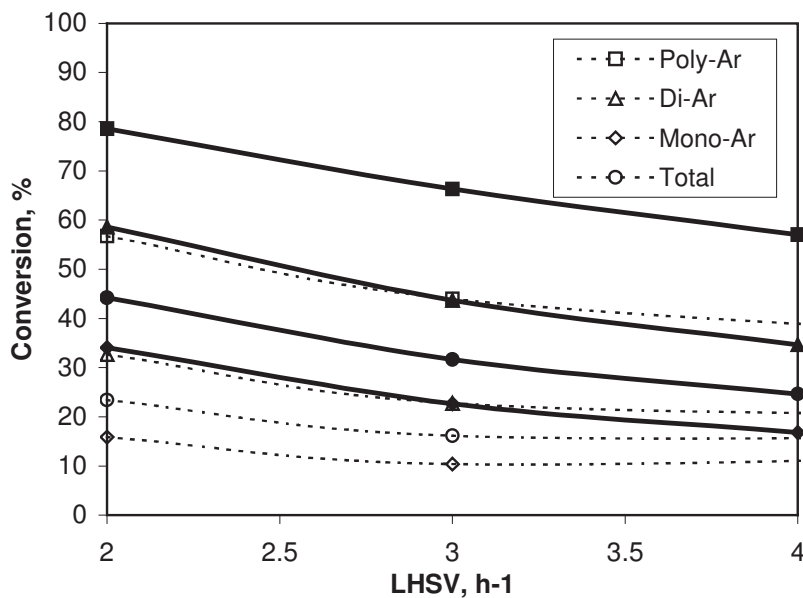


Figure 7.17: Comparison between Laboratory and Commercial Reactor: Conversion of Aromatics Compound at Different LHSV. ($P_{lab\&comm}=4$ & $4.4\ MPa$, $T=593\ K$, $(Q_G/Q_L)_{lab\&comm}=200$ & $300\ m^3/m^3$, $y_{H_2S}=1.4\%$)

all aromatic compounds were compared with laboratory data at different pressure and LHSV in Figure 7.16 and Figure 7.17 respectively. Similar trends were also observed in recent studies of Rodríguez and Ancheyta (2004)¹³⁴ when they extended their plug flow laboratory model to evaluate the performance of the commercial reactor. Objective of this work is not to compare the performance of laboratory and commercial reactor but to carry out the parametric sensitivity study using CFD model. There can be several reasons for under performance of the laboratory scale reactors such as superficial velocities of gas and liquid phases are quite lower than that of commercial bed, catalyst loading, liquid bypassing, different mass transfer rates are the possible reasons. However, present efforts will be helpful in detailed analysis of these parameters, which requires rigorous validity of model using laboratory scale reactor data before proceeding to the designing of actual commercial scale reactor or vice versa.

7.4 Conclusion

In this chapter, application of CFD model for evaluation of the performance of the hydroprocessing trickle bed reactors were studied in which basic model and kinetics parameters were considered from literature (*Chowdhury et al.*¹⁶). Performance of the laboratory scale reactor was first simulated and model results were first validated with experimental data. Observed discrepancy between experimental data and CFD model may be due to non-accounting of wetting efficiency, which is an important parameter for laboratory scale reactor. Using conventional model, this discrepancy is less may be due to assumption of uniform porosity. In trickle bed model, there are several parameters to which performance of reactor is sensitive. However, developed CFD model can be used to reduce the assumptions needed during the formulation of model. For example, pressure drop and liquid holdup are important parameters during designing the reaction, which can be predicted

using CFD model instead of relying on correlations. Apart from these hydrodynamic parameters, model also provides the detailed distribution of velocity and holdup. Developed CFD model was also extended to simulate the performance of the commercial scale reactor. Predicted results show at lower operating temperature (537 to 613 K), performance of laboratory scale reactor is lower than that of commercial scale reactor and at higher temperature reactor scale does not matter much. However, before concluding any thing, it should keep in mind that there is much scope to improve present model and check for the predicted results.

Bibliography

1. Suekane T. and Y. Yokouchi and S. Hirai. Inertial flow structures in a simple-packed bed of spheres. *AIChE J.*, 49:1, 2003.
2. Sederman A. J., Johns M. L., Bramley A. S., Alexander P., and Gladden L. F. Magnetic resonance imaging of liquid flow and pore structure within packed bed. *Chem. Engng. Sci.*, 52:2239, 1997.
3. Ranz W. E. Friction and transfer co-efficient for single particles and packed beds. *Chem. Engng Prog.*, 48(8):247, 1952.
4. Wakao N., S. Kaguei, and T. Funazkri. Effect of fluid dispersion coefficient on particle-to-fluid heat transfer coefficients in PackedBeds-correlations of nusselt numbers. *Chem Eng. Sci.*, 34:325, 1979.
5. Sie S. T. and Krishna R. Process development and scale-up-III: Scale-up and scale-down of trickle bed processes. *Rev. in Chem. Engng.*, 14:203–251, 1998.
6. Wang R., Mao Z., and Chen J. Experimental and theoretical studies of pressure drop hysteresis in trickle bed reactors. *Chem. Eng. Sci.*, 50:2321, 1995.
7. Calis H. P., Nijenhuis A. J., Paikert B. C., Dautzenberg F. M., and Van Den Bleek C.M. Cfd modelling and experimental validation of pressure drop and flow profile in a novel structured catalytic reactor packing. *Chem. Eng. Sci.*, page 1713, 2001.
8. Guardo A., Coussirat M., Larrayoz M. A., Recasens F., and Egusquiza E. CFD flow and heat transfer in nonregular packings for fixed bed equipment design. *I and EC*, 43(22):7049, 2004.
9. Ranade V. V. and R. P. Utikar. Dynamics of gas-liquid flows in bubble column reactors. *Chem. Eng. Sci.*, 54:5237, 1999.

10. Letzel H. M., Schouten J. C., Krishna R., and Van Den Bleek C. M. Characterization of regimes and regime transitions in bubble columns by chaos analysis of pressure signals. *Chem Eng. Sci.*, 52:4447, 1997.
11. Van Den Bleek, Coppensa Marc-Olivier, and Schoutenb J. C. Application of chaos analysis to multiphase reactors. *Chem. Engng. Sci.*, 57:4763, 2002.
12. Ranade V. V. *Computational flow modeling for chemical reactor engineering*. Academic Press, London., 2002.
13. Jiang Y. AndKhadilkar M. R., Al-Dahhan M., and Dudukovic M. P. Cfd of multiphase flow in packed bed reactors: I. modeling issues. *AIChE J*, 48(4):701–715, 2002.
14. ASME Symposium on Numerical Methods for Multiphase Flows. *A Cell Centered ICE Method for Multiphase Flow Simulations*, Lake Tahoe, Nevada, 1994.
15. Mueller G. E. Prediction of radial porosity distribution in randomly packed fixed beds of uniformly sized spheres in cylindrical containers. *Chem. Engng. Sci.*, 46:706, 1991.
16. Chowdhury R, Pedernera E., and Reimert R. Trickle-bed reactor model for desulfurization and dearomatization of diesel. *AIChE Journal*, 48:126, 2002.
17. Sederman A.J. and Gladden L.F. Magnetic resonance visualization of single- and two-phase flow in porous media. *Mag. Res. Img.*, 19:339, 2001.
18. Logtenberg S. A., Nijemeisland M., and Dixon A.G. Computational fluid dynamics simulations of fluid flow and heat transfer at the wall-particle contact points in a fixed bed reactor. *Chem. Engng. Sci.*, 54:2433, 1999.
19. Dixon A. G. and Nijemeisland M. CFD as a design tool for fixed-bed reactors. *Ind. Eng. Chem. Res.*, 40:5246, 2001.
20. Tobis J. Influence of bed geometry in its frictional resistance under turbulent flow conditions. *Chem. Engng. Sci.*, 55:5359, 2000.
21. Zeiser T., Steven M., Freund H., Lammers P., Brenner G., Durst F., and Bernsdorf J. Analysis of the flow field and pressure drop in fixed-bed reactors with the help of lattice boltzmann simulations. *Philosophical Transactions of the Royal Society of London A*,, 360:507, 2002.
22. Freund H., Zeiser T., Huber F., Klemm E., Brenner G., and Durst F. and Emig G. Numerical simulations of single phase reacting flows in randomly packed/fixed-bed reactors and experimental validation. *Chem. Engng. Sci.*, 58:903, 2003.

23. Nijemeisland M. and Dixon A. G. CFD study in fluid flow and wall heat transfer in a fixed bed of spheres. *AIChE J*, 50(5):906, 2004.
24. Nijemeisland M. and Dixon A. G. CFD study in fluid flow and wall heat transfer in a fixed bed of spheres. *AIChE J*, 50(5):906, 2004.
25. Dhole S. D., Chhabra R. P., and Eswaran V. Power law fluid through beds of spheres at intermediate reynolds numbers: Pressure drop in fixed and distended beds. *Chem. Eng. Res. and Des.*, 82(A6):1–11, 2004.
26. Martin J. J., McCabe W. L., and Monrad C. C. Pressure drop through stacked spheres. *Chem. Engng. Prog.*, 47(2):91, 1951.
27. SØrensen J. P. and Stewart W. E. Computation of forced convection in slow flow through ducts and packed beds-III. heat and mass transfer in a simple cubic array of spheres. *Chem. Engng. Sci.*, 29:827, 1974.
28. Seguin D., Montillet A., Comiti J., and Huet F. Experimental characterization of flow regimes in various porous media-ii: Transition to turbulent regime. *Chem. Eng. Sci.*, 53:3897–3909, 1998.
29. Seguin D., Montillet A., and Comiti J. Experimental characterization of flow regimes in various porous media-i: Limit of laminar flow regime. *Chem. Engng. Sci.*, 53(21):3751, 1998.
30. Hill R. J., D. L. Koch, and A. J. C. Ladd. The first effects of fluid inertia on flows in ordered and random arrays of spheres. *J. Fluid Mech.*, 448:213, 2001a.
31. Hill R. J., Koch D. L., and Ladd A. J. C. Moderate-reynolds-number flows in ordered and random arrays of spheres. *J. Fluid Mech.*, 448:243, 2001a.
32. Chhabra R. P., Comiti J., and Machac I. Flow of non-newtonian fluids in fixed and fluidized bed. *Chem. Eng. Sci.*, 56:1–27, 2001.
33. Jolls K.R. and Hanratty T.J. Transition to turbulence for flow through a dumped bed of spheres. *Chem. Eng. Sci.*, 21:1185–1190, 1966.
34. Latifi M.A., Midoux N., Storck A., and Gence J.M. The use of microelectrodes in the study of flow regimes in a packed bed reactor with single phase liquid flow. *Chem. Eng. Sci.*, 44:2501–2508, 1989.
35. Sangani A. S. and Acrivos A. Slow flow through a periodic array of spheres. *Int. J. Multiphase Flow*, 8:343, 1982.

36. Durst F., Haas R., and Interthal W. The nature of flows through porous media. *J. Non-Newton. Fluid Mech*, 22:169, 1987.
37. Maier R. S., Kroll D. M., Kutovsky Y. E., Davis H.T., and Bernard R. S. Simulation of flow through bead packs using the lattice-boltzmann method. *Phys. Fluids*, 10:60, 1988.
38. Magnico P. Hydrodynamic and transport properties of packed bed in small tube-to-sphere diameter ratio: Pore scale simulation using an eularian and a lagrangian approach. *Chem Engng. Sci.*, 58:5005, 2003.
39. Mantle M. D, Sederman A. J., and Gladden L. F. Single and two-phase flow in fixed-bed reactors: MRI flow visualization and lattice-boltzmann simulation. *Chem. Engng. Sci.*, 56:523–529, 2001.
40. Natarajan R. and Acrivos A. The instability of the steady flow past spheres and disks. *J. Fluid Mech.*, 254:323, 1993.
41. Launder B. E. and Spalding D. B. The numerical calculations of turbulent flows. *Computational Methods of Applied Mechanical Engineering*, 3:269, 1974.
42. Wolfstein. M. The velocity and temperature distribution of one-dimensional flow with turbulence augmentation and pressure gradient. *Int. J. Heat Mass Transfer*, 12:301, 1969.
43. Jongen. T. *Simulation and Modeling of Turbulent Incompressible Flows*. PhD thesis, EPF Lausanne, Lausanne, 1992.
44. Kader B. Temperature and concentration profiles in fully turbulent boundary Layers. *Int. J. Heat Mass Transfer*, 24(9):1541, 1993.
45. Kim S.E. and Choudhury D. A near-wall treatment using wall functions sensitized to pressure gradient. *In ASME FED, Separated and Complex Flows. ASME.*, page 217, 1995.
46. Bird R. B., Stewart W. E., and Lightfoot E. N. *Transport Phenomena*. John Wiley and Sons, 1960.
47. Gunjal P. R, Ranade V. V., and Chaudhari R. V. Liquid phase residence time distribution in trickle bed reactors: Experiments and CFD simulations. *Can. Jou. of Chem. Eng.*, 81:821, 2003.
48. Gladden L. F. Magnetic resonance: Ongoing and future role in chemical engineering research. *AIChE. J.*, 49:1, 2003.

49. Szady M. J. and Sundaresan S. Effect of boundaries on trickle-bed hydrodynamics. *AIChE J*, 37:1237–1241, 1991.
50. Liu D. Y., Wang G. X., and Litster J. D. Unsaturated liquid percolation flow through nonwetted packed beds. *AIChE. J.*, 48:953, 2002.
51. Stow C. D. and Hadfield M. G. An experimental investigation of fluid flow resulting from impact of a water drop with an unyielding dry surface. *Proc. R. Soc. Lond. A*, 373:419, 1981.
52. Chandra S. and Avedisian C.T. On the collision of a droplet with a solid surface. *Proc. R. Soc. Lond. A*, 432:13, 1991.
53. Scheller B. L. and Bousfield D.W. Newtonian drop impact with solid surface. *AIChE J.*, 41(6):1357–1367, 1995.
54. Zhang X and Basaran O. A. Dynamic surface tension effect in impact of a drop with a solid surface. *J. Colloid Interface Sci.*, 187:166, 1997.
55. Mao T., Kuhn D. C. S., and Tran H. Spread and rebound of liquid droplets upon impact on flat surfaces. *AIChE J*, 43(9):2169–2179, 1997.
56. Crooks R., Whitez J. C., and Boger D. V. The role of dynamics surface tension and elasticity on the dynamics of drop impact. *Chem. Eng. Sci.*, 56:5575, 2001.
57. Bergeron V., Bonn D., Martin J. Y., and Vovelle L. Controlling droplet deposition with polymer additives. *Nature*, 405:772, 2000.
58. Richard D., Clanet C., and Quéré D. Contact time of a bouncing drop. *Nature*, 417:6891, 2002.
59. Rioboo R., Marengo M., and Tropea C. Time evolution of liquid drop impact onto solid dry surfaces. *Experiments in Fluids*, 33:112, 2002.
60. Pasandideh-Fard M., Chandra S., and Mostaghimi J. Capillary effect during droplet impact on a solid surface. *Phys. Fluids*, 8:650, 1996.
61. Mourougou-Candoni N., Prunet-Foch B. and Legay F., Vignes-Adler M., and Wong K. Influence of dynamic surface tension on the spreading of surfactant solution droplets impacting onto a low-surface-energy solid substrate. *Jou. of Coll. and Int. Sci.*, 192:129, 1997.
62. Thoroddsen S. T. and Sakakibara J. Evolution of the fingering pattern of an impacting drop. *Physics of Fluids*, 10:1359, 1998.

63. Fukai J., Shiiba Y., Yamamoto T., Miyatake O., Poulikakos D., Megaridis C. M., and Zhao Z. Wetting effects on the spreading of a liquid droplet colliding with a surface: Experiment and modeling. *Phys. Fluids.*, 7:236, 1995.
64. Bussmann M., Chandra S., and Mostaghimi J. Modeling of a droplet impacting on solid surface. *Phys. Fluids*, 12:3121, 2000.
65. Davidson M. R. Boundary integral prediction of the spreading of an inviscid drop impacting on a solid surface. *Chem Eng. Sci.*, 55:1159, 2000.
66. Davidson M. R. Spreading of inviscid drop impacting on liquid film. *Chem. Eng. Sci.*, 57:3639, 2002.
67. Pasandideh-Fard M, Chandra S., and Mostaghimi J. A three-dimensional model of droplet impact and solidification. *Int. J. Heat and Mass Transfer*, 45:2229, 2002.
68. McHyman J. Numerical methods for tracking interfaces. *Physica D*, 12:396, 1984.
69. Unverdi S. O. and Tryggvason G. A front tracking method for viscous, incompressible, multi-fluid flows. *Journal of Computational Physics*, 100:25, 1992.
70. Monaghan J. J. Simulating free surfaces with SPH. *Journal of Computational Physics*, 110:339, 1994.
71. Ranade V.V. *Computational Flow Modeling for Chemical Reactor Engineering*. Academic Press, London, 2002.
72. Hirt C.W. and Nichols B. D. Volume of fluid (VOF) method for the dynamics of free boundaries. *J. Comput. Phys.*, 39:201–225, 1981.
73. Rider W.J. and Kothe D.B. Stretching and tearing interface tracking methods. *AIAA Paper*, 95:1717, 1995.
74. Rudman M. Volume tracking methods for interfacial flow calculations. *International Journal for Numerical Methods in Fluids*, 24:671, 1997.
75. Brackbill J.U., Kothe D.B., and Zemach C. A continuum method for modeling surface tension. *J. Comput. Phys*, 100:335, 1992.
76. Youngs D. L. Time-dependent multi-material flow with large fluid distortion. In K. W. Morton and Editors M. J. Baines, editors, *Numerical Methods for Fluid Dynamics*, 1982.
77. Rider W. J. and Kothe D. B. Reconstructing volume tracking. *Journal of Computational Physics*, 141:112–152, 1998.

78. Richard D. and Quéré D. Bouncing water drops. *Europhys. Lett.*, 50:769, 2000.
79. 8th CFD Society of Canada. *Effect of Surrounding Gas on Droplet Impact*, Montreal, Quebec, June 11-13 2000.
80. Adamson A. W. *Physical Chemistry of Surfaces*. Wiley, New York, 4th edition, 1982.
81. Latifi M.A, S. Rode, N. Midoux, and A. Storck. The use of microelectrodes for the determination of flow regimes in a tricklebed reactor. *Chem. Eng. Sci.*, 47:1955, 1992.
82. Latifi M. A., S. Rode, N. Midoux, and A. Storck. Hydrodynamic study of a trickle-bed reactor by means of microelectrodes: Analysis of the probability densities. *Chem. Eng. Sci.*, 47:2331, 1992b.
83. Drahos J., Zahradnik J., Puncochar M., Flalova M., and Bradka F. Effect of operating conditions on the characteristics of pressure fluctuations in a bubble column. *Chem. Eng. Pro.*, 29:197, 1991.
84. Lin T. J., Juang R. C., Chen Y.C., and Chen C. C. Predictions of flow transitions in a bubble column by chaotic time series analysis of pressure fluctuations signals. *Chem. Eng. Sci.*, 56:1057, 2001.
85. Krieg D. A., Helwick J. A., and McCreedy M. J. Origin of disturbances in cocurrent gas-liquid packed bed flows. *AIChE J.*, 41(7):1653, 1995.
86. Horowitz G. I., Cukierman A. L., and M. A. Cassanello. Flow regime transition in trickle beds packed with particles of different wetting characteristics- check-up on new tool. *Chem. Eng. Sci.*, 52:3747, 1997.
87. Urseanu M. I., Boelhouwer J. G., Bosmanand H. J. M., and Schroijsen J. C. Induced pulse operation of high-pressure trickle bed reactors with organic liquids: Hydrodynamics and reaction study. *Chem. Eng. and Proc.*, 43(11):1411, 2004.
88. Al-Dahhan M. H. and Dudukovic M. P. Pressure drop and liquid holdup in high-pressure trickle-bed reactors. *Chem. Engng. Sci.*, 49:5681–5698, 1994.
89. Saez A. E. and Carbonell R. G. Hydrodynamic parameters for gas-liquid co-current flow in packed beds. *AIChE. J.*, 31:52–62, 1985.
90. Herskowitz M. and Smith J. M. Trickle bed reactors: A review. *AIChE. J.*, 1:29, 1983.
91. Kan K. M. and Greenfield P. F. Multiple hydrodynamic states in cocurrent two phase down flow through packed beds. *Ind. Engng Chem. Process Des. Dev.*, 17:482, 1978.

92. Kan K. M. and Greenfield P. F. Pressure drop and hold up in two phase cocurrent trickle flows through beds of small particles. *Ind. Engng Chem. Process Des. Dev.*, 18:740, 1979.
93. Christensen G., Sundaresan S., and McGovern S. J. Cocurrent downflow of air and water in a two dimensional packed column. *AIChE Journal*, 32(10):179, 1986.
94. Levec J., Saez A. E., and Carbonell R. G. The hydrodynamics of trickling flow in packed beds, part II: Experimental observations. *AIChE Journal*, 32:369, 1986.
95. Levec J., Grosser K., and Carbonell R. G. The hysteretic behavior of pressure drop and liquid hold up in trickle beds. *AIChE Journal*, 34:1027, 1988.
96. Rode S, N. Midoux;, M. A. Latifi, and A. Storck. Multiple hydrodynamic states in trickle beds operating in high interaction regimes: Liquid saturation and flow regime transitions. *Chem. Eng. Sci.*, 49:2535, 1994.
97. Chu C. F. and Ng K. M. Model for pressure drop hysteresis in trickle beds. *AIChE Journal*, 35:1677, 1989.
98. Ravindra P. V., Rao D. P., and Rao M. S. Liquid flow texture in trickle bed reactors: An experimental study. *Ind. Eng. Chem. Res.*, 36:5133–5145, 1997.
99. Melli T. R. and Scriven L. E. Theory of two phase cocurrent downflow in networks of passages. *Ind. and Eng. Chem. Res.*, 30:951, 1991.
100. Schouten J. C., Takens F., and Van Den Bleek C. M. Estimation of the dimension of a noisy attractor. *Physical Review E*, 49:126, 1994.
101. Attou A. and Ferschneider G. A two-fluid hydrodynamic model for the transition between trickle and pulse flow in a cocurrent gas-liquid packed-bed reactor. *Chem. Engng. Sci.*, 55:491–511, 2000.
102. Boyer C., Duquenneb A., and Wild G. Measuring techniques in gas-liquid and gas-liquid-solid reactors. *Chem. Engng. Sci.*, 57:3185–3215, 2002.
103. Al-Dahhan M.H., Larachi F., Dudukovic M. P., and Laurent A. High-pressure trickle-bed reactors: A review. *IEC Res*, 36:3292, 1997.
104. Jiang Y. *Flow Distribution and its Impact on Performance of Packed-Bed Reactors*. PhD thesis, Washington University, Saint Louis, Missouri, USA., 2000.
105. Stephenson J. L. and Stewart W. E. Optical measurements of porosity and fluid motion in packed beds. *Chem. Engng. Sci.*, 41:2161–2170, 1986.

106. Spedding P. L. and Spencer R. M. Simulation of packing density and liquid flow in fixed beds. *Comp. Chem. Engng.*, 19:43–73, 1995.
107. Crine M., Marchot P., and L’Homme G. A. Mathematical modeling of the liquid trickling flow through a packed bed using the percolation theory. *Comp. Chem. Eng.*, 3:515, 1979.
108. Thompson K. E. and Fogler H. S. Modeling flow in disordered packed beds from pore-scale fluid mechanics. *AIChE. J.*, 43:1377–1389, 1997.
109. Yin F. H., Sun C. G., Afacan A., Nandakumar K., and Chung K. T. CFD modeling of mass-transfer processes in randomly packed distillation columns. *Ind. Eng. Chem. Res.*, 39:1369, 2000.
110. Attou A., Boyer C., and Ferschneider G. Modeling of the hydrodynamics of the cocurrent gas-liquid trickle flow through a trickle-bed reactor. *Chem. Engng. Sci.*, 54:785–802, 1999.
111. Grosser K., Carbonell R. G., and Sundaresan S. Onset of pulsing in two-phase concurrent downflow through a packed bed. *AIChE J.*, 34:1850–1860, 1988.
112. Holub R. A., Dudukovic M. P., and Ramachandran P. A. A phenomenological model for pressure drop, liquid holdup, and flow regime transition in gas-liquid trickle flow. *Chem. Eng. Sci.*, 47:2343, 1992.
113. Holub R. A., Dudukovic M.P., and Ramachandran P. A. Pressure drop, liquid hold-up and flow regime transition in trickle flow. *AIChE. J.*, 39:302–321, 1993.
114. Rao V.G., Ananth M. S., and Varma Y. B. G. Hydrodynamics of two-phase cocurrent downflow through packed beds. *AIChE. J.*, 29:467–473, 1983.
115. Specchia V. and Baldi G. Pressure drop and liquid holdup for two-phase concurrent flow in packed beds. *Chem. Engng. Sci.*, 32:515–523, 1977.
116. Turpin J. L. and Huntington R. L. Prediction of pressure drop for two-phase, two component cocurrent flow in packed beds. *AIChE. J.*, 13:1196–1202, 1967.
117. Boelhouwer J. G., Piepers H. W., and Drinkenburg A. A. H. Liquid-induced pulsing *Chem. Eng. Sci.*, 57:3387, 2002.
118. Ramachandran P. A. and Smith J. M. Dynamic behavior of trickle bed reactor. *Chem. Eng. Sci.*, 34:75–91, 1978.
119. Schwartz J. G., Weger E., and Dudukovic M. P. A new tracer method for the determination of liquid-solid contacting efficiency in trickle bed reactors. *AIChE. J.*, 22:953, 1976.

120. Oliveros G. and Smith J. M. Dynamic studies of dispersion and channeling in fixed beds. *AIChE J*, 28:751–759, 1982.
121. Hanratty P. J. and Dudukovic M. P. Detection of flow maldistribution in trickle-bed reactors via tracers. *Chem. Engng. Sci*, 47:3003–3014, 1992.
122. Higler A. P., Krishna R., Ellenberger J., and Taylor R. Counter-current operation of a structured catalytically packed-bed reactor: Liquid phase mixing and mass transfer. *Chem. Engng. Sci.*, 54(21):5145–5152, 1999.
123. Gulijk C. V. Using computational fluid dynamics to calculate transversal dispersion in a structured packed bed. *Comp. Chem Eng*, 22:5767–5770, 1998.
124. Gunjal P. R., Kashid M. N., Ranade V. V., and Chaudhari R. V. Chaudhari hydrodynamics of trickle-bed reactors: Experiments and CFD modeling. *Ind. Eng. Chem. Res.*, 2005.
125. Sapre A. V., Anderson D. H., and Krambeck F. J. Heater probe technique to measure flow mal-distribution in large scale trickle-bed reactors. *Chem. Engng. Sci.*, 45:2263–2268, 1990.
126. Song M. and Yin F. H. and Nandakumar K. and Chuang K. T. A three-dimensional model for simulating the mal-distribution of liquid flow in random packed beds. *Can. J. Chem. Eng.*, 76:161–166, 1998.
127. Henry C. H. and Gilbert J. B. Scaleup of pilot plant data for catalytic hydroprocessing. *Ind. Eng. Process Des. Dev.*, 12(3):328–333, 1973.
128. Iannibello A, Marengo S., Burgio G., Baldi G., Sicardi S., and Specchia V. Modeling the hydrotreating reactions of a heavy residual oil in a pilot trickle bed reactor. *Ind. Eng. Process Des. Dev.*, 24(3):531–537, 1985.
129. Froment G. F., G. A. Depauw, and V. Valerie. Kinetic modeling and reactor simulation in hydrodesulfurization of oil fractions. *Ind. Eng. Chem. Res.*, 33:2975–2988, 1994.
130. Korsten H. and Hoffmann U. Three-phase reactor model for hydro-treating in pilot trickle-bed reactors. *AIChE Journal*, 42:1350, 1996.
131. Chen J., Ring Z., and Dabros T. Modeling and simulation of a fixed-bed pilot-plant hydrotreater. *Ind. Eng. Chem. Res.*, 40:3294–3300, 2001.
132. Pedernera E., Reimert R. Amd Nguyen N. L., and Van Buren V. Deep desulfurization of middle distillates: process adaptation to oil fractions's compositions. *Catalysis Today*, 79-80:371, 2003.

133. Avraam D. G. and I. A. Vasalos. HdPro: A mathematical model of trickle-bed reactors for the catalytic hydroprocessing of oil feedstocks. *Catalysis Today*, 79-80:275, 2003.
134. Rodr ygtuez M. A. and J. Ancheyta. Modeling of hydrodesulfurization (HDS), hydrodenitrogenation (HDN), and the hydrogenation of aromatics (HDA) in a vacuum gas oil hydrotreater. *Energy and Fuels*, 18:789, 2004.
135. Bhaskar M., Valavarasu G., Sairam B., Balaraman K. S., and Balu K. Three-phase reactor model to simulate the performance of pilot-plant and industrial trickle-bed reactors sustaining hydrotreating reactions. *Ind. Eng. Chem. Res.*, 43:6654–6669, 2004.
136. Jiang Y., M. R. Khadilkar, M. H. Al-Dahhan, and M. P. Dudukovic. CFD modeling of multiphase flow distribution in catalytic packed bed reactors: Scale down issues. *Catalysis Today*, 66:209–218, 2001.
137. Ahmed T. *Hydrocarbon Phase Behavior*. Gulf Publishing, Houston, 1989.
138. Goto S. and Smith J. M. Trickle bed reactors performance: I hold-up and mass transfer effects. *AIChE J*, 21:706, 1975.

Summary

Packed bed reactors are widely used in petrochemical, fine chemical and pharmaceutical industries. Most of the previous studies were related to global flow characteristics and were largely based on empirical correlations developed from experimental data. Recent developments in computational fluid dynamics (CFD) were found to be helpful for understanding the detail transport processes occurring in the reactors. This work was focused on understanding various transport processes occurring at different scales of trickle bed reactors using CFD models and experiments. The work done during this thesis can be divided into three parts; first part dealt with study of transport processes occurring at particle scale, second part dealt with study of transport processes occurring at reactor scale and third part was related to applications of CFD model for evaluating performance of trickle bed reactors.

In particle scale studies, two cases were considered; i) single phase flow through packed bed and ii) spreading of a liquid droplet over solid surface. Computational model (Unit Cell approach) was developed for study of single-phase flow through packed geometry in which different particle arrangements were considered (i.e. simple cubic, face centered cubic and rhombohedral). Computational model was first validated using published data. It was then used to study effect of various parameters like particle orientation and particle Reynolds number on particle drag and heat transfer rate at particle surface. Relative contribution of the form drag and frictional drag was evaluated from simulated results. Overall velocity distribution and heat transfer predicted using unit cell approach was found to be agreeing well with the experimental data on packed bed reactor. In another case, spreading of a liquid drop over a solid surface was studied to understand the physical phenomena occurring during spreading. For this purpose, impact of drop on a solid surface and its spreading were experimentally captured using high-speed camera and effect of various parameters such as

Reynolds number, adsorbed moisture, impact velocity, surface tension and contact angle were studied. Volume of Fluid approach was used to simulate the dynamics of the drop spreading. Different modeling issues such as interface tracking, effect of static and dynamic contact angle were discussed. Various drop-spreading mechanisms (spreading, rebounding and splashing) were studied using experiments and simulations. Simulated results were used to calculate several parameters such as shear stress exerted by liquid on solid surface and strain rate at gas-liquid interface. The sensitivity of the spreading process to dynamic contact angle was demonstrated. Such efforts are useful for understanding wetting behavior in trickle bed reactors.

In reactor scale study, experiments were carried out at two different scales of the reactor. Overall pressure drop, dynamic liquid hold-up and wall pressure fluctuations were measured. Hysteresis was observed in the measured values of pressure drop and liquid hold-up depending on degree of bed-wetting. Effect of various parameters such as particle/bed diameter ratio, distributor type, gas and liquid flow rates on hysteresis and key hydrodynamic parameters was studied. Collected wall pressure fluctuation data was analyzed to calculate the time scales of various transport processes occurring in trickle and pulse flow regimes. A criterion based on Kolmogorov entropy was used to identify transition from trickle to pulse flow regime. CFD model based on the Eulerian-Eulerian framework was developed to simulate gas-liquid flow field in trickle bed reactors. Radial and axial porosity distribution, inter-phase drag and capillarity were considered in the model. Model captures the correct trends of hysteresis as observed in experiments. Further work is needed to fully understand hysteresis in trickle bed reactors. The computational model was used to calculate fraction of liquid hold-up suspended in gas phase. The method is useful to identify transition from trickle to spray flow regime. Validated model was further extended to simulate the periodic flow operation. Though model predictions are in good agreement with experimental data, prediction of liquid phase mixing and its effect on overall performance

of bed are needed to evaluate. Therefore, in the third part of the thesis, residence time distribution and prediction of performance of hydro-processing reactor was carried out. In residence time distribution study, experimentally tracer response was measured and effect of various parameters such as particle to bed diameter ratio, prewetting bed conditions and liquid maldistribution were studied. Bed pre-wetting condition affect the liquid phase mixing considerably especially at low liquid flow rates in trickle flow regime. Predicted flow fields using CFD model was used to predict the tracer response. Simulated results show correct trends for tracer response for pre-wetted and non-prewetted bed conditions. CFD model was also extended to study the liquid maldistribution for uniform and non-uniform liquid inlet condition. For this purpose complete 2D and 3D heterogeneous bed geometry was considered in the model.

To further evaluate the model, a case of hydro-processing reactor was considered in which along with flow, material and energy balance of individual components in gas as well as liquid phases were considered in the model. Various reactions such as hydrogenation of aromatic sulfur compounds and aromatic compounds were considered in the model. Appropriate correlations were used to account for gas-liquid, liquid-solid mass transfer coefficients. Predicted results showed good agreement with the experimental literature data. Porosity distribution in laboratory scale trickle bed reactors is much different from industrial scale reactor and one of the major advantages of CFD model is that reactor geometry and porosity variation can be accounted in model. Therefore it is worthwhile to simulate the performance at different scales of the reactor. These studies will also be useful for understanding scale-up and scale-down issues of the reactor. Such efforts were made here using developed model.

Thus this work is a comprehensive study of fluid dynamics of trickle/packed bed reactors at different scales and its impact on performance of reactors.

Abstract

Packed/trickle bed reactors are extensively used in chemical and petrochemical industries. Knowledge of fluid dynamics inside these reactors is essential for better designing and performance enhancement of the reactors. Recent advances in understanding of physics of flows, numerical techniques and computing resources can be harnessed for better engineering of these reactors. The aim of research discussed in this thesis was to understand gas-liquid flow through packed beds using CFD models and experiments. A typical packed bed consists of several thousands of small particles randomly packed in a cylindrical column. The random packing of particles results in a very complex shape of void space within the column through which gas-liquid flow occurs. It is essential to study flow and transport processes occurring on various spatio-temporal scales relevant to trickle bed reactors (micro-, meso- and macro-scale) and their effect on overall performance of reactor. In this work, comprehensive experimental as well as computational program was undertaken to study the fluid dynamics at different scales of packed bed reactors. This work was comprised of total three parts; study of particle scale flow processes, study of reactor scale flow processes and role of fluid dynamics for performance evaluation of the reactor.

In particle scale flow process study; single-phase flow through different particle arrangements was simulated to understand influence of particle arrangement on flow and key transport characteristics. The computational models were validated using the published experimental data. To understand interaction of liquid with solid surface, spreading of drop on flat as well as curved surfaces was experimentally studied using high-speed camera. CFD models based on Volume of Fluid (VOF) approach was developed to simulate spreading of a drop. Predicted results were validated using experimental data collected over a wide range of operating conditions. For understanding the reactor scale flow processes, experiments were carried out on pilot scale reactors (two different scale reactor)

to measure hydrodynamic characteristics over a wide range of operating conditions. Wall pressure fluctuations were measured to examine various time scales involved in the trickle and pulse flow regime. A criteria based on Kolmogorov entropy was used to identify the flow regime transition from trickle to pulse flow regime. CFD model based on the Eulerian-Eulerian approach was developed to simulate the gas-liquid flow through packed bed. The model was shown to capture key features of experimental data (including hysteresis in pressure drop). The computational model was further extended to quantify fraction of liquid hold-up in the form of spray for the first time. The model was also used to simulate periodic operation of trickle beds. The model was further extended to study the mixing and performance of the reactor. Mixing in trickle bed was studied experimentally using a tracer response technique over a wide range of operating parameters. The predicted tracer responses were compared with the experimentally measured responses. The model was also used to study liquid mal-distribution within the bed. Besides the mixing studies, the model was also used to predict the performance of the hydro-treating reactor.

Keywords: Packed/Trickle Bed, CFD, hydrodynamics, Volume of Fluid (VOF), Eulerian-Eulerian (E-E). RTD, liquid mal-distribution, hydro-processing.

List of Publications/Presentations

PUBLICATIONS

Gunjal P. R., V. V. Ranade and R. V. Chaudhari, Experimental and computational study of flow of liquid droplet over flat and spherical surface, *Catalysis Today*, 79-80 267, (2003).

Gunjal P. R., V. V. Ranade and R. V. Chaudhari, Liquid phase residence time distribution in trickle bed reactors: Experiments and CFD Simulations, *Can. J. Chem. Eng.*, 81, 821, (2003).

Gunjal P. R., V. V. Ranade and R. V. Chaudhari, Computational study of single-phase flow in packed bed of spheres, communicated to *AIChE. J.* 51(2), 365.

Gunjal P. R., V. V. Ranade and R. V. Chaudhari, Dynamics of drop impact on solid surface: experiments and VOF simulations, communicated to *AIChE.J.*, 50(1), 59.

Gunjal P. R., Kashid M. and V. V. Ranade, Hydrodynamics of Trickle Bed Reactors: Experiments and CFD Modeling, *I&EC* in print.

S. P. Mathew, P. R. Gunjal and R. V. Chaudhari, Hydrogenation reaction involving complex reaction network: Kinetics and modeling of semi-batch slurry and basket reactors. Submitted for publication to *IJCRE*

Gunjal P. R. A. Arora and V. V. Ranade, Understanding scale-up and scale-down of Trickle

Bed Reactor using a CFD Model: A case of Hydro-processing reaction, In preparation.

Kulkarni R., P. R. Gunjal, J. Wood and V. V. Ranade, Residence time distribution in trickle bed reactors with and without fines using experimental and CFD modeling, In preparation.

Gunjal P. R. A. K. Gorasia and V. V. Ranade, Computational Models for Packed Bed Reactors: A Review, In preparation.

PRESENTATIONS

S. P. Mathew, P. R. Gunjal, R. V. Chaudhari and P. L. Mills, Hydrogenation of Acetophenone Using Ru/Al₂O₃ in a Trickle Bed Reactor. Presented at **AICHE J annual Meeting** at USA during October 31 to November 5, 1999.

Gunjal P. R., V. V. Ranade and R. V. Chaudhari, Experimental and computational study of flow of liquid droplet over flat and spherical surface, **CAMURE-4** (2002) Switzerland.

Gunjal P. R., V. V. Ranade and R. V. Chaudhari, Liquid phase residence time distribution in trickle bed reactors: Experiments and CFD Simulations, **GLS-6**, Canada

Gunjal P. R. A. Arora and V. V. Ranade, Understanding scale-up and scale-down of Trickle Bed Reactor using a CFD Model: A case of Hydro-processing reaction, Abstract submitted for **Camure-5**, Slovenia.

Gunjal Prashant R. and Vivek V. Ranade (2002), Trickle and Pulse Flow Characterization

Using Wall Pressure Fluctuations, **Chemcon-2002**, Hyderabad, India.

Gunjal P. R and Vivek V. Ranade (2002), Modeling of gas-liquid flows in trickle bed reactors, National Workshop-cum-Symposium on **Complex Fluids**, Indian Institute of Science (IISc), Bangalore

Kashid M. N., P. R. Gunjal, V. V. Borkar and V. V. Ranade (2003), Characterization of liquid distribution in a trickle bed by conductivity mesh probes, **Chemcon-2003**, Bhuwaneshwar, India

Gunjal P. R. and V. V. Ranade (2004), Engineering Via Fluid Dynamics, Manuscript submitted for **thematic issue of INSA**, India.

Kashid M. N., P. R. Gunjal and V. V. Ranade (2004), Experimental studies on dispersion in trickle bed reactor, **Chemcon-2004**, Bombay, India

Index

- analytical results, 39
- AnTS, 120
- Bessel Function, 135
- capillary pressure, 140
- CFD model
 - hydroprocessing, 191
 - trickle bed, 131
- contact angle, 63, 93
- contact angle
 - dynamic, 65
 - static, 65
- curvature, 68
- data acquisition, 115
- dispersed bubble flow, 123
- distributor
 - perforated, 125
 - spray, 125
- distributor plate, 115
- drag coefficient, 39
- drop
 - curvature, 69
- drop dynamics, 56
- drop impact
 - physical picture, 77
 - shear stress, 100
 - strain rate, 100
 - vorticity, 100
- drop interaction, 98
- dynamics of
 - gas-liquid, 118
 - trickle bed, 118
- energy balance, 27
- Experimental setup
 - Drop Impact, 62
- Eulerian-Eulerian, 138
- exit age distribution, 172
- experiments
 - residence time distribution, 167
 - trickle bed, 110, 115

- face centered cubic, 24, 43
- flow mal-distribution, 178
- flow regime
 - drop impact, 78
 - trickle bed, 112
- flow regimes
 - trickle bed, 110
- form drag, 45
- frictional pressure drop, 133, 154
- heat flux, 29
- heat transfer, 50
- heat transfer
 - particle to fluid, 50
- hydrodynamics
 - commercial scale, 204
 - laboratory scale, 204
- hydroprocessing, 186
- hydroprocessing
 - assumptions, 192
 - CFD model, 191
 - kinetic rate expressions, 192
 - laboratory scale, 199
 - mass balance, 194
 - properties of fluids, 195
 - reactions, 192
 - reactor scale, 206
- hysteresis
 - liquid holdup, 124
 - pressure drop, 124
- hysteresis, liquid holdup, 145
- hysteresis, pressure drop, 144
- industrial scale
 - parameters, 188
- k- ϵ model, 27
- kinetic energy, 98
- Kolomogorov entropy, 120
- laboratory scale
 - parameters, 188
- Liquid Drop, 55
- liquid holdup
 - commercial reactor, 204
 - laboratory reactor, 204
 - trickle bed, 123
- low Reynolds number, 39
- momentum exchange, 140
- MRI data, 33
- non-pretreated, 142
- Nusselt Number, 52
- packed bed, 19
- packing arrangement, 42
- particle scale flow, 14
- periodic flow, 155

- periodic flow
 - forced, 155
 - natural, 155
- porosity, 135
- porosity
 - axial, 135
 - radial, 135
- potential energy, 98
- pressure drop, 147
- pressure drop
 - commercial reactor, 204
 - laboratory reactor, 204
 - trickle bed, 123
- prewetted, 142
- pulse flow, 118
- pulse to trickle, 118
- reactor scale, 15
- regime transition, 118
- residence time distribution, 166
- rhombohedral, 24, 43
- RTD
 - bed heterogeneity, 175
 - capillary pressure, 176
 - experimental, 172
 - non uniform inlet, 179
 - simulations, 175
- RTD-flow mal-distribution, 178
- scale down, 186
- scale up, 186
- scale up and scale down
 - issues, 186
- shear drag, 45
- simple cubic, 24, 43
- single phase flow, 19
- spacial scales, 3
- surface energy, 98
- surface tension, 93
- suspended liquid, 148
- temporal scales, 3
- tracer, 168
- tracer response
 - experimental, 172
 - simulation, 170
- turbulence parameters, 27
- turbulent kinematic viscosity, 26
- viscous dissipation, 100
- VOF Model, 65
- VOF model, 66
- VOF Model
 - advection, 75
 - geometric reconstruction, 72
- wall adhesion, 68
- wall pressure fluctuations, 115, 118